

Search for additional Higgs bosons with multi b-quark final states at LHC

Von der Fakultät für Mathematik, Naturwissenschaften und Informatik
der Brandenburgischen Technischen Universität Cottbus

zur Erlangung des akademischen Grades
Doktor der Naturwissenschaften
(Dr. rer. nat.)
genehmigte Dissertation
vorgelegt von

Diplom-Physiker

Ihar Marfin

geboren am 30. März 1979 in Minsk, Weißrussland

Gutachter: Prof. Dr. Wolfgang Lohmann

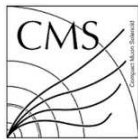
Gutachter: Prof. Dr. Götz Seibold

Gutachter: Dr. Alexei Raspereza

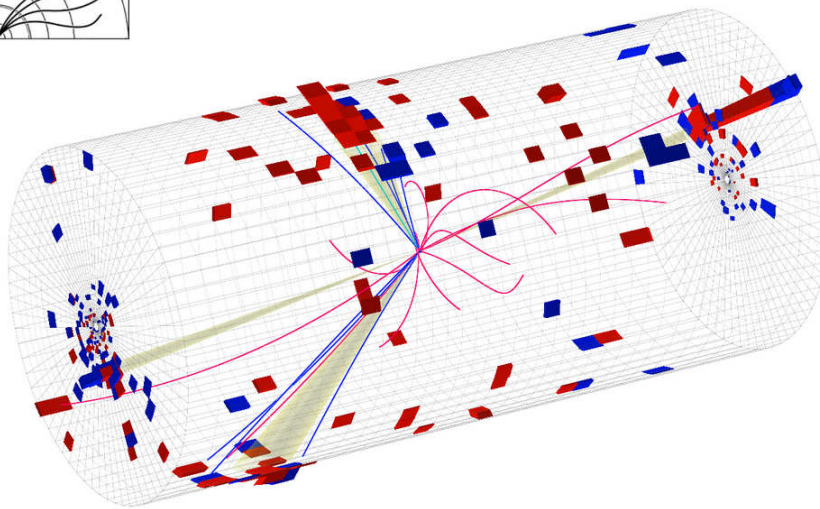
Tag der mündlichen Prüfung: 7. Juli 2014

Search for additional Higgs bosons with multi b-quark final states at LHC

Ihar Marfin



CMS Experiment at LHC, CERN
Data recorded: Sat Aug 4 21:17:51 2012 CEST
Run/Event: 200245 / 198478589
Lumi section: 175



Thesis Submitted for
the Degree of Doctor of Philosophy

April 2014

Acknowledgments

I would like to state my deep appreciation to many different people whose impacts on my progress during PhD is undeniable.

First of all, I would like to express great thanks to my supervisor Wolfgang Lohmann for patience, support, encouragement, knowledge and last minute interventions. With your inspiration, enthusiasm and great efforts to explain even very complicated subjects clearly and simply, you helped me to see how experimental physics is enjoyable. Thank you for giving me the opportunity to pursue this PhD and I am sorry for all the white hair I have caused.

It is not easy to express my deep gratitude to my second supervisor Roberval Walsh. I wish to thank you for all fruitful discussions, support, peacefulness and guidance in hard moments during this thesis-writing period.

I am grateful to all members of the DESY CMS Higgs group for friendly, productive and supportive atmosphere. Thank you, Joerg Behr, Wolfgang Lohmann, Rainer Mankel, Alexei Raspereza, Alexander Spiridonov, Roberval Walsh, Clemens Lange and Matthias Schroeder for the opportunity to work together. I was never stuck with my questions because of you, to whom I could go at any time.

Also I would like to express my gratitude to all members of the CMS/FCAL group in Zeuthen. Thank you for all your support and ideas. Special thanks to Maria Hempel, Matthias Bergholz and Ringo Schmidt for many fruitful and enjoyable discussions. Auch ich möchte euch Danke sagen für die tolle Hilfe bei Fragen zur deutschen Sprache.

I appreciate a lot being part of the CMS group at the Deutsches Elektronen-Synchrotron, my host institute. I want to thank DESY for support in various ways throughout my PhD time, for its friendly, productive and supportive environment.

I would like to thank the CMS Collaboration at CERN for its collaborative, creative and productive environment. Taking part in the Higgs Physics Analysis Group and B-tagging Physics Object Group was a pleasure for me.

Last but not least, I want to thank Julia, my wife. It has been a hard time for you. So many absences, holidays spent working... Thank you for your patience, encouragement, advices, discussions and much more. Thank you for raising Arina and Alisa. Thank you for your love. I am thankful to Elena and Boris, my parents for helping me all through my life, for putting me in the right places at the right moments, for your support in difficult moments.

Erklärung der Selbständigen Anfertigung meiner Dissertationsschrift

Hiermit erkläre ich, dass ich die Dissertationsschrift mit dem Titel

Search for additional Higgs bosons with multi b-quark final states at LHC

selbständig und unter ausschliesslicher Verwendung der angegebenen Hilfsmittel angefertigt habe.

Igor Marfin
Zeuthen, den 17.04.2014

Zusammenfassung

Die $SU(2) \otimes U(1)$ Symmetrie der elektroschwachen Wechselwirkung wird im Standardmodell durch den Higgs Mechanismus spontan gebrochen. Eichbosonen und Fermionen erhalten durch die Wechselwirkung mit dem Higgs Feld ihre Masse. Zudem wird ein neues Teilchen vorhergesagt, das Higgs Boson, als Anregung der Higgs Feldes.

Allerdings gibt es berechtigte Zweifel am fundamentalen Charakter des Standardmodells, z.B. folgt aus kosmologischen Beobachtungen die Existenz dunkler Materie, die im Standardmodell nicht erklärt werden kann. Theoretiker haben daher Erweiterungen des Standardmodells vorgeschlagen, in denen mehrere Higgs Bosonen vorhergesagt werden.

Das am CERN im Jahre 2012 entdeckte Higgs Boson kann sowohl das Higgs Boson des Standardmodells als auch eines der Higgs Bosonen der erweiterten Theorien sein. Die Entdeckung eines weiteren Higgs Bosons wäre ein klares Signal für die Notwendigkeit einer neuen Theorie.

Diese Arbeit beschreibt die Suche nach den neutralen Higgs-Bosonen $\Phi=h, H$ und A im Minimal Supersymmetrischen Standardmodell (MSSM). Von Interesse ist dabei der drei-b-Jet-Endzustand, der durch die Reaktion $pp \rightarrow b\Phi$ entsteht, und in dem das Higgs-Boson am Ende in ein Paar von b-Quarks zerfällt, $\Phi \rightarrow b\bar{b}$. Um einen möglichst reinen Datensatz zu erhalten, ist die Identifikation der b-Jets entscheidend.

Die Suche wird mit den Daten des CMS-Experimentes am Large Hadron Collider (LHC) aus dem Jahr 2011 bei einer Schwerpunktenenergie von 7 TeV durchgeführt. Für die Analyse wurden Daten verwendet, die integrierten Luminositäten der speziellen Higgs-Trigger von 2.7-4.8 fb⁻¹ entsprechen. Im Rahmen der hier vorgestellten Analyse wurden zwei Analyseszenarien entwickelt, um eine Suche nach Higgs-Bosonen von niedrigen und mittleren Massen, $90 \text{ GeV} \leq M_\Phi < 180 \text{ GeV}$ und $180 \text{ GeV} \leq M_\Phi \leq 350 \text{ GeV}$, durchzuführen.

Für die Suche wurden zweidimensionale Verteilungen hergenommen. Eine Variable ist die invariante Masse der beiden führenden b-Jets. Die zweite Variable kombiniert topologische und kinematische Eigenschaften von b-Quark-Jets. Zur Abschätzungen des Hintergrundes werden Ereignisse mit drei Jets, von denen zwei als b-Quark-Jets erkannt wurden, verwendet. Signalereignisse werden aus Monte-Carlo-Simulationen erzeugt, im Detektor rekonstruiert und durch den speziellen Higgs Boson Trigger selektiert.

Systematischen Effekte aus verschiedenen Quellen werden untersucht. Der Schwerpunkt lag dabei bei der Betrachtung solcher Effekte, die zu veränderter Signal-Effizienz und zu Hintergrundverteilungen führten. Ein χ^2 -Anpassung wird verwendet, um das Signal aus den Daten zu extrahieren.

In dieser Analyse wurde kein Signal gefunden.

Die Ergebnisse wurde für die Berechnung einer oberen Grenze für $\sigma(pp \rightarrow b\bar{b} + \Phi) \times BR(\Phi \rightarrow b\bar{b})$ in Abhängigkeit von der Masse des Higgs Bosons zwischen 90 und 350 GeV benutzt. Die

verwendete Methode basiert auf einer CL_S -Berechnung mittels einer Log-Likelihood-Funktion. Innerhalb der 2σ Bereiche ist die beobachtete Grenze in gutem Einklang mit der erwarteten Ausschlussgrenze.

Aus den Daten wurde zusätzlich eine untere Grenze auf den $\tan\beta$ -Parameter des MSSM als Funktion der Higgs Boson Masse gesetzt. Im Rahmen des m_h^{max} MSSM-Szenarios für eine Masse des Higgs Bosons zwischen 90 und 350 GeV sind folgende Bereiche mit einem Vertrauensniveau von 95% erlaubt: $27 \leq \tan\beta \leq 51$ für $\mu = +200$ GeV und $22 \leq \tan\beta \leq 37$ für $\mu = -200$ GeV, wobei μ die Higgsino Masse ist.

Die gesetzte Grenze für $\tan\beta$ ist weitaus enger als die aus früheren Messungen am CDF- und D0-Experiment.

Abstract

The Higgs mechanism is responsible for the spontaneous breaking of the electroweak symmetry leading to the generation of masses of fermions and weak bosons. This thesis is devoted to search for the neutral supersymmetric Higgs particles $\Phi=h, H$ and A decaying into b quarks produced in association with at least one more b quark at the Large Hadron Collider. Here the study of the final states characterized by three b -tagged jets is described in detail. The analysis was performed using data corresponding to $2.7 - 4.8 \text{ fb}^{-1}$ integrated luminosity of pp collisions with a centre-of-mass energy of 7 TeV collected in 2011 with the CMS detector. Two analysis scenarios were adopted to perform a search for neutral Higgs bosons of low and medium masses, $90 \text{ GeV} \leq M_\Phi < 180 \text{ GeV}$ and $180 \leq \text{GeV} M_\Phi \leq 350 \text{ GeV}$, respectively.

Two-dimensional templates, built up from double- b -tagged data and based on the invariant mass of the two leading b jets and a variable reflecting b -jet properties of three leading jets are used to model the background. The signal is modeled by templates obtained from Monte Carlo simulation.

Various systematic effects affecting the signal efficiency and changing shapes of the signal and background templates were investigated.

The fitting machinery, based on a binned least-squares fit of the signal and background templates and the systematics model dependent on the hypothesized mass of the pseudoscalar Higgs particle A , was developed to extract the signal and background yields from the data. No significant evidence for the production of the Higgs bosons is found.

Using the CL_s method, we set cross section times branching fraction upper limits at 95% confidence level (CL) on the production of such neutral Higgs bosons Φ in the mass range from 90 GeV to 350 GeV. The observed exclusion limits are well within the expected $\pm 2\sigma$ band.

The benchmark scenario of the Minimal Supersymmetric Standard Model, denoted as m_h^{max} , with the two choices of the Higgsino mass parameter, $\mu = +200 \text{ GeV}$ and $\mu = -200 \text{ GeV}$ is considered. The obtained 95% CL upper limits on $\sigma(pp \rightarrow bb + \Phi) \times BR(\Phi \rightarrow b\bar{b})$ are interpreted as the upper limits on the MSSM parameter $\tan\beta$. Ranges $27 \leq \tan\beta \leq 51$ and $22 \leq \tan\beta \leq 37$ for the masses of the Higgs boson from 90 to 350 GeV are ruled out at $\mu = +200 \text{ GeV}$ and $\mu = -200 \text{ GeV}$, respectively.

The 95% CL limits on $\tan\beta$ obtained in this channel supersede previous $\tan\beta$ limits established by CDF and D0 experiments.

Contents

Abstract	x
Introduction	4
1 The Standard Model of Elementary Particles	5
1.1 Conventions	7
1.2 Lagrangian of the electroweak theory	8
1.2.1 Matter fields	10
1.2.2 Local gauge invariance	11
1.2.3 Electroweak interaction	13
1.3 Spontaneous symmetry breaking	16
1.3.1 The Higgs mechanism	16
1.3.2 The mass eigenstates of the gauge bosons	20
1.3.3 The fermion masses	22
2 Supersymmetry	27
2.1 Basics of supersymmetry	30
2.2 Superfields	33
2.3 R-parity of the chiral and vector superfields	36
2.4 The Minimal Supersymmetric Model	37
2.5 Field Content in the MSSM	38
2.6 Lagrangian of the MSSM	39
2.7 The Higgs sector and Electroweak Symmetry Breaking in MSSM	42
2.8 MSSM implication of the discovered Higgs-like particle	46
2.9 Predictions on the production of the neutral MSSM Higgs Bosons at LHC	53
2.10 Predictions on the decays of the neutral MSSM Higgs bosons	61
3 The Large Hadron Collider	65
3.1 Physics at the LHC	67
4 The CMS experiment	71
4.1 The CMS tracking detectors	71
4.2 The CMS calorimeter system	73
4.2.1 The CMS electromagnetic calorimeter	74
4.2.2 The CMS hadronic calorimeter	75

4.3	The CMS muon spectrometer	78
4.4	Triggering system	79
4.4.1	Level-1 trigger	81
4.4.2	High Level Trigger	83
4.5	Event Reconstruction	85
4.5.1	Track reconstruction	85
4.5.2	Vertex reconstruction	87
4.5.3	The energy reconstruction and calibration in ECAL	88
4.5.4	Electron and photon identifications	91
4.5.5	Muon identification	93
4.5.6	Jet reconstruction	94
4.5.7	Particle Flow jets	103
4.5.8	Identification of b jets	107
4.6	CMS analysis software and Physics simulation	110
5	Search for a neutral Higgs boson produced in association with b quarks	115
5.1	Analysis strategy	116
5.2	Trigger in the analysis	117
5.2.1	Data samples	119
5.2.2	L1/L2 efficiencies	121
5.3	Efficiency of b-jet identification	123
5.3.1	Relative trigger b-tagging efficiency	126
5.3.2	Scale factors for the b-tagging efficiencies	128
5.4	Event-wise b-tagging	130
5.5	Offline event selection	131
5.6	Background modeling	132
5.6.1	Double-b-tagged sample	133
5.6.2	Construction of the background templates	133
5.6.3	Trigger pattern corrections	135
5.6.4	Subtraction of non-bb contamination	138
5.7	Test of background modeling in a signal-depleted data sample	142
5.7.1	The BDT method	142
5.7.2	Closure test of background modeling	144
5.8	Signal modeling	146
5.8.1	Pile-up reweighting	148
5.8.2	Di-jet mass resolution	150
5.8.3	Signal efficiencies	152
5.8.4	Signal extraction from the data	154
5.8.5	Test of the fit with signal templates	155
5.8.6	Background-only fit	156
5.9	The systematic uncertainties	158
5.9.1	The uncertainties on the signal yield	158

5.9.2	The shape uncertainties	161
5.10	Results	164
5.10.1	Cross sections	165
5.11	Limit setting procedures in the Higgs boson search	166
5.11.1	Profile likelihood ratios	168
5.11.2	Test statistic	172
5.11.3	Sensitivity of the analysis	175
5.11.4	The asymptotic CL_S technique and exclusion limits	177
5.12	95% CL upper limits on cross sections	181
5.12.1	95% CL lower limits on the MSSM $\tan\beta$ parameter	182

6	Conclusions	191
----------	--------------------	------------

List of Figures

0.1	A historical overview of the number of fundamental constituents of matter. . . .	2
1.1	The scalar field's potential $V(\Phi(x))$ as a function of $\phi_3(x)$ and $\phi_4(x)$ at $\phi_{1,2}(x) \equiv 0$ for $\mu^2 > 0$	18
1.2	The potential $V(\Phi(x))$ as a function of $\phi_3(x)$ and $\phi_4(x)$ at $\phi_{1,2}(x) \equiv 0$ for $\mu^2 < 0$	19
2.1	Evolution of the inverse of the three coupling constants in the Standard Model (left) and in the supersymmetric extension of the SM (right). The SUSY particles are assumed to contribute only above the effective SUSY scale M_{SUSY} of about 1 TeV, causing a change in the slopes of the couplings evolutions. The thickness of the lines represents statistical errors on the coupling constants from the fit [23].	28
2.2	Tadpole and self-energy Feynmann diagrams for the Higgs boson. Here V stands for gauge bosons, e_k denotes fermions.	29
2.3	Cancellation of the quadratic divergence (2.2) . The fermionic loops contribute with an additional factor (-1) originating from Fermi statistics.	30
2.4	The running SUSY breaking m_1^2 and m_2^2 parameters in the SPS1 scenario.	43
2.5	The mass of the light CP-even neutral Higgs boson h , m_h as a function of M_A and $\tan\beta$ in the MSSM.	47
2.6	The tree-level (2.57) (blue) and radiatively corrected (2.61) (red) masses m_h as functions of M_A at $\tan\beta = 5$, $M_{SUSY} = 1$ TeV, $X_t = 0$ and $m_t = 175$ GeV.	48
2.7	The radiatively corrected masses m_h as functions of M_A for $X_t = 2M_{SUSY}$ (red) and $X_t = 0$ (blue) at $\tan\beta = 5$, $M_{SUSY} = 1$ TeV and $m_t = 175$ GeV.	49
2.8	The radiatively corrected masses m_h as functions of X_t at $\tan\beta = 5$, $M_{SUSY} = 1$ (blue) and 2 (red) TeV, and $m_t = 175$ GeV.	50
2.9	The radiatively corrected mass m_h as functions of $\tan\beta$ at $M_{SUSY} = 1$ TeV, $m_t = 175$ GeV, $X_t = 2M_{SUSY}$ (red) and $X_t = 0$ (blue).	50
2.10	Higgs-strahlung: associated h/H production with W/Z	54
2.11	WW/ZZ fusion production of the bosons h/H	54
2.12	gluon-gluon fusion production of the bosons $\Phi = h/H/A$	54
2.13	Higgs boson radiation off top and bottom quarks.	55
2.14	Standard Model Higgs boson production cross section at $E_{cm} = 7$ TeV including next-to-next-to-leading order (NNLO) and next-to-leading order (NLO) effects [81].	55

2.15	The cross sections for $gg \rightarrow H$ at $E_{cm} = 14$ TeV [88]. The cross sections with contributions of NLO (green) and NNLO (red) are compared with the cross section at the leading order for two choices of the factorization and renormalization scales: $\mu_F = \mu_R = 1/2M_H$ (upper curves) and $\mu_R = \mu_F = 2M_H$ (lower curves). The MRST parton distributions are used [89, 90].	57
2.16	The total gluon-fusion cross sections of the neutral light CP-even MSSM Higgs boson h within the m_h^{max} scenario at $\tan\beta = 30$ and $\sqrt{s} = 7$ TeV [92]. The MSTW2008 PDFs are used [96].	58
2.17	Total inclusive cross section for $gg \rightarrow b\bar{b} + H$ at the LHC at $\sqrt{s} = 14$ TeV as a function of M_H with the factorization and renormalization scales set to $\mu_R = \mu_F = 1/4(M_H + 2m_b)$ where CTEQ6 PDF are adopted [97].	59
2.18	Total production cross sections of $pp \rightarrow b\bar{b}H + X$ at $\sqrt{s} = 7$ TeV within the 5FS and 4FS using the MSTW2008 set of parton distribution functions. The bands exhibit the scale uncertainties in calculations [82].	60
2.19	The total MSSM production cross sections for gluon-gluon fusion and Higgs radiation off bottom quarks calculated in the 5FS at NNLO and $\sqrt{s} = 7$ TeV. The m_h^{max} scenario at $\tan\beta = 30$ is chosen to evaluate MSSM couplings [82].	60
2.20	Partial decay widths of the light scalar, $\Gamma(h \rightarrow b\bar{b})$, and the pseudoscalar, $\Gamma(A \rightarrow b\bar{b})$ in the “small α_{eff} ” scenario [56]. The shaded bands reflects uncertainties due to the factorization scale.	62
2.21	Branching ratios of the light scalar, $Br(h \rightarrow b\bar{b})$ and the pseudoscalar, $Br(A \rightarrow b\bar{b})$ in the “small α_{eff} ” scenario [56]. The shaded bands reflects uncertainties due to the factorization scale.	63
3.1	Schematic view of the CERN accelerator complex. The four interaction regions hosting the main LHC experiments, ALICE, ATLAS, CMS and LHCb, are also shown.	66
3.2	The recorded integrated luminosity of the experiments at the LHC in 2011 and 2012 [114].	68
3.3	Cross sections for selected processes to be observed at the LHC . The event rate for the luminosity $\mathcal{L} \simeq 10^{33} \text{cm}^{-2}\text{s}^{-1}$ is shown [115].	69
4.1	The CMS detector [112]. The total weight is 14000 tonnes, the overall diameter is 15 m, and the overall length is 28.7 m. All main components, the tracker, the preshower, the muon system, the calorimeter and the solenoid magnet are shown.	72
4.2	The Layout of a quarter of the CMS tracker in (R, z) view. Bold lines represent double-sided modules [125].	73
4.3	Layout of the CMS electromagnetic calorimeter. The barrel supermodules, two endcaps and the preshower detectors are shown as well [126, 132].	74
4.4	The measured (black) and fitted (red) resolutions as functions of the electron energy in a 3×3 array of crystals with beam incident in an area of $4 \times 4 \text{mm}^2$ around the crystal cross section center [134].	76

4.5	Layout of the CMS HCAL . The barrel (HB), endcap (HE), forward (HF) and “tails-catcher” (HO) parts are shown [112].	77
4.6	Energy response as a function of pion beam energy (a). Relative energy resolution $\sigma(E)/E$ versus pion beam energy (b). $\sigma(E)/E$ is measured using mean and RMS of the energy distribution as well as the mean and variance of the fitted Gaussian [136].	78
4.7	View of the CMS muon system [112]. The dashed lines corresponds to the given values of η	79
4.8	An overview of the two-level trigger system used at the CMS. The Level-1 (Lvl-1) selects events from the pipeline of front-end electronics. A software-implemented High Level Trigger (HLT) filters the Level-1 output and reduces the data rate by a factor of $\mathcal{O}(1000)$ [137].	80
4.9	An overview of the Level-1 trigger [137]. The regional triggers of the calorimeter and the muon systems provide information to the Global Trigger.	81
4.10	The structure of the regional L1 calorimeter trigger [138]. The 3×3 trigger cells (in blue and green) are compound of 5×5 crystal arrays (in yellow and red).	82
4.11	The 12×12 window used for the L1 jet reconstruction. The trigger patterns on the energy deposits, shown on the right side, are used to identify jet constituents [138].	83
4.12	An overview of the HLT . The HLT reconstructs Level-2 tracks in the tracker regions seeded by the Level-1 electrons and photons. The rejection of an event happens, if Level-2 or Level-3 objects fail to pass selection criteria in the filtering steps.	84
4.13	The algorithmic track-reconstruction efficiency for muons (a) with $p_T = 1$ (black), 10 (blue) and 100 GeV (red). The algorithmic (open points) and global (solid points) efficiencies for tracks in b jets with transverse momenta, p_T , between 120 and 170 GeV (b) [142].	86
4.14	The trajectory of a charged particle in the pixel tracker. The measurements of the first two pixels determine the transverse and longitudinal impact parameters, d_{xy} and d_z , respectively.	89
4.15	The distribution of di-electron invariant mass M_{ee} reconstructed in $Z \rightarrow e^+e^-$ decays in EB . The cases of no correction (blue), interchannel calibration C_i applied (red), both interchannel C_i and radiation-induced S_i corrections applied (black) are shown [134].	91
4.16	The matching between the GSF track and the SC (a). The angular coordinates of the SC , ϕ_{SC} and the outermost part of the GSF track ϕ_{out}^{track} , are compared. The reconstruction of an electron candidate as a combination of two-component GSF track, with the 4-momenta p_{in} and p_{out} in the inner and outer parts of the tracker, respectively (b).	93
4.17	Jet reconstruction in the CMS . On the left side, tracks (black), ECAL (green) and HCAL (blue) energy deposits are used to cluster jets. Constituents of jets like neutral and charged hadrons, photons are shown on the right side.	95

4.18	Reconstruction efficiency of CaloJets in simulations and data as a function of the jet p_T [162].	98
4.19	Steps of correction applied to the raw jet energy.	99
4.20	The MC jet-energy-correction factor for CaloJets , TrackJets and PFJets of $p_T = 200$ GeV as function of η (a). The MC jet-energy-correction factor for the different jet types, as a function of jet p_T (b) [163].	101
4.21	Jet resolution functions for the iterative cone algorithm with cone size $R = 0.5$ in the barrel, endcap and forward regions [165].	102
4.22	An event display of a simple hadronic jet containing four particles (π^+ , π^- , π^0 , K_L^0) in the (x, y) view (a) and in the (η , ϕ) view of the ECAL (b) and the HCAL detectors (c). The tracks of charged pions, T1 and T2, as well as energy deposits in the ECAL , E1 from π^- , and E2,E3 from $\pi^0 \rightarrow \gamma\gamma$, and the energy in HCAL , H1 and H2, are reconstructed by the PF algorithm. The link between the tracks and the clusters are shown as green vertical lines obtained from the track extrapolation to the calorimeter surface [168].	105
4.23	Energy resolution $\sigma(E^{rec} - E^{gen})/E^{rec}$ of a PF cluster as a function of the particle energy E^{gen} simulated in the Particle-Flow superclusters in the barrel ECAL [168].	106
4.24	Jet reconstruction efficiency (a) and mismatching jet rate (b) for PFJets (red) and CaloJets (blue) as a function of the GenJet p_T . The barrel region of the CMS is considered [168].	106
4.25	Basic PF jet properties in di-jet back-to-back events in the Monte Carlo simulations (blue) and data (black). The distributions of the PF jet transverse momentum (a) and azimuth (b) are depicted [169].	107
4.26	The impact parameters of tracks in jets. PV denotes the primary vertex, and SV represents the secondary interaction vertex.	109
4.27	Distributions of the three-dimensional impact parameter significance of tracks, associated with b (red), c (green), light-flavor (blue) jets and jets (cyan) originated by b quarks from the gluon splitting, with $p_T > 1$ GeV, at least eight hits associated to the track and a good fit quality, $\chi^2/\text{ndof} < 5$ [174].	109
4.28	The distribution of the CSV discriminator for jets of b (red), c (green), light (blue) and b from gluon splitting (cyan) flavors [174].	111
5.1	p_T distributions of the leading (a) and sub-leading (b) jets in simulated events. The blue histograms are obtained from the signal process, $bb + \Phi \rightarrow 4b + \text{jets}$, for $M_H = 120$ GeV, and the red histograms are the distributions in QCD events enriched by b quarks.	116
5.2	η distributions of the leading jet in the simulated events after reconstruction. The blue histogram is obtained from the signal process, $bb + \Phi \rightarrow 4b + \text{jets}$, for with $M_H = 120$ GeV, and the red histogram is the distribution in QCD events enriched by b quarks.	117

5.3	Sketch of all important procedures performed in the search for the neutral MSSM Higgs bosons.	118
5.4	Efficiencies for the Level-2 selection with 20, 38, 46, 53 and 60 GeV thresholds on the jet p_T , seeded by the Level-1 jets selected using the cuts of 12, 36, 36,44 and 44 GeV on the jet p_T	122
5.5	Using TCHE and CSV algorithms applied to jets in simulated QCD events, the mistag fraction of non-b jets is obtained as functions of the b-jet tagging efficiency.	124
5.6	The offline b-tagging probabilities for b (a), c(b) and light-flavor (c) jets at the CSVT working point.	125
5.7	The CSV b-tagging efficiency for b jets as a function of p_T at the tight working point.	126
5.8	The relative trigger b-tagging efficiency for b (a), c(b) and light-flavor (c) jets at the CSVT working point.	127
5.9	The scale factors SF_b (a) and SF_{udsg} (b) at the CSVT b-tagging point as functions of the jet p_T	129
5.10	Normalized distribution of M_{SV} in jets for different flavors in simulated $t\bar{t}$ events.	131
5.11	The probabilities P_{B_1} (a) and P_{B_3} (b) that the b, c or udsg jets will be assigned to the bins B_1 and B_3 of the SV mass distribution as a function of the jet p_T	134
5.12	The M_{12} (a) and X_{123} (b) projections of the five templates (Bb) b, (Cb) b, (Qb) b, bbB, bbX for the CSVT b-tagging in the low-mass scenario.	135
5.13	The b-tag trigger patterns for the bbX (a), bXb (b) and Xbb templates from events selected in the low-mass scenario.	137
5.14	The M_{12} projections of the templates Xbb and bXb, where X=B, C, before (black) and after (pink) applying the trigger pattern correction (5.18).	138
5.15	The absolute values of the nTCHE thresholds applied on the first (leading) and second (sub-leading) b-tagged jet in the Xbb and bbX samples at the CSVT working point.	139
5.16	Fraction of non-bb events as a function of the di-jet mass M_{12} in the bbX (a), bXb (b) and Xbb (c) categories of the double-b-tagged sample, where b jets are tagged at the CSVT working point. The solid blue and open red triangles show the fractions of non-bb events obtained by the method of the negative fraction thresholds in data and Monte Carlo, respectively. The solid red circles represent the fractions obtained using the information from the Monte Carlo generator.	140
5.17	Normalized M_{12} spectra of the bbX (a), bXb (b) and Xbb (c) categories before (circles) and after (squares) the correction, and the non-bb contribution (triangles) using events selected in the low-mass scenario. The ratios of the corrected over uncorrected di-jet invariant mass distributions are shown at the bottom of the plots.	141
5.18	Normalized distributions of the input variables used in the MVA training: $p_{T,3}/p_{T,1}$ (a), η_1 (b), sphericity (c), $\Delta\phi_{23}$ (d).	143

5.19	The distributions of the BDT for events in the signal (blue) and background (red) samples. The “control region” denotes the BDT discriminant range, where the signal is depleted.	144
5.20	The di-jet mass M_{12} distribution for events selected in the low-mass scenario for the heavy-flavor multijet QCD enriched by b quarks (red) and Higgs boson signal with $M_H = 120$ GeV in the m_h^{max} scenario at $\tan = 20$ (blue) samples selected by the requirement $BDT \leq -0.06$	145
5.21	The distributions of di-jet invariant mass M_{12} in the low-mass scenario for the whole background sample (red) and for events in the control region (blue). Both distributions are normalized to unity.	145
5.22	The M_{12} distributions of events in the BDT control sample (solid points) and of the background prediction from the extrapolation of the double-btag sample (open squares) and their ratio in the low-mass scenario.	146
5.23	The M_{12} (a) and X_{123} projections after the fit of the (Bb) b, (Cb) b, (Qb) b, bbB bbX templates to the data using events from the BDT sample in the low-mass scenario. The dots are data and the stacked histograms are the combination of the templates normalized to data.	147
5.24	The M_{12} normalized to unity distributions of the signal events with the assumed Higgs boson mass of 120 GeV selected with “Trig0” (blue) and “Trig1” (green) triggers in the low-mass scenario. The red histogram, normalized to unity, represents M_{12} after merging the “Trig0” and “Trig1” distributions.	148
5.25	The M_{12} (a) and X_{123} (b) projections of the signal templates for three different masses of the Higgs boson, $M_A = 120, 180, 250$ GeV applying the low-mass scenario selection.	149
5.26	The distribution of the number of pile-up interactions per BX in data (black) and Monte Carlo (red).	150
5.27	Distributions of the number of reconstructed primary vertices with (red) and without (blue) pile-up reweighting in simulated events, The black histogram is the distribution of the number of the PV observed in 2011 data.	151
5.28	The M_{12} distributions in the triple-b-tagged signal samples generated with the Higgs boson masses of 120 GeV (a) and 200 GeV (b). The green distributions originate from events of the first category, while the brown distributions correspond to the second event category.	152
5.29	The di-jet mass resolution (a) and signal purities (b) as functions of the Higgs boson mass. The blue curve in (b) is the purity obtained for events within the \pm RMS window around M_{peak} , while the black graph is the purity estimated in the whole range of M_{12} values.	153
5.30	Signal efficiencies as function of M_A in the low-mass (red curve) and medium-mass (blue curve) scenarios.	154

5.31	The results of the background-only fit in the triple-btag data sample selected in the low-mass scenario: the projection to di-jet invariant mass (a), the projection to the X_{123} axis (b). The cyan area corresponds to uncertainties originating from statistical errors of the templates.	157
5.32	The results of the background-only fit in the triple-btag data sample selected in the medium-mass scenario: the projection to di-jet invariant mass (a), the projection to the X_{123} axis (b). The cyan area corresponds to uncertainties originating from statistical errors of the templates.	157
5.33	The combined statistical and systematic uncertainties on the scale factors $SF_{b,c}$ (a) as functions of the jet p_T , presented as bands of yellow, for b jets, and cyan, for c jets, colors. The systematic uncertainty on the scale factor $SF_{uds g}$ as a function of the jet p_T (b).	158
5.34	The relative uncertainties of the jet energy scale shown as a function of the jet p_T for the jet $\eta = 1.0$ (a) and $\eta = 2.0$ (b).	159
5.35	The ratio r^{JER} and its uncertainty as a function of the jet η for $p_T = 100$ GeV of the jet.	160
5.36	The effects of systematic uncertainties on the signal efficiency ε_S in the signal samples with the Higgs boson masses of 120 GeV (a), 200 GeV (b), 300 GeV (c). The green bars show the relative change of ε_S for a $+2\sigma$ variation of $SF_{b,c,uds g}$, JES and JER, while the red bars illustrates the relative effect for -2σ systematic shifts.	161
5.37	The change of the shape of the M_{12} projection under variations of the scale factors $SF_{b,c}$ within $\pm 2\sigma$ for the Bbb (a) and Cbb (b) background templates. The yellow band in the plot of the ratio indicates the statistical uncertainty in the bins of the background templates.	162
5.38	The change of the M_{12} shape under variations of JES (a) and JER (b) within $\pm 2\sigma$ for the signal template corresponding to the Higgs boson mass $M_H = 300$ GeV. The yellow band in the plot of the ratio indicates the statistical uncertainty in the bins of the signal template.	163
5.39	Results of the fit including a signal template for a Higgs boson with a mass of 200 GeV in the triple-b-tagged sample, of the medium-mass scenario: (a) the projection in the di-jet invariant mass, (b) the projection on the X_{123} axis. . . .	165
5.40	Measured cross sections times branching fractions as a function of the mass of the Higgs boson A . In (a) the full mass range and in (b) $M_A \geq 130$ GeV are shown.	167
5.41	Measured $-\ln(\lambda(\mu))$ as a function of the signal strength μ for the signal with the pseudoscalar Higgs boson mass $M_A = 200$ GeV: The blue graph shows the behavior of $-\ln(\lambda(\mu))$ calculated with the conditional and unconditional maximum-likelihood estimators $\{\hat{v}_k\}$ and $\{\hat{v}_k\}$. The red one is the case when the nuisance parameters $\{v_k\}$ are fixed to their true values.	171

5.42	The pdf of the test statistic for the signal with $M_A = 200$ GeV (red) and background-only (blue) models for the hypothesized values $\mu = 27.5$ (a) and $\mu = 45$ (b). The measured t_μ and expected t_μ^A are shown as black and green vertical lines, respectively. The solid curves in colors correspond to asymptotic predictions of formula (5.41). All nuisance parameters $\{v_k\}$ are maximum-likelihood fitted.	176
5.43	The pdf of the test statistic in the signal with $M_A = 200$ GeV (red) and background-only (blue) models for the hypotheses with $\mu = 27.5$ (a) and $\mu = 45$ (b). Measured t_μ and expected t_μ^A are shown as black and green vertical lines, respectively. The solid curves in colors correspond to asymptotic predictions of the formula (5.41). All nuisance parameters $\{v_k\}$ are fixed at their nominal values.	177
5.44	The scan of the asymptotic CL_{S+B} (blue), $1 - CL_B$ (black), CL_S (red) using data. The signal model with $M_A = 200$ GeV is used in the calculations. The dashed line indicates $\text{med}[CL_S]$ obtained from Asimov data set. The green (yellow) area corresponds to the $\pm 1(2)\sigma$ error band for $\text{med}[CL_S]$. The red horizontal line is placed at 0.05 corresponding to the 95% confidence level $CL_{95\%}$	180
5.45	The observed 95% CL upper limits on the cross section times the branching fraction, (a) linear scale and (b) logarithmic scale for the ordinate.	183
5.46	The scan of the cross section $\sigma(pp \rightarrow bb + \Phi)^{MSSM} \times Br(\Phi \rightarrow b\bar{b})$ as a function of $\tan\beta$ and M_A . The m_h^{max} benchmark scenario with $\mu = +200$ GeV is used.	184
5.47	The function $\tan\beta(\sigma[gg \rightarrow bb + \Phi]^{MSSM} \times Br(\Phi \rightarrow b\bar{b}))$ obtained for the fixed $M_A = 200$ GeV in the m_h^{max} benchmark scenario with the Higgsino mass parameter $\mu = +200$ GeV.	185
5.48	The effect of the scale $\mu_{r,f}$ (a) and $pdf + \alpha_S$ (b) uncertainties on the cross section as a function of $\tan\beta$ at $M_A = 200$ GeV in the m_h^{max} benchmark scenario with the Higgsino mass parameter $\mu = +200$ GeV. The green band (and red dashed curves) indicates the interval of the cross section variations due to the uncertainties.	187
5.49	Measured $-\ln(\lambda(\mu))$ as a function of the signal strength μ . The expectation values s_j in the data model $L(X \mu, \{v\})$ correspond to the signal hypothesis of the Higgs mass $M_A = 200$ GeV. The blue graph shows the behavior of $-\ln(\lambda(\mu))$ including the scale and parton distribution uncertainties. The red dashed curve corresponds to the case when the $\mu_{r,f}$ and $pdf + \alpha_S$ uncertainties are not considered.	188
5.50	Observed and median expected 95% CL upper limits on $\tan\beta$ as a function of M_A in the m_{max}^h scenario for $\mu = +200$ GeV. The expected 1σ (green) and 2σ (yellow) bands are also shown.	189
5.51	Observed and median expected 95% CL upper limits on $\tan\beta$ versus M_A in the m_{max}^h scenario for $\mu = -200$ GeV. One- and two-standard deviation ranges for the expected upper limit are represented by the gray bands. Previous exclusion regions from LEP [222] and Tevatron in the multi-b jet channel [221] are overlaid.	190

List of Tables

1.1	Gauge bosons of the Standard Model.	6
1.2	Fundamental interactions relevant in the particle physics, their strengths and ranges.	7
1.3	The matter content of the SM	11
2.1	Particle content of the MSSM	38
2.2	Neutral Higgs bosons couplings to the u- and d-type quarks.	51
2.3	Neutral Higgs bosons couplings to the gauge bosons.	52
3.1	The machine parameters relevant to the LHC for the proton- proton (pp) and heavy ions, Pb, (HI) runs [111, 112].	67
4.1	Ratios, between the jet energy resolutions in data and simulations, measured, using the asymmetry method [166], for different jet η ranges.	102
4.2	The list of the generated events. The number of produced events and corresponding cross sections are given.	113
5.1	The HLT paths and the appropriate Level-1 seeds used in the analysis.	119
5.2	The datasets, run ranges and corresponding integrated luminosities for the low di-jet mass triggers.	120
5.3	The datasets, run ranges and corresponding integrated luminosities for the triggers in the medium mass scenario.	121
5.4	Parameters of the L1/L2 efficiencies resulting from the fit.	123
5.5	Flavor content fractions of the background events, simulated by Alpgen and Pythia6 programs, which are accepted in the signal region.	133
5.6	Signal efficiencies ϵ_S for several masses of the MSSM pseudoscalar neutral Higgs boson in the low- and medium-mass scenarios.	153
5.7	The fit results on $f_s \cdot (N^s + N^{obs})$ and $\sigma(f_s) \cdot (N^s + N^{obs})$ for various masses of the MSSM pseudoscalar neutral Higgs in N^{obs} events of the triple-b-tagged BDT sample, when N^s signal events were injected.	156
5.8	The fractions of the various background templates in the data samples selected in the low- and medium-mass scenarios from the background-only fit.	156
5.9	Summary of the shape-altering systematic uncertainties, expressed in their effects on the fitted signal fraction f_s	163
5.10	Summary of the systematic uncertainties.	164

5.11	The signal fractions obtained by the fit and the number of observed signal events for different masses of the MSSM pseudoscalar Higgs boson. The uncertainties of the fractions include statistical and shape-altering systematics.	165
5.12	The measured cross sections times branching fraction, $\sigma(pp \rightarrow b\bar{b} + \Phi) \times Br(\Phi \rightarrow b\bar{b})$ for different masses of the neutral pseudoscalar Higgs boson. The uncertainties includes normalization, statistical and shape-altering systematic effects.	166
5.13	Observed and median expected limits at the 95% CL on $\sigma(pp \rightarrow b\bar{b} + \Phi) \times BR(\Phi \rightarrow b\bar{b})$	181
5.14	Observed and median expected lower limits at 95% CL on $\tan\beta$ in the m_h^{max} benchmark scenario for the Higgsino mass parameter $\mu = +200$ GeV.	190

List of Abbreviations

SM	Standard Model
SSB	Spontaneous Symmetry Breaking
EWK	ElectroWeaK interaction
QCD	Quantum ChromoDynamics
VEV	Vacuum Expectation Value
h.c.	Hermitian Conjugate
MS	Minimal Subtraction scheme
GUT	Grand Unification Theory
SUSY	Supersymmetry
MSSM	Minimal Supersymmetric Standard Model
LSP	Lightest Supersymmetric Particle
4FS	Four Flavor Scheme
5FS	Five Flavor Scheme
LHC	Large Hadron Collider
CMS	Compact Muon Solenoid
ATLAS	A Toroidal LHC ApparatuS
ALICE	A Large Ion Collider Experiment
LHCb	Large Hadron Collider beauty
LEP	Large Electron-Positron Collider
PXL	Pixel Layer
TIB	Tracker Inner Barrel
TOB	Tracker Outer Barrel
TEC	Tracker End-Cap
TID	Tracker Inner Disks
ECAL	Electromagnetic CALorimeter
HCAL	Hadronic CALorimeter
EB	Electromagnetic calorimeter in the Barrel
EE	Electromagnetic calorimeter in the Endcap
HB	Hadronic calorimeter in the Barrel
HE	Hadronic calorimeter in the Endcap
HF	Hadronic calorimeter in the Forward region
HO	Hadronic calorimeter Outside of solenoid
DT	Drift Tubes
CSC	Cathode Strip Chambers
RPC	Resistive Plate Chambers

DAQ	Data AcQuisition
L1	Level-1 trigger
HLT	High Level Trigger
L1A	Level-1 Accept
GT	Global Trigger
L2	Level-2 trigger
DA	Deterministic Annealing
PV	Primary Vertex
SV	Secondary Vertex
SC	SuperCluster
ADC	Analogue-to-Digital Converter
GSF	Gaussian Sum Filter
GM	Global Muon
TM	Tracker Muon
IC	Iterative Cone
SISCone	Seedless Infrared-Safe Cone
JER	Jet Energy Resolution
PF	Particle-Flow algorithm
IP	Impact Parameter
WP	b-tagging Working Point
TCHE	Track Counting High Efficiency b-tagging algorithm
CSV	Combined Secondary Vertex b-tagging algorithm
AVF	Adaptive Vertex Fitter
CMSSW	CMS SoftWare
L1/L2	Level-1/Level-2 trigger efficiency
CSVT	Tight working point of CSV b-tagging algorithm
pdf	probability distribution function
BDT	Boosted-Decision Trees method
BX	Bunch Crossing
LS	Luminosity Section
RMS	Root Mean Square
JES	Jet Energy Scale
JER	Jet Energy Resolution
CL	Confidence Level
CI	Confidence Interval

Introduction

Throughout the last century, the knowledge of the fundamental constituents of matter experienced a tremendous progress. This progress was only possible thanks to ambitious curious scientists, whose work shed light on many of the former mysteries of nature. Their ultimate aim was (and is) the formulation of laws that describe and predict the observed phenomena of nature. The scientists make use of theory and experiment, where the results of either have fruitful influence on the development of the other. The main particle physics interests is to find the answers on two questions:

- What are the basic constituents of the universe?
- How does the basic constituents interact with each other?

Figure 0.1 shows how these questions were historically answered. The idea that matter consists of indivisible particles, called atoms, was firstly brought up by the Greek philosopher Democritus in the 5th century BC. Dalton in the 19th century picked up the idea of a fundamental constituent of matter to explain chemical reactions. Modern atomic theory is, of course, a little more evolved than Dalton's theory but the essence of Dalton's theory remains valid. The discovery of the electron in 1897 by Thomson proved a substructure of the atoms. He proposed in 1904 the plum pudding model of the atoms as a conglomerate of negatively charged electrons surrounded by a soup of positive charge. The Thomson model was disproved in 1909 by Geiger and Marsden, who fired alpha particles at a very thin sheet of gold foil. The first, effective description of the atoms with small, positively charged nucleus surrounded by electrons traveling in circular orbits, was introduced by Bohr in 1913. Using Planck's constant, Bohr obtained an accurate formula for the energy levels of the hydrogen atom. He postulated that the angular momentum of the electron is quantized, i.e. it can have only discrete values. This model had several shortcomings, which were overcome by the quantum mechanics. Later, research focused on the structure of the atomic nucleus. The model, in which the nucleus consists of protons and neutrons, was established after the discovery of the neutron by Chadwick in 1932. The known electromagnetic force could not explain how particles inside the nucleus are bounded. The explanation appeared later when the theory of an additional strong interaction between protons and neutrons was introduced. Also in 1932 there was the first discovery of a particle that was not a constituent of atoms. The anti-particle of the electron, predicted by Dirac in 1928, the positron, was found by Anderson.

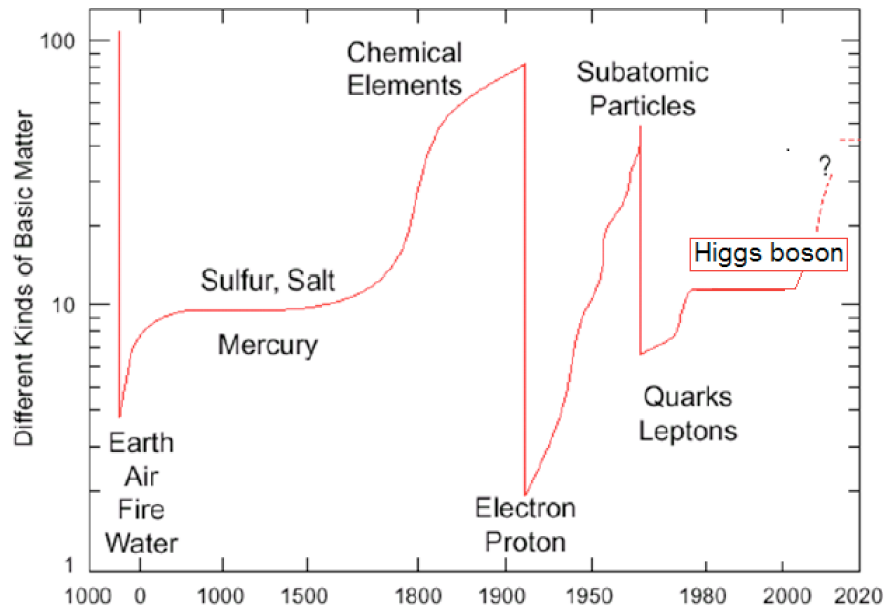


Figure 0.1: A historical overview of the number of fundamental constituents of matter.

In the middle of the last century, first particle accelerators allowed the discovery of many new strongly interacting particles, called hadrons. Because there were some regularities in the properties of these particles, it was assumed that hadrons were not fundamental but they had a substructure. The model describing the hadron constituents, called the quark model, was verified by deep inelastic scattering experiments in the 70s and 80s of the last century. The discovery of the J/ψ particle in 1974 was a great success confirming the existence of the predicted charm quark. Up to now, six different quarks were discovered. They were found to be point like and are considered as fundamental particles. A second type of fundamental particles observed so far are the six leptons like electron, muon, tau, and the respective neutrinos.

In 2009, the new Large Hadron Collider (**LHC**) became operational at the CERN laboratory, near Geneva, Switzerland. This collider and its experiments provide the possibility to probe nature with about one order of magnitude increase in energy (14 TeV) compared to last century accelerators. Because of this, the LHC is able to probe an energy domain in which many predictions from theories beyond the Standard Model may be observed. Thus the **LHC** will answer many of the open questions of physics at both sub-atomic and cosmological scales.

In parallel to the discoveries of the fundamental particles, the forces that act on these particles were an important subject of the particle physics research. Three fundamental forces are observed. The electromagnetic force acts on charged particles. The phenomenology of this force was described by Maxwell in 1865 in his theory of the electromagnetism. Nowadays the electromagnetic force is postulated by laws of the quantum dynamics and Einstein's special relativity in the theory of Quantum Electrodynamics, first introduced by Feynman, Schwinger

and Tomonaga. Two other fundamental forces, which were discovered, are the weak and the strong forces. The weak force plays the prominent role in the explanation of the nuclear decays, while the strong force is responsible for the formation of hadrons and nuclei from quarks and gluons.

The Standard Model, **SM**, of elementary particles is a relativistic quantum field theory that describes all fundamental forces observed in nature except for gravitation. The predictions of this theory astonishingly coincide with observations in experiments, making it the most stringently tested existing theory. Within the framework of the quantum field theories, particles interact with each other exchanging massless gauge bosons. The discoveries of the gauge bosons of all three interactions confirmed this theoretical picture. The bosons, which carry the electromagnetic and the strong interaction were indeed found to be massless. In contrast, the gauge bosons of the weak interaction, called W and Z bosons, have been observed as massive particles with masses of about ~ 100 times the proton mass. A theoretical mechanism was invented by Higgs, Brout and Englert in 1964 to introduce these masses. This is the so called Higgs mechanism and it requires the existence of a scalar particle, the Higgs boson.

Although the Standard Model is found to be self-consistent, it exhibits several shortcomings. First, the Higgs mechanism to give masses to the particles was introduced ad-hoc. A Higgs boson has been discovered at the **LHC** in 2012. So far it is not clear whether it is the **SM** Higgs boson and whether it is fundamental or composite. Another problem of the **SM** are the neutrinos. They are predicted to be massless left-handed Weyl fermions. However, recent observations gave evidence that neutrinos must be massive particles. There is also no description of gravity in the **SM**, leading to the belief that this model is effective up to some energy scale, Λ . At energies higher than Λ “new” physics appears.

One of the most attractive extensions of the Standard Model, which is able to solve many of its shortcomings, introduces a so-called supersymmetry, **SUSY**, that relates fermions and bosons. The supersymmetry requires an extension of the Standard Model Higgs sector, which in its minimal form gives rise to three neutral and two charged Higgs bosons. In this thesis, I present a search for neutral Higgs bosons in the $H \rightarrow b\bar{b}$ decay channel using pp-collisions recorded with the Compact Muon Solenoid, **CMS**, experiment at the **LHC**. For a discovery in this channel, the identification of b-quark jets is crucial to search for a signal and suppress background.

The thesis is structured as follows. **Chapter 1** introduces the theoretical framework of the Standard Model. In **Chapter 2** I will give a brief overview about the shortcomings of the **SM** and the basic concept of the supersymmetry. I will describe the enlarged Higgs sector of the **SUSY** in the specific example of the two-Higgs-doublet model, the Minimal Supersymmetric Model, **MSSM**. Here the neutral Higgs bosons, being the main subject of this thesis, are discussed in more details from the phenomenological and experimental point of view. In **Chapter 3** the LHC accelerator is introduced and its physics program is outlined. The **CMS** detector, low-level and high-level reconstruction tools, needed to conduct the search for the neutral Higgs bosons, are summarized in **Chapter 4**. It includes a description of reconstruction methods for jets which are subjects of the analysis, software and computing environment, together with the analysis tools and Monte-Carlo simulations. The search of neutral Higgs bosons produced in association with b-quark(s) and decaying into b-quark pairs is explained in **Chapter 5**. The interpretation of

the results obtained is performed within the **MSSM**. Finally, the conclusions are discussed in **Chapter 6**.

1 The Standard Model of Elementary Particles

The current knowledge of elementary particle physics is the result of theoretical and experimental complementarity the last 50 years. Today, we call the theory of elementary particles the Standard Model, **SM**, a field theory which combines special relativity and quantum mechanics [1, 2, 3, 4, 5, 6]. The SM considers all matter as being made up from spin-1/2 particles, called fermions. The theory is built upon the following two ideas:

- non-abelian local gauge symmetry;
- spontaneous symmetry breaking, **SSB**.

The local gauge symmetry requires the Lagrangian of the Standard Model to be invariant under local transformations generated by elements of the $SU(3) \otimes SU(2) \otimes U(1)$ group [5, 6, 7]. However, the $SU(2) \otimes U(1)$ symmetry requires all particles to be massless, what contradicts the observations. Therefore, the symmetry must be broken in order to induce masses.

The weak and electromagnetic interactions between fermions are mediated through the exchange of spin-1 gauge fields, called vector bosons, W_μ^i , B_μ ($i = 1, 2, 3; \mu = 0, 1, 2, 3$), which are understood to arise from invariance of the theory under the local non-abelian $SU(2)$ and abelian $U(1)$ gauge symmetries, respectively [7]. The electroweak interaction, **EWK**, between the matter fields characterized by their couplings to the gauge vector bosons, g and g' , which are related to the electric charge e as

$$g \sin \theta_W = g' \cos \theta_W = e, \quad (1.1)$$

where θ_W is the electroweak mixing angle.

Electromagnetic interactions are associated to the fermion electric charges, while weak phenomena are determined by the fermion flavors. The $SU(2)$ and $U(1)$ gauge interactions cannot be identified directly with the weak and electromagnetic interactions. This can be understood from the fact that the same $SU(2)$ doublet comprises two leptons of different electric charges. Instead, the observed weak and electromagnetic interactions are a manifestation of the combined electroweak gauge group, $SU(2) \otimes U(1)$.

The physical gauge fields, A_μ , Z_μ and W_μ^\pm , for the massless photon and the massive vector bosons, respectively, arise as superpositions of the $U(1)$ and $SU(2)$ gauge fields, B_μ and W_μ^i . Table 1.1 summarizes the properties of the gauge bosons associated with the local $SU(2) \otimes U(1)$ invariance of the electroweak theory.

The generators of the $U(1)$ and $SU(2)$ subgroups are the weak hypercharge Y and weak isospin \vec{T} , respectively. The weak isospin is expressed in terms of Pauli matrices $\vec{\sigma}$,

$$\vec{T} = 1/2 \cdot \vec{\sigma}. \quad (1.2)$$

The weak hypercharge Y is related to 3rd component of the weak isospin T_3 and to the electric charge Q ¹ as

$$Q = T_3 + Y/2. \quad (1.3)$$

Because of the $U(1)$ and $SU(2)$ symmetries in the **EWK** interaction, the electric charge Q is conserved. However, the weak isospin \vec{T} is conserved partly: the conservation holds for T_3 only.

Table 1.1: Gauge bosons of the Standard Model.

Interaction	Boson	Q	M [GeV]
Electromagnetic	A_μ	0	0
Weak	W_μ^\pm	± 1	80.4
	Z_μ	0	91.2

The strong interaction, described by a theory called Quantum Chromodynamics, **QCD**, is invariant under the $SU(3)$ color gauge group. The interacting quarks are grouped into $SU(3)$ triplets² which define the physical states of matter. Experimental observations suggest that the quarks can not exist as free particles, since the strength of the strong interaction increases as the energy scale of the physical process is decreased. This means that colored objects, at low energies, are confined in colorless states, the hadrons and mesons. Due to this confinement, direct probes of the **QCD** are difficult at low energies.

Eight massless spin-1 gauge bosons with zero electric charge, G_μ^a , $a = [1, 2, \dots, 8]$, gluons, mediate the strong force. The gluons are associated to 8 Gell-Mann matrices [8], which define the generators of the $SU(3)$ group. The strong interaction is characterized by the coupling g_s introduced as a free parameter of infinitesimal $SU(3)$ transformations.

The perturbative strong theory combined with models of hadronisation make predictions of the **QCD** to be testable. For instance, the processes with jets like $e^+e^- \rightarrow 2, 4$ jets were used to directly probe the gauge structure of the **QCD** at the **LEP** experiments [9]. The obtained results are in good agreement with the **QCD** predictions. Table 1.2 shows main characteristics of the

¹in units of positron charge, i.e. $Q(e^+) = 1$, $Q(u) = 2/3$ etc

² $SU(3)$ symmetry is associated with the color charge - the quantum number conserved in strong interactions.

interactions discussed.

Table 1.2: Fundamental interactions relevant in the particle physics, their strengths and ranges.

Interaction	Coupling constant	Range, cm
Electromagnetic	$e^2/4\pi \simeq 1/137$	∞
Weak	$g^2/4\pi \simeq 1/30$	10^{-16}
Strong	$g_s^2/4\pi \simeq 1/10$	10^{-13}

1.1 Conventions

For the thesis I have adopted the following conventions. All calculations are carried out in the natural units such that

$$\hbar = c = 1, \quad (1.4)$$

where \hbar is the reduced Planck constant and c is the speed of light in vacuum. In this system length, time, energy, momentum and mass have the following units:

$$\begin{aligned} [length] &= GeV^{-1}, \\ [time] &= GeV^{-1}, \\ [energy] &= GeV, \\ [momentum] &= GeV, \\ [mass] &= GeV. \end{aligned} \quad (1.5)$$

The Minkowski space in calculations is determined by the metric tensor as

$$g_{\mu\nu} = g^{\mu\nu} = \begin{pmatrix} 1 & 0 & 0 & 0 \\ 0 & -1 & 0 & 0 \\ 0 & 0 & -1 & 0 \\ 0 & 0 & 0 & -1 \end{pmatrix}. \quad (1.6)$$

Unless noted otherwise, repeated indices will imply Einstein summation. Cross sections of processes, σ , are given in picobarn, pb

$$1 \text{ pb} = 10^3 \text{ fb} = 10^{-40} \text{ m}^2 = 10^{-36} \text{ cm}^2 \quad (1.7)$$

In natural units (1.5), 1 pb corresponds to $k \cdot GeV^{-2}$, where $k \simeq 2.6 \cdot 10^{-9}$.

Given the luminosity L of an accelerator in units of $\text{cm}^{-2}\text{s}^{-1}$, the event rate, dN/dt , of a process with a cross section σ reads

$$\frac{dN}{dt} = L \cdot \sigma. \quad (1.8)$$

1.2 Lagrangian of the electroweak theory

Particles are described by relativistic fields that allow a particle to choose between several different paths (transitions from one state to another), each path with some probability. The actual path along which a dynamical particle system may move from one point to another within a specified time interval is that for which the action has a stationary value (either a minimum or a maximum, or a saddle point) [10]. Because in a relativistic theory space and time should be on equal footing, one writes the action as

$$S[\phi] = \int_{t_1}^{t_2} \int_V \mathcal{L} dx dt = \int \mathcal{L} d^4x, \quad (1.9)$$

where the function $\mathcal{L}(\partial_\mu \phi(x), \phi(x), x)$ is called the Lagrangian density, often simply referred to as the Lagrangian. The stationary principle mentioned above is expressed as the Euler-Lagrange equations,

$$\frac{\partial \mathcal{L}}{\partial \phi_i} - \partial_\mu \frac{\partial \mathcal{L}}{\partial (\partial_\mu \phi_i)} = 0. \quad (1.10)$$

The motion of non-interacting spin-0, spin-1/2 and spin-1 particles are described by the Klein-Gordon, Dirac and Proca Lagrangians, \mathcal{L}_{KG} , \mathcal{L}_D and \mathcal{L}_{Proca} , respectively, as

$$\begin{aligned} \mathcal{L}_{KG} &= \partial_\mu \phi(x)^* \partial^\mu \phi(x) - m_\phi^2 \phi(x) \phi(x)^*, \\ \mathcal{L}_D &= i \overline{\psi}(x) \gamma^\mu \partial_\mu \psi(x) - m_\psi \overline{\psi}(x) \psi(x), \\ \mathcal{L}_{Proca} &= -\frac{1}{4} F^{\mu\nu}(x) F_{\mu\nu}(x) + \frac{1}{2} m_A^2 A_\mu(x) A^\mu(x), \text{ where} \\ F_{\mu\nu}(x) &= \partial_\mu A_\nu(x) - \partial_\nu A_\mu(x). \end{aligned} \quad (1.11)$$

Here $\phi(x)$ is a complex scalar field describing the particle with zero spin and mass m_ϕ , $\psi(x)$ is a four-component spinor representing the particle with spin 1/2 and mass m_ψ and $A^\mu \equiv (A^0, \vec{A})$, is a four-component vector field describing the particle with spin 1 and mass m_A . $F_{\mu\nu}(x)$ is the anti-symmetric strength tensor of the vector field describing the kinetic energy. The 4×4 Dirac matrices $\gamma^\mu (\mu = 0, 1, 2, 3)$ in the Dirac Lagrangian (1.11) determine generators of the Lorentz group, $SO(1, 3)$, under transformations of which \mathcal{L}_D is invariant. Such matrices are expressed as

$$\gamma^\mu = \begin{pmatrix} 0 & \sigma^\mu \\ \bar{\sigma}^\mu & 0 \end{pmatrix}, \quad (1.12)$$

with

$$\sigma^\mu = (\hat{I}_2, \sigma^k), \quad \bar{\sigma}^\mu = (\hat{I}_2, -\sigma^k),$$

where \hat{I}_2 is the 2×2 identity matrix, while σ^k are the Pauli matrices. The Dirac spinor $\psi(x)$ is a composition of the left-handed and right-handed two-components spinors $\psi(x)_L$ and $\psi(x)_R$

$$\psi(x) = \begin{pmatrix} \psi_L(x) \\ \psi_R(x) \end{pmatrix}. \quad (1.13)$$

The spinors $\psi_L(x)$ and $\psi_R(x)$ are two eigenstates of the chirality operator γ^5 ,

$$\begin{aligned} \gamma^5 &= \begin{pmatrix} -\hat{I}_2 & 0 \\ 0 & \hat{I}_2 \end{pmatrix}, \\ \gamma^5 \begin{pmatrix} \psi_L \\ 0 \end{pmatrix} &= - \begin{pmatrix} \psi_L \\ 0 \end{pmatrix}, \\ \gamma^5 \begin{pmatrix} 0 \\ \psi_R \end{pmatrix} &= + \begin{pmatrix} 0 \\ \psi_R \end{pmatrix}. \end{aligned} \quad (1.14)$$

It so happens that only left-handed spinor fields $\psi_L(x)$ interact via the weak force. This means that the left-handed and the right-handed spinors are treated separately in the **SM**. The electroweak theory suggests that the $\psi_L(x)$ and $\psi_R(x)$ spinors have fundamentally different origins, mathematically saying, different irreducible representations of the $SU(2)$ group. Due to this reasons, the mass term $m_\psi \bar{\psi}(x) \psi(x)$, in equation (1.11) and the parity transformations, P ,

$$P: \quad \psi_L(x) \leftrightarrow \psi_R(x), \quad \psi_R(x) \leftrightarrow \psi_L(x),$$

are forbidden in the **SM**.

The massive vector field $A_\mu(x)$ is characterized by three degrees of freedom, $e_{1,2,3}^\mu$,

$$A^\mu(x) = e_i^\mu e^{-ip_\nu x^\nu}.$$

The vectors of polarization, $e_{1,2,3}^\mu$, are orthonormal and orthogonal to the momentum p_μ of the field A_μ ,

$$e_i^\mu \cdot e_{\mu,j} = \delta_{ij}, \quad e_{1,2,3}^\mu \cdot p_\mu = 0.$$

In terms of $A_\mu(x)$, this corresponds to

$$\partial_\mu A^\mu(x) = 0. \quad (1.15)$$

1.2.1 Matter fields

In the **SM** the matter fields are elementary spin-1/2 fermions, $\psi(x)$, which represent the leptons and the quarks. These two groups of particles appear in three flavor families, that behave identically under the **EWK** interaction.

No experimental evidence has been found for the existence of a fourth generation so far [11, 12]. The known leptons are the electron e , the muon μ , the tau-lepton τ , and the three corresponding neutrinos, ν_e , ν_μ , ν_τ . The six known quarks are labeled as up, u , down, d , strange, s , charm, c , bottom or beauty, b , and top, t , quarks. The left-handed fermions, $\psi_L(x)$, are grouped as the following doublets:

$$L = \begin{pmatrix} \nu_{e,L} \\ e_L \end{pmatrix}, \begin{pmatrix} \nu_{\mu,L} \\ \mu_L \end{pmatrix}, \begin{pmatrix} \nu_{\tau,L} \\ \tau_L \end{pmatrix}, \begin{pmatrix} u_L \\ d_L \end{pmatrix}, \begin{pmatrix} c_L \\ s_L \end{pmatrix}, \begin{pmatrix} t_L \\ b_L \end{pmatrix}. \quad (1.16)$$

The fermion families are identified by columns of equation (1.16). The right-handed fermions, $\psi_R(x)$ are given by the singlets,

$$l_R = \begin{pmatrix} e_R \end{pmatrix}, \begin{pmatrix} \mu_R \end{pmatrix}, \begin{pmatrix} \tau_R \end{pmatrix}, \begin{pmatrix} u_R \end{pmatrix}, \begin{pmatrix} c_R \end{pmatrix}, \begin{pmatrix} t_R \end{pmatrix}, \begin{pmatrix} d_R \end{pmatrix}, \begin{pmatrix} s_R \end{pmatrix}, \begin{pmatrix} b_R \end{pmatrix}. \quad (1.17)$$

The charged leptons are described by left-handed and right-handed massive spinors, while the neutrinos are presented by massless left-handed spinors only. The non-vanishing masses of neutrinos can be implied by mixing in the neutrino sector, i.e. the transition from one neutrino species to another. For every fermion an antiparticle exists with the same mass, spin, lifetime and decay width, but with the quantum number of opposite sign. All stable matter observed in the Universe is made from the first generation of fermions. No stable antimatter has been found so far. Unless otherwise explicitly mentioned, throughout this thesis all statements referring to particles are also valid for their corresponding antiparticles.

Table 1.3 shows the quantum numbers, T_3 , Y and Q , assigned to the matter content of the **SM**.

Table 1.3: The matter content of the SM.

	First family	Second family	Third family
Leptons	$\begin{pmatrix} \nu_{eL}^{[1/2;-1;0]} \\ e_L^{[-1/2;-1;-1]} \\ e_R^{[0;-2;-1]} \end{pmatrix}$	$\begin{pmatrix} \nu_{\mu L}^{[1/2;-1;0]} \\ \mu_L^{[-1/2;-1;-1]} \\ \mu_R^{[0;-2;-1]} \end{pmatrix}$	$\begin{pmatrix} \nu_{\tau L}^{[1/2;-1;0]} \\ \tau_L^{[-1/2;-1;-1]} \\ \tau_R^{[0;-2;-1]} \end{pmatrix}$
Quarks	$\begin{pmatrix} u_L^{[1/2;1/3;2/3]} \\ d_L^{[-1/2;1/3;-1/3]} \\ u_R^{[0;4/3;2/3]} \\ d_R^{[0;-2/3;-1/3]} \end{pmatrix}$	$\begin{pmatrix} c_L^{[1/2;1/3;2/3]} \\ s_L^{[-1/2;1/3;-1/3]} \\ c_R^{[0;4/3;2/3]} \\ s_R^{[0;-2/3;-1/3]} \end{pmatrix}$	$\begin{pmatrix} t_L^{[1/2;1/3;2/3]} \\ b_L^{[-1/2;1/3;-1/3]} \\ t_R^{[0;4/3;2/3]} \\ b_R^{[0;-2/3;-1/3]} \end{pmatrix}$

In Table 1.3 the quantum numbers T^3 , Y and Q are reported using the following notation:

$$u_L^{[1/2;1/3;2/3]} = u_L^{[T^3;Y;Q]}, \Rightarrow T_{u_L}^3 = 1/2; Y_{u_L} = 1/3; Q_{u_L} = 2/3;$$

$$u_R^{[0;4/3;2/3]} = u_R^{[T^3;Y;Q]}, \Rightarrow T_{u_R}^3 = 0; Y_{u_R} = 4/3; Q_{u_R} = 2/3;$$

etc.

1.2.2 Local gauge invariance

The spinor $\psi(x)$ in equation (1.11) is not experimentally observed, but what has a physical meaning and can be measured is $\bar{\psi}(x)\psi(x) = |\psi(x)|^2$. This leads to the fact that the fields can be adjusted by the unitary transformation U

$$\bar{\psi}(x)\psi(x) \rightarrow \bar{\psi}(x)U^\dagger U\psi(x), \Rightarrow U^\dagger U = \hat{I}_{4 \times 4}. \quad (1.18)$$

The unitary transformation U might be either a phase factor $e^{i\alpha}$, called the $U(1)$ transformation, or any 4×4 unitary matrix $U_{4 \times 4}$. The Dirac Lagrangian \mathcal{L}_D is invariant under the unitary transformation

$$\begin{aligned} e^{i\alpha} : \gamma^\mu &\rightarrow \gamma^\mu, \quad \psi(x) \rightarrow e^{i\alpha} \psi(x), \\ U_{4 \times 4} : \gamma^\mu &\rightarrow U_{4 \times 4} \gamma^\mu U_{4 \times 4}^\dagger, \quad \psi(x) \rightarrow U_{4 \times 4} \psi(x), \\ \mathcal{L}'_D &= i\bar{\psi} e^{-i\alpha} \gamma^\mu \partial_\mu e^{i\alpha} \psi = i\bar{\psi} \gamma^\mu \partial_\mu \psi = \mathcal{L}_D. \end{aligned} \quad (1.19)$$

This is so called the “global gauge invariance”. The word “global” is used because the transformation U is the same for all points in the Minkowski space. An interesting thing happens

if we demand that \mathcal{L}_D is not just globally invariant, but also locally invariant to the unitary transformations

$$\begin{aligned}\psi(x) &\rightarrow U(x)\psi(x), \\ \overline{\psi(x)} &\rightarrow \overline{\psi(x)}U^\dagger(x).\end{aligned}\tag{1.20}$$

Here a local transformation means that we do a different transformation at each point. However, applying the local transformation to the derivatives, involved in the Dirac Lagrangian, results in a new term which alters the formula of \mathcal{L}_D . Therefore the derivative ∂_μ must be replaced by the covariant derivative $D_\mu(x)$, which satisfies the requirement that $D_\mu(x)\psi(x)$ transforms under $U(x)$ like $\psi(x)$

$$\begin{aligned}\psi(x) &\rightarrow U(x)\psi(x), \\ D_\mu(x)\psi(x) &\rightarrow U(x)D_\mu(x)\psi(x),\end{aligned}\tag{1.21}$$

In general, any unitary group $U_{N \times N}$ is reducible and decomposed into two subgroups: $U(1)$ and the special unitary group $SU(N)$, i.e. $U(N) \equiv SU(N) \otimes U(1)$ ³.

Because the left-handed $\psi_L(x)$ and right-handed $\psi_R(x)$ spinors in the SM have different origins, the transformation $U(x)_{4 \times 4}$ is decomposed into two different transformations $U(x)_{2 \times 2}$, which independently act on $\psi_L(x)$ and $\psi_R(x)$:

$$\psi(x)' = U(x)_{4 \times 4} \begin{pmatrix} \psi_L(x) \\ \psi_R(x) \end{pmatrix} = \begin{pmatrix} U(x)_{2 \times 2, L} \psi_L(x) \\ U(x)_{2 \times 2, R} \psi_R(x) \end{pmatrix}\tag{1.22}$$

The chiral field $\psi_L(x)$ is a doublet of the unitary group $U(2)_L$, and transformed under $U(2)_L \equiv SU(2) \otimes U(1)$, while the chiral field $\psi_R(x)$ is a singlet of $U(2)_R$, meaning that only elements of the subgroup $U(1)$ are used to transform $\psi_R(x)$. $U(2)_L$ and $U(2)_R$ are expressed as

$$\begin{aligned}U_L(x) &= \exp(ig' \frac{Y_L}{2} \alpha(x)) \exp(ig \frac{T^a(x) \sigma_a}{2}), \\ U_R(x) &= \exp(ig' \frac{Y_R}{2} \alpha(x)),\end{aligned}\tag{1.23}$$

where g and g' are arbitrary coupling constants, Y_L and Y_R are the hypercharges for the left-handed and right-handed fermions, $T^a(x) \equiv T^a \beta^a(x)$, with $a = 1, 2, 3$, defines a weak isospin in the local coordinate x of the space-time. σ_a are the Pauli matrices, determining the generators of the $SU(2)$ group. $\alpha(x)$ and $\beta^a(x)$ are arbitrary transformation functions of x . The covariant

³The notation $U(N)$ represents the unitary $U_{N \times N}$ matrix.

derivative $D_\mu(x)$ is also decomposed into the left-handed and right-handed components, $D_\mu(x) = D_{\mu,L}(x) \oplus D_{\mu,R}(x)$, which are formulated in the following way:

$$\begin{aligned} D_{\mu,L}(x) &= \partial_\mu + ig' B_\mu(x) \frac{Y_L}{2} + ig W_\mu^a(x) \frac{\sigma_a}{2}, \\ D_{\mu,R}(x) &= \partial_\mu + ig' B_\mu(x) \frac{Y_R}{2}. \end{aligned} \quad (1.24)$$

The fields $B_\mu(x)$ and $W_\mu^a(x)$ are vector gauge bosons. These vector fields are transformed under $U(x)$ in a specific way to guarantee that equation (1.21) holds

$$\begin{aligned} W_\mu^a(x) &\rightarrow W_\mu^a(x) - \epsilon_{abc} \beta^b(x) W_\mu^c(x) - \partial_\mu \beta^a(x), \\ B_\mu(x) &\rightarrow B_\mu(x) - \partial_\mu \alpha(x). \end{aligned} \quad (1.25)$$

The gauge bosons are required to be massless, because their mass terms of the Proca Lagrangian (1.11), $\frac{1}{2} m_B^2 B_\mu(x) B^\mu(x)$ and $\frac{1}{2} m_W^2 W_\mu^a(x) W^{a,\mu}(x)$, are not locally invariant under $U(x)$

$$\begin{aligned} W_\mu^a(x) W^{\mu,a}(x) &\rightarrow W_\mu^a(x) W^{\mu,a}(x) - (\beta^b(x) W_{\mu,b}(x))^2 + (\beta^b(x))^2 W_\mu^b W^{b,\mu} - \\ &2(\partial_\mu \beta^b(x)) W_b^\mu(x) + (\partial^\mu \beta^a(x))^2, \\ B_\mu(x) B^\mu(x) &\rightarrow B_\mu(x) B^\mu(x) - 2(\partial_\mu \alpha(x)) B^\mu(x) + (\partial^\mu \alpha(x))^2. \end{aligned} \quad (1.26)$$

1.2.3 Electroweak interaction

Requiring the local gauge invariance, the total electroweak Lagrangian, \mathcal{L}_{EWK} , of the fermions and vector bosons is given by the sum of the Dirac Lagrangian, \mathcal{L}_D , and the Proca Lagrangians, \mathcal{L}_B and \mathcal{L}_W , of the gauge fields B_μ and W_μ^a ,

$$\begin{aligned} \mathcal{L}_{EWK} &= \mathcal{L}_D + \mathcal{L}_B + \mathcal{L}_W = \\ &\bar{L} \gamma^\mu D_{\mu,L} L + \bar{l}_R \gamma^\mu D_{\mu,R} l_R - \frac{1}{4} B_{\mu\nu} B^{\mu\nu} - \frac{1}{4} W_{\mu\nu}^a W^{a,\mu\nu}. \end{aligned} \quad (1.27)$$

Here L denotes the left-handed doublets (1.16) and l_R represents the right-handed singlets (1.17). $B_{\mu\nu}$ and $W_{\mu\nu}^a$ are the vector field strength defined as

$$\begin{aligned} B_{\mu\nu} &= \partial_\mu B_\nu - \partial_\nu B_\mu, \\ W_{\mu\nu}^a &= (\partial_\mu W_\nu^a - \partial_\nu W_\mu^a) - g \epsilon_{abc} W_\mu^b W_\nu^c. \end{aligned} \quad (1.28)$$

The Lagrangian \mathcal{L}_{EWK} introduces the electroweak fermion-boson and boson-boson interactions. Because of the non-abelian gauge structure ϵ_{abc} present in the field strength $W_{\mu\nu}^a$ (1.28), there are trilinear (1.29) and quadratic (1.30) self-interactions of the vector field W_μ^a

$$\mathcal{L}_W = -\frac{1}{4}(\partial_\mu W_\nu^a - \partial_\nu W_\mu^a)^2 + g\epsilon_{abc}\partial_\mu W_\nu^a W^{b,\mu} W^{c,\nu} \quad (1.29)$$

$$-\frac{g^2}{4}(W_\mu^a W_\nu^b W_a^\mu W_b^\nu - W_\mu^a W_\nu^b W_b^\mu W_a^\nu). \quad (1.30)$$

The electroweak fermion-boson interactions are the result of the covariant derivatives $D_{\mu,L}$ and $D_{\mu,R}$ present in \mathcal{L}_D

$$\begin{aligned} \mathcal{L}_D &= i\bar{L}\gamma^\mu D_{\mu,L}L + i\bar{l}_R\gamma^\mu D_{\mu,R}l_R = \\ &= i\bar{L}\gamma^\mu(\partial_\mu - ig'\frac{Y_L}{2}B_\mu - ig\frac{\sigma_a}{2}W_\mu^a)L + i\bar{l}_R\gamma^\mu(\partial_\mu - ig'\frac{Y_R}{2}B_\mu)l_R = \\ &= i\bar{L}\gamma^\mu\partial_\mu L + i\bar{l}_R\gamma^\mu\partial_\mu l_R + \mathcal{L}_{intL}, \end{aligned} \quad (1.31)$$

$$\mathcal{L}_{int} = g'\frac{Y_L}{2}\bar{L}\gamma^\mu B_\mu L + g'\frac{Y_R}{2}\bar{l}_R\gamma^\mu B_\mu l_R + g\bar{L}\gamma^\mu\frac{\sigma_a}{2}W_\mu^a L.$$

Here \mathcal{L}_{int} is the part of the electroweak Lagrangian describing the fermion-boson interaction. \mathcal{L}_{int} determines the electromagnetic j_{QED}^μ and weak $j_{a,weak}^\mu$ currents which are coupled to the gauge bosons B_μ and W_μ^a

$$\begin{aligned} j_{QED}^\mu &= g'\frac{Y_L}{2}\bar{L}\gamma^\mu L + g'\frac{Y_R}{2}\bar{l}_R\gamma^\mu l_R, \\ j_{a,weak}^\mu &= g\bar{L}_f\gamma^\mu\frac{\sigma_a}{2}L_f, \\ \mathcal{L}_{int} &= j_{QED}^\mu B_\mu + j_{a,weak}^\mu W_\mu^a. \end{aligned} \quad (1.32)$$

In components, the Lagrangian⁴ of the **EWK** interaction is written as

$$\mathcal{L}_{int} = \frac{1}{2}(gW_\mu^3 + g'Y_L B_\mu)\bar{\nu}_{e,L}\gamma^\mu \nu_{e,L} + \frac{1}{2}(-gW_\mu^3 + g'Y_L B_\mu)\bar{e}_L\gamma^\mu e_L + \quad (1.33)$$

$$\frac{g}{\sqrt{2}}(W_\mu^- \bar{e}_L\gamma^\mu \nu_{e,L} + W_\mu^+ \bar{\nu}_{e,L}\gamma^\mu e_L) + \quad (1.34)$$

$$\frac{1}{2}g'Y_R B_\mu \bar{e}_R\gamma^\mu e_R, \quad (1.35)$$

⁴Here we restrict ourselves to the electron flavor in the consideration of \mathcal{L}_{int} .

where $W_\mu^\pm = \frac{W_\mu^1 \pm iW_\mu^2}{\sqrt{2}}$. The terms in (1.33), (1.34), (1.35) describe the left-handed component of the neutral current, the left-handed component of the charged current and the right-handed component of the electromagnetic current, respectively. The gauge bosons W_μ^3 and B_μ are coupled diagonally to the left-handed electron and neutrino keeping the charge of the leptons unchanged. In the equation (1.34), the gauge eigenstates W_μ^1 and W_μ^2 are expressed in terms of the mass eigenbasis, W_μ^\pm . The W_μ^\pm bosons change the charge of the fermions, i.e they transform the electron into the neutrino and vice versa. Neither W_μ^3 nor B_μ can be directly identified with the photon because they couple to the neutrino which is electrically neutral. The mass eigenbasis, (Z_μ, A_μ) , is introduced by the rotation of the gauge fields W_μ^3 and B_μ , to eliminate the neutrino in the left-handed component of the neutral current (1.33).

$$\begin{pmatrix} W_\mu^3 \\ B_\mu \end{pmatrix} = \begin{pmatrix} \cos \theta_W & \sin \theta_W \\ -\sin \theta_W & \cos \theta_W \end{pmatrix} \begin{pmatrix} Z_\mu \\ A_\mu \end{pmatrix}. \quad (1.36)$$

The weak mixing angle θ_W is expressed as functions of the g and g' couplings

$$\sin \theta_W = \frac{g'}{\sqrt{g^2 + g'^2}}, \quad \cos \theta_W = \frac{g}{\sqrt{g^2 + g'^2}}. \quad (1.37)$$

Requiring that left-handed and right-handed electrons, e_L and e_R , are equally coupled to the photon, A_μ , with the same charge of the electron e (1.1), i.e

$$\begin{aligned} Y_L &= \frac{Y_R}{2}, \\ Y_L &= -1, \\ Y_R &= -2, \\ e &= -g'Y_L \cos \theta_W \equiv -\frac{Y_R}{2} \cos \theta_W, \end{aligned} \quad (1.38)$$

the left-handed component of the neutral (1.33) and the right-handed component of the electromagnetic (1.35) currents in the mass eigenbasis (1.36), are expressed by the Lagrangian $\mathcal{L}_{int;A+Z}$

$$\mathcal{L}_{int;A+Z} = j_{QED}^\mu A_\mu + j_{3,weak}^\mu Z_\mu, \quad (1.39)$$

$$j_{QED}^\mu = -e(\bar{e}_L \gamma^\mu e_L + \bar{e}_R \gamma^\mu e_R), \quad (1.40)$$

$$j_{3,weak}^\mu = \frac{e}{2 \cos \theta_W \sin \theta_W} \bar{v}_{e,L} \gamma^\mu v_{e,L} \quad (1.41)$$

$$+ \frac{e}{\cos \theta_W \sin \theta_W} \left(-\frac{1}{2} + \sin^2 \theta_W \right) \bar{e}_L \gamma^\mu e_L - \quad (1.42)$$

$$- \frac{e}{\cos \theta_W \sin \theta_W} \sin^2 \theta_W \bar{e}_R \gamma^\mu e_R. \quad (1.43)$$

In general, the neutral Z_μ gauge boson is coupled to the neutral-weak current $j_{3,weak}^\mu$ in the form:

$$Z_\mu j_{3,weak}^\mu \sim \frac{e}{\cos \theta_W \sin \theta_W} (T^3 - Q \sin^2 \theta_W), \quad (1.44)$$

where T_3 and Q are the third component of the weak isospin and electric charge of the fermions.

The same equations, (1.34), (1.40) and (1.44), are used to describe electroweak interaction of gauge bosons, W_μ^\pm , A_μ and Z_μ , with the other fermion fields of the doublet and singlet representations, (1.16) and (1.17), respectively.

1.3 Spontaneous symmetry breaking

The reason why all particles are massless is because the symmetry $SU(2) \otimes U(1)$ forbids the mass terms in the Lagrangian \mathcal{L}_{EWK} , as we have discussed in Section 1.2. Therefore the way to solve the problem of mass generation is to break the symmetry. But we cannot just leave out the symmetry, because that would ruin the whole theory. We need a more subtle way of symmetry breaking.

There are really two ways for doing this. We could argue, for instance, that the symmetry was never truly exact but just an approximate symmetry. That means that small mass terms in the Lagrangian are allowed that do not satisfy the symmetry. This is called explicit symmetry breaking. The Standard Model uses a different way of the symmetry breaking. By introducing a scalar field with a specific potential which makes it possible to induce mass terms for all gauge bosons and fermions. However this can be done in such a way that all interactions still respect the symmetry, although the ground state does not. This mechanism is called spontaneous symmetry breaking, **SSB**.

1.3.1 The Higgs mechanism

The Higgs mechanism allows to generate mass terms for the fermions and gauge bosons in the electroweak theory. The local gauge group $SU(2) \otimes U(1)$ of the **SM** is spontaneously broken. The scalar doublet $\Phi(x)$ is introduced to make its vacuum state to be non- $SU(2)$ invariant:

$$\Phi(x) = \begin{pmatrix} \phi^+(x) \\ \phi^0(x) \end{pmatrix} = \frac{1}{\sqrt{2}} \begin{pmatrix} \phi_1(x) + i\phi_2(x) \\ \phi_3(x) + i\phi_4(x) \end{pmatrix}, \quad (1.45)$$

where $\phi_{1,2,3,4}(x)$ are real fields. The motion of these fields, hereafter denoted as Higgs fields, is described by the local gauge invariant Lagrangian \mathcal{L}_Φ

$$\mathcal{L}_\Phi = (D_{\mu,L}\Phi(x))^\dagger D^{\mu,L}\Phi(x) - \mu^2 \Phi^\dagger(x)\Phi(x) - \lambda(\Phi^\dagger(x)\Phi(x))^2 \quad (1.46)$$

where $D_{\mu,L}$ is the left-handed covariant derivative

$$D_{\mu,L} = \partial_\mu + ig' \frac{Y_\Phi}{2} B_\mu + ig \frac{\sigma_a}{2} W_\mu^a. \quad (1.47)$$

The quantity Y_Φ is the hypercharge of the field $\Phi(x)$ and equal to 1. Because $\Phi(x)$ is a doublet under $SU(2)$, its weak isospin must be $|\vec{T}| = 1/2$. The charge of the fields in the equation (1.45) is determined by the Gell-Mann-Nishijima formula (1.3), such that $\phi^0(x)$ is a neutral field while $\phi^+(x)$ is positively charged.

The Higgs potential $V(\Phi(x))$,

$$V(\Phi(x)) = \mu^2 (\Phi^\dagger(x) \Phi(x)) + \lambda (\Phi^\dagger(x) \Phi(x))^2, \quad (1.48)$$

is determined by the mass parameter μ^2 , which is either $\mu^2 \geq 0$ or $\mu^2 < 0$, and the strength of the scalar field self-interaction λ , which is required to be positive, $\lambda > 0$.

For $\mu^2 \geq 0$ the potential $V(\Phi(x))$ is a four-dimensional parabola, two projections of which are shown in Figure 1.1, which has a global minimum⁵ at

$$\begin{aligned} \langle \Phi(x)^\dagger \Phi(x) \rangle &= 0, \\ \langle \phi_1(x) \rangle &= \langle \phi_2(x) \rangle = \langle \phi_3(x) \rangle = \langle \phi_4(x) \rangle = 0. \end{aligned} \quad (1.49)$$

⁵We use the bra and kets to denote the vacuum state.

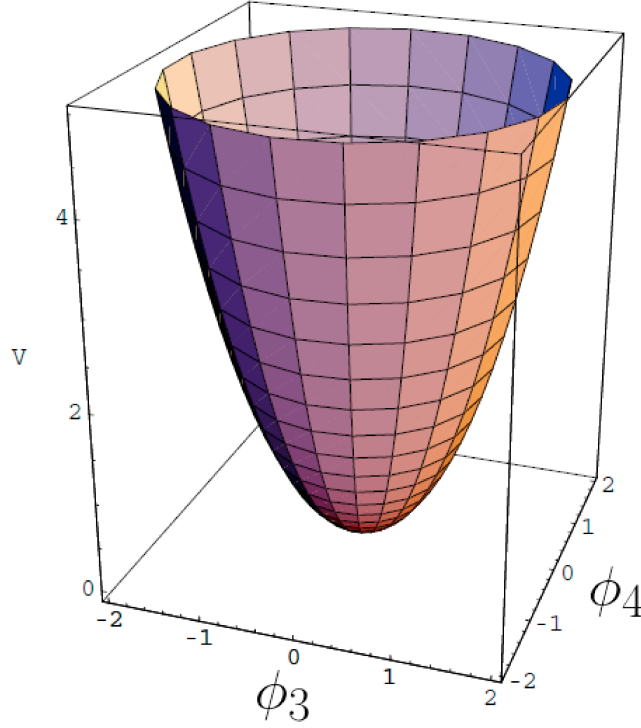


Figure 1.1: The scalar field's potential $V(\Phi(x))$ as a function of $\phi_3(x)$ and $\phi_4(x)$ at $\phi_{1,2}(x) \equiv 0$ for $\mu^2 > 0$.

The solution (1.49) is unique and $SU(2)$ invariant

$$\langle \Phi(x)^{\dagger'} \Phi(x)' \rangle = 0, \text{ where}$$

$$\Phi' = \frac{1}{\sqrt{2}} \begin{pmatrix} \phi'_1 + i\phi'_2 \\ \phi'_3 + i\phi'_4 \end{pmatrix}, \quad (1.50)$$

$$\begin{pmatrix} \phi'_{1,3} \\ \phi'_{2,4} \end{pmatrix} = U \cdot \begin{pmatrix} \phi_{1,3} \\ \phi_{2,4} \end{pmatrix} \text{ with } U \in SU(2).$$

The scalar sector of the electroweak theory is unbroken and described by four real fields with the same masses

$$M_1^2 = M_2^2 = M_3^2 = M_4^2 = \mu^2.$$

If $\mu^2 < 0$, the potential $V(\Phi(x))$ has the shape of a Mexican hat shown in Figure 1.2. In this case, the ground state, at which $V(\Phi(x))$ reaches the non-zero minimum, is defined as

$$\langle \Phi^{\dagger} \Phi \rangle = \frac{1}{2} (\langle \phi_1^2(x) \rangle + \langle \phi_2^2(x) \rangle + \langle \phi_3^2(x) \rangle + \langle \phi_4^2(x) \rangle) = \frac{-\mu^2}{2\lambda} \equiv \frac{v^2}{2}. \quad (1.51)$$

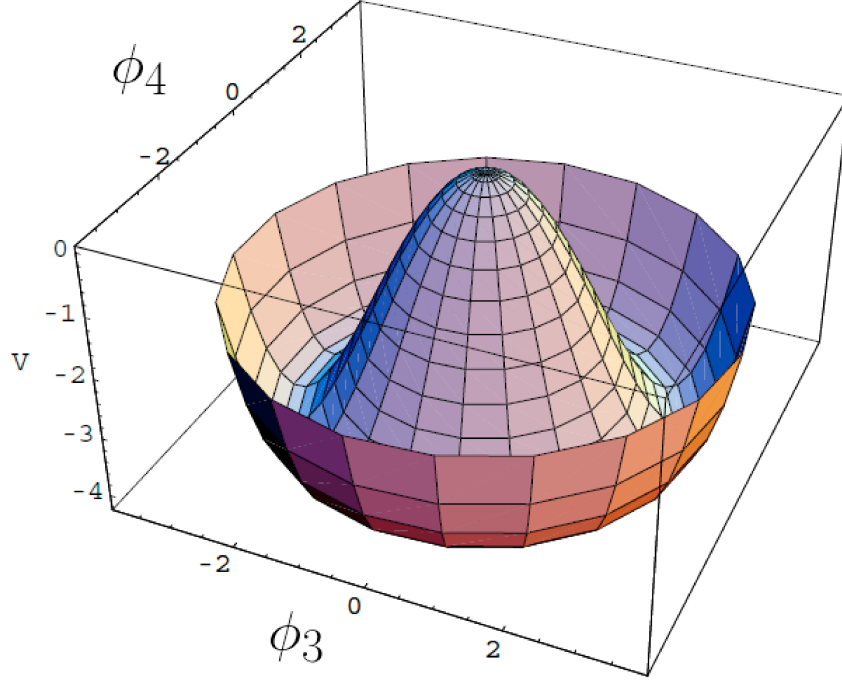


Figure 1.2: The potential $V(\Phi(x))$ as a function of $\phi_3(x)$ and $\phi_4(x)$ at $\phi_{1,2}(x) \equiv 0$ for $\mu^2 < 0$.

This ground state degenerates: it is not unique and present as four-dimensional space of the $\langle \phi_i(x) \rangle$ functions satisfying the equation (1.51). The simplest expression for the vacuum expectation value, \mathbf{VEV} , $\langle \Phi(x) \rangle$ is

$$\langle \Phi(x) \rangle = \frac{1}{\sqrt{2}} \begin{pmatrix} 0 \\ v \end{pmatrix}. \quad (1.52)$$

Using definitions (1.45) and (1.52), the scalar doublet $\Phi(x)$ can be expressed as

$$\Phi(x) = \frac{1}{\sqrt{2}} \begin{pmatrix} \pi_1(x) + i\pi_2(x) \\ v + H(x) + i\pi_3(x) \end{pmatrix}, \quad (1.53)$$

where the fields $\pi_i(x)$, with $i = 1, 2, 3$, and $H(x)$ are vacuum excitations with zero \mathbf{VEV} ,

$$\langle \pi_1(x) \rangle = \langle \pi_2(x) \rangle = \langle \pi_3(x) \rangle = \langle H(x) \rangle \equiv 0. \quad (1.54)$$

The scalar potential $V(\Phi(x))$, expanded at the ground state, has then the following form:

$$\begin{aligned}
V(\Phi(x)) &= \frac{\mu^2}{2}(\pi_1(x)^2 + \pi_2(x)^2 + (v + H(x))^2 + \pi_3(x)^2) + \\
&\frac{\lambda}{4}(\pi_1(x)^2 + \pi_2(x)^2 + (v + H(x))^2 + \pi_3(x)^2)^2 = \\
&V(v) + \lambda v^2 H(x)^2 + \\
&\frac{\mu^2 + \lambda v^2}{2}(\pi_1(x)^2 + \pi_2(x)^2 + \pi_3(x)^2 + H(x)^2) + \\
&\frac{\lambda}{4}\left(\sum_{i,j=1}^3 \pi_i(x)^2 \pi_j(x)^2 + 2H(x)(2v + H(x)) \sum_{i=1}^3 \pi_i(x)^2\right) + \\
&H(x)(\lambda v^3 + \mu^2 v).
\end{aligned} \tag{1.55}$$

Taking into account the ground state definition (1.51), the expression (1.55) is simplified to

$$\begin{aligned}
V(\Phi(x)) &= V(v) + \lambda v^2 H(x)^2 + \\
&\frac{\lambda}{4}\left(\sum_{i,j=1}^3 \pi_i(x)^2 \pi_j(x)^2 + 2H(x)(2v + H(x)) \sum_{i=1}^3 \pi_i(x)^2\right).
\end{aligned} \tag{1.56}$$

The potential (1.56) describes the three massless Goldstone bosons $\pi_i(x)$ and the “radial” fluctuation $H(x)$ with a mass $M_H = \lambda v^2 = -2\mu^2$. The field $H(x)$ is called the Higgs boson. The Goldstone bosons $\pi_i(x)$ are gauged away, i.e. $\pi_i(x) \equiv 0$, if the unitary basis is considered. The $SU(2)$ symmetry of the ground state (1.52) is spontaneously broken, leaving only the unbroken $U(1)$, under which the Higgs field $H(x)$ remains invariant

$$\begin{aligned}
\langle \Phi(x) \rangle &\rightarrow e^{i\alpha(x)Q} \langle \Phi(x) \rangle = (1 + i\alpha(x)Q + \dots) \begin{pmatrix} 0 \\ v + H(x) \end{pmatrix} = \begin{pmatrix} 0 \\ v + H(x) \end{pmatrix}, \\
Q \langle \Phi(x) \rangle &= 0 \Rightarrow QH(x) = 0, \\
H(x) &\rightarrow e^{i\alpha(x)Q} H(x) = H(x), \quad e^{i\alpha(x)Q} \in U(1),
\end{aligned} \tag{1.57}$$

where the operator Q is related to the electric charge of the field $H(x)$.

This spontaneous symmetry breaking for the vacuum state of the scalar doublet, $\langle \Phi(x) \rangle$, is called the Brout-Englert-Higgs mechanism.

1.3.2 The mass eigenstates of the gauge bosons

The masses of W_μ^\pm , Z_μ and A_μ are obtained by substituting the Higgs VEV into the kinetic part of the Lagrangian \mathcal{L}_Φ (1.46),

$$\mathcal{L}_{k\Phi} = (D_{\mu,L}\Phi(x))^\dagger D^{\mu,L}\Phi(x).$$

Expanding the Pauli matrices σ_a , the left-handed covariant derivative $D_{\mu,L}$ is rewritten as

$$D_{\mu,L} \equiv \partial_\mu + \frac{i}{2} \begin{pmatrix} g'Y_\Phi B_\mu + gW_\mu^3 & g(W_\mu^1 - iW_\mu^2) \\ g(W_\mu^1 + iW_\mu^2) & g'Y_\Phi B_\mu - gW_\mu^3 \end{pmatrix}. \quad (1.58)$$

For the vacuum state (1.52), we find that

$$\begin{aligned} D_{\mu,L} < \Phi > &= \frac{1}{\sqrt{2}} D_{\mu,L} \begin{pmatrix} 0 \\ v \end{pmatrix} = \frac{-iv}{2\sqrt{2}} \begin{pmatrix} g(W_\mu^1 - iW_\mu^2) \\ g'Y_\Phi B_\mu - gW_\mu^3 \end{pmatrix}, \\ (D_{\mu,L} < \Phi >)^\dagger &= \frac{1}{\sqrt{2}} (D_{\mu,L})^\dagger \begin{pmatrix} 0 & v \end{pmatrix} = \frac{iv}{2\sqrt{2}} \begin{pmatrix} g(W_\mu^1 + iW_\mu^2) & g'Y_\Phi B_\mu - gW_\mu^3 \end{pmatrix}. \end{aligned} \quad (1.59)$$

Hence, the kinetic part of the Higgs sector in the vacuum state gives

$$\mathcal{L}_{k\Phi} = (D_{\mu,L} < \Phi >)^\dagger D^{\mu,L} < \Phi > = \frac{1}{2} \frac{g^2 v^2}{4} |W_\mu^1 - iW_\mu^2|^2 + \frac{1}{2} \frac{v^2}{4} (g'Y_\Phi B_\mu - gW_\mu^3)^2. \quad (1.60)$$

The first term in equation (1.60) is the mass term of the complex, and therefore charged, vector fields W_μ^\pm with masses $m_W = gv/2$. The second term in equation (1.60) is the mass term of an electrically neutral particle, Z_μ boson

$$\frac{1}{2} \frac{v^2}{4} (g'Y_\Phi B_\mu - gW_\mu^3)^2 = \frac{1}{2} m_Z^2 (Z_\mu)^2. \quad (1.61)$$

To find this mass eigenstate, one must notice that the mass term (1.61) is expressed as

$$\begin{aligned} \frac{1}{2} \frac{v^2}{4} (g'Y_\Phi B_\mu - gW_\mu^3)^2 &= \frac{1}{2} \frac{v^2}{4} (g'^2 Y_\Phi^2 B_\mu B^\mu - 2gg'Y_\Phi B_\mu W_3^\mu + g^2 W_3^\mu W_{3\mu}) = \\ &= \frac{1}{2} \begin{pmatrix} B^\mu & W_3^\mu \end{pmatrix} M^2 \begin{pmatrix} B_\mu \\ W_{3\mu} \end{pmatrix}, \end{aligned} \quad (1.62)$$

with the mass matrix M^2 ,

$$M^2 = \frac{v^2}{4} \begin{pmatrix} g'^2 Y_\Phi^2 & -gg'Y_\Phi \\ -gg'Y_\Phi & g^2 \end{pmatrix}. \quad (1.63)$$

The mass eigenstates are found by diagonalizing the matrix (1.63) with the diagonal elements to be squared masses, m^2 , of the neutral gauge bosons. There are two normalized eigenstates

$$Z_\mu = \frac{g'Y_\Phi B_\mu - gW_\mu^3}{\sqrt{g^2 + g'^2Y_\Phi^2}}, \quad A_\mu = \frac{g'Y_\Phi B_\mu + gW_\mu^3}{\sqrt{g^2 + g'^2Y_\Phi^2}}, \quad (1.64)$$

with the masses given by

$$m_Z = \frac{v}{2}\sqrt{g^2 + g'^2Y_\Phi^2}, \quad m_A = 0. \quad (1.65)$$

Recalling the mass eigenbasis (1.36) for the neutral gauge bosons and comparing it with equation (1.64), one derives the following relations:

$$\cos \theta_W = \frac{g}{\sqrt{g^2 + g'^2Y_\Phi^2}}, \quad \sin \theta_W = \frac{Y_\Phi g'}{\sqrt{g^2 + g'^2Y_\Phi^2}}. \quad (1.66)$$

Equation (1.66) is consistent with the $\sin \theta_W$ definition (1.37), if the following statement holds:

$$Y_\Phi = +1.$$

Using the gauge bosons masses, m_W and m_Z , and the electroweak mixing angle θ_W , we formulate the important relation

$$\frac{m_W}{m_Z} = \frac{vg}{v\sqrt{g^2 + g'^2}} = \cos \theta_W, \quad (1.67)$$

which was proven in experiments.

1.3.3 The fermion masses

The masses of fermions are generated at the vacuum state due to their interactions with the Higgs doublet (1.45). The interactions between the Higgs field, left- and right-handed fermions are described by the Yukawa Lagrangian, \mathcal{L}_{Yukawa} ,

$$\mathcal{L}_{Yukawa} = -y_f(\bar{L}_f\Phi l_{R,f} + \bar{l}_{R,f}\Phi^\dagger L_f), \quad (1.68)$$

where the index f denotes the fermion family of the left- (1.16) and right-handed (1.17) spinors. Such interaction flips the chiralities of the matter fields, from left-handed to right-handed

fermions. The interaction (1.68) is invariant under the local gauge $SU(2) \otimes U(1)$ transformations, preserving the hypercharge,

$$-Y_L + Y_\Phi + Y_R = -(-1) + 1 - 2 = 0, \quad (1.69)$$

where the case of the Higgs boson $H(x)$ with $Y_\Phi = +1$, interacting with an electron e with $Y_L = -1$, $Y_R = -2$, has been considered. The constants y_f are free real parameters of the theory; their values are not predicted by the Standard Model itself. Because we need a different constant for each fermion in the model, we have to add nine extra free parameters (not considering the neutrinos) to the theory. The generation of the mass is a bit different for the quarks than for the leptons. This is because of the fact that there are no right-handed neutrinos in the model.

If we expand the Higgs doublet (1.45) at the **VEV** (1.52), the Yukawa Lagrangian turns into

$$\begin{aligned} \mathcal{L}_{Yukawa} = & -\frac{y_f}{\sqrt{2}} \left(\begin{pmatrix} \bar{\nu}_{f,L} & \bar{l}_{f,L} \end{pmatrix} \begin{pmatrix} 0 \\ v+H \end{pmatrix} l_{f,R} + \bar{l}_{f,R} \begin{pmatrix} 0 & v+H \end{pmatrix} \begin{pmatrix} \nu_{f,L} \\ l_{f,L} \end{pmatrix} \right) = \\ & -\frac{y_f v}{\sqrt{2}} (\bar{l}_{f,R} l_{f,L} + \bar{l}_{f,L} l_{f,R}) - \frac{y_f H}{\sqrt{2}} (\bar{l}_{f,R} l_{f,L} + \bar{l}_{f,L} l_{f,R}) = \\ & -\frac{y_f v}{\sqrt{2}} \bar{l}_f l_f - \frac{y_f H}{\sqrt{2}} \bar{l}_f l_f, \end{aligned} \quad (1.70)$$

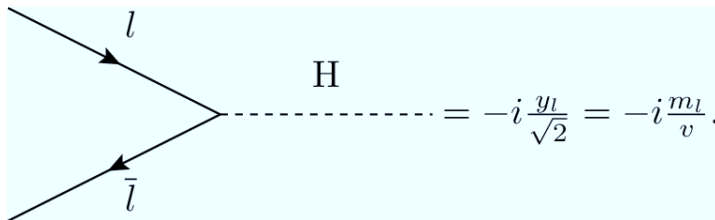
where $l_{f,L}$ and $l_{f,R}$ represent the 2×2 left- and right-handed lepton spinors of the f^{th} fermion family. In the last step of equation 1.70 we have used the formula

$$\bar{\psi}\psi \equiv \bar{\psi}_R\psi_L + \bar{\psi}_L\psi_R.$$

The mass of the lepton l_f is equal to

$$m_f = \frac{y_f v}{\sqrt{2}}, \quad (1.71)$$

while the second term in the last line of (1.70) describes an interaction between the Higgs field H and the lepton l_f



Such the coupling to the Higgs boson is proportional to the mass of the lepton. This is true for all matter in the Standard Model.

In a similar way, the Yukawa interaction generates masses for the quarks. However, if one would use the same procedure as for the leptons, only the lower half of each left-handed fermion doublet will acquire a mass. This is fine for the leptons since the neutrinos are massless. To obtain masses for the upper halves of the left-handed quark doublets, a Higgs doublet of antiparticles, $\bar{\phi}^0$ and ϕ^- , must be used. The Higgs doublet of antiparticles, Φ^c , is written as

$$\Phi^c = i\sigma^2 \Phi^* = i \begin{pmatrix} 0 & -i \\ i & 0 \end{pmatrix} \begin{pmatrix} \phi^+ \\ \phi^0 \end{pmatrix}^* = \begin{pmatrix} \bar{\phi}^0 \\ -\phi^- \end{pmatrix}. \quad (1.72)$$

Remembering the properties of the Pauli matrices σ^a , it is easy to verify that Φ^c transforms just like Φ under $SU(2)$ transformations

$$\Phi^c = i\sigma^2 \Phi^* \rightarrow i\sigma^2 (e^{i\sigma_a T^a/2} \Phi)^* = i\sigma^2 e^{-i\sigma_a T^a/2} \Phi^* = e^{i\sigma_a T^a/2} \Phi^c. \quad (1.73)$$

Near the **VEV** the doublet Φ^c can be expanded as

$$\Phi^c = \frac{1}{\sqrt{2}} \begin{pmatrix} v + H(x) \\ 0 \end{pmatrix}. \quad (1.74)$$

In general, the Yukawa interactions of quarks with the Higgs doublets Φ and Φ^c are given by

$$\mathcal{L}_{Yukawa} = -Y_{ij}^d \bar{Q}_{iL} \Phi d_{jR} - Y_{ij}^u \bar{Q}_{iL} \Phi^c u_{jR} + h.c., \quad (1.75)$$

where the h.c. stands for Hermitian conjugate. Y_{ij}^d and Y_{ij}^u are 3×3 complex matrices, mixing the flavors of quarks; i, j are labels of the fermion families; Q_{iL} are left-handed quark doublets; d_{jR} and u_{jR} are right-handed down- and up-type quark singlets, respectively. When Φ and Φ^c acquire vacuum expectation values, the equation (1.75) yields mass terms for the quarks. The physical states in the mass-eigenstate basis are obtained by diagonalizing $Y^{u,d}$ with four unitary matrices $V_{L,R}^{u,d}$ as

$$M_{f,diag}^{u,d} \equiv (Y^{u,d})_{ff} = V_{fi,L}^{u,d} Y_{ij}^{u,d} V_{jf,R}^{u,d\dagger}. \quad (1.76)$$

The diagonalization (1.76) means that the down-type quarks are rotated, using the matrix V_{CKM} , from weak-isospin (gauge) basis to the mass eigenstates

$$\begin{pmatrix} d' \\ s' \\ b' \end{pmatrix} = V_{CKM} \begin{pmatrix} d \\ s \\ b \end{pmatrix} = \begin{pmatrix} V_{ud} & V_{us} & V_{ub} \\ V_{cd} & V_{cs} & V_{cb} \\ V_{td} & V_{ts} & V_{tb} \end{pmatrix} \begin{pmatrix} d \\ s \\ b \end{pmatrix}. \quad (1.77)$$

The 3×3 unitary matrix V_{CKM} is Cabibbo-Kobayashi-Maskawa (CKM) matrix [13, 14]. It is parametrized by three mixing angles and one CP-violating phase [14, 15]. As a result of the rotation (1.77), the weak-charged interaction of the gauge bosons W^\pm (1.34) with quarks takes the form

$$-\frac{g}{\sqrt{2}}W_\mu^+ \begin{pmatrix} \bar{u}_L & \bar{c}_L & \bar{t}_L \end{pmatrix} \gamma^\mu V_{CKM} \begin{pmatrix} d_L \\ s_L \\ b_L \end{pmatrix} + h.c. \quad (1.78)$$

Substitution of the expanded $\Phi(x)$ and $\Phi^c(x)$ at the **VEV** into equation (1.75), written in the mass-eigenstate basis (1.77), leads to (taking u and d quarks from the 1st family as an example):

$$\begin{aligned} \mathcal{L}_{Yukawa} &= -Y_{11}^d \bar{Q}_{uL} \Phi d'_R - Y_{11}^u \bar{Q}_{uL} \Phi^c u_R + h.c. = \\ &= -\frac{Y_{11}^d}{\sqrt{2}}(v+H)(\bar{d}'_L d'_R + \bar{d}_R d'_L) - \frac{Y_{11}^u}{\sqrt{2}}(v+H)(\bar{u}_L u_R + \bar{u}_R u_L) = \\ &= -\frac{Y_{11}^d}{\sqrt{2}}(v\bar{d}' d' + H\bar{d}' d') - \frac{Y_{11}^u}{\sqrt{2}}(v\bar{u}u + H\bar{u}u) = \\ &= -\frac{Y_{ij}^d}{\sqrt{2}}V_{ij}(v\bar{d}_i d_j + H\bar{d}_i d_j) - \frac{Y_{ij}^u}{\sqrt{2}}(v\bar{u}u + H\bar{u}u). \end{aligned} \quad (1.79)$$

The Lagrangian \mathcal{L}_{Yukawa} (1.79) introduces the mass terms of the quarks and their interaction with the Higgs boson.

2 Supersymmetry

Despite of tremendous success, the Standard Model is not theoretically satisfactory, and is regarded as a low-energy effective theory of a more fundamental theory. There are many reasons for the conceptual incompleteness: the assignment of the quantum numbers to the fermions is not fully clear; we do not understand why there are three apparently unrelated gauge groups and what rules the strength of their coupling constants; there is no reason for which there are only three generations of fermions and it is not explained why the fermion mass spectrum ranges over five orders of magnitude. Moreover, the presence of the scalar field in the **SM** is completely artificial, since it is introduced just for the purpose of breaking the electroweak symmetry. We do not understand the flavor mixing. In the strict framework of the **SM**, the neutrinos are assumed to be massless, there is experimental evidence that neutrinos must be massive particles, although very light ones.

The Standard Model depends on nineteen parameters: the three gauge coupling constants, the two parameters, μ^2 and λ , which determine the mass and the self-coupling of the Higgs field, the nine quark and charged lepton masses, the three angles and one phase specifying the quark mixing matrix and the θ_{QCD} phase related to strong spontaneous CP violation [16, 17]. Moreover, many more parameters are needed to accommodate non-accelerator observations [18, 19] of Gravity phenomena. Although, Gravity is not united with the other interactions in the Standard Model, it is possible that it can be explained by the classical general relativity. However, the general relativity is not a quantum theory, and there is no obvious way to introduce quantum Gravity within the **SM** context. Possible solutions include supergravity theories [20].

Another question is: can all the interactions be unified? Radiative effects make gauge couplings dependent on the energy scale. The couplings, when defined as renormalized values including loop corrections, require the specification of a renormalization prescription, for which the modified minimal subtraction scheme, **MS**, [21, 22] is usually used. In the **SM** the strong and weak couplings, associated with non-Abelian gauge groups, decrease with energy, while the electromagnetic coupling related to an Abelian group increases. Thus, it becomes possible that all couplings could be equal at some energy scale. According to the Grand Unification Theory, **GUT**, this equality is not occasional, but it is a manifestation of a unique origin of these three interactions. As a result of the spontaneous symmetry breaking, the unifying group is broken and the unique interaction is splitted into three branches: strong, weak and electromagnetic. The left plot of Figure 2.1 clearly demonstrates that the unification of the coupling constants within the **SM** at a single point is impossible. The unification can only be reached, if new physics enters between the electroweak, M_{EWK} , and Planck scales, M_{Pl} ,

$$M_{EWK} \sim M_Z \sim 10^2 \text{ GeV}, \quad M_{Pl} = \sqrt{\hbar c^5 / G_N} \sim 10^{19} \text{ GeV},$$

where Newton's constant G_N is about of $7 \cdot 10^{-39} \text{ GeV}^{-2}$. It turns out that a perfect unification can be obtained within the Supersymmetric model, **SUSY**, if masses of SUSY particles, M_{SUSY} , are of an order of 1 TeV [23]. This is shown on the right side of Figure 2.1. From the global fit of GUT expectations on experimental observables, one finds the SUSY and GUT scales, M_{SUSY} and M_{GUT} ,

$$\begin{aligned} M_{SUSY} &= 10^{3.4 \pm 0.9 \pm 0.4} \text{ GeV}, \\ M_{GUT} &= 10^{15.8 \pm 0.3 \pm 0.1} \text{ GeV}, \end{aligned} \quad (2.1)$$

at which the spontaneous symmetry breaking and the grand unification, respectively, occur in the **SUSY**.

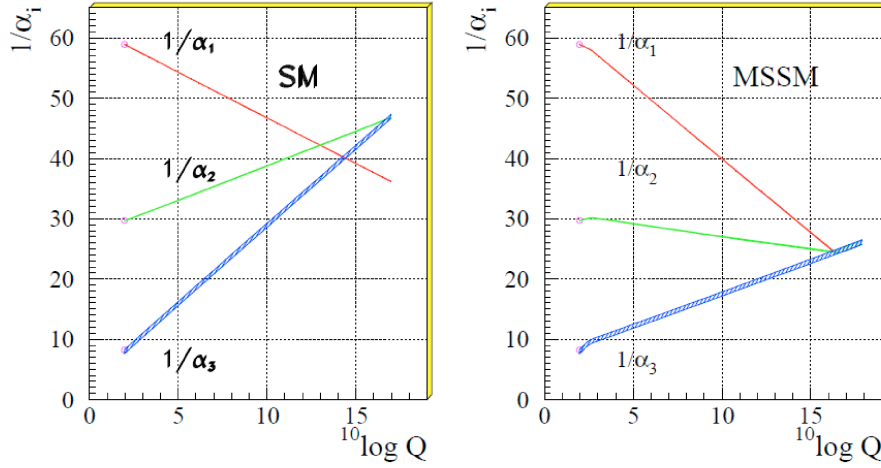


Figure 2.1: Evolution of the inverse of the three coupling constants in the Standard Model (left) and in the supersymmetric extension of the SM (right). The SUSY particles are assumed to contribute only above the effective SUSY scale M_{SUSY} of about 1 TeV, causing a change in the slopes of the couplings evolutions. The thickness of the lines represents statistical errors on the coupling constants from the fit [23].

The discrepancy of about 12 orders of magnitude between M_{GUT} and M_{SUSY} scales leads to a very serious problem, called the hierarchy problem. The scales roughly correspond to masses of scalar fields responsible for the spontaneous GUT and SUSY symmetry breakings. To get such small value of M_{SUSY}/M_{GUT} in a natural way, one needs some kind of fine tuning. Another aspect of the hierarchy problem is the preservation of the given hierarchy. Any high-order radiative effects in the scalar sector might destroy it. This is illustrated by the radiative correction to the Higgs boson mass M_H , described by the Feynman diagrams of Figure 2.2.

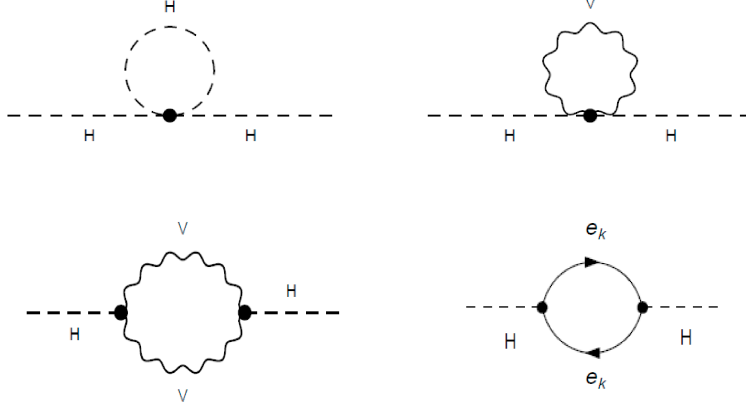


Figure 2.2: Tadpole and self-energy Feynmann diagrams for the Higgs boson. Here V stands for gauge bosons, e_k denotes fermions.

The diagrams lead to ultra-violet quadratically divergence

$$\delta M_H^2 \sim y_k^2 \int \frac{d^4 k}{(2\pi)^4} \frac{i}{k^2 - M_H^2} \sim y_k^2 \Lambda^2, \quad (2.2)$$

where y_k is a Yukawa coupling of the Higgs field to the fermion e_k , and Λ is a cut-off scale of order of the M_{Pl} or M_{GUT} scales. The divergence will spoil the hierarchy (2.1). The significant reduction of the contribution from δM_H^2 (2.2) requires a fine tuning of the coupling constants y_k . The only known way of achieving such reduction and even cancellation is the Supersymmetry. Moreover, in the unbroken **SUSY**, cancellation of δM_H^2 (2.2) automatically happens in all orders of perturbation theory. The reason is the presence of superpartners for ordinary particles. The contribution from bosonic loops cancels those arising from loops with fermions as shown in Figure 2.3.

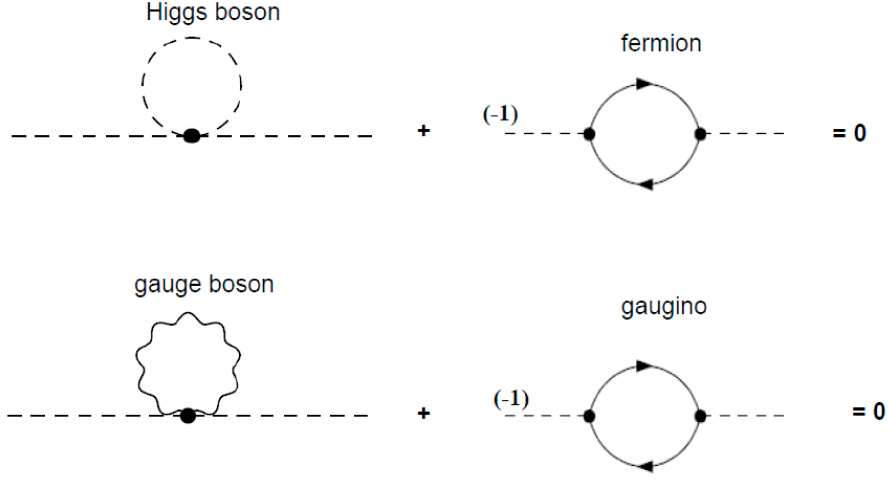


Figure 2.3: Cancellation of the quadratic divergence (2.2) . The fermionic loops contribute with an additional factor (-1) originating from Fermi statistics.

The top diagrams of Figure 2.3 are tadpole Feynman diagrams for contributions from the Higgs boson and its superpartner in the **SUSY**. The bottom diagrams characterize the loop contributions of gauge fields, gauge bosons and gauginos, to the mass of a Higgs boson. The full cancellation takes place in the case of unbroken supersymmetry, when the sum of squared masses is the same for bosons and fermions,

$$\sum_{bosons} m^2 = \sum_{fermions} m^2. \quad (2.3)$$

If equation (2.3) does not hold,

$$\sum_{bosons} m^2 - \sum_{fermions} m^2 = M_{SUSY}^2, \quad (2.4)$$

the **SUSY** is not an exact symmetry, and the divergence (2.2) is reduced to the scale of about $y_k^2 \cdot M_{SUSY}^2$. The scale M_{SUSY} should not be very large, $M_{SUSY} \simeq 1 \text{ TeV}$, in order to have a natural fine tuning:

$$\delta M_H^2 \sim y_k^2 \cdot M_{SUSY}^2 \sim 10^{-2} \cdot 10^6 \text{ GeV}^2 \sim 10^4 \text{ GeV}^2 \sim M_H^2. \quad (2.5)$$

2.1 Basics of supersymmetry

The Supersymmetry is based on the superspace, superfields and an algebra of supersymmetric transformations, the Super-Poincare Lie Algebra, describing the relations between SUSY gen-

erators Q_α^i and \bar{Q}_α^i . Here α and i are spinorial and supersymmetric indexes. To illustrate the ideas of the Supersymmetry, a simple example having only one supersymmetric dimension $i = 1$ usually denoted as the **SUSY** with only one chiral supermultiplet, $N = 1$, is considered [24].

The spinorial SUSY charge Q_α performs transformations of the matter fields, when supertranslation in the superspace is done. The superspace [20] differs from the ordinary Minkowski space by adding two new coordinates, θ_α and $\bar{\theta}_\alpha$ which are Grassmanian, i.e. anti-commuting, variables,

$$\begin{aligned} \{\theta_\alpha, \theta_\beta\} &= \{\bar{\theta}_\alpha, \bar{\theta}_\beta\} = 0, \\ \left\{ \frac{\partial}{\partial \theta_\alpha}, \theta_\beta \right\} &= \left\{ \frac{\partial}{\partial \bar{\theta}_\alpha}, \bar{\theta}_\beta \right\} = \delta_{\alpha\beta}, \\ \left\{ \frac{\partial}{\partial \theta_\alpha}, \bar{\theta}_\beta \right\} &= \left\{ \frac{\partial}{\partial \bar{\theta}_\alpha}, \theta_\beta \right\} = 0, \end{aligned} \quad (2.6)$$

where $\bar{\theta}_\alpha$ is obtained by conjugating θ_α . The Minkowski space is extended to the superspace as

$$\{x_\mu\} \rightarrow \{x_\mu, \theta_\alpha, \bar{\theta}_\alpha\}. \quad (2.7)$$

A SUSY transformation, G , is constructed on the superspace basis in the same way as an ordinary translation in the Minkowski space

$$G(x_\mu, \theta_\alpha, \bar{\theta}_\alpha) = e^{i(-x^\mu P_\mu + \theta_\alpha Q_\alpha + \bar{\theta}_\alpha \bar{Q}_\alpha)}, \quad (2.8)$$

where P_μ is an operator of translation in the Minkowski space. In further discussions we skip the spinorial index α , assuming the following notation:

$$\theta\theta \rightarrow \varepsilon^{\alpha\beta} \theta_\alpha \theta_\beta, \bar{\theta}\bar{\theta} \rightarrow \varepsilon^{\dot{\alpha}\dot{\beta}} \bar{\theta}_{\dot{\alpha}} \bar{\theta}_{\dot{\beta}}, \bar{\theta}\sigma^\mu\theta \rightarrow \bar{\theta}^{\dot{\alpha}} \sigma_{\dot{\alpha}\alpha}^\mu \theta^\alpha,$$

to describe scalars, pseudoscalars and 4-vectors constructed on the Grassman variables. Here σ^μ are the 2×2 Pauli matrices and $\varepsilon^{\alpha\beta}$ is the antisymmetric tensor. Any infinitesimal transformation in the superspace, takes the form

$$\begin{aligned} x_\mu &\rightarrow x_\mu + i\theta\sigma_\mu\bar{\varepsilon} + i\varepsilon\sigma_\mu\bar{\theta}, \\ \theta &\rightarrow \theta + \varepsilon, \\ \bar{\theta} &\rightarrow \bar{\theta} + \bar{\varepsilon}, \end{aligned} \quad (2.9)$$

where ε and $\bar{\varepsilon}$ are infinitesimal translations. From equations (2.8) and (2.9), the Q_α and \bar{Q}_α generators are expressed in terms of the partial derivatives $\partial/\partial\theta_\alpha$ and $\partial/\partial\bar{\theta}_\alpha$ as

$$\begin{aligned}
Q_\alpha &= \frac{\partial}{\partial \theta_\alpha} - i \bar{\theta}_\beta \sigma_{\beta\alpha}^\mu \frac{\partial}{\partial x^\mu}, \\
\bar{Q}_\alpha &= -\frac{\partial}{\partial \bar{\theta}_\alpha} + i \sigma_{\alpha\beta}^\mu \theta_\beta \frac{\partial}{\partial x^\mu}.
\end{aligned} \tag{2.10}$$

Using the definitions (2.10), one can formulate the main rule of the graded (Super-Poincare) Lie Algebra, the anti-commutator of Q and \bar{Q} , as

$$\{Q_\alpha, \bar{Q}_\beta\} = 2i \sigma_{\alpha\beta}^\mu P_\mu. \tag{2.11}$$

The presence of the translation generator P_μ in equation (2.11) means that the Supersymmetry is a spacetime symmetry, conserving in time and space

$$[Q_\alpha, P^\mu] = 0. \tag{2.12}$$

Equation (2.12) is the second rule of the graded Lie Algebra. We immediately see that the rules (2.11) and (2.12) implies a zero-energy state, the ground state. Such state appears in a degenerate pair, where one member is a boson and the other one is a fermion

$$\begin{aligned}
E = \langle 0 | P_\mu | 0 \rangle &= 1/4 \text{Tr} \langle 0 | \{Q_\alpha, \bar{Q}_\alpha\} | 0 \rangle = 1/4 (|\bar{Q}_\alpha | 0 \rangle|^2 + |Q_\alpha | 0 \rangle|^2) = 0, \Rightarrow \\
Q_\alpha | 0, \lambda \rangle &= | 0, \lambda \rangle = 0, \quad \bar{Q}_\alpha | 0, \lambda \rangle = | 0, \lambda + 1/2 \rangle = 0.
\end{aligned} \tag{2.13}$$

Here λ is the helicity of the ground state. This degeneracy of the vacuum is destroyed, if the invariance of the vacuum is spontaneously broken, i.e

$$\begin{aligned}
E > 0, \Rightarrow Q_\alpha | 0 \rangle &= | E, \lambda \rangle \neq | 0 \rangle, \\
\bar{Q}_\alpha | 0 \rangle &= | E, \lambda + 1/2 \rangle \neq | 0 \rangle, \quad Q_\alpha | 0 \rangle \neq \bar{Q}_\alpha | 0 \rangle.
\end{aligned} \tag{2.14}$$

Therefore, the supersymmetry is spontaneously broken, i.e. the vacuum is not invariant under $G(x_\mu, \theta_\alpha, \bar{\theta}_\alpha)$ transformations (2.8), if and only if the minimum of the potential, E , is positive. The number of supersymmetries N relates to the maximal allowed spin S of particles in multiplets as

$$-S + N/2 \leq S.$$

The $N = 1$ theory contains chiral and vector superfields defined as multiplets of the scalar $\phi(x)$, fermion $\xi(x)$ and vector $A_\mu(x)$ fields,

$$\begin{aligned}
\text{Chiral multiplet: } \{ \phi(x) = | E, \lambda = 0 \rangle, \xi(x) = \bar{Q} | \phi \rangle = | E, \lambda = 1/2 \rangle \}, \\
\text{Vector multiplet: } \{ \xi(x) = | E, \lambda = 1/2 \rangle, A_\mu(x) = \bar{Q} | \xi \rangle = | E, \lambda = 1 \rangle \}.
\end{aligned} \tag{2.15}$$

Every particle of the supermultiplet has a partner with the same mass but with a spin differing by $1/2$, because of the spinorial **SUSY** generators \bar{Q}_α acting on the helicity. Since the generator \bar{Q}_α commutes with the hypercharge Y and weak isospin \vec{T} operators, the corresponding quantum numbers, the electric charge and isospin are identical for a particle and its superpartner.

2.2 Superfields

The construction of the SUSY Lagrangian requires the introduction of chiral and vector superfields (2.15) in the calculations. They are used to write a Lagrangian, invariant under global SUSY and local gauge transformations.

In general, the superfield is any analytic function $\mathcal{F}(x, \theta, \bar{\theta})$ defined in the superspace $\{x, \theta, \bar{\theta}\}$. The function contains terms proportional to Grassmannians in some power of θ and $\bar{\theta}$, up to four at most:

$$1, \theta, \bar{\theta}, \theta\theta, \bar{\theta}\bar{\theta}, \theta\theta\bar{\theta} \text{ etc.}$$

Since

$$\bar{\theta}\sigma^\mu\theta = -\theta\sigma^\mu\bar{\theta},$$

and

$$\theta\sigma^{\mu\nu}\theta = 0 = \bar{\theta}\bar{\sigma}^{\mu\nu}\bar{\theta},$$

the most general expression for the superfield is

$$\begin{aligned} \mathcal{F}(x, \theta, \bar{\theta}) = & f(x) + \sqrt{2}\theta\xi(x) + \sqrt{2}\bar{\theta}\bar{\chi}(x) + \theta\theta M(x) + \bar{\theta}\bar{\theta}N(x) + \\ & \theta\sigma^\mu\bar{\theta}A_\mu(x) + \theta\theta\bar{\theta}\bar{\lambda}(x) + \bar{\theta}\bar{\theta}\theta\zeta(x) + \frac{1}{2}\theta\theta\bar{\theta}\bar{\theta}D(x), \end{aligned} \quad (2.16)$$

where $f(x)$, $M(x)$, $N(x)$ and $D(x)$ represent scalar fields, $A_\mu(x)$ is a vector field, $\xi(x)$, $\zeta(x)$ are left-handed Weyl spinors and $\bar{\chi}(x)$ and $\bar{\lambda}(x)$ are right-handed Weyl spinor fields. The Hermitian conjugate $\mathcal{F}^\dagger(x, \theta, \bar{\theta})$ is considered as an independent superfield. All fields, being complex, give sixteen real bosonic and sixteen real fermionic degrees of freedom. They correspond (though not necessarily in a one to one way) to particles that neatly fall into complete supermultiplets [24, 25, 26].

The superfield representation (2.16) is highly reducible, i.e. it is physically redundant. It is possible to obtain an irreducible representation, if we introduce additional constraints on supermultiplets. Specific types of irreducible superfields are chiral and vector superfields.

The first class of constraints, determining the chiral superfield, is obtained by application of the chiral covariant derivatives $D_\alpha(x)$ and $\bar{D}_{\dot{\alpha}}(x)$ [24]

$$\begin{aligned} \partial_\alpha &= \frac{\partial}{\partial\theta^\alpha}, \quad \bar{\partial}_{\dot{\alpha}} = \frac{\partial}{\partial\bar{\theta}^{\dot{\alpha}}}, \\ D_\alpha &\equiv \partial_\alpha - i\sigma_{\alpha\beta}^\mu \bar{\theta}^\beta \partial_\mu, \\ \bar{D}_{\dot{\alpha}} &\equiv -\bar{\partial}_{\dot{\alpha}} + i\theta^\beta \sigma_{\beta\dot{\alpha}}^\mu \partial_\mu. \end{aligned} \quad (2.17)$$

To define the chiral representation of $\mathcal{F}(x, \theta, \bar{\theta})$ (2.16), we find points $y^\mu = x^\mu - i\theta\sigma^\mu\bar{\theta}$ and $\bar{y} = x^\mu + i\theta\sigma^\mu\bar{\theta}$, satisfying the criteria of the extrema in the superspace

$$\bar{D}_\alpha y^\mu = 0, D_\alpha \bar{y}^\mu = 0. \quad (2.18)$$

Therefore, for any analytical function $\Phi(y, \theta)$ in the superspace, the following equations hold:

$$\bar{D}_\alpha \Phi(y, \theta) = 0, D_\alpha \Phi^\dagger(\bar{y}, \bar{\theta}) = 0. \quad (2.19)$$

The function $\Phi(y, \theta)$ is the irreducible representation of $\mathcal{F}(y, \theta, \bar{\theta})$, and called the chiral superfield. It is expressed in terms of component fields, two scalars, $\phi(y)$ and $F(y)$, and one spinor, $\xi(y)$, as

$$\begin{aligned} \Phi(y, \theta) &= \phi(y) + \sqrt{2}\theta\xi(y) + \theta\theta F(y), \\ \Phi^\dagger(\bar{y}, \bar{\theta}) &= \phi^*(\bar{y}) + \sqrt{2}\bar{\theta}\bar{\xi}(\bar{y}) + \bar{\theta}\bar{\theta}F^*(\bar{y}). \end{aligned} \quad (2.20)$$

Products of chiral superfields, $\Phi_1\Phi_2\cdots\Phi_l$ or $\Phi_1^\dagger\Phi_2^\dagger\cdots\Phi_l^\dagger$, are themselves chiral superfields

$$\begin{aligned} \Phi_i\Phi_j &= \phi_i\phi_j + \sqrt{2}\theta(\xi_i\phi_j + \phi_i\xi_j) + \theta\theta(\phi_iF_j + \phi_jF_i - \xi_i\xi_j), \\ \Phi_i\Phi_j\Phi_k &= \phi_i\phi_j\phi_k + \sqrt{2}\theta(\xi_i\phi_j\phi_k + \xi_j\phi_k\phi_i + \xi_k\phi_i\phi_j) \\ &\quad + \theta\theta(F_i\phi_j\phi_k + F_j\phi_k\phi_i + F_k\phi_i\phi_j - \xi_i\xi_j\phi_k - \xi_j\xi_k\phi_i - \xi_k\xi_i\phi_j), \\ \bar{D}_\alpha[\Phi_i\Phi_j] &= \bar{D}_\alpha[\Phi_i\Phi_j\Phi_k] = \dots = 0 \end{aligned} \quad (2.21)$$

The $F(y)$ -component of $\Phi(y, \theta)$ (2.20) transforms into itself plus a spacetime derivative under the supersymmetric variations $G(y_\mu, \theta, \bar{\theta})$ (2.8),

$$\begin{aligned} F(y) &\rightarrow F(y) + \delta F(y), \\ \delta F(y) &= i\partial_\mu(\sqrt{2}\xi(y)\sigma^\mu\bar{\epsilon}). \end{aligned} \quad (2.22)$$

The important point to note is that the $F(y)$ -component of the products of chiral superfields, denoted as $|_{\theta\theta}$, being a part of the SUSY Lagrangian, would yield a supersymmetric-invariant action

$$\begin{aligned} S &= \int d^4y d^2\theta \Phi_1(y, \theta)\Phi_2(y, \theta) \cdots \Phi_N(y, \theta)|_{\theta\theta} = \int d^4y \tilde{F}(y), \\ \delta S &= \int d^4y \delta \tilde{F}(y) = i\sqrt{2} \int d^4y \partial_\mu(\tilde{\xi}(y)\sigma^\mu\bar{\epsilon}) = 0. \end{aligned} \quad (2.23)$$

Here $\tilde{F}(y)$ and $\tilde{\xi}(y)$ are coefficients of $\theta\theta$ - and θ -terms of the product (2.21).

The product of a chiral superfield with its Hermitian conjugate defines the vector superfield,

$$V(x, \theta, \bar{\theta}) = \Phi^\dagger(x, \bar{\theta}) \cdot \Phi(x, \theta),$$

constrained by the requirement of a reality

$$V(x, \theta, \bar{\theta}) = V^\dagger(x, \theta, \bar{\theta}).$$

In the particular choice of **Wess-Zummino** gauge [24, 27], the vector superfield $V(x)$ is expressed as

$$V(x, \theta, \bar{\theta}) = \theta \sigma^\mu \bar{\theta} A_\mu(x) + \theta \theta \bar{\theta} \bar{\lambda}(x) + \bar{\theta} \bar{\theta} \theta \lambda(x) + \frac{1}{2} \theta \theta \bar{\theta} \bar{\theta} D(x), \quad (2.24)$$

where $D(x)$ is a scalar field, $A_\mu(x)$ is a vector field and $\lambda(x)$ is a complex spinor field. $D(x)$ is supersymmetric-invariant as $F(x)$. From the definition (2.24), the vector superfield satisfies the following constraints in the **Wess-Zummino** gauge:

$$\begin{aligned} V^2(x, \theta, \bar{\theta}) &= \frac{1}{2} \theta \theta \bar{\theta} \bar{\theta} A^\mu(x) A_\mu(x), \\ V^n(x, \theta, \bar{\theta}) &= 0, \quad \forall n \geq 3. \end{aligned} \quad (2.25)$$

As we know from the consideration of the Standard Model, the vector field is introduced in the Lagrangian using the vector field strength. To construct a **SUSY** invariant vector superfield strength term, the left- and right-chiral vector-superfield strengths, $W_\alpha(x)$ and $\bar{W}_\alpha(x)$, are introduced as

$$\begin{aligned} W_\alpha(x, \theta, \bar{\theta}) &= -\frac{1}{4} \bar{D}^\beta \bar{D}_\beta D_\alpha V(x, \theta, \bar{\theta}) = -\frac{1}{4} \bar{D} \bar{D} D_\alpha V(x, \theta, \bar{\theta}), \\ \bar{W}_\alpha(x, \theta, \bar{\theta}) &= -\frac{1}{4} D D \bar{D}_\alpha V(x, \theta, \bar{\theta}). \end{aligned} \quad (2.26)$$

They are chiral superfields, which obey to the requirement (2.19)

$$\bar{D}_\alpha W_\alpha(y, \theta) = 0, \quad D_\alpha \bar{W}_\alpha(\bar{y}, \bar{\theta}) = 0. \quad (2.27)$$

Equation (2.27) means that the vector superfield is presented in the **SUSY**-invariant Lagrangian \mathcal{L}_V , describing the dynamics of $V(x, \theta, \bar{\theta})$, only as $|\theta\theta$ terms of products of the vector-superfield strengths $W_{\alpha, \theta, \bar{\theta}}$, i.e.

$$\mathcal{L}_V = -1/4 |W_\alpha(x) W^\alpha(x) + \bar{W}_\alpha(x) \bar{W}^\alpha(x)|_{\theta\theta} = \frac{1}{2} D^2(x) - \frac{1}{4} F_{\mu\nu}(x) F^{\mu\nu}(x) - i\lambda(x) \sigma^\mu \partial_\mu \bar{\lambda}(x). \quad (2.28)$$

Here $F_{\mu\nu}$ is the vector field strength of $A_\mu(x)$ given by equation (1.28).

2.3 R-parity of the chiral and vector superfields

The R -symmetry is a symmetry under global $U(1)_R$ transformations of the superspace which leaves Super-Poincare Lie Algebra (2.10), (2.11) and (2.12) unchanged. The $U(1)_R$ transformation rotates phases of the SUSY operators $Q_\alpha(\bar{D}_\alpha)$ and $\bar{Q}_\alpha(D_\alpha)$, and the Grassmanians θ_α and $\bar{\theta}_\alpha$ by an angle ϕ

$$\begin{aligned} Q_\alpha &\rightarrow e^{i\phi R} Q_\alpha e^{-i\phi R} = e^{-i\phi} Q_\alpha, \\ \bar{Q}_\alpha &\rightarrow e^{i\phi R} \bar{Q}_\alpha e^{-i\phi R} = e^{i\phi} \bar{Q}_\alpha, \\ \theta_\alpha &\rightarrow e^{i\phi} \theta_\alpha, \quad \bar{\theta}_\alpha \rightarrow e^{-i\phi} \bar{\theta}_\alpha. \end{aligned} \quad (2.29)$$

The operator R is a generator of the group $U(1)_R$ and it is related to the R -parity. Equation (2.29) leads to the commutation rules

$$\begin{aligned} [Q_\alpha, R] &= Q_\alpha, \\ [\bar{Q}_\alpha, R] &= -\bar{Q}_\alpha. \end{aligned} \quad (2.30)$$

We can assign the R -parity, R_Φ , to the chiral superfield $\Phi(x)$, transforming under $U(1)_R$ as

$$\begin{aligned} \Phi'(x, e^{i\phi} \theta, e^{-i\phi} \bar{\theta}) &\rightarrow e^{i\phi R_\Phi} \Phi(x, \theta, \bar{\theta}), \\ \Phi'^{\dagger}(x, e^{i\phi} \theta, e^{-i\phi} \bar{\theta}) &\rightarrow e^{-i\phi R_\Phi} \Phi^{\dagger}(x, \theta, \bar{\theta}). \end{aligned} \quad (2.31)$$

The R -parity of the vector superfield, R_V , is zero because of its reality

$$V(x, \theta, \bar{\theta}) = V^{\dagger}(x, \theta, \bar{\theta}) \Rightarrow R_V = -R_V \Rightarrow R_V = 0.$$

The R -parities of the components of superfields are determined as

$$\begin{aligned} R(\phi) &= R_\Phi, \\ R(\xi) &= -R(\bar{\xi}) = R_\Phi - 1, \\ R(F) &= R_\Phi - 2, \\ R(A_\mu) &= 0, \\ R(\lambda) &= -R(\bar{\lambda}) = 1, \\ R(D) &= 0. \end{aligned} \quad (2.32)$$

The R -parity of a state containing several particles is the product of the individual parities.

2.4 The Minimal Supersymmetric Model

The SUSY theories must have the equal number of bosonic and fermionic degrees of freedom. The minimal version of the SUSY generalization of the Standard Model, **MSSM**, doubles the number of particles, introducing a superpartner to each particle [28, 29, 30]. If supersymmetry is exact, superpartners of ordinary particles have the same masses and have to be observed. The absence of them at currently available energies is explained by the fact that their masses are very large. This means that the Supersymmetry should be broken. The **MSSM** introduces a hidden sector, where the Supersymmetry is spontaneously broken via $F(x)$ -mechanism [31]. The heavy scalar singlet $F_X(x)$ of the hidden sector develops the non-zero VEV [32, 33],

$$M_{F_X}^2 \sim \langle 0 | F_X(x) | 0 \rangle \sim M_{SUSY} \times M_{Pl} \sim 10^{22} \text{GeV}^2. \quad (2.33)$$

The field $F_X(x)$, called a “messenger”, is coupled to the chiral sector of the **MSSM** via the superpotential

$$W'(\Phi, F_X) = \frac{c}{M_{Pl}} F_X(x) \Phi_i^\dagger(x) \Phi(x),$$

where the interaction coupling c is determined by the mass of the chiral superfield

$$c = \frac{M_\Phi}{M_{SUSY}}.$$

The superpotential $W'(\Phi, F_X)$ mediates the **SUSY** breaking from the hidden sector of the **MSSM** into the chiral sector. In the gravity mediation, **mSUGRA** [34, 35, 36], breaking scenario, the messenger $F_X(x)$ is a spin-3/2 particle, the gravitino.

In addition to the hidden sector, the **MSSM** imposes several requirements on the Higgs sector:

- The Higgs fields, developing non-zero VEV after the electroweak **SSB**, can not be superpartners of quarks and leptons. Otherwise, this would induce the spontaneous violation of baryon and lepton numbers through Yukawa interaction.
- At least two chiral Higgs multiplets are needed to give masses to “up” and “down” quarks.

The last requirement is a result of the chirality of matter superfields. The Yukawa interaction in the Standard Model is presented by two Lagrangians (see the subsection 1.3.3):

$$\mathcal{L}_{Yukawa}^{l_f, d} = -y_f \bar{L}_f \Phi l_{R, f} - Y_{ij}^d \bar{Q}_{iL} \Phi d_{jR} + h.c.,$$

to generate masses of charged leptons and down quarks, and

$$\mathcal{L}_{Yukawa}^u = -Y_{ij}^u \bar{Q}_{iL} \Phi^c u_{jR} + h.c.,$$

to introduce masses of up quarks. The Higgs doublet Φ^c is the charge conjugate, $\Phi^c = i\sigma^2 \Phi^\star$, with $Y_{\Phi^c} = -1$. However, the **SUSY**, built only on the left-handed chiral superfields, forbids the right-handed Higgs doublet Φ^c .

Another reason for introducing the second left-handed Higgs doublet, H_2 , is the cancellation of chiral anomalies. The chiral anomalies appear if the the sum of 3rd powers of hypercharges, Y , for chiral fields is non zero,

$$Tr(\sum_i Y_i^3) \neq 0.$$

The anomalies spoil the gauge invariance and, hence, the renormalizability of the theory. The Standard Model is free of such chiral anomalies

$$Tr(\sum_{i=e_L, e_R, \nu_L, u_L, etc} Y_i^3) = 0.$$

In **SUSY**, however, the chiral Higgs multiplet contains higgsinos, which are fermions with non-zero hypercharges, and introduce the chiral anomaly $Tr\sum_i(Y_i^3) \neq 0$. To compensate the anomaly from the hypercharges of higgsinos, one has to add a second Higgs doublet with an opposite hypercharge.

2.5 Field Content in the MSSM

The **MSSM** associates the SM bosons with new fermions and the SM fermions with new bosons. The second Higgs doublet is added to cancel the chiral anomalies and to make up quarks massive. The particle content of the **MSSM** is illustrated in Table 2.1 [29, 30].

Table 2.1: Particle content of the **MSSM**.

Superfield	Bosons (spin 0,1)	Fermions (spin 1/2)
Gauge		
V^k	weak, W^k	wino, \tilde{W}^k
B	hypercharge, B	bino, \tilde{B}
Matter		
L_f	sleptons, $(\tilde{\nu}_{f,L}, \tilde{l}_{f,L})$	leptons, $(\nu_f, l_f)_L$
E_f^C	$\tilde{l}_{f,R}^C$	l_R^C
Q_f	squarks, $(\tilde{u}_{f,L}, \tilde{d}_{f,L})$	quarks, $(u_f, d_f)_L$
U_f^C	$\tilde{u}_{f,R}^C$	u_R^C
D_f^C	$\tilde{d}_{f,R}^C$	d_R^C
Higgs		
H_1	Higgses, H_1	higgsinos, \tilde{H}_1
H_2	H_2	\tilde{H}_2

The gauge (vector) superfields consist of the SM gauge bosons B and W^k , $k = 1, 2, 3$ accompa-

nied by their superpartners, spin-1/2 Majorana particles, called gauginos. The gauginos consist of the bino \tilde{B} and the winos \tilde{W}_k . Hereafter, tilde denotes a superpartner of an ordinary particle, and the superscript C indicates on the charge conjugation, $\psi_L^C = i\sigma_2 \psi_R^*$, $\psi_R^C = -i\sigma_2 \psi_L^*$. The index f in Table 2.1 denotes the fermion family.

The chiral, matter, content of the **MSSM** is exactly the same as in the **SM**: three families of the chiral quarks and leptons. Each family f has five different gauge representations, described by the quantum numbers T^3 , Y and Q in the notation of Table 1.3:

$$Q_f = q_{f,L}^{[1/2;1/3;2/3]}, U_f^C = u_{f,R}^{C[0;-4/3;-2/3]}, D_f^C = d_{f,R}^{C[0;2/3;1/3]},$$

$$L_f = l_{f,L}^{[\pm 1/2;-1;0;-1]}, E_f^C = l_{f,R}^{C[0;2;1]}.$$

In addition, in the **MSSM**, the matter families are populated by five gauge representations of spin-0 particles, \tilde{L}_f , \tilde{Q}_f , \tilde{U}_f^C , \tilde{D}_f^C and \tilde{E}_f , with the same $SU(2) \otimes U(1)$ quantum numbers as their SM partners.

The presence of an extra Higgs doublet in the **MSSM** is a novel feature. The two doublets, $H_1(x)$ and $H_2(x)$, are defined as

$$H_1(x) = \begin{pmatrix} H_1^0(x) \\ H_1^-(x) \end{pmatrix} = \begin{pmatrix} v_1 + \frac{S_1^0(x) + iP_1^0(x)}{\sqrt{2}} \\ \frac{S_1^-(x) + iP_1^-(x)}{\sqrt{2}} \end{pmatrix}, H_2(x) = \begin{pmatrix} H_2^+(x) \\ H_2^0(x) \end{pmatrix} = \begin{pmatrix} \frac{S_2^+(x) + iP_2^+(x)}{\sqrt{2}} \\ v_2 + \frac{S_2^0(x) + iP_2^0(x)}{\sqrt{2}} \end{pmatrix},$$

where the complex scalar fields $S_1^{0,-}(x)$, $S_2^{0,+}(x)$, $P_1^{0,-}(x)$ and $P_2^{0,+}(x)$ represent eight degrees of freedom. The quantities v_1 and v_2 are VEV of $H_1(x)$ and $H_2(x)$, respectively. The $H_1(x)$ and $H_2(x)$ have opposite hypercharges, $Y_{H_1} = 1$ and $Y_{H_2} = -1$. If the vacuum state is not $SU(2)$ invariant, the three degrees of freedom, $P_1^0(x)$, $P_1^-(x)$, $P_2^+(x)$, become the Goldstone modes [37, 38] which can be gauged away [39], using unitary gauge [40]. The remaining five degrees of freedom result into five massive scalar states

$$h(x) \sim S_1^0(x), H(x) \sim S_2^0(x), H^-(x) \sim S_1^-(x), H^+(x) \sim S_2^+(x), A(x) \sim P_2^0(x),$$

where $h(x)$ and $H(x)$ are CP even neutral Higgs bosons, $A(x)$ is a CP odd neutral Higgs boson and $H^\pm(x)$ are two charged Higgs bosons.

2.6 Lagrangian of the MSSM

The Lagrangian of the **MSSM** consists of two parts. The first part is the SUSY generalization of the Standard Model, while the second one represents the **SUSY** breaking mechanism. The

expression of the MSSM Lagrangian reads

$$\begin{aligned}
\mathcal{L}_{SUSY} &= \mathcal{L}_{gauge} + \mathcal{L}_{Yukawa} + \mathcal{L}_{breaking} \\
\mathcal{L}_{gauge} &= \sum_{k=SU(2), U(1)} \frac{1}{4} \left(\int d^2\theta Tr[W^{\alpha,k} W_{\alpha}^k] + \int d^2\bar{\theta} Tr[\bar{W}^{\alpha} \bar{W}_{\alpha}] \right) + \\
&\sum_{f=1}^5 \prod_{k=SU(2), U(1)} \int d^2\theta d^2\bar{\theta} \Phi_i^{\dagger} e^{g_k V_k} \Phi_i, \\
\mathcal{L}_{Yukawa} &= \int d^2\theta \mathcal{W}_R + h.c.
\end{aligned} \tag{2.34}$$

Here $W_{\alpha}(x)$ and $\bar{W}_{\alpha}(x)$, are left- and right-chiral vector-superfield strengths (2.26), Φ_i are the matter supermultiplets determined by the index i , $i=Q_f, L_f, E_f, U_f^C$ and D_f^C . The vector superfields V_k are used to conserve the local gauge $SU(2)$ and $U(1)$ invariance of the **SUSY** Lagrangian, the couplings g_k are assigned to the corresponding symmetries. The superpotential W_R introduces the Yukawa interaction. The formula of W_R is the following:

$$\mathcal{W}_R = \varepsilon_{\alpha\beta} (y_{ab}^U Q_a^{\alpha} U_{\beta}^C H_2^{\alpha} + y_{ab}^D Q_a^{\beta} D_b^C H_1^{\alpha} + y_{ab}^L L_a^{\beta} E_b^C H_1^{\alpha} + \mu H_1^{\alpha} H_2^{\beta}), \tag{2.35}$$

where $y_{ab}^{U,D,L}$ with $a, b = 1, 2, 3$ are 3×3 flavor-mixing matrices, α and β are spinorial indexes, and Q_f, L_f, E_f, U_f^C and D_f^C are the **SM** parts of the multiplets from Table 2.1. The self-interaction between the Higgs doublets is proportional to the coupling μ .

Performing the integration over the Grassmanians in equation (2.34), the Lagrangians \mathcal{L}_{gauge} and \mathcal{L}_{Yukawa} are evaluated in terms of the component fields as

$$\begin{aligned}
\mathcal{L}_{gauge} &= \sum_{a=SU(2), U(1)} \left(-\frac{1}{4} F_{\mu\nu}^a F^{a\mu\nu} - i\lambda^a \sigma^{\mu} D_{\mu} \bar{\lambda}^a + \frac{1}{2} D^a D^a + D_{\mu} \phi_i^* D^{\mu} \phi_i + \right. \\
&i\xi^{\dagger} \sigma^{\mu} D_{\mu} \xi - i\sqrt{2} g^a (\phi_i^* T^a \phi_i \lambda_a^T \xi_i - \xi_i^{\dagger} T^a \lambda_a^* \phi_i) + D^a g^a \phi_i^* T^a \phi_i + F_i^* F_i, \\
\mathcal{L}_{Yukawa} &= \frac{\partial \mathcal{W}_R}{\partial \phi_i} F_i - \frac{1}{2} \xi_i^T \frac{\partial^2 \mathcal{W}_R}{\partial \phi_i \partial \phi_j} \xi_j + h.c.
\end{aligned} \tag{2.36}$$

In equations (2.36) a denotes the group index, ($a = 1$ for $U(1)$ and $a = 1, 2, 3$ for $SU(2)$), T^a are the group generators. Depending on the index i , D_{μ} is either the left-handed, for $i=Q_f, L_f, E_f$, or right-handed, for $i=U_f^C$ and D_f^C , covariant derivative defined in equation (1.24). The $F_i(x)$ and $D^a(x)$ fields are auxiliary fields. They can be expressed as functions of the scalars $\phi_i(x)$ and spinors $\xi_i(x)$, and excluded from further considerations, using the equations of motion

$$F_i^* = -\frac{\partial \mathcal{W}_R}{\partial \phi_i}, \quad D^a = -g^a \phi_i (T^a)_{ij} \phi_j. \tag{2.37}$$

The **SUSY** breaking mechanism via the hidden sector is incorporated into the **MSSM** as an extension $\mathcal{L}_{\text{breaking}}$ of the **SUSY** Lagrangian. The contribution $\mathcal{L}_{\text{breaking}}$ describes the mass terms of all **MSSM** scalars and Yukawa interaction of the SM parts of the Higgs supermultiplets, H_1 and H_2 , with superparticles of the matter supermultiplets, \tilde{Q}_f , \tilde{U}_f^C , \tilde{D}_f^C , \tilde{L}_f and \tilde{E}_f^C . The general form of $\mathcal{L}_{\text{breaking}}$ is

$$\begin{aligned} \mathcal{L}_{\text{breaking}} = & -\sum_i M_i^2 |\phi_i|^2 - \sum_\alpha M_\alpha \tilde{\lambda}_\alpha^C \tilde{\lambda}_\alpha - \epsilon_{\alpha\beta} (B\mu H_1^\alpha H_2^\beta + A_{ab}^U \tilde{Q}_a^\alpha \tilde{U}_b^C H_2^\beta + \\ & A_{ab}^D \tilde{Q}_a^\alpha \tilde{D}_b^C H_1^\beta + A_{ab}^L \tilde{L}_a^\alpha \tilde{E}_b^C H_1^\beta + h.c.). \end{aligned} \quad (2.38)$$

The quantities M_i and M_α correspond to the masses of spin-0 and Majorana spin-1/2 sparticles. The bilinear and trilinear couplings B and A_{ab} are fixed to keep the gauge and Lorentz invariance of $\mathcal{L}_{\text{breaking}}$. The Lagrangian (2.38) is the only possible choice that does not destroy the renormalizability of the supersymmetric theory [21, 30]. The superpotential (2.35) and the **SUSY** breaking Lagrangian (2.38) provide the mass splitting between particles and sparticles living in the same supermultiplet and ensures the high masses of sparticles. The **SUSY** breaking Lagrangian $\mathcal{L}_{\text{breaking}}$ introduces 104 additional parameters which are purely phenomenological.

The kinetic term $W_\alpha W^\alpha|_{\theta\theta}$, the gauge interaction term $\Phi_i^\dagger e^{gkV_k} \Phi_i|_{\theta\theta\bar{\theta}\bar{\theta}}$ and the superpotential \mathcal{W}_R are R -invariant, because their R -parities are zeros. However, the **SUSY** breaking Lagrangian $\mathcal{L}_{\text{breaking}}$ (2.38) violates the R -invariance. Indeed, the gaugino mass term, $M_\alpha \tilde{\lambda}_\alpha^C \tilde{\lambda}_\alpha$ happens to be R -invariant only for rotation (2.29) angles $\varphi = \pm\pi$. This reduces the $U(1)_R$ -symmetry to the discrete group Z_2 defined by the two values of φ . The possible values of R -parity in the case of Z_2 ,

$$Z_2 = e^{i\pi R}, \quad (2.39)$$

are either +1 or -1. In the supermultiplets fields corresponding to the Standard Model particles, have positive R -parities, $R = 1$, while their superpartners have negative R -parities, $R = -1$. Such requirement is ensured by the rule

$$R = (-1)^{3(B-L)+2S}, \quad (2.40)$$

where B and L are the baryon and lepton numbers associated with the supermultiplet, and S is the spin of either a particle or a sparticle.

In the **MSSM**, where the R -parity is conserved at any interaction vertex, sparticles must be produced in even numbers (usually a pair). There is the Lightest Supersymmetric Particle, **LSP**, which is stable. Usually it is the photino $\tilde{\gamma}$, the superpartner of a photon. Every sparticle other than **LSP** will eventually decay into a SM particle plus an odd number (usually one) of the **LSP**.

2.7 The Higgs sector and Electroweak Symmetry Breaking in MSSM

The Higgs potential in the **MSSM** is fully determined by the superpotential \mathcal{W}_R (2.35) and the symmetry breaking Lagrangian $\mathcal{L}_{breaking}$ (2.38). It has the form

$$V(H_1, H_2) = m_1^2 |H_1|^2 + m_2^2 |H_2|^2 - m_3^2 (H_1 H_2 + h.c.) + \frac{g_2^2 + g_1^2}{8} (|H_1|^2 - |H_2|^2)^2 + \frac{g_2^2}{2} |H_1^\dagger H_2|^2, \quad (2.41)$$

where $m_{1,2,3}^2$ parameters are

$$\begin{aligned} m_1^2 &= M_{H_1}^2 + \mu^2, \\ m_2^2 &= M_{H_2}^2 + \mu^2, \\ m_3^2 &= -B\mu. \end{aligned} \quad (2.42)$$

The potential (2.41) is positive defined. Its minima are determined by the tadpole equations

$$\begin{aligned} \frac{1}{2} \frac{\partial V}{\partial H_2} &= \frac{1}{8} \left(-4v_1 (B + B^*) + (g_1^2 + g_2^2) v_2^3 + v_2 (8m_{H_2}^2 + 8|\mu|^2 - (g_1^2 + g_2^2) v_1^2) \right) = 0, \\ \frac{1}{2} \frac{\partial V}{\partial H_1} &= \frac{1}{8} \left(-4v_2 (B + B^*) + v_1 (8m_{H_1}^2 + 8|\mu|^2 - (g_1^2 + g_2^2) (-v_1^2 + v_2^2)) \right) = 0. \end{aligned} \quad (2.43)$$

Solving equations (2.43), we find the non-trivial VEV of the Higgs doublets, v_1 and v_2 . They are parametrized as

$$v_1 = v \cdot \cos \beta, \quad v_2 = v \cdot \sin \beta.$$

In terms of v^2 and $\sin 2\beta$, the solution of equation (2.43) is

$$\begin{aligned} v^2 &= \frac{4(m_1^2 - m_2^2 \tan^2 \beta)}{(g_2^2 + g_1^2)(\tan^2 \beta - 1)}, \\ \sin 2\beta &= \frac{2m_3^2}{m_1^2 + m_2^2}. \end{aligned} \quad (2.44)$$

The non-trivial minimum of the Higgs potential exists, if the following criteria are fulfilled:

$$v^2 > 0, \quad |\sin 2\beta| \leq 1. \quad (2.45)$$

These requirements are translated to the inequalities

$$\begin{aligned} m_1^2 + m_2^2 &> 2m_3^2, \\ m_1^2 m_2^2 &< m_3^4. \end{aligned} \quad (2.46)$$

The relations (2.45) are not satisfied at the GUT scale when v^2 becomes negative,

$$m_1^2 = m_2^2 = m_0^2 + \mu_0^2, \quad v_0^2 = \frac{-4(m_0^2 + \mu_0^2)}{g_2^2 + g_1^2} < 0.$$

However, inequalities (2.46) can be fulfilled at the lower energy scale. This happens because of the radiative corrections. Most of Feynman diagrams describing the radiative effects of high orders are ultraviolet divergent. A renormalization procedure is used to eliminate all ultraviolet divergences from the Feynman integrals. This procedure makes parameters of the SUSY Lagrangian to be “running”, i.e dependent on the energy scale. To calculate the renormalized parameters, the method of the renormalization group [41] is applied. The squared running parameters m_1^2 and m_2^2 change their positive values to negatives at running down from the Q_{GUT} scale, $Q_{GUT} \sim 10^{16}$ GeV, to the **EWK** symmetry breaking scale Q_{EWSB} , $Q_{EWSB} \sim 10^2$ GeV. Indeed, Figure 2.4 shows the behavior of the m_1^2 and m_2^2 masses predicted with the two-loop accuracy from equations of the renormalization group [42, 43, 44, 45].

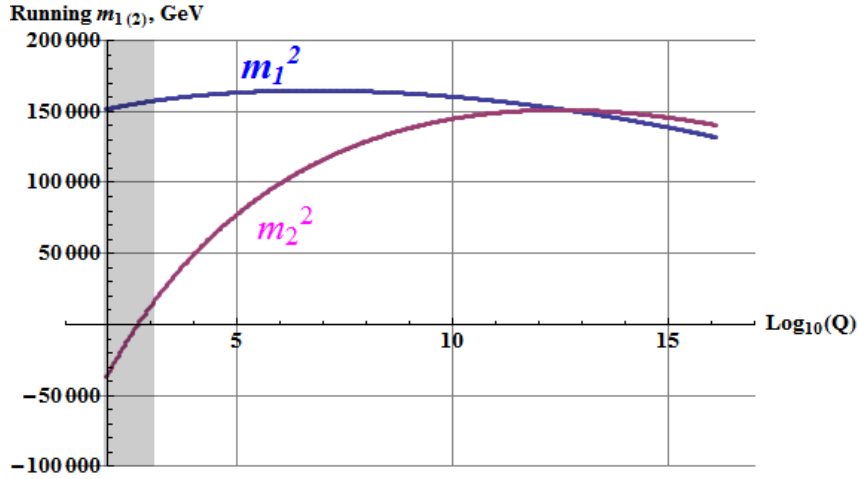


Figure 2.4: The running **SUSY** breaking m_1^2 and m_2^2 parameters in the SPS1 scenario.

The **SPS1** [46, 47, 48] benchmark scenario was taken as the initial condition of the **MSSM** at the GUT scale to numerically evaluate the two-loop equations of the renormalization group. The gray-colored region in Figure 2.4 corresponds to positive values of the squared Higgs doublets VEV, v^2 . Since m_2^2 is logarithmically decreasing, one needs over twelve orders, $Q_{EWSB}/Q_{GUT} \sim 10^{-12}$, to reach negative values.

The running of the Higgs parameters provides non-trivial minima of the Higgs potential (2.41) and leads to the radiative **EWK** symmetry breaking. The non-zero **VEV** of the Higgs doublets, determines the physical spectrum, mass eigenstates, of the **MSSM** Higgs sector. The mass eigenstates for the Higgs fields are found by diagonalization of mass matrices.

The mass matrix of CP-odd components P_1^0 and P_2^0 in the gauge basis is

$$m_{CP-odd}^2 = \frac{\partial^2 V(H_1, H_2)}{\partial P_i^0 \partial P_j^0} = \begin{pmatrix} \frac{1}{8} \left(8m_{H_1}^2 + 8|\mu|^2 + (g_1^2 + g_2^2) (-v_2^2 + v_1^2) \right) & \Re(B\mu) \\ \Re(B\mu) & m_{22} \end{pmatrix},$$

$$m_{22} = \frac{1}{8} \left(8m_{H_2}^2 + 8|\mu|^2 - (g_1^2 + g_2^2) (-v_2^2 + v_1^2) \right). \quad (2.47)$$

It is diagonalized by the matrix Z^A ,

$$Z^A m_{CP-odd}^2 Z^{A,\dagger} = m_{A^0}^{diag,2},$$

$$Z^A = \begin{pmatrix} -\cos\beta & \sin\beta \\ \sin\beta & \cos\beta \end{pmatrix}, \quad (2.48)$$

which rotates the pseudoscalars, P_1^0 and P_2^0 to a Goldstone boson G^0 and the massive physical pseudoscalar A

$$G^0 = \sum_j Z_{j1}^A P_j^0, \quad A = \sum_j Z_{j2}^A P_j^0. \quad (2.49)$$

The G^0 boson is gauged away providing the longitudinal polarization of the massive Z boson. β is the rotation angle. The mass and rotation matrices of the charged Higgs components, S_1^- and S_2^+ , have the forms

$$m_{charged}^2 = \frac{\partial^2 V}{\partial S_i^+ \partial S_j^-} = \begin{pmatrix} m_{11} & \frac{1}{4}g_2^2 v_1 v_2 + B\mu^* \\ \frac{1}{4}g_2^2 v_1 v_2 + B\mu & m_{22} \end{pmatrix},$$

$$m_{11} = \frac{1}{8} \left(8m_{H_1}^2 + 8|\mu|^2 + g_1^2 (-v_2^2 + v_1^2) + g_2^2 (v_1^2 + v_2^2) \right),$$

$$m_{22} = \frac{1}{8} \left(8m_{H_2}^2 + 8|\mu|^2 + (-g_1^2 + g_2^2) v_1^2 + (g_1^2 + g_2^2) v_2^2 \right),$$

$$Z^+ m_{charged}^2 Z^{+,\dagger} = m_{charged}^{diag,2},$$

$$Z^+ = \begin{pmatrix} -\cos\beta & \sin\beta \\ \sin\beta & \cos\beta \end{pmatrix}. \quad (2.50)$$

The rotation matrix Z^+ , which is the same as Z^A , defines the mass basis of the charged Higgs bosons,

$$H^+ = \sum_j Z_{j1}^+ S_j^+, \quad H^- = \sum_j Z_{j2}^+ S_j^- \quad (2.51)$$

The mass and rotation matrices of the CP-even scalar components, S_1^0 and S_2^0 , are given by

$$m_{h,H}^2 = \frac{\partial^2 V}{\partial S_i^0 \partial S_j^0} = \begin{pmatrix} m_{11} & -\frac{1}{4}(g_1^2 + g_2^2)v_1 v_2 - \Re(B\mu) \\ -\frac{1}{4}(g_1^2 + g_2^2)v_1 v_2 - \Re(B\mu) & m_{22} \end{pmatrix},$$

$$m_{11} = \frac{1}{8} \left(8m_{H_1}^2 + 8|\mu|^2 + (g_1^2 + g_2^2)(3v_1^2 - v_2^2) \right),$$

$$m_{22} = \frac{1}{8} \left(8m_{H_2}^2 + 8|\mu|^2 - (g_1^2 + g_2^2)(-3v_2^2 + v_1^2) \right),$$

$$Z^H m_{h,H}^2 Z^{H,\dagger} = m_{h,H}^{diag,2}, \quad (2.52)$$

where the rotation matrix Z^H is

$$Z^H = \begin{pmatrix} -\cos\alpha & \sin\alpha \\ \sin\alpha & \cos\alpha \end{pmatrix}. \quad (2.53)$$

The rotated basis, two CP-even neutral Higgs bosons, h and H , is

$$h = \sum_j Z_{j1}^H S_j^0$$

$$H = \sum_j Z_{j2}^H S_j^0. \quad (2.54)$$

The rotation angle α of the matrix (2.53) is a function of the $\tan\beta$ and the $m_{1,2}^2$ parameters,

$$\tan 2\alpha = -\tan 2\beta \left(\frac{m_A^2 + M_Z^2}{m_A^2 - M_Z^2} \right). \quad (2.55)$$

Here m_A is the mass of the CP-odd Higgs boson A,

$$m_A^2 = m_1^2 + m_2^2. \quad (2.56)$$

After the diagonalizations (2.50) and (2.52), the masses of the m_{H^\pm} , H and h bosons are expressed as

$$m_{H^\pm}^2 = m_A^2 + M_{W^\pm}^2, \\ m_{H,h}^2 = \frac{1}{2}(m_A^2 + M_Z^2 \pm \sqrt{(m_A^2 + M_Z^2)^2 - 4m_A^2 M_Z^2 \cos^2 2\beta}). \quad (2.57)$$

From the definitions (2.56) and (2.57) the allowed mass ranges of the MSSM Higgs sector is estimated as

$$m_{H^\pm} \geq M_W, \\ m_h \leq m_A \leq M_H, \\ m_h \leq M_Z |\cos 2\beta| \leq M_Z, \\ m_h^2 + m_H^2 = m_A^2 + M_Z^2. \quad (2.58)$$

At the tree level the mass of the light CP-even neutral Higgs boson, h , is smaller than the mass of the Z boson. Hence, the h boson must have been observed at the LEP-2 experiments [49, 50]. But they had failed to detect the Higgs boson. However, it was realized [51, 52, 53] that radiative corrections, in particular from top-quark and scalar stop-quark loops, could considerably increase the mass of the light Higgs boson to values beyond the reach of LEP-2, up to about 135 GeV [54, 55, 56].

2.8 MSSM implication of the discovered Higgs-like particle

The scalar particle with a mass of about 126 GeV has been discovered at the LHC [57, 58]. In the **MSSM**, it is obvious to interpret the new state as the light CP-even Higgs boson h [55, 59, 60, 61]. Also it was pointed out in Refs. [59, 62, 63] that a much more exotic interpretation of the discovered state could be possible in terms of the heavy CP-even Higgs boson H .

Equation (2.58) indicates that the mass of the light neutral CP-even Higgs boson must be below M_Z at the tree level [64]. The upper bound $m_h \simeq M_Z$ is reached, when the mass of the CP-odd neutral Higgs boson A , M_A , is much larger than M_Z , and $\beta \rightarrow \pi/2$. This saturation of m_h is shown in Figure 2.5.

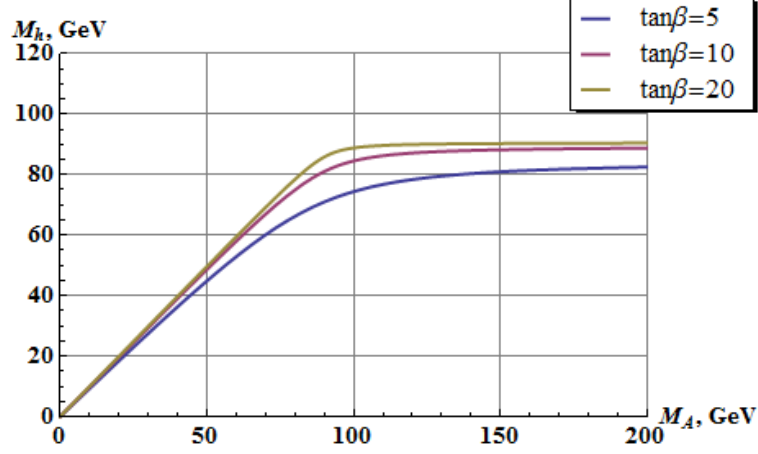


Figure 2.5: The mass of the light CP-even neutral Higgs boson h , m_h as a function of M_A and $\tan\beta$ in the **MSSM**.

However, the radiative effects, mainly from top, stop and sbottom loops, push m_h upwards from the tree-level bound of M_Z to the mass range $123 \text{ GeV} \leq m_h \leq 135 \text{ GeV}$ in the limit of large values of M_A and $\tan\beta$. Calculations of radiative corrections are simplified, if all squarks are assumed to have the same masses,

$$m_{\tilde{t}} = m_{\tilde{b}} = m_{\tilde{l}} = M_{SUSY},$$

and the masses of the Higgs bosons h and H are negligible,

$$M_{h,H} \ll M_{SUSY}.$$

Using the Feynman-diagrammatic approach and on-shell renormalization, the leading one-loop radiative correction $\Delta\mathcal{M}^2$ [65] to the CP-even Higgs mass matrix $m_{h,H}^2$ (2.52) is written as

$$m_{h,H}^2 + \Delta\mathcal{M}^2 = \begin{bmatrix} m_{11}^2 + \Delta\mathcal{M}_{11}^2 & m_{12}^2 + \Delta\mathcal{M}_{12}^2 \\ m_{12}^2 + \Delta\mathcal{M}_{12}^2 & m_{22}^2 + \Delta\mathcal{M}_{22}^2 \end{bmatrix}. \quad (2.59)$$

The expression of $\Delta\mathcal{M}^2$ has the form of

$$\Delta\mathcal{M}^2 \equiv \frac{3m_t^4}{2\pi^2 v^2 \sin^2\beta} \left[\log\left(\frac{M_{SUSY}^2}{m_t^2}\right) + \frac{X_t^2}{2M_{SUSY}^2} \left(1 - \frac{X_t^2}{6M_{SUSY}^2}\right) \right] \begin{pmatrix} 0 & 0 \\ 0 & 1 \end{pmatrix}, \quad (2.60)$$

where the mixing of the stop and sbottom particles is described by

$$X_t = A_t - \mu \cot\beta.$$

The contribution (2.60) increases quartically with the top quark mass m_t and logarithmically with the stop mass $m_{\tilde{t}} \equiv M_{SUSY}$. Because of both top and stops loops the $\sqrt{\Delta\mathcal{M}^2}$ correction may reach the value of about 50 GeV.

Performing diagonalization of the corrected mass matrix (2.59), we get the one-loop corrected masses of the CP-even neutral Higgs bosons h and H [66, 53, 67, 54] as

$$m_{h,H}^2 = \frac{1}{2}(M_A^2 + M_Z^2 + \Delta\mathcal{M}_{22}^2) \cdot [1 \mp \sqrt{1 - 4 \frac{M_Z^2 M_A^2 \cos^2 2\beta + \Delta\mathcal{M}_{22}^2 (M_A^2 \sin^2 \beta + M_Z^2 \cos^2 \beta)}{(M_A^2 + M_Z^2 + \Delta\mathcal{M}_{22}^2)^2}}]. \quad (2.61)$$

The upper bound on m_h at $M_A \gg M_Z$ for a given $\tan \beta$ reads

$$m_h^{max} = M_Z^2 \cos^2 2\beta + \Delta\mathcal{M}_{22}^2 \sin \beta + \frac{M_Z^4}{M_A^2} (\cos^2 2\beta - 1) + \frac{\Delta\mathcal{M}_{22}^2}{M_A^2} (M_Z^2 (\cos \beta - \cos^2 2\beta + \cos 4\beta \sin \beta) + \sin \beta (\sin \beta - 1) \Delta\mathcal{M}_{22}^2). \quad (2.62)$$

In the case of the “non-mixing” stop and sbottom particles,

$$X_t = 0, \quad (2.63)$$

the impact of the radiative correction $\Delta\mathcal{M}_{22}^2$ on the upper bound of m_h (2.62) is shown in Figure 2.6.

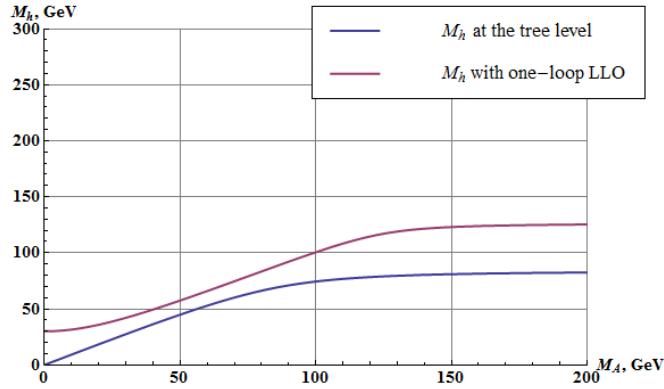


Figure 2.6: The tree-level (2.57) (blue) and radiatively corrected (2.61) (red) masses m_h as functions of M_A at $\tan \beta = 5$, $M_{SUSY} = 1$ TeV, $X_t = 0$ and $m_t = 175$ GeV.

Even at small values of $\tan\beta$, the corrected m_h (2.61) reaches values of about 130 GeV. The effect of stop and sbottom mixing brings the corrected m_h^{max} to the values up-to 3-4 GeV higher. The comparisons of upper bounds on m_h in the “maximal-mixing” scenario,

$$X_t = A_t - \mu \cot\beta = 2M_{SUSY}, \quad (2.64)$$

and the “no-mixing” scenario (2.63) is illustrated in Figure 2.7.

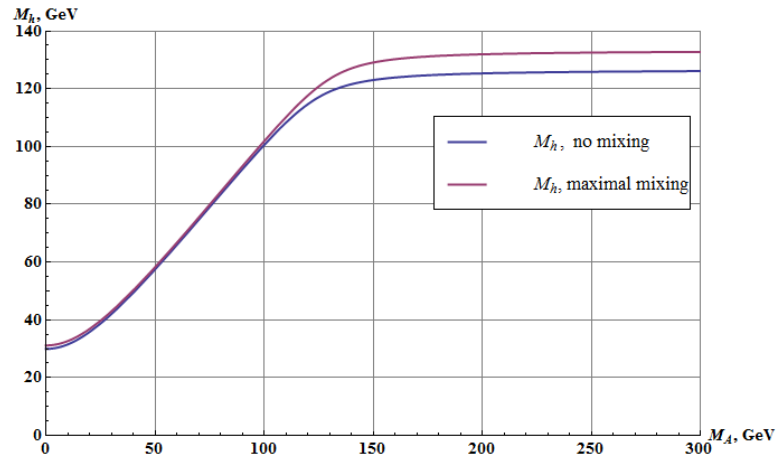


Figure 2.7: The radiatively corrected masses m_h as functions of M_A for $X_t = 2M_{SUSY}$ (red) and $X_t = 0$ (blue) at $\tan\beta = 5$, $M_{SUSY} = 1$ TeV and $m_t = 175$ GeV.

The **SUSY** scale M_{SUSY} plays a crucial role, since the radiative effects are proportional to the logarithm of M_{SUSY} . Increasing M_{SUSY} up to 2 TeV brings the mass m_h to 135 GeV even in the “no-mixing” scenario. Figure 2.8 shows the dependence of m_h on the mixing parameter X_t for $M_{SUSY} = 1$ TeV and $M_{SUSY} = 2$ TeV.

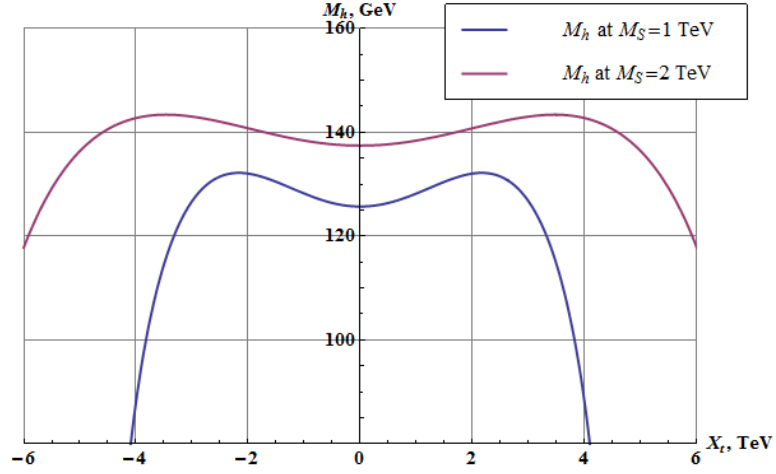


Figure 2.8: The radiatively corrected masses m_h as functions of X_t at $\tan\beta = 5$, $M_{SUSY} = 1$ (blue) and 2 (red) TeV, and $m_t = 175$ GeV.

The impact of the $\tan\beta$ parameter on the mass m_h in the “maximal-mixing” scenario is depicted in Figure 2.9. The upper bound on m_h of 135 GeV for the given $M_{SUSY} = 1$ TeV is reached when $\tan\beta$ increases to $\tan\beta \sim 50$.

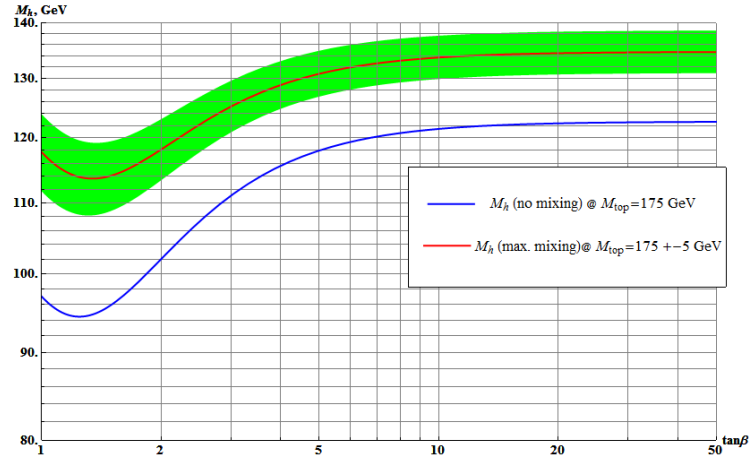


Figure 2.9: The radiatively corrected mass m_h as functions of $\tan\beta$ at $M_{SUSY} = 1$ TeV, $m_t = 175$ GeV, $X_t = 2M_{SUSY}$ (red) and $X_t = 0$ (blue).

The green band in Figure 2.9 illustrates the impact on m_h from the uncertainty of the top quark

mass, m_t , assumed to be ± 5 GeV.

The Yukawa Lagrangian, given by superpotential \mathcal{W}_R (2.35), can be rewritten in terms of the component fields for the 1st quark family as

$$\mathcal{L}_{Yukawa} = -\lambda_u[\bar{u}P_L u H_2^0 - \bar{u}P_L d H_2^+] - \lambda_d[\bar{d}P_L d H_1^0 - \bar{d}P_L u H_1^-] + \text{h.c.} \quad (2.65)$$

P_L is left-handed projection operator, $P_L = \frac{1-\gamma^5}{2}$. The 3×3 flavor mixing matrices $y_{ab}^{U,D}$ introduced in equation (2.35) are assumed to be diagonal with the elements λ_i , where $i = u, d$. The fermion masses generated by the spontaneous **EWK** symmetry breaking relate to the Yukawa couplings λ_i as

$$\lambda_u = \frac{\sqrt{2}m_u}{v_2} = \frac{\sqrt{2}m_u}{v \sin \beta}, \quad \lambda_d = \frac{\sqrt{2}m_d}{v_1} = \frac{\sqrt{2}m_d}{v \cos \beta}. \quad (2.66)$$

Transforming the gauge eigenbasis, $H_1(x)$ and $H_2(x)$ to the mass eigenstates, $h(x)$, $H(x)$, $A(x)$ and $H^\pm(x)$, the Yukawa Lagrangian (2.65) takes the form

$$\begin{aligned} \mathcal{L}_{Yukawa} = & -\frac{g_2 m_u}{2M_W \sin \beta} [\bar{u}u(H \sin \alpha + h \cos \alpha) - i\bar{u}\gamma_5 u A \cos \beta] \\ & -\frac{g_2 m_d}{2M_W \cos \beta} [\bar{d}d(H \cos \alpha - h \sin \alpha) - i\bar{d}\gamma_5 d A \sin \beta] \\ & + \frac{g_2}{2\sqrt{2}M_W} V_{ud} \{H^+ \bar{u}[m_d(1 + \gamma_5) + m_u \cot \beta(1 - \gamma_5)]d + \text{h.c.}\}, \end{aligned} \quad (2.67)$$

where V_{ud} is the element of the CKM matrix. From equation (2.67) the couplings of neutral Higgs bosons A , H and h to fermions strongly depend on the rotation angles α and β . Table 2.2 summarizes the couplings relative to their SM predictions.

Table 2.2: Neutral Higgs bosons couplings to the u- and d-type quarks.

Higgs	$g(\Phi, \bar{u}u)$	$g(\Phi, \bar{d}d)$
H_{SM}	1	1
H	$\cos \alpha / \sin \beta$	$-\sin \alpha / \cos \beta$
h	$\sin \alpha / \sin \beta$	$\cos \alpha / \cos \beta$
A	$\cot \beta$	$\tan \beta$

Table 2.3 contains the predictions of “one-scalar-two-gauge-boson”, $g(\Phi, VV)$, and “two-scalars-one-gauge-boson”, $g(\Phi, AV)$, couplings for the neutral Higgs bosons, $\Phi = h, H$ and A .

Table 2.3: Neutral Higgs bosons couplings to the gauge bosons.

Higgs	$g(\Phi, ZZ), g(\Phi, W^+W^-)$	$g(\Phi, AZ)$
H_{SM}	$ig_Z M_Z, ig_W M_W$	0
H	$ig_Z M_Z \cos(\beta - \alpha), ig_W M_W \cos(\beta - \alpha)$	$g_Z \cos(\beta - \alpha)(p_2^\mu + p_3^\mu)$
h	$ig_Z M_Z \sin(\beta - \alpha), ig_W M_W \sin(\beta - \alpha)$	$-g_Z \sin(\beta - \alpha)(p_2^\mu + p_3^\mu)$
A	0,0(CP-invariance forbids)	0(CP-invariance forbids)

The introduced couplings g_Z and g_W are related to the weak neutral and charged currents, and defined as

$$g_Z = g_2 / \cos \theta_W, \quad g_W = g_2.$$

The p_2^μ and p_3^μ are 4-momenta of the bosons A and Z , incoming in an interaction vertex. Table 2.3 does not contain the couplings like $g(\Phi, \gamma\gamma), g(\Phi, Z\gamma)$, because it is kinematically forbidden.

The difference between angles α and β determines the strength of the Higgs interactions with fermions and gauge bosons. The ratios $\cos \alpha / \sin \beta$ and $\sin \alpha / \sin \beta$ can be expressed as functions of $\sin(\beta - \alpha)$, $\cos(\beta - \alpha)$ and $\tan \beta$

$$\begin{aligned}
 g(h, \bar{d}d) &= -\frac{\sin \alpha}{\cos \beta} = \sin(\beta - \alpha) - \tan \beta \cos(\beta - \alpha), \\
 g(h, \bar{u}u) &= \frac{\cos \alpha}{\sin \beta} = \sin(\beta - \alpha) + \cot \beta \cos(\beta - \alpha), \\
 g(H, \bar{d}d) &= \frac{\cos \alpha}{\cos \beta} = \cos(\beta - \alpha) + \tan \beta \sin(\beta - \alpha), \\
 g(H, \bar{u}u) &= \frac{\sin \alpha}{\sin \beta} = \cos(\beta - \alpha) - \cot \beta \sin(\beta - \alpha)
 \end{aligned} \tag{2.68}$$

Recalling that the rotation angle α is determined by the parameter $\tan \beta$ and the masses m_A , m_h and m_H ,

$$\cos 2\alpha = -\cos 2\beta \frac{m_A^2 - M_Z^2}{m_H^2 - m_h^2}, \quad \sin 2\alpha = -\sin 2\beta \frac{m_H^2 + m_h^2}{m_H^2 - m_h^2}, \tag{2.69}$$

we derive that

$$\cos^2(\beta - \alpha) = \frac{m_h^2(M_Z^2 - m_h^2)}{m_A^2(m_H^2 - m_h^2)}. \tag{2.70}$$

At the large values of the mass of the boson A , $m_A \gg M_Z$, the Higgs sector of **MSSM** turns into the so-called “decoupling” regime in which the CP-even neutral light scalar state h has the same couplings to fermions and gauge bosons, as the SM Higgs boson. Indeed, as it follows from expression (2.70), the decoupling regime $m_A \gg M_Z$ corresponds to

$$\cos(\beta - \alpha) \rightarrow 0. \quad (2.71)$$

From equations (2.68) and (2.71), and Table 2.3, the boson H is decoupled from the gauge bosons, and its couplings to up and down quarks are suppressed and enhanced, respectively, by a factor of $\tan\beta$. In this regime the couplings of the h boson to quarks and gauge bosons are the same as in the SM:

$$\begin{aligned} g(h, \bar{u}u), g(h, \bar{d}d) &= g(H_{SM}, \bar{u}u), g(H_{SM}, \bar{d}d), \\ g(h, ZZ), g(h, W^+W^-) &= g(H_{SM}, ZZ), g(H_{SM}, W^+W^-), \\ g(H, \bar{u}u) &= -\cot\beta \cdot g(H_{SM}, \bar{u}u), \\ g(H, \bar{d}d) &= \tan\beta \cdot g(H_{SM}, \bar{d}d), \\ g(H, ZZ), g(H, W^+W^-) &= 0. \end{aligned} \quad (2.72)$$

The neutral CP-even H and CP-odd A Higgs bosons degenerate in mass

$$m_A \simeq m_H. \quad (2.73)$$

The couplings of the A boson to down (up) quarks are (inversely) proportional to $\tan\beta$.

2.9 Predictions on the production of the neutral MSSM Higgs Bosons at LHC

The most important production mechanisms of the MSSM neutral CP-even Higgs bosons are those that involve gauge bosons and top quarks. In the decoupling limit (2.71) the MSSM scalar sector is effectively reduced to the SM features. However, in the region of large $\tan\beta$, the MSSM Higgs boson couplings to down-type fermions are strongly enhanced. Therefore the bottom quarks play a much more important role in the **MSSM** than in the **SM**.

The main processes for the neutral Higgs boson production in the **MSSM** are

- the associated production with W/Z bosons [68, 69, 70], $q\bar{q} \rightarrow W/Z + h/H$;

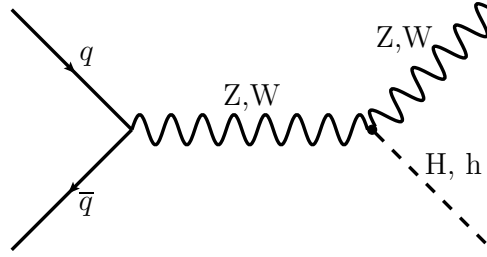


Figure 2.10: Higgs-strahlung: associated h/H production with W/Z .

- vector boson fusion [71, 72, 73], $q\bar{q} \rightarrow V^*V^* \rightarrow q\bar{q} + h/H$;

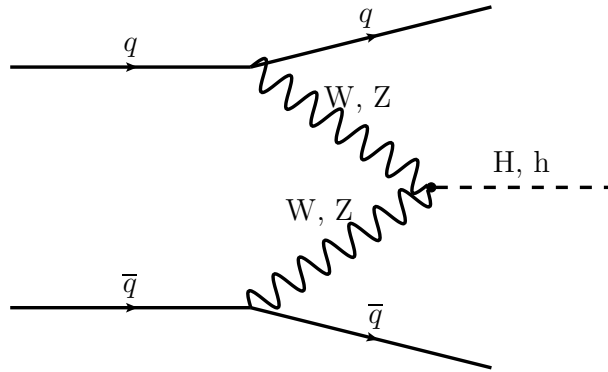


Figure 2.11: WW/ZZ fusion production of the bosons h/H .

- gluon-gluon fusion [74], $gg \rightarrow \Phi(= h/H/A)$;

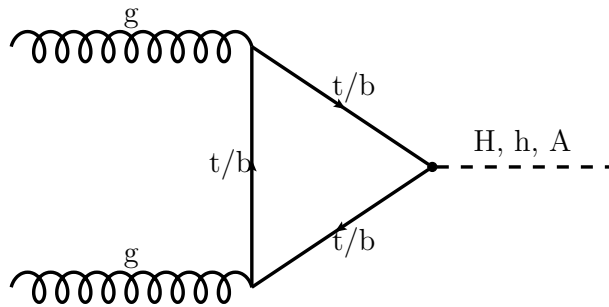


Figure 2.12: gluon-gluon fusion production of the bosons $\Phi = h/H/A$.

- the associated Higgs production with heavy top or bottom quarks [75, 76, 77, 78, 79], $gg \rightarrow b\bar{b} + \Phi(= h/H/A)$;

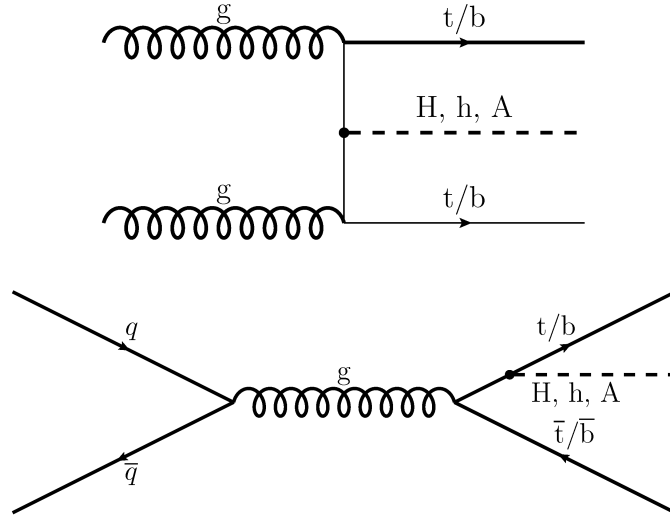


Figure 2.13: Higgs boson radiation off top and bottom quarks.

The calculation of the MSSM Higgs cross sections and decay widths can be done in the effective coupling approximation [80]. The approximation utilizes the corresponding SM cross sections including high-order corrections. Rescaling the SM cross sections with the ratios of the **MSSM** $g_{\Phi,VV}^{MSSM}$ and $g_{\Phi,\bar{b}b}^{MSSM}$ couplings over the **SM** equivalents, $g_{H_{SM},VV}^{SM}$ and $g_{H_{SM},\bar{b}b}^{SM}$, is needed [80].

The gluon-gluon fusion process is the dominant production mechanism for the SM Higgs boson at LHC, as shown in Figure 2.14 [81, 82].

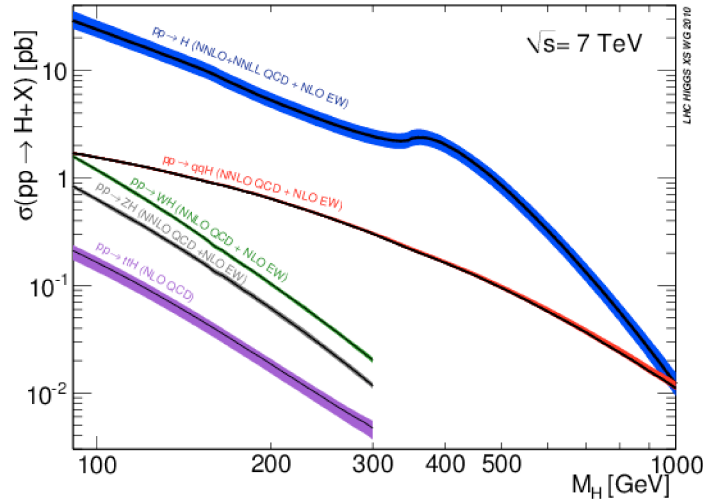


Figure 2.14: Standard Model Higgs boson production cross section at $E_{cm} = 7$ TeV including next-to-next-to-leading order (NNLO) and next-to-leading order (NLO) effects [81].

Also, $gg \rightarrow \Phi(=h/H/A)$, dominates in the **MSSM** at low and moderate $\tan\beta$ values. The process in the **MSSM** is predominantly mediated not only by top loops as in the **SM**, but also bottom and sbottom loops [83, 84]. The increasing importance of the bottom-quark loops is a result of the $\tan\beta$ enhancement for $g^{MSSM}(\Phi, b\bar{b})$ and suppression of $g^{MSSM}(\Phi, t\bar{t})$ couplings (2.68) at leading order as

$$\begin{aligned}\frac{g^{MSSM}(H, t\bar{t})}{g^{MSSM}(H, b\bar{b})} &= -\frac{1}{\tan\beta} \frac{m_t}{m_b} \tan\alpha, \\ \frac{g^{MSSM}(h, t\bar{t})}{g^{MSSM}(h, b\bar{b})} &= \frac{1}{\tan\beta} \frac{m_t}{m_b} \frac{1}{\tan\alpha}, \\ \frac{g^{MSSM}(A, t\bar{t})}{g^{MSSM}(A, b\bar{b})} &= \frac{1}{\tan\beta^2} \frac{m_t}{m_b}.\end{aligned}\tag{2.74}$$

In the effective coupling approximation, the MSSM cross section of the process $gg \rightarrow \Phi(h/H/A)$ reads

$$\begin{aligned}\sigma(gg \rightarrow h/H/A)^{NNLO, MSSM} &= \left(\frac{g^{MSSM}(h/H/A, t\bar{t})}{g^{SM}(H, t\bar{t})} \right)^2 \sigma_{t\bar{t}}^{NNLO, SM}(gg \rightarrow H) + \\ &\quad \left(\frac{g^{2, MSSM}(h/H/A, b\bar{b})}{g^{2, SM}(H, b\bar{b})} \right)^2 \sigma_{b\bar{b}}^{NNLO, SM}(gg \rightarrow H) + \\ &\quad \frac{g^{MSSM}(h/H/A, t\bar{t})}{g^{SM}(h/H/A, t\bar{t})} \frac{g^{MSSM}(h/H/A, b\bar{b})}{g^{SM}(H, b\bar{b})} \sigma_{t\bar{b}}^{NNLO, SM}(gg \rightarrow H),\end{aligned}\tag{2.75}$$

where $\sigma_{t\bar{t}}^{NNLO, SM}$, $\sigma_{b\bar{b}}^{NNLO, SM}$, $\sigma_{t\bar{b}}^{NNLO, SM}$ denote two-loops contributions from top, bottom quarks and their interference, to the cross section of the gluon-gluon fusion in the **SM**. Using the heavy-top-quark limit [85, 86, 84], the LO, NLO and NNLO cross sections, $\sigma^{LO, NLO, NNLO; SM}(gg \rightarrow H)$, at $\sqrt{s} = 14$ TeV are calculated [87], [54] and shown as functions of the mass of the Higgs boson in Figure 2.15 [88].

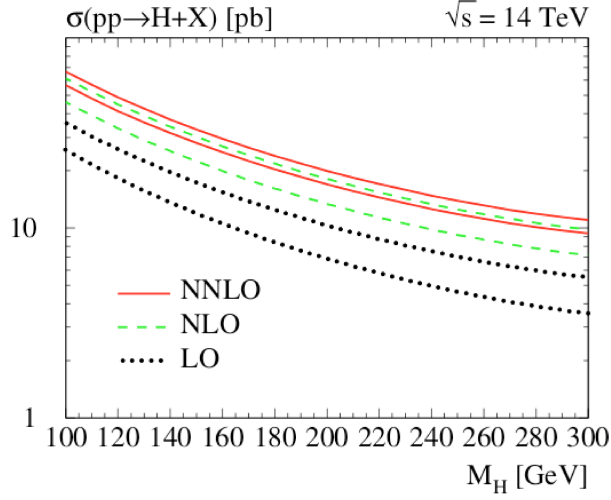


Figure 2.15: The cross sections for $gg \rightarrow H$ at $E_{cm} = 14$ TeV [88]. The cross sections with contributions of NLO (green) and NNLO (red) are compared with the cross section at the leading order for two choices of the factorization and renormalization scales: $\mu_F = \mu_R = 1/2M_H$ (upper curves) and $\mu_R = \mu_F = 2M_H$ (lower curves). The MRST parton distributions are used [89, 90].

The NNLO cross section $\sigma^{NNLO,SM}(gg \rightarrow H)$ varies between 15 pb, at $M_H \simeq 100$ GeV, and 8 pb at $M_H \simeq 300$ GeV. The NNLO radiative effects brings about 30% increase of the cross section $\sigma^{LO,SM}(gg \rightarrow H)$.

In the **MSSM** the same NNLO cross section of the process is enhanced, comparing with the **SM**. Taking into account the radiatively corrected Higgs boson masses (2.61) and resumming the contributions from the SUSY-QCD radiative effects $\mathcal{O}((\alpha_s/M_{SUSY})^n(\mu \tan \beta)^m A_b^{n-m})$ in the factor Δ_b [91, 92, 93, 94], the MSSM Higgs couplings $g^{MSSM}(\Phi, \bar{b}b)$, with $\Phi = h, H$ and A have the form

$$\begin{aligned}
 g^{MSSM}(h, \bar{b}b) &= -g^{SM}(H, \bar{b}b) \frac{1}{1 + \Delta_b} \left[\frac{\sin \alpha}{\cos \beta} - \Delta_b \frac{\cos \alpha}{\sin \beta} \right], \\
 g^{MSSM}(H, \bar{b}b) &= g^{SM}(H, \bar{b}b) \frac{1}{1 + \Delta_b} \left[\frac{\cos \alpha}{\cos \beta} + \Delta_b \frac{\sin \alpha}{\sin \beta} \right], \\
 g^{MSSM}(A, \bar{b}b) &= g^{SM}(H, \bar{b}b) \frac{1}{1 + \Delta_b} \tan \beta.
 \end{aligned} \tag{2.76}$$

The couplings $g^{MSSM}(\Phi, \bar{t}t)$ are obtained substituting the definitions (2.76) into the expressions (2.74). Figure 2.16 illustrates the m_h behavior of $\sigma^{NNLO,MSSM}(gg \rightarrow h)$ calculated in the m_h^{max} scenario [95] at $\tan \beta = 30$.

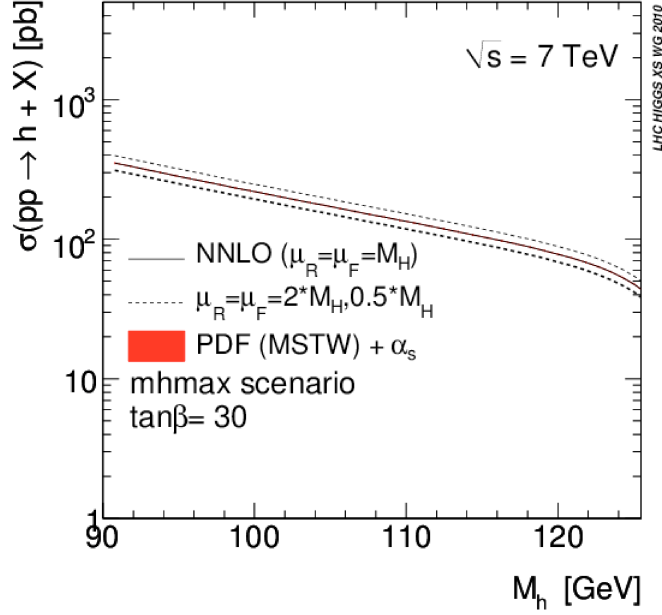


Figure 2.16: The total gluon-fusion cross sections of the neutral light CP-even MSSM Higgs boson h within the m_h^{max} scenario at $\tan\beta = 30$ and $\sqrt{s} = 7$ TeV [92]. The MSTW2008 PDFs are used [96].

Comparing Figures 2.15 and 2.16, we see that the MSSM cross section $\sigma(gg \rightarrow h)^{NNLO, MSSM}$ for $m_h = 125$ GeV at $\tan\beta = 30$ and $\sqrt{s} = 7$ TeV is about one order of magnitude larger than the SM cross section $\sigma(gg \rightarrow H)^{NNLO, SM}$ at $\sqrt{s} = 14$ TeV.

At large values of $\tan\beta$, the Higgs boson radiation off bottom quarks, $gg \rightarrow bb + \Phi (= h/H/A)$, becomes the dominant Higgs boson production process in the **MSSM**. The inclusive total cross section of the process can be calculated using two different approaches.

In the first approach, the mass of b quark are considered to be large comparing to the QCD scale

$$m_b \gg \Lambda_{QCD}.$$

The cross section of the production of the Higgs boson associated with b quarks is calculated order by order. The LO calculations in this scheme, called four flavor scheme, **4FS**, are described in Refs. [75, 76, 88]. In the **SM** the 4FS LO cross section varies strongly with the mass of the Higgs boson M_H and it is of the order of 1 pb for small masses $M_H \sim 100$ GeV, and dropping by more than one order of magnitude when M_H increases to 250 GeV. The NLO correction to the 4FS **SM** cross section of the process, presented in Refs. [97, 98, 88, 99], turns out to be large. Because of the small b -quark mass, m_b , the NLO correction develops large logarithms [84, 88]

$$l_b = \log(m_b^2/\mu_R^2),$$

where the renormalization factor μ_R is of the M_H order. Every on-shell gluon, that splits into $b\bar{b}$

pair, generates one power of this logarithm. Therefore, the K^{NLO} factor,

$$K^{NLO} = \sigma_{4FS}^{NLO} / \sigma_{4FS}^{LO},$$

reaches 2 at large values of M_H for the cross sections estimated at $\sqrt{s} = 14$ TeV as seen from Figure 2.17.

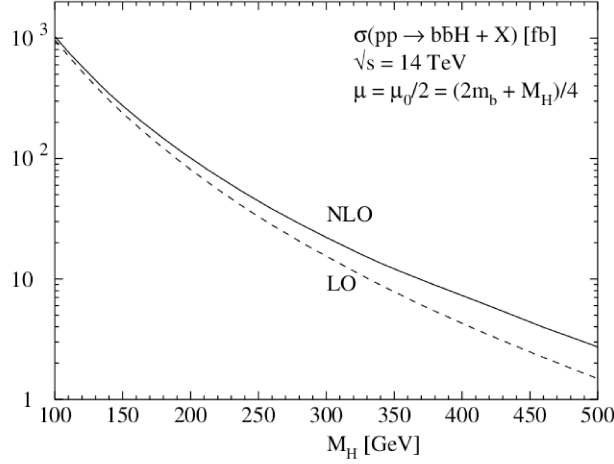


Figure 2.17: Total inclusive cross section for $gg \rightarrow b\bar{b} + H$ at the LHC at $\sqrt{s} = 14\text{TeV}$ as a function of M_H with the factorization and renormalization scales set to $\mu_R = \mu_F = 1/4(M_H + 2m_b)$ where CTEQ6 PDF are adopted [97].

In the second approach, called five flavor scheme, **5FS**, all terms $\sim l_b$ are summed at all orders in the bottom parton density function [100],

$$b(\mu_R, x, Q^2) = \left(\sum_{n,m} (\alpha_s(\mu_R))^n \log(m_b^2/\mu_R^2)^{n-m} \right) \cdot b(x, Q^2).$$

This is not a normal parton distribution function, which is usually determined by the fitting to the hadronic data. $b(\mu_R, x, Q^2)$ is generated from the parton distribution functions of light partons using the **DGLAP** evolution [101]. If we could take all orders of the perturbation theory in calculation of cross sections, the 4FS and 5FS expressions would be identical [99]. At any finite order, the two schemes include different parts of the all-order result, and thus they do not match exactly. The 5FS cross section has been calculated at NNLO accuracy [84, 100], while **4FS** is at NLO. As it is shown in Figure 2.18, there is a good agreement of the 5FS and 4FS results in the **SM** at small Higgs boson masses, while at large Higgs boson masses the 5FS cross section is considerably larger than the corresponding 4FS result. The difference between the 4FS and 5FS cross sections may be up to 30%.

In Figure 2.19, the **5FS** NNLO cross sections of the gluon-gluon fusion, $gg \rightarrow h/H/A$, and the radiation off bottom quarks, $gg \rightarrow b\bar{b} + h/H/A$, are compared and shown as functions of

the Higgs boson mass [82]. All **MSSM** parameters are evaluated in the m_h^{max} scenario [95] at $\tan\beta = 30$ and $\sqrt{s} = 7$ TeV.

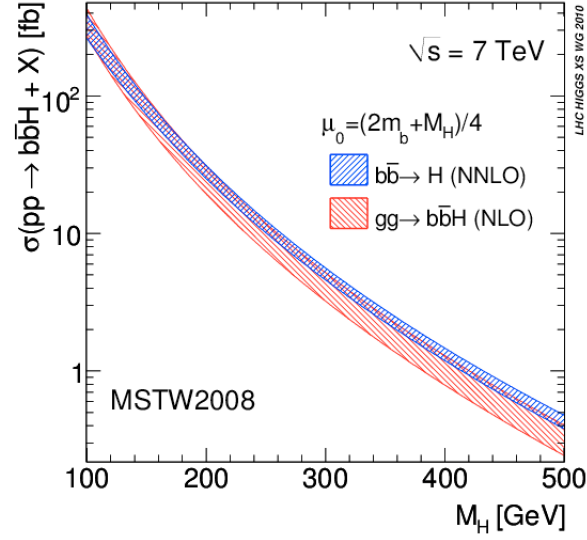


Figure 2.18: Total production cross sections of $pp \rightarrow b\bar{b}H + X$ at $\sqrt{s} = 7$ TeV within the **5FS** and **4FS** using the MSTW2008 set of parton distribution functions. The bands exhibit the scale uncertainties in calculations [82].

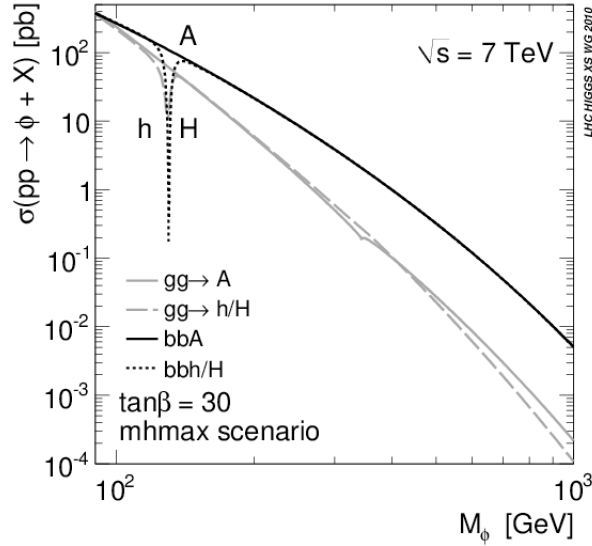


Figure 2.19: The total MSSM production cross sections for gluon-gluon fusion and Higgs radiation off bottom quarks calculated in the **5FS** at NNLO and $\sqrt{s} = 7$ TeV. The m_h^{max} scenario at $\tan\beta = 30$ is chosen to evaluate MSSM couplings [82].

The Higgs-boson radiation off bottom quarks is dominant at large $\tan\beta$. The mass degeneracy between CP-odd, A and the CP-even H Higgs boson (2.73) doubles the cross sections of both processes.

2.10 Predictions on the decays of the neutral MSSM Higgs bosons

The partial decay widths of Higgs boson decays are significantly affected by large radiative effects resulted in the resummation factor Δ_b (2.76). The particular interest of the neutral **MSSM** Higgs boson decays is related to the region of the large values of $\tan\beta$. In this region, even at LO, the neutral MSSM Higgs bosons decay mainly into bottom quarks and tau-leptons because of the $\tan\beta$ -enhanced couplings $g^{MSSM}(h/H/A, b\bar{b})$ [94, 102, 103, 104],

$$\begin{aligned}\Gamma_{LO}(H/h \rightarrow f\bar{f}) &= \frac{G_F N_c M_{h/H}}{4\sqrt{2}\pi} (g^{MSSM}(h/H, f\bar{f}))^2 m_f^2 \beta_f^3, \\ \Gamma_{LO}(A \rightarrow f\bar{f}) &= \frac{G_F N_c M_A}{4\sqrt{2}\pi} (g^{MSSM}(A, f\bar{f}))^2 m_f^2 \beta_f.\end{aligned}\quad (2.77)$$

Here G_F is Fermi constant and β_f is the velocity of the fermions in the final state

$$\beta_f = \sqrt{1 - 4m_f^2/M_H^2}.$$

$N_c = 3$ (1) for quarks (leptons).

The partial decay widths, $\Gamma(H/h/A \rightarrow f\bar{f})$, at NNLO accuracy is cast to the form [94]

$$\Gamma_{NNLO}(H/h/A \rightarrow f\bar{f}) = \frac{G_F N_c M_{h/H/A}}{4\sqrt{2}\pi} (g^{MSSM}(h/H/A, f\bar{f}))^2 \bar{m}_f^2 [\Delta_{QCD}^{NNLO} + \Delta_t^{NNLO}], \quad (2.78)$$

where \bar{m}_f is the running fermion mass in the **MS** renormalization. Δ_{QCD}^{NNLO} is the two-loop contributions from light quarks and Δ_t^{NNLO} is the top-quark induced correction. The couplings $g^{MSSM}(h/H/A, b\bar{b})$ in the partial decay widths (2.78) are estimated using the approach (2.76).

The partial decay widths $\Gamma_{NNLO}(h \rightarrow b\bar{b})$ and $\Gamma_{NNLO}(A \rightarrow b\bar{b})$ for the “small α_{eff} ” **MSSM** scenario [56] are shown in Figure 2.20 as functions of M_A .

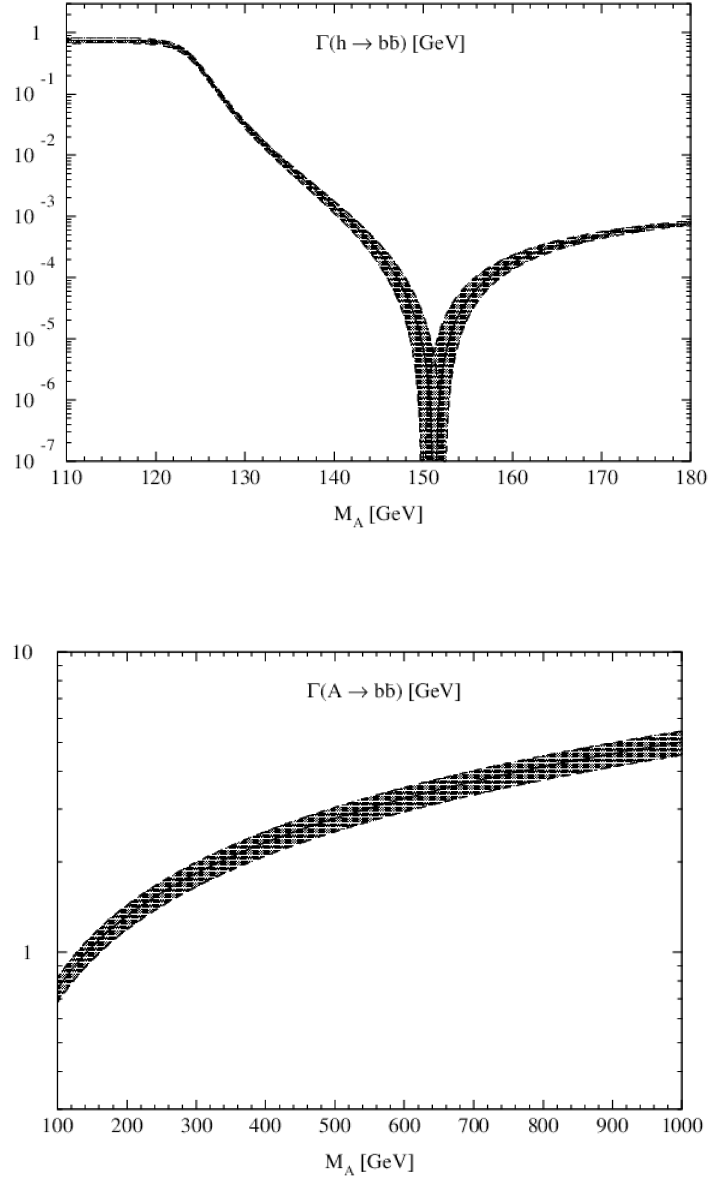


Figure 2.20: Partial decay widths of the light scalar, $\Gamma(h \rightarrow b\bar{b})$, and the pseudoscalar, $\Gamma(A \rightarrow b\bar{b})$ in the “small α_{eff} ” scenario [56]. The shaded bands reflect uncertainties due to the factorization scale.

The region of $M_A \simeq 150$ GeV corresponds to the vanishing Yukawa coupling,

$$g^{MSSM}(h, b\bar{b}) = -\frac{\sin \alpha}{\cos \beta} \frac{1}{1 + \Delta_b} \left(1 - \frac{\Delta_b}{\tan \alpha \tan \beta} \right) \rightarrow 0, \quad \tan \beta \tan \alpha \rightarrow \Delta_b,$$

and shown as a drop in the upper Figure. Branching ratios $\Gamma(h/A \rightarrow b\bar{b}, \tau\bar{\tau}, gg, t\bar{t})/\Gamma_{total}$ for the

scalar h and pseudoscalar A as functions of m_h and m_A , respectively, are illustrated in Figure 2.21.

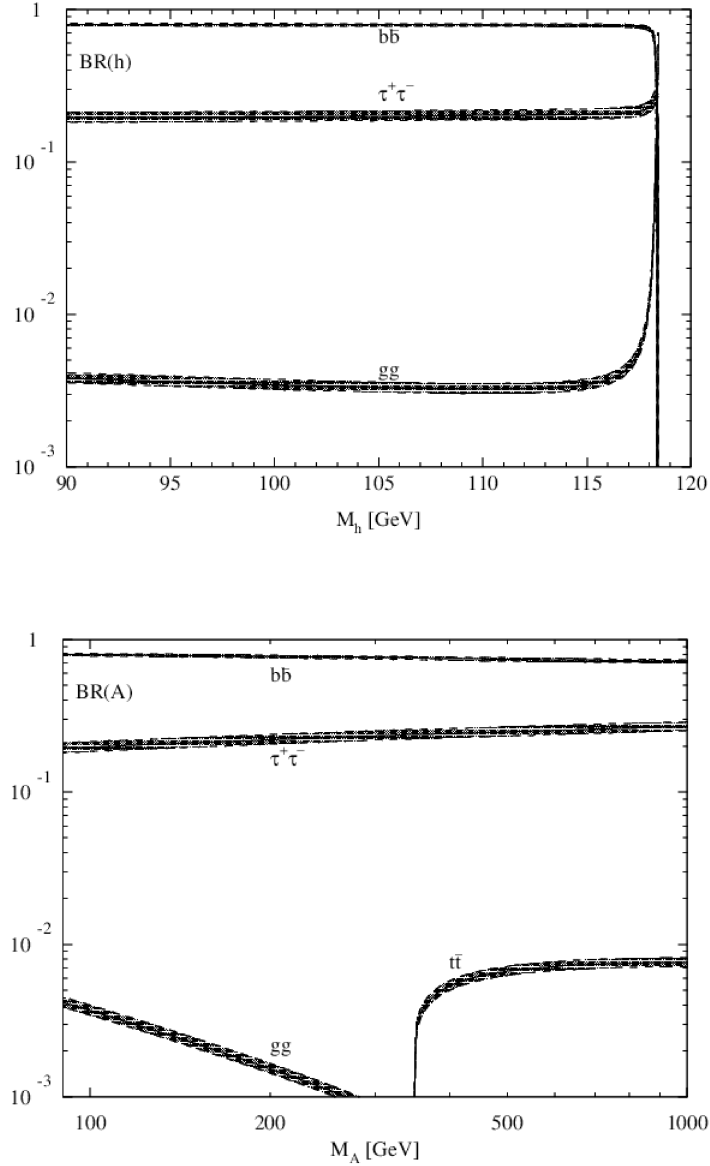


Figure 2.21: Branching ratios of the light scalar, $Br(h \rightarrow b\bar{b})$ and the pseudoscalar, $Br(A \rightarrow b\bar{b})$ in the “small α_{eff} ” scenario [56]. The shaded bands reflect uncertainties due to the factorization scale.

The branching ratios of main decay channels, $h/A \rightarrow b\bar{b}$ and $h/A \rightarrow \tau\bar{\tau}$ is about 98% and 1.5% respectively. The branching ratios of the decays $h/A \rightarrow g\bar{g}, t\bar{t}$ are about 0.5% for the Higgs boson mass range between 50 GeV and 1 TeV.

3 The Large Hadron Collider

The Large Hadron Collider, **LHC**, is a particle accelerator installed in a tunnel with a circumference of 27 km, 50 to 175 meters underground, located at CERN on the border between Switzerland and France. It is designed for proton-proton and lead-ion collisions at high energies and luminosities. Two beams of particles are accelerated and directed by electric and magnetic fields and brought together for head-on collisions at the interaction points surrounded by several detectors, CMS [105], ATLAS [106], ALICE [107] and LHCb [108]. CMS and ATLAS are multi-purpose detectors designed to reveal the physics in the Standard Model and beyond and to search for new particles of various kinds. The other two experiments serve more specific aims. ALICE is focused on studies of properties of the quarkgluon plasma with collisions of heavy ions. Finally, LHCb is dedicated to measuring various aspects of the b-quark physics, e.g. CP-violation.

The choice to build a 14 TeV centre-of-mass energy collider [109, 110] within the former LEP tunnel sets the magnetic field requirements of 8.33 T for 1232 superconducting dipole magnets at their nominal current 12 kA. This allows to keep the beams on an almost circular trajectory at the nominal energy of 14 TeV.

The LHC is supplied with protons from the injector chain Linac2 - PS Booster - PS - SPS [110, 111], which is shown in Figure 3.1. The acceleration of the beams from their injection energy of 450 GeV up to the nominal energy of 7 TeV is performed by 8 so-called radio-frequency cavities, boosting the beams in total by 16 MeV per turn in an electric field of 5.5 MV/m, oscillating at 400 MHz.

The beam-pipes are embedded in a common cryostat that surrounds the bipolar superconducting dipole magnets, Superfluid helium at 1.9 K is used to cool the Nb-Ti alloy coil down to superconductive state.

The acceleration of protons in colliders is performed in bunches with a high particle density. The interaction rate is proportional to the luminosity \mathcal{L} of the accelerator, which is given for head-on collisions by

$$\mathcal{L} = \frac{fn_p^2}{4\pi\sigma_x\sigma_y}, \quad (3.1)$$

where f is the bunch collision frequency, n_p is the number of particles in the colliding bunches and $\sigma_{x,y}$ are the transverse sizes of the bunches at the interaction point.

At the interaction points of the two largest experiments, CMS and ATLAS, the bunches are squeezed to a transverse size of a few μm , to achieve a maximal instantaneous luminosity of up to $10^{34} \text{ cm}^{-2} \text{ s}^{-1}$, corresponding to 10 events/s for a process with cross section of 1 nb, such as

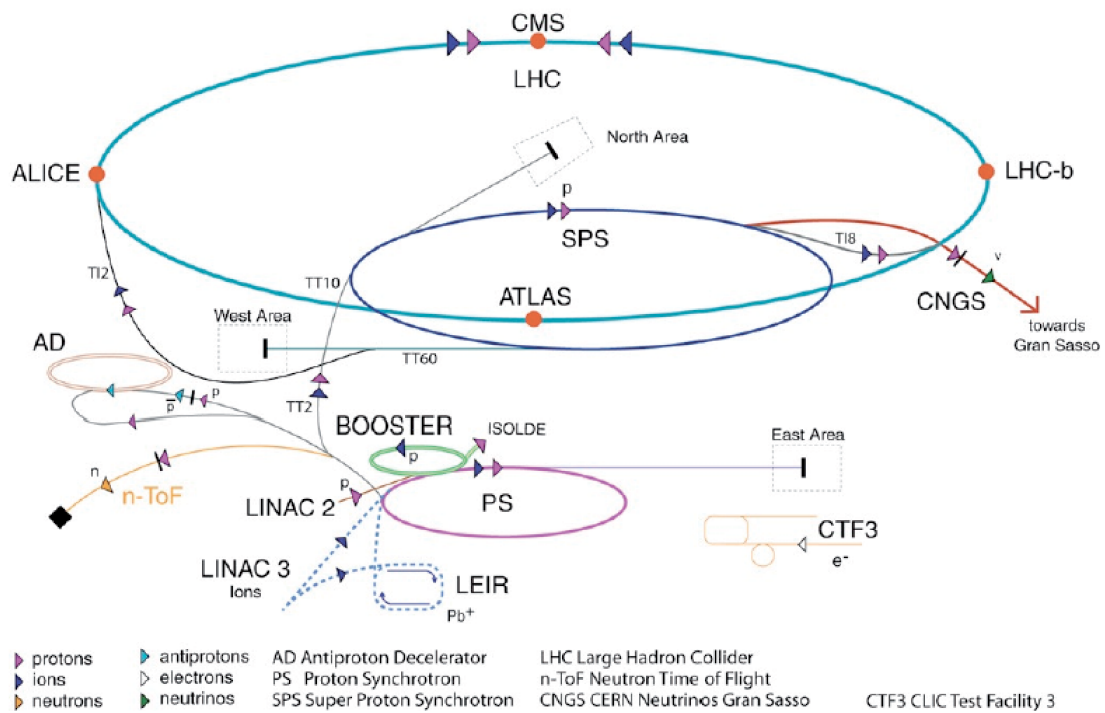


Figure 3.1: Schematic view of the CERN accelerator complex. The four interaction regions hosting the main LHC experiments, ALICE, ATLAS, CMS and LHCb, are also shown.

the production of top quarks. The design bunch collision frequency is 40 MHz implying one bunch crossing each 25 ns. Table 3.1 shows a summary on the LHC parameters.

Table 3.1: The machine parameters relevant to the LHC for the proton- proton (**pp**) and heavy ions, Pb, (**HI**) runs [111, 112].

Parameter	pp	HI	metric units
Beam energy at collision E	7	2.76	TeV
Dipole field B	8.4	8.4	T
Design Luminosity \mathcal{L}	10^{34}	10^{27}	$cm^{-2}s^{-1}$
Bunch spacing	25	100	ns
No. of bunches k_B	2808	592	
No. of particles/bunch n_p	10^{11}	10^7	
Average crossing rate f	32	0.1	MHz
Bunch radius $\sigma_x = \sigma_y$	16	1.5	μm
Number of inelastic events/crossing n_c	19	--	

During the period from 2009 until 2010, all main components of the LHC like the beam dump and the collimation systems were tested and commissioned [113]. Starting in the middle of 2010 up to the end of 2012, the LHC operated at the 7 and 8 TeV centre-of-mass energy achieving respectively peak luminosities of 3.3 and $7.6 \times 10^{33} cm^{-2}s^{-1}$. The integrated luminosities, $\int_{year} \mathcal{L} dt$, of $6 fb^{-1}$ and $23 fb^{-1}$ were recorded by the CMS experiment, in 2011 and 2012 respectively. The integrated luminosities recorded by the LHC experiments as functions of time are shown in the Figure 3.2.

During 2010-2012, LHC performed shorter runs with heavy ions as well. In these runs completely ionized lead nuclei Pb^{82+} were accelerated up to an energy of 2.76 TeV per nucleon. Ion beams were collided with bunch spacing of 1350 ns achieving the maximal instantaneous luminosity of $10^{25} cm^{-2}s^{-1}$ what was considerably different from the nominal values shown in Table 3.1.

The final jump to the design energy of 14 TeV should happen in 2015. The accelerator complex and the hardware of all detectors will be upgraded through the two-years long shutdown.

3.1 Physics at the LHC

To express the probability that two particles will collide and react in a certain way, the term cross section is used. The cross sections of interesting processes at the LHC with $\sqrt{s} = 7(8)$ TeV are given in Figure 3.3.

As one can see from Figure 3.3, the expected cross sections of the interesting SM processes vary between 10 pb and 10 nb, which are ten or more orders of magnitude smaller than the total cross section σ_{tot} in pp collisions at the LHC.

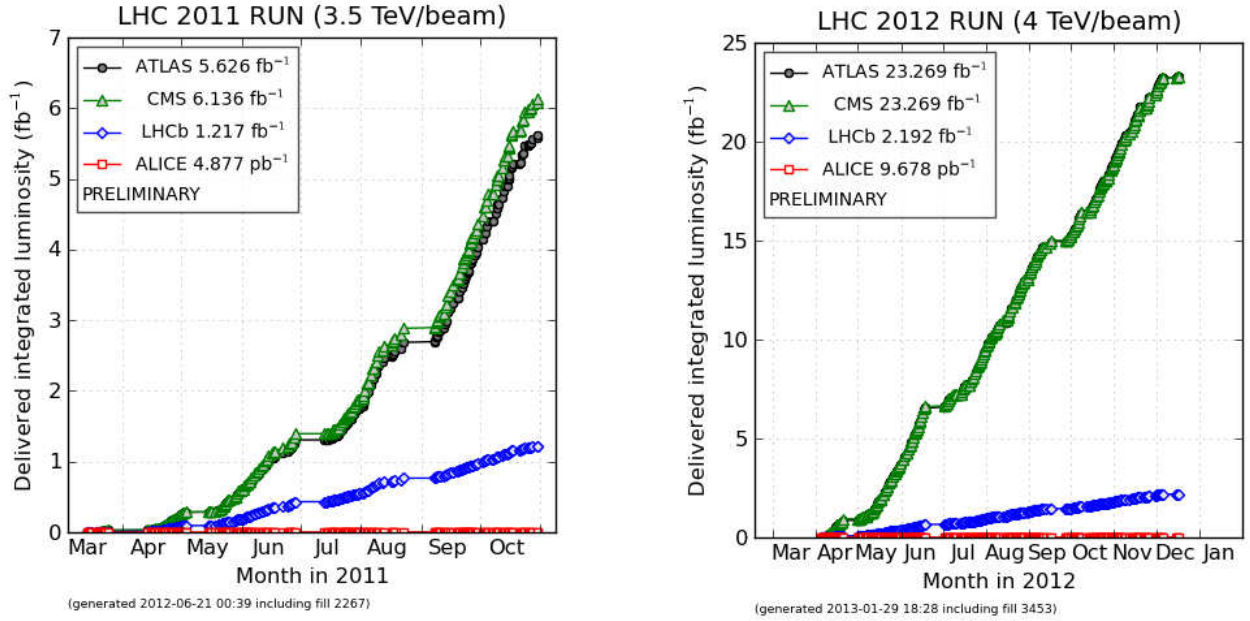


Figure 3.2: The recorded integrated luminosity of the experiments at the LHC in 2011 and 2012 [114].

All processes in hadronic collisions, even those intrinsically of electroweak nature such as the production of W or Z bosons or photons, are induced by the quarks and gluons contained inside the proton. The particular classes of the hadronic scattering can be distinguished depending on experimental signatures of either soft or hard inelastic partonic interactions.

- **Processes induced by soft partonic interactions**

The majority of pp collisions are soft, i.e. without any hard scattering of the partonic constituents of the proton. In contrast to the higher- p_T regime, in principal described by perturbative QCD, particle production in soft collisions is modeled phenomenologically to describe different pp scattering processes: elastic scattering, single-diffractive and double-diffractive dissociation, and inelastic non-diffractive scattering [116]. The total cross section of pp scattering, σ_{tot} , extrapolated from previous experiments at lower energies, is expected to be about 110 mb, of which 30 mb is due to elastic scattering, 24 mb due to diffractive processes and 55 mb due to nondiffractive inelastic interactions [117]. Measurements of the double-diffractive and non-diffractive inelastic collision were performed by CMS in 2010 [118].

- **Hard inelastic processes**

The pp-collisions at large centre-of-mass energy, \sqrt{s} , lead to inelastic interaction with large momentum transfer between partons. The result of hard interactions could be scattering of constituents at large angles, their annihilation into new massive resonances,

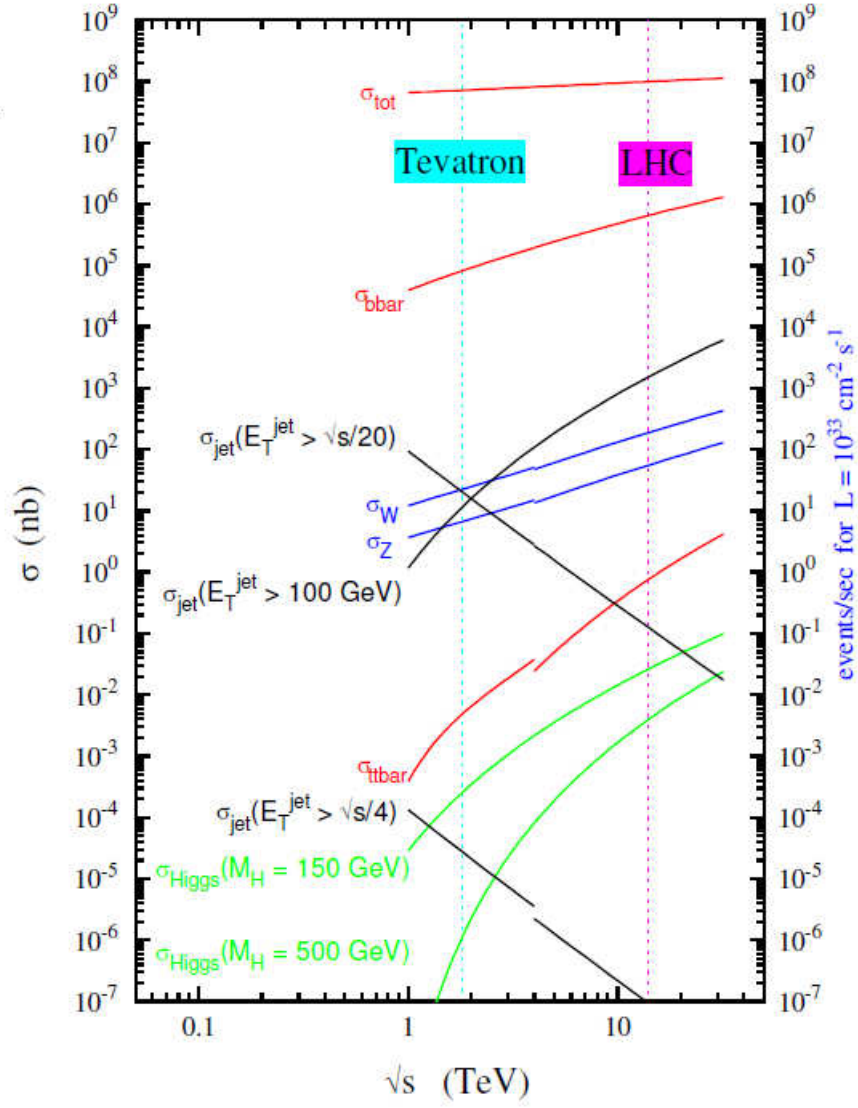


Figure 3.3: Cross sections for selected processes to be observed at the **LHC**. The event rate for the luminosity $\mathcal{L} \simeq 10^{33} \text{ cm}^{-2} \text{ s}^{-1}$ is shown [115].

or a combination of the both processes. The final state consists of a large multiplicity of particles, associated to the evolution of the fragments from the initial hadrons, as well as to the new states produced.

A summary on the physics program that the CMS experiment conducts at the **LHC** can be found in Refs. [112, 119]. The main topics were:

- **The search for the Higgs boson**

For masses of the Higgs boson up to 130 GeV, the two-photon decay channel provides an interesting signature. For this channel, the electromagnetic calorimeter of the **CMS** with excellent granularity and energy resolution allows to resolve the small and narrow Higgs-boson mass peak on the exponentially decreasing background spectrum. If the mass of the Higgs boson is larger than twice the Z boson mass, the Higgs boson is expected to decay to two on-shell Z bosons. The CMS has presented a search for the Higgs boson in the $H \rightarrow ZZ \rightarrow 2l + 2 \text{ jets}$ decay channel, where $l = e$ or μ [120]. The existence of a heavy Higgs boson would appear as a resonance in the invariant mass distribution of the $2l + 2 \text{ jet}$ system.

- **Exploration of the SM**

Precise measurements of the W/Z gauge bosons properties, their production and decays parameters, allow to test the SM. The measurement of the forward-backward asymmetry, A_{FB} , of the Drell-Yan process $q\bar{q} \rightarrow Z/\gamma^* \rightarrow l^+l^-$ was performed by the CMS experiment [121]. The observed asymmetry A_{FB} as a function of the dilepton mass was found to be consistent with the SM predictions within the estimated uncertainties.

The mass of the top quark, m_t , is an essential parameter of the **SM**. Its measurement also provides an important benchmark for the performance and calibration of the detectors at the LHC. The ATLAS and CMS experiments has recently announced a combination of top-quark measurements [122], reporting $m_t = 173.3 \pm 0.23(stat.) \pm 0.92(syst.)$.

- **Searches beyond the SM**

The MSSM Higgs sector significantly deviates from the SM expectations. At the large values of $\tan\beta$, the h/H/A bosons decay mainly to b-quarks. In addition, they are often produced in the association with b-quarks. Hence, the good tracking system is required to efficiently identify b-jets. Supersymmetric signals are also searched for at the LHC. Considering the R -parity conserving **MSSM**, all SUSY decays end at the stable **LSP** which gives rise to significant missing energy. Therefore, energy resolutions of electromagnetic and hadron calorimeters play the main role for such studies. The LHCb experiment, focused on the physics of B-mesons, has recently put tight constraints on various extensions of the Standard Model [123].

4 The CMS experiment

The Compact Muon Solenoid (CMS) detector is one of the two general purpose detectors that are aimed to discover the new physics at the LHC. At the design luminosity many inelastic collisions, called pile-up, will overlay the events of interest. To reconstruct the latter, the CMS detector must meet severe design requirements, which are very good resolutions of charged-particle and muon momenta, and calorimeter energies.

The large solenoid magnet, surrounding the central part of the detector, generates a magnetic field of 4 T which is needed to measure transverse momenta p_T of charged particles with high resolution. For example, the transverse momentum a muon with p_T up to 1 TeV is measured with only 10% resolution at most. As most of the modern, large scale particle detectors, **CMS** is composed of several layers of detectors starting from the innermost silicon pixel and strip trackers, followed by the electromagnetic and the hadron calorimeters. The outermost part of the detector is a muon system. A detailed overview of the layout of the CMS detector is shown in the Figure 4.1.

The CMS uses a right-handed coordinate system, with the origin at the nominal interaction point, where the x-axis pointing to the center of the **LHC**, the y-axis pointing vertically upward (perpendicular to the LHC plane), and the z-axis along the anticlockwise-beam direction. The azimuthal angle ϕ is measured from the x-axis in the xy plane and the radial coordinate in this plane is denoted by R. The polar angle θ is defined from z-axis in the xz plane and the pseudorapidity is

$$\eta = -\ln[\tan(\theta/2)].$$

The CMS detector is divided into three parts: the barrel part, covering the central region of the detector, up to $|\eta| \sim 1$ and two endcap disks located at opposite sides of the central barrel.

4.1 The CMS tracking detectors

The tracker is designed to provide a precise and efficient measurement of trajectories of charged particles originating from collisions as well as a precise reconstruction of vertices.

With an overall radius of 110 cm and a length of 540 cm, made of 200 m² of silicon sensors, the tracker provides coverage up to $|\eta| < 2.5$. Its layout is shown in Figure 4.2. The three layers of hybrid pixel (PXL) detectors are placed close to the interaction point at radii of 4, 7, and 11 cm. In total, they contain 66 million pixels, with a size of $100 \mu\text{m} \times 150 \mu\text{m}$, yielding a single point resolution of $10 \mu\text{m}$ in the (R, ϕ) plane and $20 \mu\text{m}$ in the (R, η) plane. In each endcap there are two pixel disks of inner radius of 6 cm and outer radius of 15 cm. The disks are located at

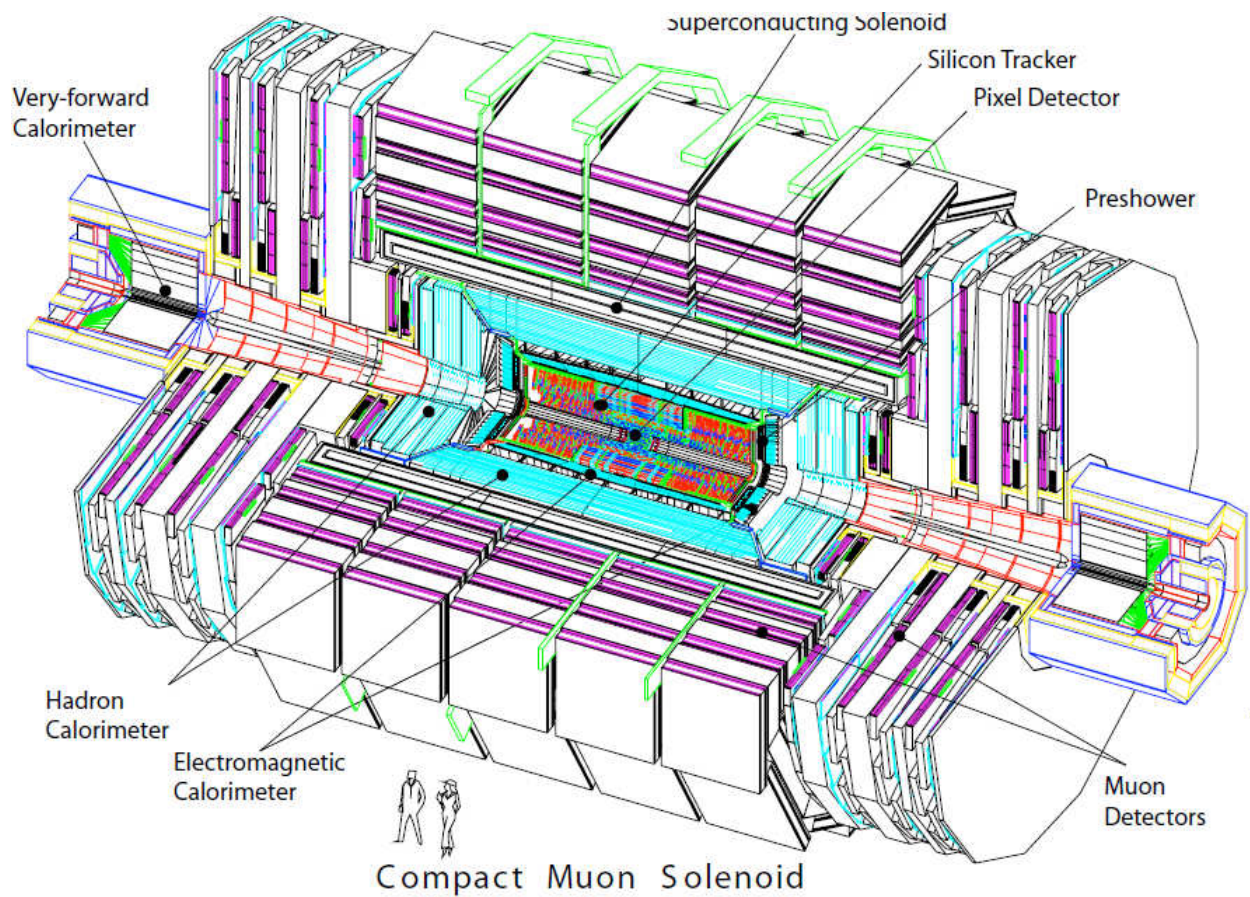


Figure 4.1: The CMS detector [112]. The total weight is 14000 tonnes, the overall diameter is 15 m, and the overall length is 28.7 m. All main components, the tracker, the preshower, the muon system, the calorimeter and the solenoid magnet are shown.

the distance of 34.5 and 46.5 cm from the center of the detector. The large magnetic field of 4 T leads to a Lorentz angle of 32° which induces significant charge sharing between pixels. The endcap sensors are tilted by 20° around the radial direction to compensate the resolution degradation because of the Lorentz angle [124].

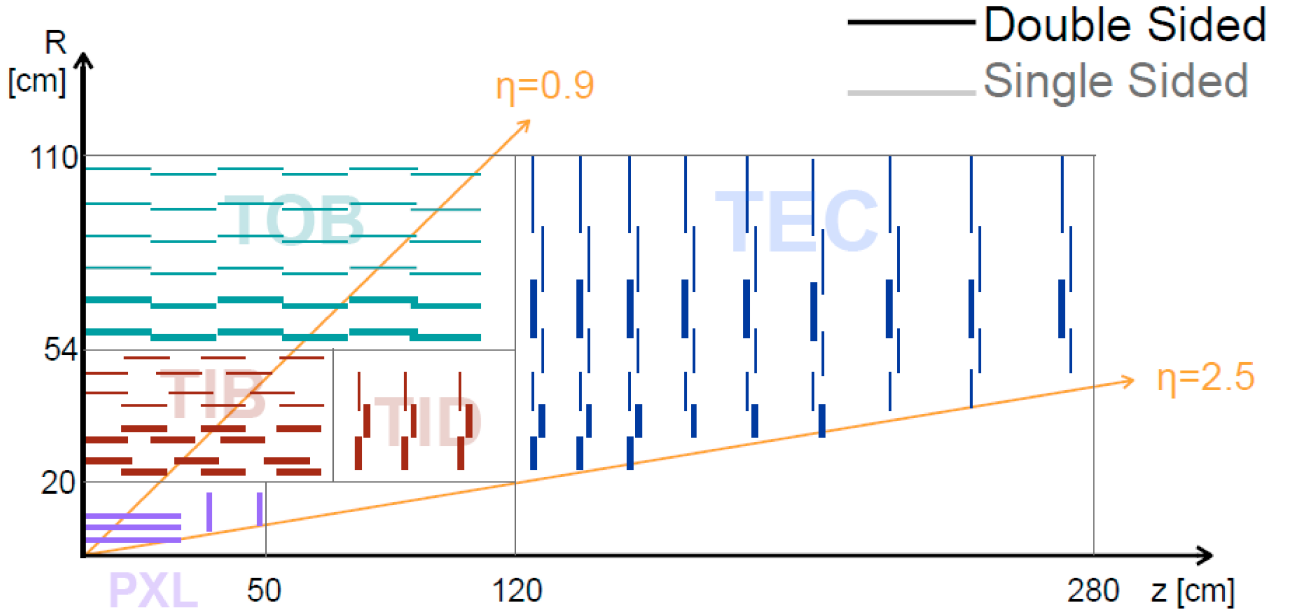


Figure 4.2: The Layout of a quarter of the CMS tracker in (R, z) view. Bold lines represent double-sided modules [125].

The barrel part, $|z| < 110$ cm is composed of the Tracker Inner Barrel, **TIB**, with four layers of silicon strips, and the Tracker Outer Barrel, **TOB**, with six layers. The **TIB**, is placed at 20 cm radius and covers the region up to $|z| < 65$ cm, and complemented by three Tracker Inner Disks, **TID**, per side. The **TOB** is placed at 54 cm from the beam position. It covers the region up to $|z| < 110$ cm. The forward and backward regions, $120 \text{ cm} < |z| < 280$ cm are covered by nine Tracker End-Cap, **TEC**, disks per side.

The pitch size for the silicon-strip layers, ranging between 80 and $180 \mu\text{m}$, is chosen such that the larger pitch is further from the beam, where a lower detector occupancy is expected. A few layers of double-sided modules provide a measurement in the (R, ϕ) plane as well as in the (R, η) plane with resolutions in the ranges of $35 \div 52 \mu\text{m}$ and $230 \div 520 \mu\text{m}$, respectively.

4.2 The CMS calorimeter system

The CMS is equipped with an almost hermetic calorimetry system which allows to precisely measure the energy of particles. The electromagnetic calorimeter, **ECAL**, which is placed just outside the tracker, measures the energy of electrons, positrons and photons [126], while the

hadronic calorimeter, **HCAL**, surrounding **ECAL**, is designed to measure charged- and neutral-hadron energies [127]. Both systems infer the particle's energy from the energy contained in the particle shower caused by the inelastic interaction of the incident particle with the calorimeter material.

4.2.1 The CMS electromagnetic calorimeter

The **ECAL** is built from 64200 lead tungsten ($PbWO_4$) crystals in the barrel, **EB**, and 7324 crystals in each endcap, **EE**, parts. Each crystal has a cross section of approximately $22 \times 22 \text{ mm}^2$, which corresponds to one Moliere radius and a length of 230 mm, which corresponds to 25.8 radiation lengths, X_0 [128, 129]. The crystals are tilted such that they almost point towards the interaction point. Each crystal has a front-face cross section of $\Delta\eta \times \Delta\phi = 0.174 \times 0.174$. The calorimeter is compact with fine granularity, which allows to measure the shower shape of incident particles very accurately [130, 131].

The **EB** covers the region up to pseudorapidity $|\eta| = 1.5$, and the two endcaps extend the coverage to $|\eta| = 3.0$. In the forward region, $1.7 < |\eta| < 2.6$, a silicon/lead preshower detector is installed. It has a much finer granularity than the ECAL with detector strips of 2 mm wide. This allows to resolve closely-spaced lower energy photons, mimicking a high-energy photon, from neutral pions decays. An illustration of the CMS ECAL detector is shown in Figure 4.3.

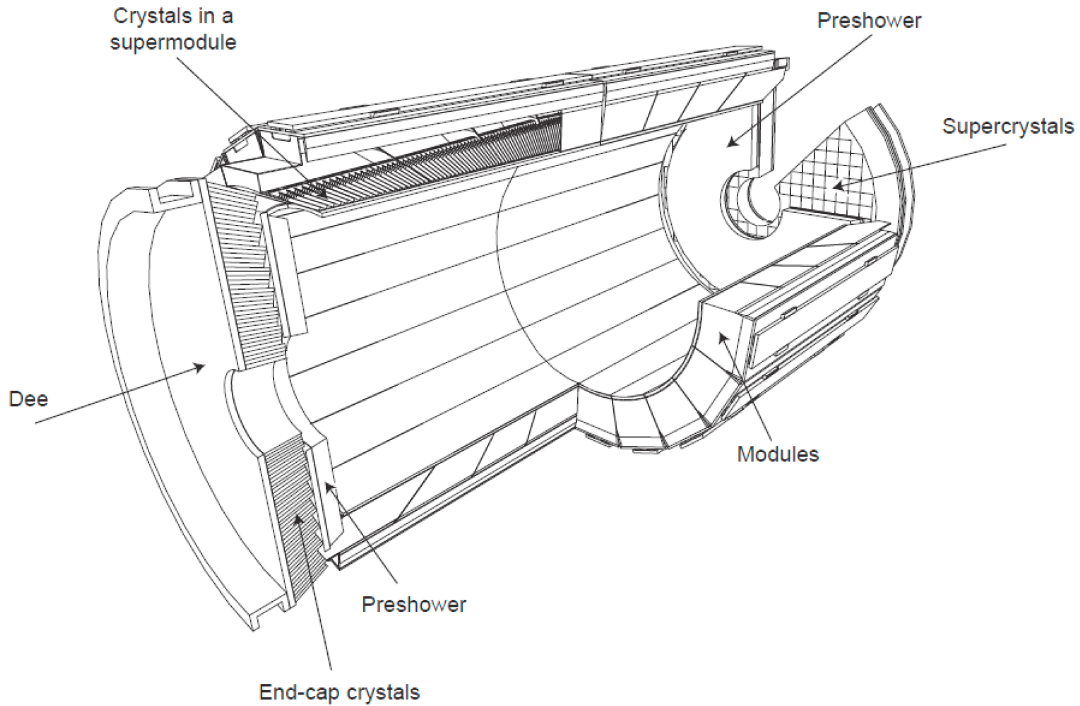


Figure 4.3: Layout of the CMS electromagnetic calorimeter. The barrel supermodules, two endcaps and the preshower detectors are shown as well [126, 132].

The **EB** is organized in 36 supermodules, each containing 1700 crystals, which are arranged in 4 modules of 400 or 500 crystals depending on η . Four half-disk dees, forming the **EE**, are composed of 3662 tapered crystals each. The crystals of the **EE** are grouped into 138 5×5 crystal arrays, supercrystals, in each dee. The superclusters are arranged in a rectangular xy grid with 18 partial supercrystals on the inner and outer circumferences.

The **ECAL** resolution is parametrized in terms of the stochastic (**S**), noise (**N**) and the constant (**C**) contributions,

$$\frac{\sigma(E)}{E} = \frac{S}{\sqrt{E(\text{GeV})}} \oplus \frac{N}{E(\text{GeV})} \oplus C. \quad (4.1)$$

The symbol \oplus means adding in quadrature. The contributions [126] to each term of the parametrization (4.1) are as follows:

- **The stochastic term** is mainly given by two contributions.
Fluctuations of the number of photoelectrons released in the photodetectors give a contribution of about 2.3%, and fluctuations on the lateral containment give about 1.5%.
- **The noise term** contains contributions from readout electronics and pile-up collisions.
- **The constant term** is dominated by crystal-to-crystal intercalibration errors and non-uniformity for the longitudinal shape of the collected light.

The values of the parameters in formula (4.1) are fitted to the test beam data [133],

$$\frac{\sigma(E)}{E} = \frac{2.8\%}{\sqrt{E(\text{GeV})}} \oplus \frac{12\%}{E(\text{GeV})} \oplus 0.3\%, \quad (4.2)$$

and shown in Figure 4.4. The energy resolution of the **ECAL** is better than 0.4% for electrons with $E > 100$ GeV.

This measured energy resolution was obtained by reconstruction of the showers in a matrix of 3×3 crystals to ensure the containment of 94% of the electromagnetic shower.

4.2.2 The CMS hadronic calorimeter

The hadronic calorimeter, **HCAL**, provides measurements of the energy of strongly interacting particles. There are several parts of **HCAL**:

- the barrel part, **HB**, covering the range $|\eta| < 1.4$,
- the endcap part, **HE**, installed in the range $1.4 < |\eta| < 3$,
- the forward part, **HF**, in the region $3 < |\eta| < 5$.

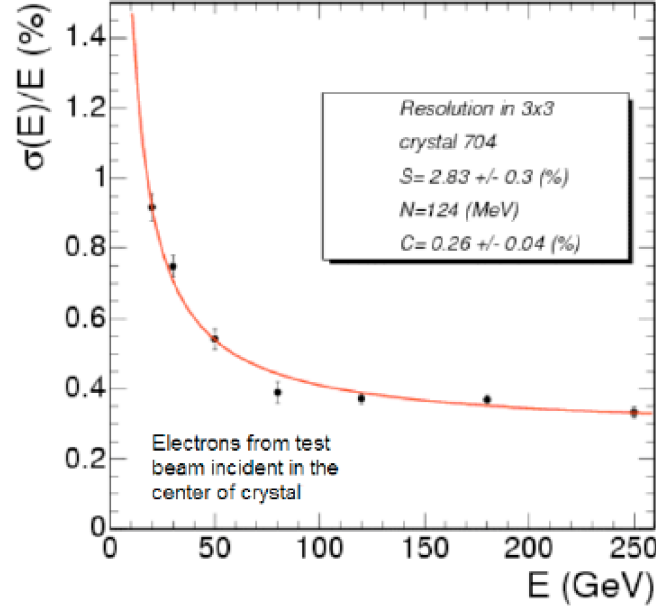


Figure 4.4: The measured (black) and fitted (red) resolutions as functions of the electron energy in a 3×3 array of crystals with beam incident in an area of $4 \times 4 \text{ mm}^2$ around the crystal cross section center [134].

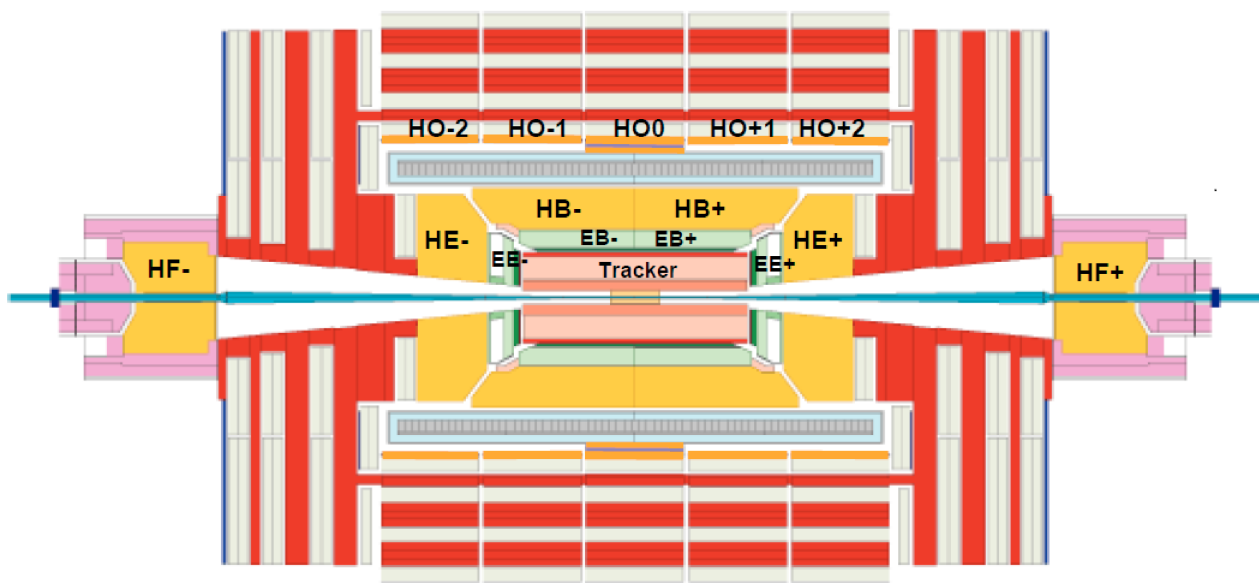
An additional scintillator layer, **HO**, is placed in the region $|\eta| < 1.2$ to catch the tails of showers leaving the barrel part of **HCAL**. The hadron calorimeter uses brass plates as absorbers, which are interspersed with plastic scintillator tiles playing the role of sensors. The layout of the **HCAL** is depicted in Figure 4.5.

The characteristic HCAL segmentation for the barrel in the (η, ϕ) plane is 0.087×0.087 . In the endcap the segmentation varies from 0.087×0.087 at the small values of η to 0.37×0.175 at the larger η . The forward hadron calorimeter has sections of 0.175×0.175 size.

The CMS HCAL system is a non-compensating calorimeter. Its response for electromagnetic energy depositions is larger than for hadronic ones. The deposited energy in HCAL cells is not linearly proportional to the hadron energy [135]. As a result, the ratio of contributions from electromagnetic and hadronic interactions is energy dependent, and it is about 1.2. Figure 4.6 (a) shows the non-linear energy response of the HB calorimeter obtained from test-beam measurements with π^- beams at different energies [136].

The energy resolution $\sigma(E)/E$ of the **HB** has been measured using 20-300 GeV pions. $\sigma(E)/E$ as a function of the energy E is shown in Figure 4.6 (b), and approximated as

$$\frac{\sigma(E)}{E} = \frac{115\%}{\sqrt{E(\text{GeV})}} \oplus 5.5\%. \quad (4.3)$$



HB Brass Absorber (5cm) + Scintillator Tiles(3.7mm)
HE Brass Absorber (8cm) + Scintillator Tiles(3.7mm)
HO Scintillator Tile (10mm) outside of solenoid
HF Iron Absorber + Quartz Fibers

Figure 4.5: Layout of the CMS **HCAL**. The barrel (HB), endcap (HE), forward (HF) and “tails-catcher” (HO) parts are shown [112].

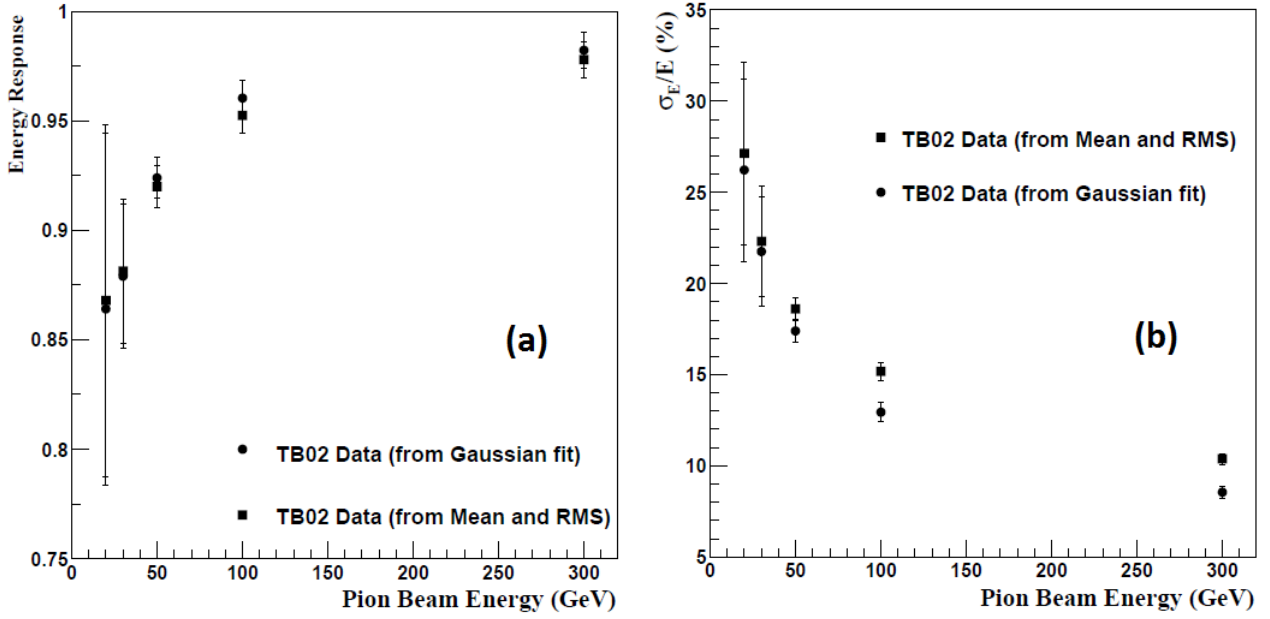


Figure 4.6: Energy response as a function of pion beam energy (a). Relative energy resolution $\sigma(E)/E$ versus pion beam energy (b). $\sigma(E)/E$ is measured using mean and RMS of the energy distribution as well as the mean and variance of the fitted Gaussian [136].

This is consistent with characteristics expected from the **HB** design. Effects from the non-linear response of **HCAL** is taken into account in formula (4.3) [136].

4.3 The CMS muon spectrometer

The CMS muon system provides geometric coverage for detection of muons up to $|\eta| = 2.4$. The detectors are embedded in the iron structure of the magnet return yoke. The muon momentum and charge measurements exploit the strong magnetic return field. There are three types of the gaseous detectors in the muon system:

- the drift tubes, **DT**, located in the barrel region, $|\eta| < 1.2$
- the cathode strip chambers, **CSC**, in the endcap region $1.2 < |\eta| < 2.4$
- the resistive plate chambers, **RPC**, in the whole detector up to $|\eta| = 2.1$.

In Figure 4.7 an (R, z) view is given for a quarter of the CMS muon system.

The muon systems allow fast muon identification together with perfect spatial resolution of muon tracks in the whole volume of the CMS detector.

The **DT** are long aluminum cells of a few centimeters wide, filled with a fast-drift gas, having anode wires in the centre to collect ionization charges. The **DT** are arranged into three

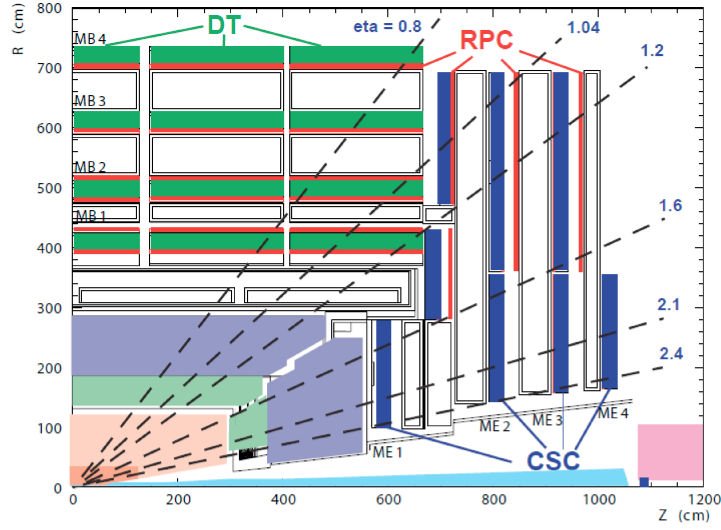


Figure 4.7: View of the CMS muon system [112]. The dashed lines corresponds to the given values of η .

superlayers that are shifted by half of the width with respect to each other. Two superlayers have anode wires parallel to the beam pipe, providing a measurement of the R and ϕ coordinates while the third superlayer, which is disposed perpendicular to the others, performs η —measurements for traversing muons.

The **CSC** consist of arrays of anode wires perpendicular crossed with radial cathode strips within a gas volume. A muon traversing the **CSC** creates electrons and muons. The electrons drifts to the anode, and due to the high electric field near the anode, an avalanche of electrons is formed, leaving ions in space. The anode wire produces a fast signal, while the cathode strips collect the image charge of ions much slower. The **CSC** cells, organized into six layers, measure three muon coordinates, R , ϕ and η . The **CSC (DT)** detectors provide a track measurement with spatial resolution of $100\mu\text{m}$ in R and 10 (1) mrad in ϕ directions.

The **RPC** system consists of double-gap bakelite chambers, where two parallel plates, being the anode and the cathode, are separated by 2 mm distance filled with a special gas mixture. Despite the worse spatial resolution, **RPC** provides a very fast response of 2 ns which is used by a trigger, as described below.

The different muon chambers are segmented in disks, placed approximately at 4, 5, 6 and 7 meter radii in the barrel part and 7, 8.5, 9 and 10 meters in z direction for the endcap stations.

4.4 Triggering system

In 2011 and 2012 years the proton beams was composed, at most, of 1380 bunches with minimum 50 ns spacing, corresponding to the minimum bunch crossing rate of 16 MHz. The peak recorded luminosity was $6.8 \times 10^{33} \text{cm}^{-2}\text{s}^{-1}$. The total event rate at the $\sigma_{tot} = 90 \text{ mb}$ was expected to be

about 3×10^8 events per second.

However, the cross sections of the most interesting physics channels are rather small. For example, the process, in which a 125 GeV Standard Model Higgs boson decays to two photons, has a cross section of only 3.94 pb, corresponding to an event rate of 3×10^{-4} Hz, which is 10^{12} times smaller compared to the total event rate. Assuming the event size of the order ~ 1 MB, the data stream produced by the CMS detector was of order of 0.3 PB/s in 2011, which is far beyond current data storage capabilities. The storage capacity of the CMS computing system corresponds to processing 500 events per second or 500 MB/s data rate. Therefore the primary goal of the CMS Data Acquisition, **DAQ**, and Trigger systems is to reduce the total event rate from collisions to a manageable level of a few hundred Hz while keeping the most interesting and precious events with high efficiency.

Because of the required high event rejection power, the **CMS** performs an online selection in two steps [137]. An overview of the two-level trigger system is shown in Figure 4.8.

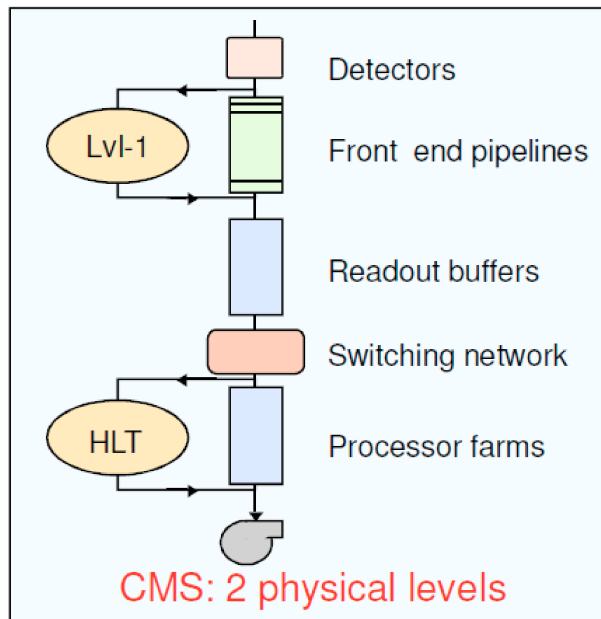


Figure 4.8: An overview of the two-level trigger system used at the CMS. The Level-1 (Lvl-1) selects events from the pipeline of front-end electronics. A software-implemented High Level Trigger (HLT) filters the Level-1 output and reduces the data rate by a factor of $\mathcal{O}(1000)$ [137].

The pipeline length on the front-end electronics has been designed to be $4.0 \mu\text{s}$ to store information on 128 bunch crossing. During this period, the Level-1 trigger must have made a decision on whether or not to pass the temporary-stored events onto the High Level Trigger.

4.4.1 Level-1 trigger

The first step of online selection is performed by the Level-1 trigger, **L1**, [137] implemented on dedicated programmable hardware.

The **L1** is designed to reduce the total rate from 40 MHz to less than 100 kHz based on fast signals from detector electronics. It uses only coarsely segmented raw data from calorimeter and muon detectors in order to make a fast decision to keep or reject one particular event for further processing. The **L1** selects events using physics objects reconstructed from data stored in the front-end pipeline. To make a decision, the so-called “Level-1 Accept”, **L1A**, the Level-1 trigger requires about 1 μ s. The logical view of the L1 structure is illustrated in Figure 4.9.

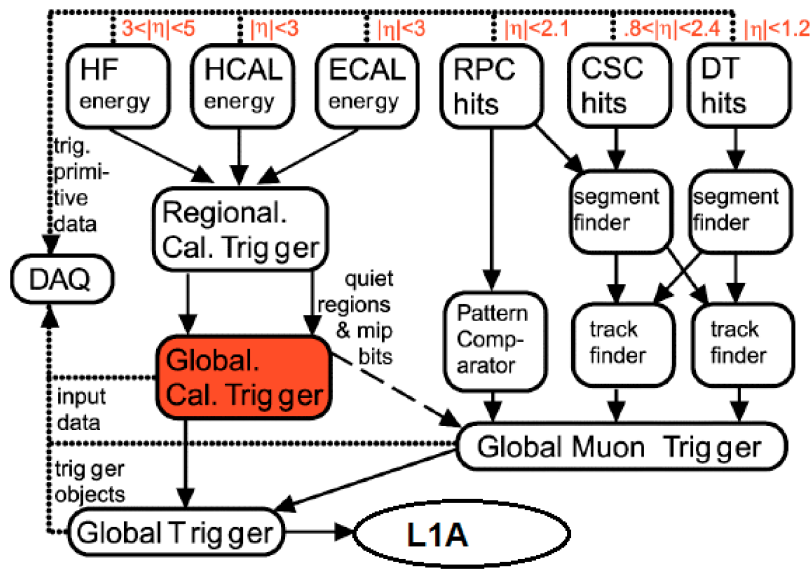


Figure 4.9: An overview of the Level-1 trigger [137]. The regional triggers of the calorimeter and the muon systems provide information to the Global Trigger.

The main module of the **L1** is the Global Trigger, **GT**, which consumes the information from regional calorimeter and muon triggers in order to make the **L1A**. The regional triggers identify and reconstruct objects of several types, which are:

- isolated and non-isolated electrons
- photons
- forward and central jets
- τ jets
- muons.

The four best candidates of each type, together with measurements of their positions, transverse energy or momentum and a quality word, are passed to the **GT**. The regional calorimeter trigger also sends the total and missing transverse energies in an event. Events with trigger objects, passing programmable thresholds, are tested for topological conditions and correlations between objects. A total of 128 topological conditions, called primitives, are processed in parallel.

Electron and photon candidates are treated simultaneously at the regional calorimeter trigger. They are reconstructed from energy of one or two adjacent 3×3 arrays of ECAL and HCAL trigger cells, as shown in Figure 4.10. The trigger cell accumulates the transverse energy of 5×5 crystal groups. Depending on the electromagnetic shower profile detected in the 5×5 group, a quality bit of the calorimeter trigger object is set to either “isolated” or “non-isolated” [138].

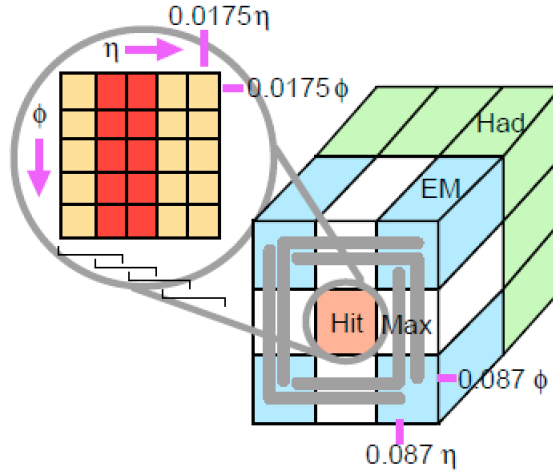


Figure 4.10: The structure of the regional L1 calorimeter trigger [138]. The 3×3 trigger cells (in blue and green) are compound of 5×5 crystal arrays (in yellow and red).

The four isolated and non-isolated candidates with the highest energies are selected and sent to the Global Trigger.

The L1 calorimeter window, made of 12×12 trigger cells, and shown in Figure 4.11, is used to reconstruct jets. The global calorimeter trigger slides the window by increments of four towers both in the η and ϕ directions. Applying the 2×2 crystal patterns, shown on the right side of Figure 4.11, to the energy deposits for each of nine 4×4 groups in the window, the global calorimeter trigger identifies jet constituents. If there are no more than two 4×4 crystal groups, which follow either the 1×1 , or 1×2 , or 2×1 patterns, a jet is identified as τ jet. To suppress reconstruction of “fake jets” due to pile-up interactions, a cut on the jet transverse energy, $E_T \geq 30$ GeV, is imposed. The L1 jet reconstruction is done only for the region of $|\eta| < 1.95$. The global calorimetric trigger sends the most energetic eight jets and four tau jets to the **GT**.

Muon **L1** objects are reconstructed from track segments of different muon stations. The regional track finders build their segments in parallel. The four muons with the highest p_T are

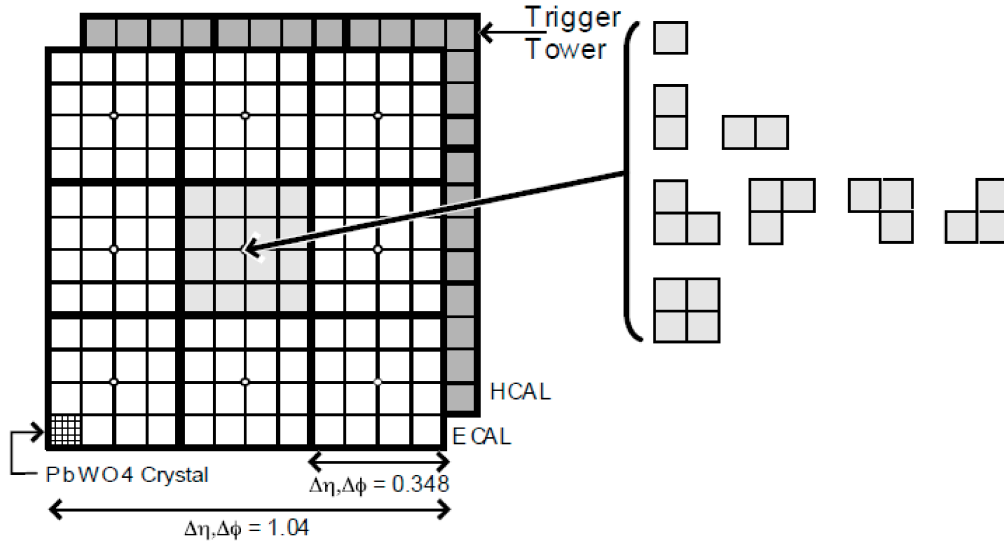


Figure 4.11: The 12×12 window used for the L1 jet reconstruction. The trigger patterns on the energy deposits, shown on the right side, are used to identify jet constituents [138].

sent to the **GT**.

4.4.2 High Level Trigger

The CMS High Level Trigger, **HLT**, [139] processes all events accepted by the L1 trigger. The **HLT** runs dedicated software on a farm of commercial processors. There are two steps of **HLT** selection: Level-2 and Level-3 triggers. The High Level Trigger reduces the rate of 100 kHz incoming from the **L1** to 500 Hz. The structure of the **HLT** is shown in Figure 4.12.

The **HLT** algorithms utilize the full information available from the CMS detector. First, the **L1** objects are packed together to the 128-bit **L1A**. Then **HLT** starts the partial reconstruction of the event: objects necessary for the trigger decision are reconstructed and selected step-by-step, the reconstruction process immediately stops, if the object does not satisfies selection criteria, and the event is rejected.

The Level-2 trigger reads bits (seeds) of the **L1A** to extract logical combinations of L1 objects. Then algorithms, based on partial tracker information, e.g. pixel hits, perform fast reconstruction of tracks and energies of charged candidates. Pixel hits are also used to reconstruct interaction vertices.

At the Level-2.5 quality of objects passed the L2 selection is validated. The Level-3 trigger chain reconstructs not only tracks and vertices, but also particles, employing information from the pixel and silicon trackers and the calorimeter. Because of the high number of channels, complex pattern recognition and large combinatorics and sophisticated algorithms, the Level-3 trigger demands large amounts of CPU time.

Following the structure, shown in Figure 4.12, the Level-2, Level-2.5 and Level-3 algorithms

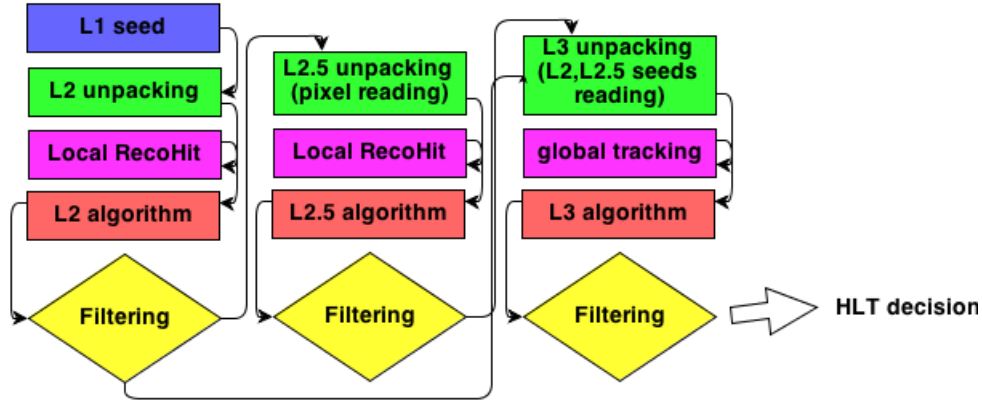


Figure 4.12: An overview of the **HLT**. The **HLT** reconstructs Level-2 tracks in the tracker regions seeded by the Level-1 electrons and photons. The rejection of an event happens, if Level-2 or Level-3 objects fail to pass selection criteria in the filtering steps.

are arranged in several programming units, which are called the Electron, Muon and Jet triggers.

Electron Trigger

The Level-2 electron reconstruction starts from searches for calorimeter superclusters according to **L1** primitives. Next, the Level-2.5 algorithms match pixel hits to calorimeter superclusters by extrapolating from the positions of the calorimeter supercluster through the magnetic field. Finally, the Level-3 electron track parameters are fitted to associated hits. Electrons are filtered according to the quality constraints, which are the χ^2 value of the fit, the value of p_T and the number of the associated hits. The event is rejected at any level, if no electron candidates remain.

Muon Trigger

The muon selection proceeds in two steps. First, tracks are built at the Level-2 using available information from all muon chambers, seeded by L1 trigger primitives. This reconstruction refines the p_T measurement already made at the Level-1. The energy of calorimeter towers in a cone around the muon direction is summed at the Level-2.5 to assign the flag “isolated” or “non-isolated” to the muon. Then at the Level-3, the muon trajectory, seeded by Level-2 tracks, are rebuilt using the Kalman filter [140]. This method iteratively proceeds tracker layers including the information of the successive reconstructed hits one by one. On each layer, i.e. with every new measurement, the track parameters are known with a better precision. The algorithm searches for compatible hits taking into account energy loss and multiple scattering.

The procedure is repeated until the outermost layer of the tracker is reached.

Jet Trigger

To identify and select jets, a simple and fast Anti- k_T algorithm [141] is applied. It exploits all calorimeter towers composed of ECAL and HCAL superclusters. Finally, energy of the jet is corrected for noise in electronics and for the pile-up interactions.

Apart from electrons, muons and jets, many other physics objects, such as photons, τ jets, missing energy and b jets, are reconstructed within the specialized programming units, the sequences of the Level-2, Level-2.5 and Level-3 algorithms. The High Level Trigger usually combines several reconstruction sequences and apply topological cuts on possible kinematics of the objects in the combined sequences in order to loosen thresholds applied in the selection. The triggering in a search for the neutral Higgs bosons in the multi b-jet final states is described later.

4.5 Event Reconstruction

The event reconstruction starts from building sub-detector specific objects: charged particles tracks, vertices and calorimeter clusters. To perform physics studies with these building blocks, they need to be combined into higher-level physics objects, that allow to identify final states of interest. The reconstruction of the physics objects is a trade-off between efficiency and fake rate. Therefore, the identification of the high-level objects often involves analysis-specific quality requirements applied at different stages of the reconstruction. This section describes the basic principles and reconstruction techniques which are adopted and used in the search for neutral Higgs bosons in multi b-jet final states. Details on the reconstruction of the physical objects, like electrons, muons, photons, τ -leptons and jets can be found in Ref. [112].

4.5.1 Track reconstruction

Track reconstruction is decomposed into hit reconstruction, seed generation, trajectory building, ambiguity resolution and the final track fit.

- The hit reconstruction clusters strip and pixel signals produced by charged particles. The positions of the hits are measured along with the corresponding uncertainties. As the track of a charged particle in the presence of the magnetic field is described by a helix, it requires six parameters to be fully determined: the position, \vec{r}_0 and the momentum, \vec{p}_0 , vectors of the initial point. However, considering the point of the closest approach of the track to the beam axis as the initial point of the helix, azimuthal angles of the two vectors are related as $\phi_{\vec{r}_0} = \pi/2 + \phi_{\vec{p}_0}$. Therefore, only five parameters remain to be reconstructed.
- A seed defines initial trajectory parameters and errors. For each hit the R and ϕ coordinates are measured. Since the track is described by five parameters, at least three hits (triplets) must be reconstructed. For fast seeding, two hits (pairs) and a constraint on the origin of

the helix from the interaction point are used. Only information of the pixel detectors are used at this step.

- The pattern recognition module performs an iterative process, which, starting from the seed, collects all hits compatible with the track. The iterative Kalman filter [142, 143] method is used during this step. Because trajectories are build in parallel, allowing to share hits, the Kalman filter is also responsible for cleaning the track candidates and removing duplicates.
- After cleaning tracks, the Kalman filter performs a fit, determining the final parameters of trajectories with ultimate precision.

Simulation results of track-reconstruction efficiency, fake rate and parameter resolutions are summarized in Ref. [112, 142]. Two definitions of efficiency are used:

- the algorithmic efficiency is the efficiency of reconstructing tracks with $p_T > 0.9$ GeV and simulated hits in at least eight layers of the tracker, of which at least two are in the pixel detector;
- the global efficiency is the reconstruction efficiency for all tracks with $p_T > 0.9$ GeV.

The track-reconstruction efficiency of single tracks has been estimated using Monte Carlo samples of muons with transverse momenta of 1, 10 and 100 GeV, and samples enriched by b quarks. The results are shown in Figures 4.13 (a) and 4.13 (b).

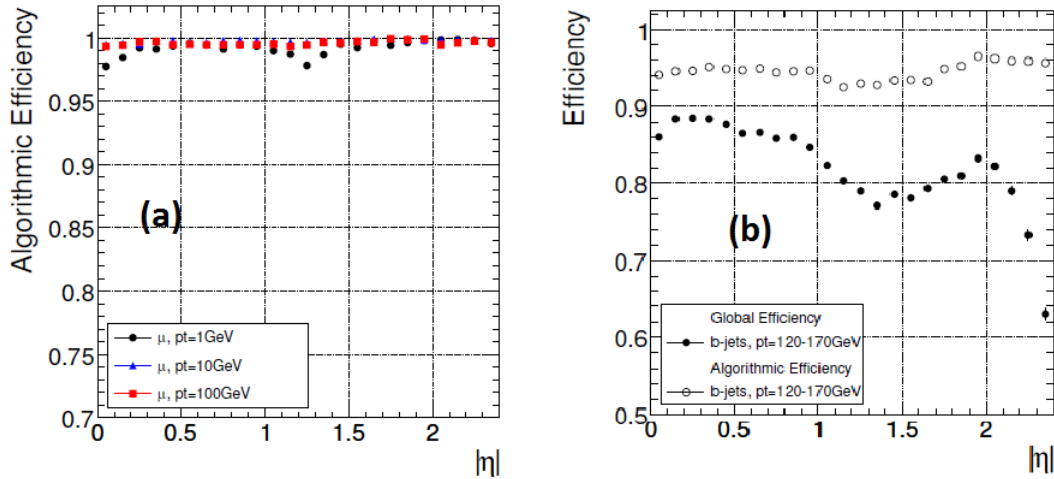


Figure 4.13: The algorithmic track-reconstruction efficiency for muons (a) with $p_T = 1$ (black), 10 (blue) and 100 GeV (red). The algorithmic (open points) and global (solid points) efficiencies for tracks in b jets with transverse momenta, p_T , between 120 and 170 GeV (b) [142].

For isolated muons about 99% algorithmic reconstruction efficiency is obtained, except in the regions of $\eta \simeq 0$ and $\eta \simeq 1.3$. For muon tracks in b-flavored jets with $120 \text{ GeV} < p_T < 170 \text{ GeV}$, about 90% global tracking efficiency is obtained in the barrel, and 80% in the forward region.

The minimal p_T of a track to be reconstructed in the central region is 0.7 GeV. At this p_T the track curvature radius is equal to the distance to the outermost tracker layer. The maximal p_T possible to reconstruct is determined by the tracker strip pitch. If the track bending inside the tracker volume is less than the strip pitch, the track is reconstructed as a straight line, and p_T is undetermined. The maximum reconstructed p_T in the CMS tracker is 1 TeV.

4.5.2 Vertex reconstruction

The vertex reconstruction involves two steps:

- the vertex finding and grouping tracks to vertex candidates;
- vertex fitting with determination of the vertex position.

Either pixel tracks from pixel-hit triplets or fully reconstructed tracks are used to find vertex candidates [144]. There are two algorithms used to group tracks in vertex candidates. The algorithm, called the Deterministic Annealing [145], **DA**, is applied for the reconstruction of primary vertices, **PV**. The algorithm, called the Adaptive Vertex Fitter [146, 147], is utilized to reconstruct secondary vertices, **SV**.

The **DA** algorithm assigns the i^{th} track to the k^{th} vertex candidate with the assignment probability p_{ik} . The distance between the track and vertex plays the role of the energy,

$$E_{ik} = \frac{(z_i - z_k)^2}{\sigma_i^2}, \quad (4.4)$$

where z_i and z_k are z-coordinates of the point of the closest approach of the track i and the position of the vertex k . The measurement uncertainty of z_i is σ_i . The energy of the vertex ensemble is determined as

$$E = \sum_{ik} \rho_k p_{ik} E_{ik}, \quad (4.5)$$

where the factor ρ_k describes the probability to reconstruct the vertex k . As the energy E (4.5) is gradually decreased, while keeping the probabilities p_{ik} as highest as possible, the vertex k becomes unstable at some crucial energy E_c [145], and splits into two new vertices with lower crucial energies, and smaller reconstruction probabilities, $\rho_{k,1} + \rho_{k,2} = \rho_k$. The splitting is continued until the minimal energy E_{min} [145] is reached.

The reconstructed primary vertices are required to have z-coordinates within 24 cm of the nominal detector centre and radial positions within 2 cm from the beamspot. In each reconstructed vertex k the number of degrees of freedom must be larger than four [145],

$$\text{Ndof} = 2 \sum_i p_{ik} - 2 > 4.$$

Before DA primary vertices are stored in the vertex collection, they are sorted according to their sum of p_T^2 of all tracks in the vertex. The primary vertex with the largest value of the p_T^2 -sum is chosen as the one originating from a hard interaction.

To reconstruct the **SV**, the Adaptive Vertex Fitter starts from computing an initial (seed) vertex as a crossing point of the tracks. This crossing point is the weighted mean of points of closest approach of the tracks. The seed defines a geometric region constrained on η and ϕ . For each track in the region the transverse impact parameter

$$d_{xy} = |\sqrt{x_C^2 + y_C^2} - R| \quad (4.6)$$

and its uncertainty $\sigma_{d_{xy}}$ are determined. Here x_C , y_C and R , as shown in Figure 4.14, are coordinates of the centre and radius of the unique circle that passes through three pixel hits of the track. The longitudinal impact parameter, d_z is estimated using a helix parametrization. The pixel hits are projected on the (ξ, z) plane where ξ is the azimuthal angle between the hit and the point of closest approach to the beam line. The longitudinal impact parameter is defined as the point of intercept between the line joining the first two pixel hits with the $(\xi_{1,2}, z_{1,2})$ coordinates and the z -axis

$$d_z = z_1 - \frac{\xi_1}{\xi_1 - \xi_2}(z_1 - z_2). \quad (4.7)$$

The significance, S_{IP} , of the transverse impact parameter is the ratio of the transverse impact parameter d_{xy} and its uncertainty $\sigma_{d_{xy}}$

$$S_{IP} = \frac{d_{xy}}{\sigma_{d_{xy}}}. \quad (4.8)$$

The SV reconstruction accepts tracks with a significance S_{IP} smaller than 3. Then tracks are grouped with accordance to their d_z . The algorithm progressively merges tracks close enough to each other, forming vertex candidates. Several secondary vertices, which may be found, are sorted in decreasing order of the sum of p_T^2 of the tracks associated.

The **SV** candidates must not share more than 65% of the track with the primary vertex and the distance between SV and PV must exceed 3σ . We suppress the vertices of long-lived particles, rejecting the **SV** candidates with the radial distance to the **PV** larger than 2.5 cm or the **SV** candidates for which mass is compatible with that of the K_S^0 particle or greater than 6.5 GeV. The flight direction of the SV candidate must lie within a cone $\Delta R < 0.5$ around the jet direction.

4.5.3 The energy reconstruction and calibration in ECAL

Energy deposits in the **ECAL** due to electromagnetic showers are spread over several crystals. Approximately 97% of the incident energy of a single electron or photon is contained within the 5×5 array of crystals [112] around the point of impact.

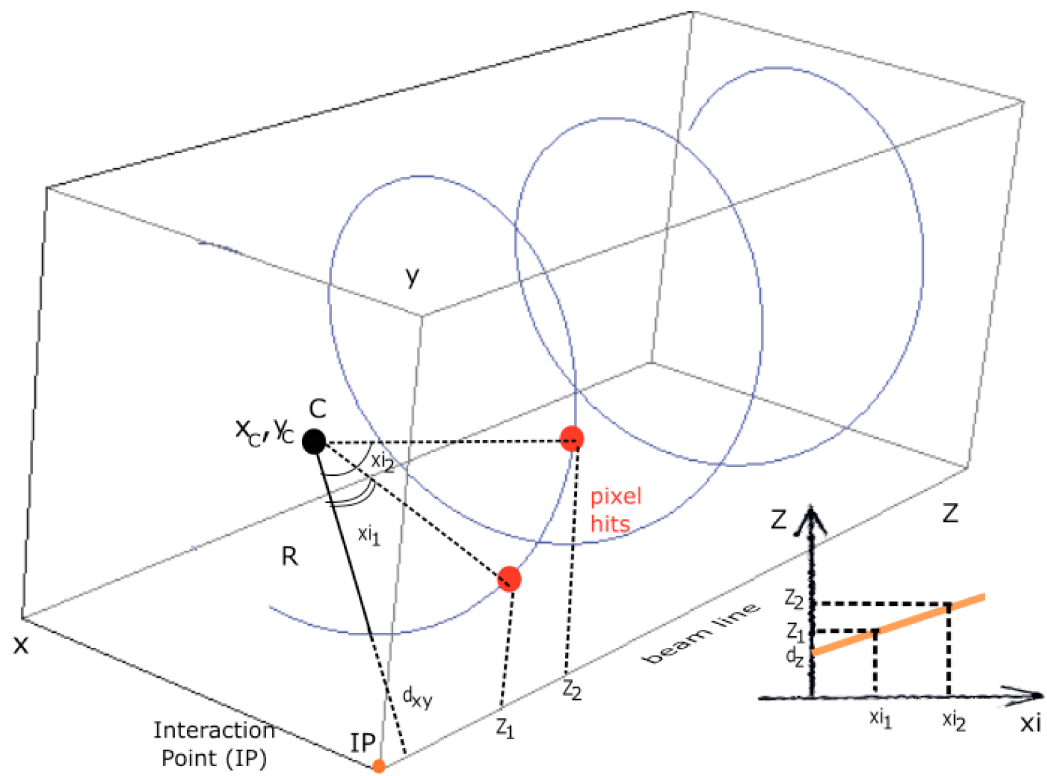


Figure 4.14: The trajectory of a charged particle in the pixel tracker. The measurements of the first two pixels determine the transverse and longitudinal impact parameters, d_{xy} and d_z , respectively.

The presence of material in front of the calorimeter can cause conversion of photons and bremsstrahlung from electrons and positrons. Because of the strong magnetic field, the energy flow, associated to primary electrons or converted primary photons, spreads in ϕ at large distances from the interaction point. The fraction of the bremsstrahlung energy radiated by electrons before reaching ECAL crystals was estimated in Monte Carlo studies [148] of back-to-back e^+e^- pairs. Electrons radiate inside the tracker about 70% and 95% of their energy in 35% and 10% of the cases, respectively. Bremsstrahlung photons may convert into electron-positron pairs before the calorimeter. This leads to electromagnetic shower patterns.

The total electron (photon) energy has to be determined as the sum of energy deposits along a ϕ road to collect energies from bremsstrahlung photons. Different algorithms are employed for summing ECAL energies into superclusters [112, 149, 137]. They collect together energy deposits in adjacent 5×5 crystal groups, forming the superclusters, **SC**. There are two algorithms, called “Hybrid” and “Island”, which are used to build the **SC** in the ECAL barrel and endcaps, respectively.

The “Hybrid” algorithm starts from a single crystal, called the seed crystal, which has the maximum energy deposit in the **EB**, of at least 1 GeV. Subsequently, a row of 3 or 5 crystals in the η direction is build symmetrically around the seed crystal. Additional rows of 3 or 5 crystals are added to the **SC** in the ϕ direction. The algorithm stops if a number of added rows reaches 10 in either direction of ϕ , or if a valley with the energy deposit less than 100 MeV is found.

The “Island” algorithm constructs the **SC** by forming rows in η of **EE** crystals with decreasing energies when moving away from the seed crystal. The supercluster is built by connecting with E_T -ordered “Island” rows reconstructed at adjacent positions of ϕ around the seed 5×5 crystal array. The minimal threshold for the seed cluster energy, E_T^{seed} , is taken to be 1 GeV in order to reconstruct **SC** candidates for low- p_T electrons in 99% cases.

Bremsstrahlung photons can produce the secondary **SC** separated from the seed supercluster by a crystal valley with total energy less than 100 MeV. If the distance between seed and secondary superclusters is no more than 10 crystals, they are combined. The same superclustering algorithms are used to reconstruct electrons and photons. The position of the supercluster is obtained as an energy-weighted mean position of all crystals in the **SC**.

The energy in a supercluster, $E_{e,\gamma}$, is estimated as

$$E_{e,\gamma} = F_{e,\gamma} \cdot (G \cdot \sum_i S_i \cdot C_i \cdot A_i), \quad (4.9)$$

where the sum is over all crystals i belonging to the supercluster. A_i is the pulse amplitude, measured as the number of counts, s_i , of analogue-to-digital converter, **ADC**, multiplied by a optimization weight w_i ,

$$A_i = w_i \cdot s_i.$$

The quantities S_i [150, 151] and C_i [152] are correction terms due to radiation-induced changes in channels responses and a relative calibration of crystals, making A_i to be equal for all channels, respectively. The coefficients $F_{e,\gamma}$ and G are corrections on the energy scale. The relative impacts of the individual calibrations S_i and C_i on the reconstructed energy are illustrated in Figure 4.15.

The distributions of di-electron invariant mass from Z -boson decays, $Z \rightarrow e^+e^-$, were obtained from pp collisions data recorded in 2011 at a centre-of-mass energy $\sqrt{s} = 7$ TeV [134]. Various reconstruction scenarios for supercluster energy are considered: the corrections S_i and C_i are not applied (blue), the only intercalibration factor C_i is applied (red) and both the S_i and C_i corrections are applied (black).

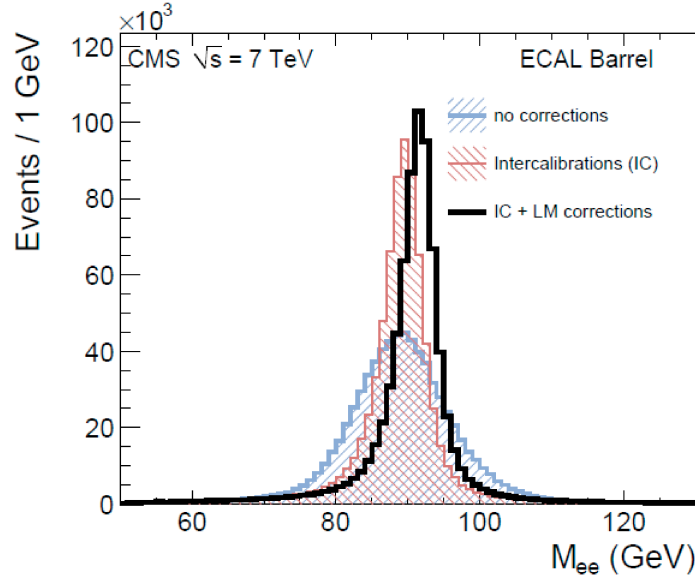


Figure 4.15: The distribution of di-electron invariant mass M_{ee} reconstructed in $Z \rightarrow e^+e^-$ decays in **EB**. The cases of no correction (blue), interchannel calibration C_i applied (red), both interchannel C_i and radiation-induced S_i corrections applied (black) are shown [134].

4.5.4 Electron and photon identifications

Electron identification

Electrons and photons are built from the reconstructed superclusters in the ECAL barrel and endcaps. The superclusters serve as seeds for reconstruction of tracks: supercluster are matched to triplets of hits in the inner tracker layers in a relatively wide $\Delta\eta \times \Delta\phi$ window. For electron tracks, in order to better deal with the non-Gaussian fluctuations induced by bremsstrahlung emission, a non-linear generalization of the Kalman filter, the Gaussian Sum Filter [153], **GSF**, is applied in the track fitting instead of the standard Kalman filtering technique.

Tracks are described by a five-dimensional state vector containing the information about the momentum, the direction and the position at some reference surface. To model Bethe-Heitler energy loss of electrons due to the bremsstrahlung process, the **GSF** utilizes a weighted sum

of Gaussians for state vectors. The track building procedure iterates over triplets of hits in silicon layers calculating the trajectory state at each layer as the Gaussian-weighted mean of the predicted state and of the measured hit. The track quality is defined in terms of a χ^2 test. If many hits are found on neighboring layers, many candidate trajectories are grown in parallel, keeping the best two candidates, with the smallest χ^2 , in the end.

The **GSF** algorithm provides complementary segments of the trajectory, which allow to measure the state vectors of the track in the innermost, $(p_{in}^{track}, \eta_{in}^{track}, \dots)$, and outermost, $(p_{out}^{track}, \eta_{out}^{track}, \dots)$, tracker parts. As a final step, to resolve ambiguity in tracks, the matching in η and ϕ between the outermost part of the GSF track and the corresponded **SC** is made [148]:

- $\Delta\eta = |\eta^{SC} - \eta_{out}^{track}| < 0.01$, where η^{SC} is η of the weighed supercluster position, and η_{out}^{track} is η of the track in the outermost tracker;
- $\Delta\phi = |\phi^{SC} - \phi_{out}^{track}| < 0.1$.

To suppress fakes from jets in the electron-track reconstruction, a few requirements are imposed in addition:

- the ratio $H/E < 0.1$, where H and E are HCAL and ECAL constituents of the energy deposit of a supercluster;
- the transverse energy of the candidate, $E_T = E \sin \theta > 4$ GeV, where θ is the polar angle of the weighted position of the **SC** and E is the ECAL SC energy.

The procedure of matching between a supercluster and GSF track is shown in Figure 4.16 (a). The electron track in the inner and outer parts of the tracker are depicted in Figure 4.16 (b). The supercluster, “ElectronCluster”, with energy E_e , is matched to the track. The bremsstrahlung photons form the secondary **SC**, “BremCluster”, with energy E_γ .

Photon identification

The energy-weighted mean position of the **SC** determines the transverse energy of a photon candidate as

$$E_T = E \sin \theta,$$

where E and θ are the **SC** energy and a polar angle of the **SC** position. After reconstructing the superclusters, photon candidates are selected from them applying the following isolation and identification criteria [154]:

- There are no pixel seeds in the innermost tracker region matched to **SC**;
- ECAL isolation: the sum of ECAL E_T must be $\sum E_T < 4.2$ GeV, in an annular region with inner radius, $\Delta R_{in} = \sqrt{\Delta\eta^2 + \Delta\phi^2} = 0.06$, and outer radius, $\Delta R_{out} = 0.4$, around the photon candidate;
- HCAL isolation: the sum of HCAL E_T around the photon candidate in the annulus with the inner radius of 0.15 and outer radius of 0.4 is required to be less than 2.2 GeV;

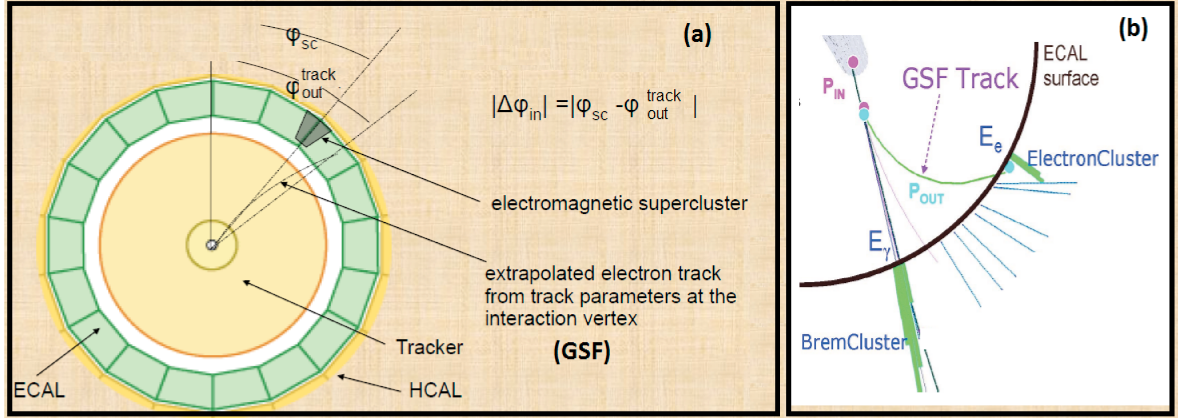


Figure 4.16: The matching between the GSF track and the SC (a). The angular coordinates of the SC, ϕ_{SC} and the outermost part of the GSF track ϕ_{out}^{track} , are compared. The reconstruction of an electron candidate as a combination of two-component **GSF** track, with the 4-momenta p_{in} and p_{out} in the inner and outer parts of the tracker, respectively (b).

- Tracker isolation: the scalar sum of p_T for tracks consistent with the primary vertex in a annulus around the photon candidate having the inner radius of 0.04 and outer radius of 0.4 is required to be less than 2 GeV; The cone is taken in such way that the conversion tracks are not counted in the isolation criterion;
- $\text{Cov}_{\eta\eta}$ element of the $\eta - \phi$ covariance matrix must be less than 0.1. This element is calculated with logarithmic weights w_i as

$$\text{Cov}_{\eta\eta}^2 = \frac{\sum_i^{5 \times 5} w_i (\eta_i - \eta_{seed})^2}{\sum_i^{5 \times 5} w_i}, \quad w_i = \max(0, 4.7 + \ln \frac{E_i}{E_{5 \times 5}}),$$

where E_i and $\eta_{i(seed)}$ are energy and η of the i^{th} (seed) crystal in the SC, and $E_{5 \times 5}$ is the total energy of the SC;

- The ratio of HCAL energy over ECAL energy, H/E , should not exceed 0.05.

4.5.5 Muon identification

Global Muons (GM)

The standard CMS offline muon reconstruction exploits hits, reconstructed in the muon stations and tracker, forming **global-muon** tracks. The pseudo-rapidity coverage of the **GM** is $|\eta| < 2.4$. At low muon p_T , below 30 GeV, the **GM** reconstruction suffers from a high rate of muon candidates from hadron showers, which are not fully absorbed in the calorimeters. This

results in worse momentum resolution and low reconstruction efficiency of the **global-muon** tracks. To overcome such degeneracy of muon identification, **Tracker Muons, TM**, consisting only of silicon tracks with $p_T > 0.5$ GeV, a sum of which has the momentum $p > 2.5$ GeV, and matched to at least one muon segment in the DT or CSC stations, are used as muons candidates at low values of the muon p_T . For example, quarkonia and B-physics analyses in the CMS [155] perform searches using the **TM**.

For the region of $p_T > 30$ GeV, where muons from decays of W and Z bosons are dominant, two muon identification schemes, **Soft Muon** and **Tight Muon**, are applied.

The **Soft Muon** is required to be a **Tracker Muon**, which has pulls of local x and y coordinates for the matched muon segment in the first station and the silicon track less than 3.

Tight Muon identification is based on selection criteria aimed to improve the reconstruction efficiency of muons from semileptonic decays of hadrons or decays of W and Z bosons. This scheme suppress reconstruction of muons originated from parton showers. The following conditions to select **Tight Muons** are used:

- A reconstructed muon must be identified as a **GM**.
- The number of valid tracker hits associated to the muon must exceed 10. This ensures a good estimation of the muon transverse momentum.
- The χ^2 , normalized to the number of degrees of freedom, of the global muon fit must be smaller than 10.
- The transverse impact parameter of the muon should be less than 2 mm. This is essential to reject reconstructed cosmic muons.
- The number of pixel hits must be at least one, suppressing contributions from hadron showers.
- In addition, the tracker track is required to be matched to muon segments in at least two muon stations.
- A reconstructed muon is marked as isolated, if the isolation variable,

$$I_{iso} = \frac{\sum_i^{tracks} p_T(i) + E_T^{ECAL} + E_T^{HCAL}}{p_T(\mu)},$$

satisfies $I_{iso} < 0.10$. Here $p_T(i)$, E_T^{ECAL} and E_T^{HCAL} are transverse momenta of the i^{th} silicon track, and total ECAL and HCAL energies of the superclusters within a cone of $\Delta R = 0.3$ around the direction of the reconstructed muon.

4.5.6 Jet reconstruction

The analysis of the physics processes investigated in this thesis is based on identification of jets. Jets are collimated bundles of particles, that originate from the outgoing partons (plus initial

and final-state radiation) of the hard interaction and from the breakup of the proton and antiproton (beam-beam remnants). These bundles are built, using different algorithms, from the calorimeter towers and tracks as shown in Figure 4.17 (left). Energy and direction of the jet is determined by particles as shown in Figure 4.17 (right). Everything except outgoing hard scattered jets is called the underlying event, and it consists of the beam-beam remnants plus initial and final-state radiation.

The jet energy and direction are used to suggest the kinematics of the original parton. Such association of measured energy in clusters with scattered partons is a complex problem, because of the multitude of physics and detector effects that needed to be accounted for. These are

- initial and final-state radiation;
- interaction of beam-beam remnants, left after hard-interacting partons are knocked out of the initial two beam hadrons;
- uncertainties in jet-fragmentation models;
- out-of-cone showering;
- loss of low-momentum charged particles due to the magnetic field;
- pile-up and noise contributions;
- energy loss due to cracks in the detector;
- interactions with tracker material;
- leakage in the calorimeter.

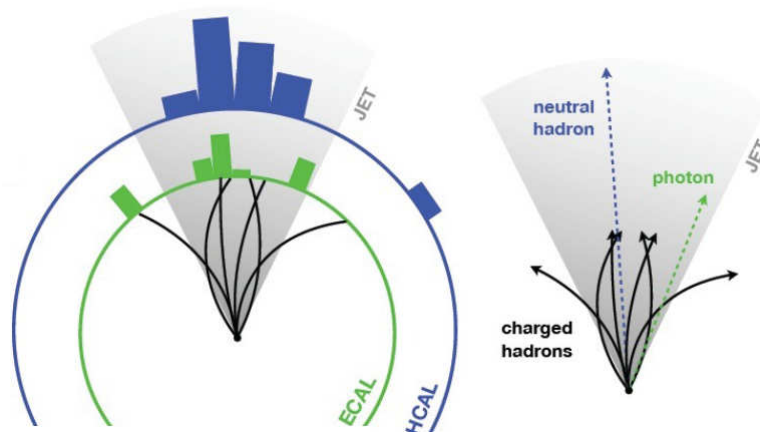


Figure 4.17: Jet reconstruction in the **CMS**. On the left side, tracks (black), ECAL (green) and HCAL (blue) energy deposits are used to cluster jets. Constituents of jets like neutral and charged hadrons, photons are shown on the right side.

First, we will discuss the reconstruction of jets, using only energy deposits in calorimeter towers, the so-called **CaloJets**. Then the reconstruction of jets based on the Particle Flow technique, the **PFJets**, is introduced.

4.5.6.1 Jet clustering

There are two broad classes of jet algorithms: cone algorithms and sequential recombination algorithms, which are described in the following:

- **Cone algorithms** collect together particles within a specific cone defined by the rapidity and azimuth spans, $(\Delta y, \Delta \phi)$. Jets are clustered by finding directions that maximize the amount of hadronic energy flowing through a cone of fixed radius $R = \sqrt{\Delta y^2 + \Delta \phi^2}$, drawn around them. They are physically close to the direction and energy of the original partons.
- **Sequential recombination (cluster-based) algorithms** consider the pair of particles that are closest in distance, combine them, and then repeat the procedure over and over again, until some stopping criterion is reached. The various sequential recombination algorithms differ mainly in their particular choices of distance definition and stopping criterion.

In the **CMS** two cone-based methods, Iterative Cone, **IC**, [156, 157] and the Seedless Infrared-Safe Cone, **SIS Cone**, [158], and two cluster-based methods, Inclusive k_T [141, 157] and Anti- k_T [141] algorithms, are included in the standard sequence of the jet reconstruction [159].

The IC algorithm starts by ordering the input objects according to decreasing E_T . The first object in the list is taken as a jet seed which defines an initial direction of the jet. By collecting towers in a cone with the radius R around the jet direction, a so-called proto-jet is constructed. The proto-jet is used as a new seed, and one iterates the procedure until the direction of the resulting cone stabilizes. At that point the proto-jet is added to the list of jets, and its objects are deleted from the list of input towers. The jet cone size R and the minimal threshold on the seed's E_T are parameters of the algorithm. The **IC** uses the cone sizes of $R = 0.5$ and $R = 0.7$. The E_T threshold is 1 GeV. The jet transverse energy, E_T , pseudo-rapidity, η , and azimuth, ϕ , are calculated from its constituents as

$$\begin{aligned}
 E_T &= \sum_{i \in \text{cone}} E_{T_i}, \\
 \eta &= \frac{1}{E_T} \sum_{i \in \text{cone}} \eta_i E_{T_i}, \\
 \phi &= \frac{1}{E_T} \sum_{i \in \text{cone}} \phi_i E_{T_i}.
 \end{aligned} \tag{4.10}$$

The IC method is collinear unsafe. If the hardest particle undergoes a collinear gluon emission, jets clustered by the IC algorithm will be changed [157]. This leads to the fact that jets reconstructed before hadronization do not correspond to jets reconstructed after hadronization

in simulated events. To avoid problems with collinear and infra-red safety in jets, a modified version of the **IC**, the SIScone algorithm, is applied [158].

The k_T and Anti- k_T algorithms utilize a quantity d_{ij} as measure of the distance between the calorimeter towers i and j ,

$$\begin{aligned} d_{ij} &= \min(E_{T_i}^{2p}, E_{T_j}^{2p}) \frac{\Delta_{ij}}{R^2}, \\ d_{iB} &= E_{T_i}^{2p}, \\ \Delta_{ij}^2 &= (y_i - y_j)^2 + (\phi_i - \phi_j)^2, \end{aligned} \tag{4.11}$$

where E_{T_i} , y_i , ϕ_i are, respectively, the transverse energy, rapidity and azimuth of the tower i . Here R is a dimensionless parameter which is either 0.5 or 0.7 in the CMS reconstruction scheme. The power p is 1 for the k_T algorithm and -1 for the Anti- k_T algorithm.

The algorithms form clusters by identifying the smallest measure of the distance, either d_{ij} or d_{iB} , for the object i . If it is the d_{ij} , the two entities i and j are combined, while if it is the d_{iB} the i^{th} object is called a jet and removed from the list of entities. Two different options are available in the procedure of the combining. Either four-vectors are added, which results in a massive jet, or the E_T of the constituents are summed to produce a massless jet. The first option is called “E” scheme, another one is “ E_T ” scheme. When no input towers are available to build jets, a new iteration merges all jets i and j with distances $\Delta_{ij} < R$. The merging is repeated until $\Delta_{ij} > R$ for all jets left. R can be interpreted as the jet cone size.

Both algorithms are free of any infra-red and collinear issues. The Anti- k_T algorithm grows up jets outwards around hard towers resulting in geometrically circular jets.

4.5.6.2 Efficiency of CaloJet reconstruction

The high-efficient reconstruction of jets is important in the search of the neutral Higgs bosons decaying in b jets. There are three reasons which degrade the efficiency of **CaloJet** reconstruction:

- pile-up interactions, which contribute with sizable amounts of energy in the calorimeter cells;
- electronic noise;
- low- p_T charged particles, escaping the calorimeter due to the strong CMS magnetic field.

There is a data-driven method, introduced in Refs. [160, 161], which allows to estimate the jet efficiency both in data and Monte Carlo events. The method is based on the reconstruction of jets from tracks of charged particles only, **TrackJets**. **TrackJets** are used for jet counting and estimation of jet kinematics, because the tracking momentum measurements are more accurate than the calorimeter ones for charged hadrons up to several hundreds of GeV

First, the performance of **TrackJets** reconstruction has been studied in Monte Carlo simulations [162]. The Anti- k_T algorithm was applied to stable particles after hadronization step,

producing **GenJets**. Reconstructed tracks from the simulation of the CMS detector were used to cluster the **TrackJets**. Then a matching between **GenJets** and **TrackJets** was performed. The efficiency of the matching is almost 100% for jets with $p_T > 15$ GeV [162].

Afterwards, the **CaloJet** reconstruction efficiency was evaluated using the tag-and-probe approach in the back-to-back di-jets data of $100 \mu\text{b}^{-1}$ luminosity selected by the CMS minimum bias trigger at $\sqrt{s} = 7$ TeV in 2010. First, in each di-jet event one jet was reconstructed using only tracks, **TrackJet**, and called the tag jet. The another jet was reconstructed using the calorimeter towers and called the probe jet. The energy of the tag jet was corrected to the **GenJet** energy. The jet reconstruction efficiency of **CaloJets**, defined as the ratio between the numbers of the probes and tags [162], is shown in Figure 4.18 for the Anti- k_T algorithm with $R = 0.5$.

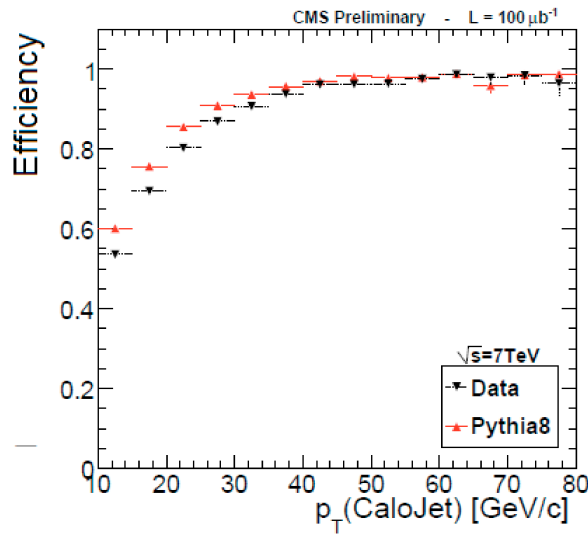


Figure 4.18: Reconstruction efficiency of **CaloJets** in simulations and data as a function of the jet p_T [162].

The high p_T **CaloJets** demonstrate reconstruction with efficiency of 100% both in Monte Carlo simulations and data. The low reconstruction efficiency observed at low transverse momenta can be understood as mis-measurement of the **CaloJet** direction since low p_T charged particles are deflected in the 4 T magnetic field and do not reach the calorimeter.

4.5.6.3 Jet energy correction

The calorimeter response to particles is not linear as a function of the energy and therefore the energy of the reconstructed jet is not simply proportional to the energy of the parton. Corrections to the raw jet energy measurement have to be applied. This is done by the proper mapping of measured jet energy to the energy of either the parton or particle. However, several effects complicate the translation of the measured jet energy, at a given jet definition, into the corresponding parton energy. A first class of effects relates to physics of jets in hadron

collisions. Initial and final-state radiation blurs the connection between the parton and the jet. Hence, on average, the energy correction should compensate for the energy loss due to the radiation. At the same time pile-up collisions give additional external energy deposits to the jet energy measurement. A second class of effects stems from detector imperfectness. Low-momentum charged particles are swept out of jet cones due to the magnetic field. Electronic noise generates additional contributions to jet energy. Also the energy loss due to dead material, cracks, interactions with material in front of the calorimeters and leakage in the calorimeters render the correction of jet energy to be a highly non-trivial task.

The CMS jet energy correction is a factorized multi-level jet correction [163], where each sub-correction is associated with a different class of the physics and detector effects described above. The main three steps of correction in the CMS are depicted in Figure 4.19.

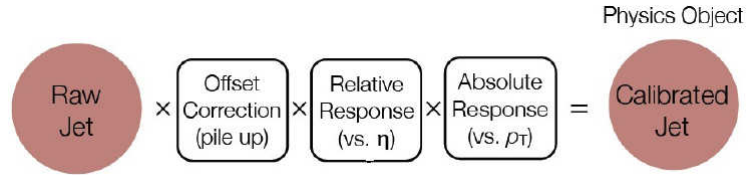


Figure 4.19: Steps of correction applied to the raw jet energy.

The correction is applied as a multiplicative factor \mathcal{E} to each component of the raw jet four-momentum vector p_μ^{raw} ,

$$p_\mu^{cor} = \mathcal{E} p_\mu^{raw}. \quad (4.12)$$

The factor \mathcal{E} is a product of three quantities, corresponding to the sub-corrections illustrated by Figure 4.19, and it is expressed as

$$\mathcal{E} = C_{offset}(p_T^{raw}) \cdot C_{rel}(\eta) \cdot C_{abs}(p_T'), \quad (4.13)$$

where the scale factor C_{offset} is the correction removing extra energy due to noise and pile-up, the correction C_{rel} makes the jet response uniform in η and the correction C_{abs} provides the linearity in p_T of the calorimeter response. Here p_T' is the transverse momentum of the jet after applying the offset correction C_{offset} ,

$$p_\mu' = C_{offset} p_\mu^{raw}.$$

It is worth to mention that the steps of the correction should be applied sequentially, as shown in Figure 4.19 and equation (4.13), where the output of each step is the input to the next.

The correction C_{offset} is expected to be relatively small, i.e. on average the difference between p_T' and p_T^{raw} is smaller than 2 GeV. There are a few approaches for the treatment of this type of the correction [163]. One of them is based on the measurement of the jet area A [164]. The jet

area provides a measure of the surface in the (y, ϕ) plane over which a jet extends. The method calculates p_T -density of jets, ρ , per unit of the jet area A in an event. The p_T -density ρ is defined as the median of the distribution of $p_{T,j}/A_j$,

$$\rho = \text{median}\left[\frac{p_{T,j}}{A_j}\right],$$

where j runs over all jets in the event. First, the average contribution from electronic noise, $\langle \rho_{noise} \rangle$, to ρ is estimated using Monte Carlo simulations with exactly one reconstructed primary vertex. Next, based on the knowledge of the jet areas A_j and ρ in the event, the correction factor C_{offset} to the j^{th} jet is determined [163] as

$$C_{offset}(p_{T,j}^{raw}, A_j, \rho) = 1 - \frac{(\rho - \langle \rho_{noise} \rangle) A_j}{p_{T,j}^{raw}}. \quad (4.14)$$

The quantity $\langle \rho_{noise} \rangle$ is estimated to be 1.08 [163].

Currently several methods for corrections applied at the second and third steps are available in the **CMS**. One method is based on Monte Carlo simulations, in which one traces the reconstructed jet energy E_T^{raw} back to the energy, E_T^{gen} , of the initial parton. Two other methods exploit data-driven approaches based on the p_T -balancing in events [163]. A good agreement between results of MC and data-driven methods is observed [163].

As an example, the approach, using Monte Carlo simulations, is discussed. The method reconstructs jets after a realistic detector simulations of QCD events. The Anti- k_T algorithm was applied to simulated stable particles after the hadronization, producing the **GenJets**, and calorimeter towers, resulting in the **CaloJets**. The matching between **CaloJets** and **GenJets** is done in the (η, ϕ) space, requiring $\Delta R = \sqrt{(\Delta\eta)^2 + (\Delta\phi)^2} < 0.25$. The ratio, $\mathcal{R} = p_T^{raw}/p_T^{gen}$, between the transverse momenta of the **CaloJet**, p_T^{raw} , and the **GenJet**, p_T^{gen} , is calculated and added to histograms in several bins of p_T^{raw} and η . The average effect of the relative, $C_{rel}(\eta)$, and absolute, $C_{abs}(p_T')$ corrections in each (p_T^{raw}, η^{raw}) bin is defined as the inverse of the average of \mathcal{R} ,

$$C_{rel}(\eta) \cdot C_{abs}(p_T^{raw}) = C_{MC}(\eta, p_T^{raw}) = \frac{1}{\langle \mathcal{R} \rangle}. \quad (4.15)$$

Figure 4.20(a) shows the jet energy correction factors C_{MC} for the **CaloJets**, **TrackJets** and jets reconstructed using the Particle-Flow algorithm, **PFJets**, as functions of η . A large correction factor C_{MC} for the **CaloJets**, as it is illustrated in Figure 4.20 (b), is due to the non-linear response of the CMS calorimeter. The structures observed at $|\eta| \sim 1.3$ are because of the barrel-endcap boundary and tracker material budget, which is maximal in this region.

In the **TrackJets** and **PFJets** the charged components of the hadron showers are accurately measured by the **CMS** tracker up to $|\eta| = 2.4$. This fact explains much smaller correction factor C_{MC} for these types of jets. The fast rise of the correction factor for the **TrackJets** in the region $2.0 \leq |\eta| \leq 2.5$ is explained by the fact that tracks are not fully reconstructed in the tracker.

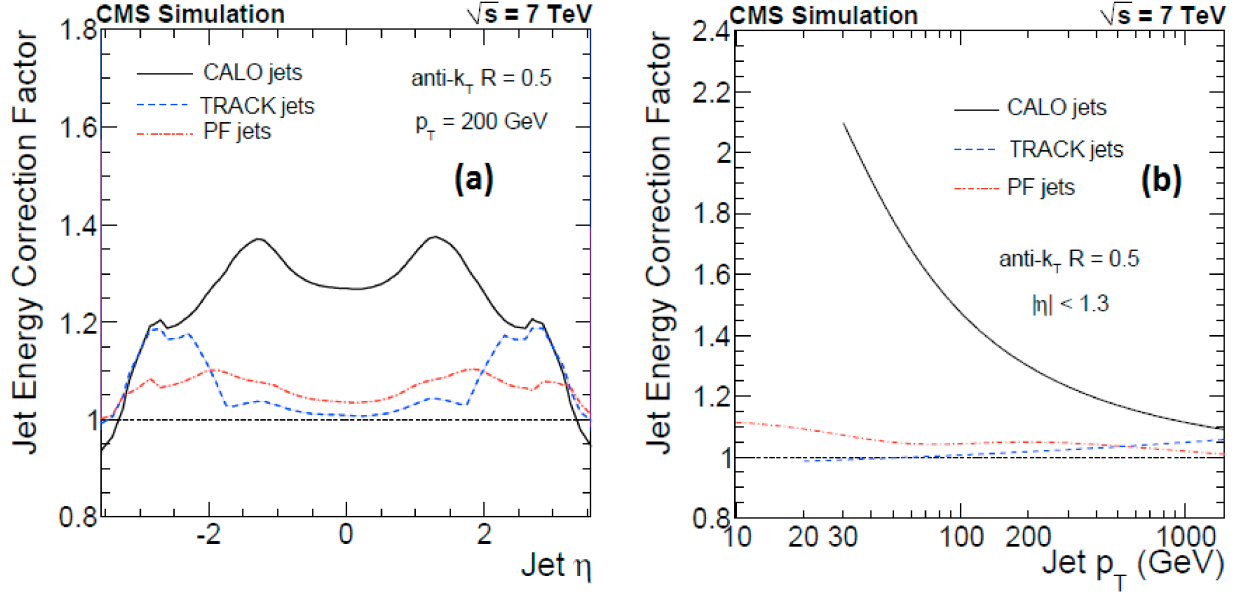


Figure 4.20: The MC jet-energy-correction factor for **CaloJets**, **TrackJets** and **PFJets** of $p_T = 200$ GeV as function of η (a). The MC jet-energy-correction factor for the different jet types, as a function of jet p_T (b) [163].

4.5.6.4 Jet energy resolution

To estimate the jet energy resolution, **JER**, in several bins of E_T^{gen} and η^{gen} , the distribution of the ratio E_T^{raw}/E_T^{gen} between the transverse energies for the matched **CaloJet** and **GenJet**, is obtained and fitted in each bin by a Gaussian. The matching requires between **CaloJet** and **GenJet** the distance $\Delta R < 0.25$. The jet transverse energy of the **CaloJets**, E_T^{raw} , are corrected for using the factor (4.15). The widths of the Gaussians are stored in a histogram built on the E_T^{gen} bins. The jet energy resolution is obtained from a fit of this histogram to the functional form [165]

$$\sigma\left(\frac{E_T^{raw}}{E_T^{gen}}\right) = \sqrt{\frac{N^2}{E_T^{gen,2}} + S^2 \frac{1}{E_T^{gen}} + C^2}, \quad (4.16)$$

where the first term describes energy fluctuations in the jet, originating from electronic noise and pile-up interactions, the second term corresponds to the stochastic nature of the calorimeter measurements, and the last term is the constant term from residual non-uniformity in the detector response.

The results of the fit, using formula (4.16), in the barrel, endcap and forward regions of the CMS calorimeter are shown in Figure 4.21 for jets reconstructed by the **IC** algorithm with $R = 0.5$ in QCD di-jet Monte-Carlo samples [165].

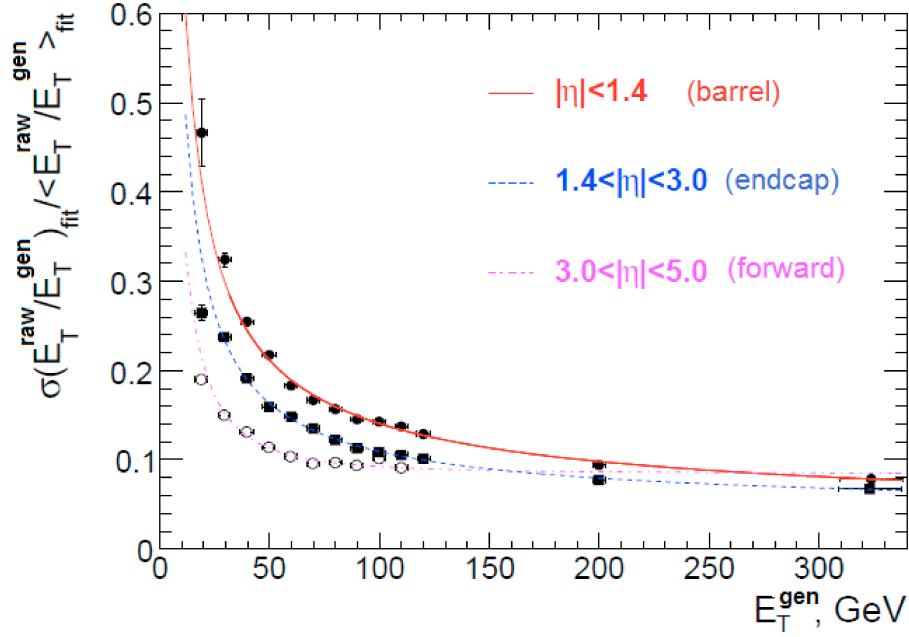


Figure 4.21: Jet resolution functions for the iterative cone algorithm with cone size $R = 0.5$ in the barrel, endcap and forward regions [165].

The obtained jet energy resolution in the barrel region reads $N = 5.6 \text{ GeV}$, $S = 1.25 \text{ GeV}^{1/2}$ and $C = 0.033$.

The jet energy resolution (4.16), which is derived from Monte Carlo simulations, can be used as a benchmark only. One expect a different resolution in collision data, due to instrumental effects which are hardly ever parametrized in Monte Carlo. The di-jet asymmetry method [166] is used to estimate the jet energy resolution from data. This method exploits the momentum conservation in the transverse plane of the di-jet system. Using the method both in Monte Carlo simulation of QCD di-jet events and data of 36 pb^{-1} luminosity recorded by CMS at $\sqrt{s} = 7 \text{ TeV}$ in 2010, the ratio $\mathbf{JER}^{\text{data}}/\mathbf{JER}^{\text{MC}}$ for Anti- k_T jets with $R = 0.5$ is measured as a function of the jet η . Table 4.1 summarizes the results.

Table 4.1: Ratios, between the jet energy resolutions in data and simulations, measured, using the asymmetry method [166], for different jet η ranges.

$\mathbf{JER}^{\text{data}}/\mathbf{JER}^{\text{MC}}$	$ \eta $ bin
1.079 ± 0.006	0.0 - 1.1
1.054 ± 0.013	1.1 - 1.7
1.061 ± 0.020	1.7 - 2.3
1.174 ± 0.027	2.3 - 5.0

Here the error quoted is the statistical uncertainty. The close agreement between the jet energy resolutions, measured in data and Monte Carlo simulations, is observed for all regions of the CMS detector. The ratio $\text{JER}^{\text{data}}/\text{JER}^{\text{MC}}$ is used to correct the energy resolution of jets reconstructed in MC simulations as discussed in subsection 5.9.1.

4.5.7 Particle Flow jets

The Particle-Flow, **PF**, algorithm provides an event reconstruction on the level of individually reconstructed particles. It optimally combines the information coming from all CMS subdetectors. The particles reconstructed by the PF algorithm are muons, electrons, photons, either unconverted or converted, charged and neutral hadrons. The complete list of PF particles is used to cluster jets using the jet algorithms.

The PF jet reconstruction starts with building sub-detector specific objects: calorimeter clusters and tracks from the tracker and the muon stations. All these objects are delivered with a high efficiency and a low fake rate. High efficiency of PF identification is provided above a few GeV for p_T of particles.

There are four main steps of the Particle Flow algorithm [167, 168]:

- track reconstruction;
- calorimeter clustering;
- linking tracks with calorimeter cluster;
- particle identification.

The momenta of charged hadrons, electrons and muons are measured in the tracker with the precision much better than calorimeter-based measurements. The track reconstruction is the cornerstone of the PF algorithm because about two thirds of the energy of a jet is on average carried by charged particles. An iterative-tracking strategy described in subsection 4.5.1 allows to reconstruct 99% of isolated tracks and up to 90% of non-isolated tracks, for instance, tracks of charged hadrons in b jets.

An example of the track reconstruction and association with the calorimeter clusters in the (x,y) view is shown in Figure 4.22 (a). The “Hybrid” algorithm, described in subsection 4.5.3, of the supercluster reconstruction is adopted for the **PF** with the aim of a high detection efficiency even for low-energy particles [167, 168]. The reconstructed superclusters are translated to **PF** clusters with an iterative determination of the cluster energies and positions. The reconstruction of PF superclusters in the **ECAL** and the **HCAL** is illustrated in Figures 4.22 (b) and 4.22 (c), respectively. For a given particle the **PF** creates several elements - a track and calorimeter clusters. It iteratively calculates distances between two different PF elements and combines them, if the distance is small enough. In such way, the PF algorithm links the elements, corresponding to one particle, into one composite PF object. The example of such connection between the PF track and supercluster is shown as a green line in Figures 4.22 (a), (b) and (c).

To perform the track-supercluster linking, first the track is extrapolated from its last measured hit in the tracker to the **ECAL** to a depth of a typical longitudinal electron shower profile. Then the track is prolonged to the **HCAL** to a depth of a typical hadron shower. The track is linked to any given cluster, if the distance, in the (η, ϕ) plane, to the cluster is smaller than the cluster size.

The particle identification is finally performed on the list of linked PF composite objects. The PF muon is obtained from the **Global Muon**, reconstructed as described in subsection 4.5.5, if the **GM** momentum is compatible with that determined from tracker hits only within three standard deviations. The electron reconstructed by the GSF algorithm, discussed in subsection 4.5.4, is recognized as the PF electron. The tracks and calorimeter clusters of the PF muon and PF electron are removed from the list of the linked objects.

The remaining PF tracks linked to the ECAL and HCAL clusters must have satisfied several quality criteria summarized in Ref [168]. An iterative reassignment [168] of PF tracks and ECAL clusters is run to properly accumulate the energy from hadronic showers. Afterwards, remaining linked pairs are assigned to Particle-Flow charged hadrons. The standalone ECAL and HCAL clusters, not linked to any track, create Particle-Flow photons and neutral hadrons.

The Monte-Carlo based approach described in Ref. [168] is used to calibrate the energy, E^{rec} , of the PF superclusters. To estimate the resolution of E^{rec} , the width of a Gaussian fitted to the distribution of $(E^{rec} - E^{gen})$ in each bin of E^{gen} is estimated. Here E^{gen} is the energy of a particle, which is simulated in the supercluster. Figure 4.23 demonstrates the energy resolution of the PF supercluster as a ratio of the width over E^{rec} .

If one compares the energy resolution of the **HCAL** cells with the energy resolution of the PF clusters, shown in Figures 4.6 (b) and 4.23, respectively, one notices that the stochastic term, $\frac{S}{\sqrt{E}}$, is reduced from $S = 115\%$ to $S = 104\%$.

The PF algorithm reconstructs jets from all PF composite objects without distinction of particle type and without any energy threshold. To estimate the reconstruction efficiency of the **PFJets**, they are matched to the **GenJets** in Monte Carlo simulations. The matching requires the distance between jets in the (η, ϕ) plane to be less than 0.1. Also the **CaloJets** are clustered, using calorimeter towers, and matched to the **GenJets**. Figure 4.24 shows the comparison of the reconstruction efficiencies and fake rates [168] for the **PFJets** and **CaloJets**.

Jets are reconstructed in QCD-multijet events [168], using the IC algorithm with $R=0.5$. In the PF approach the efficiency of the jet reconstruction is increased by 50% in comparison with the **CaloJets** for jet $p_T < 40$ GeV. From Figure 4.24 (a) the **CaloJets** are efficiently reconstructed starting from $p_T > 80$ GeV, Both the efficiency and fake rate, shown in Figures 4.24 (a) and (b), respectively, favour the PF approach.

The commissioning of the PF jet reconstruction has been done in di-jet back-to-back events of the data sample corresponding to an integrated luminosity of 6.2 nb^{-1} luminosity recorded by the **CMS** detector at $\sqrt{s} = 7$ TeV during the first half of 2010 [169]. The Anti- k_T algorithm with $R=0.5$ was used to cluster PF jets with $p_T > 25$ GeV. The distributions of **PF** jets kinematics, such as the transverse momentum and the azimuth angular, obtained in data and Monte Carlo are presented in Figure 4.25.

The results show a good agreement between data and simulation for the reconstructed **PF** jets.

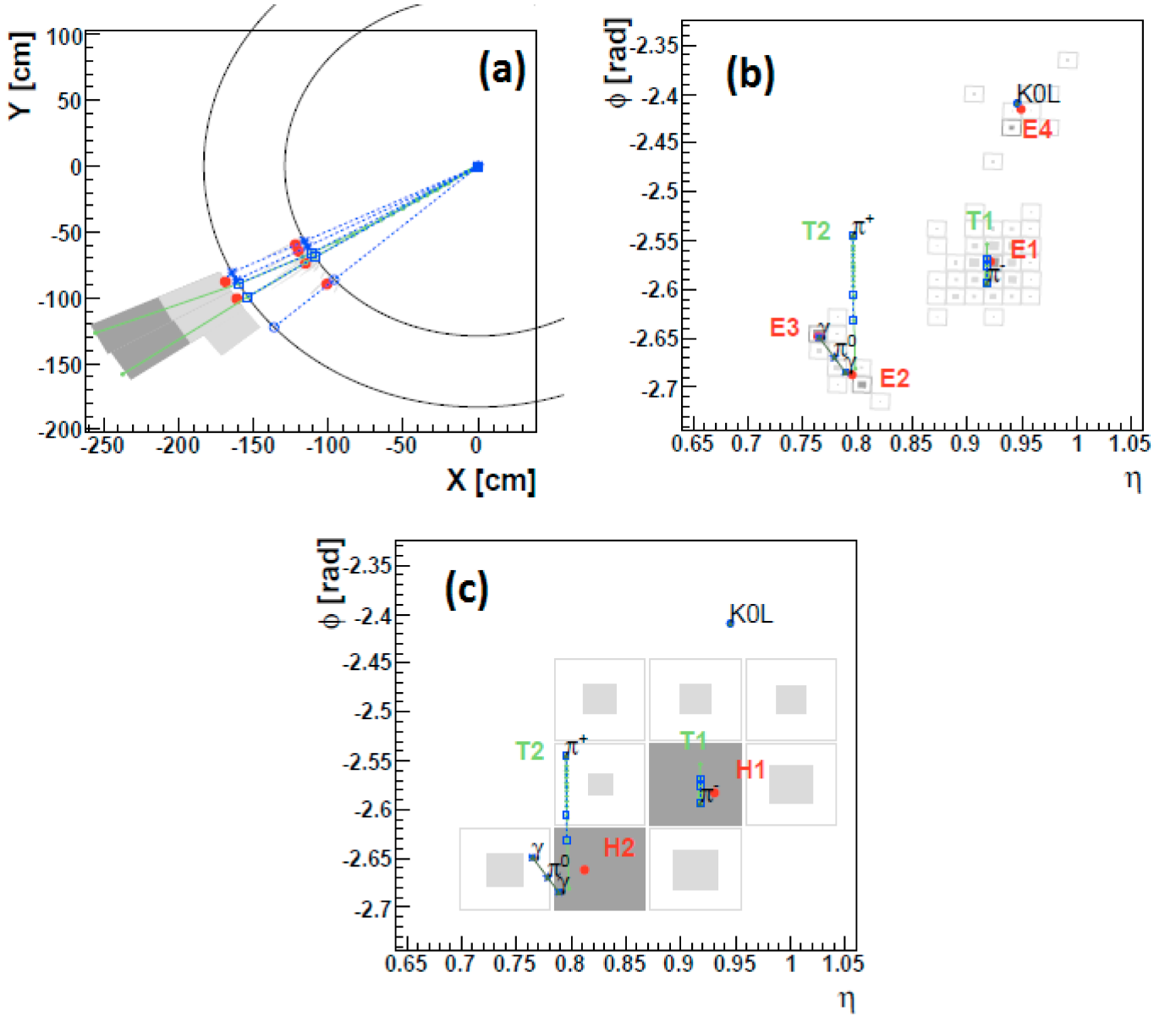


Figure 4.22: An event display of a simple hadronic jet containing four particles (π^+ , π^- , π^0 , K_L^0) in the (x, y) view (a) and in the (η, ϕ) view of the ECAL (b) and the HCAL detectors (c). The tracks of charged pions, T1 and T2, as well as energy deposits in the **ECAL**, E1 from π^- , and E2, E3 from $\pi^0 \rightarrow \gamma\gamma$, and the energy in **HCAL**, H1 and H2, are reconstructed by the PF algorithm. The link between the tracks and the clusters are shown as green vertical lines obtained from the track extrapolation to the calorimeter surface [168].

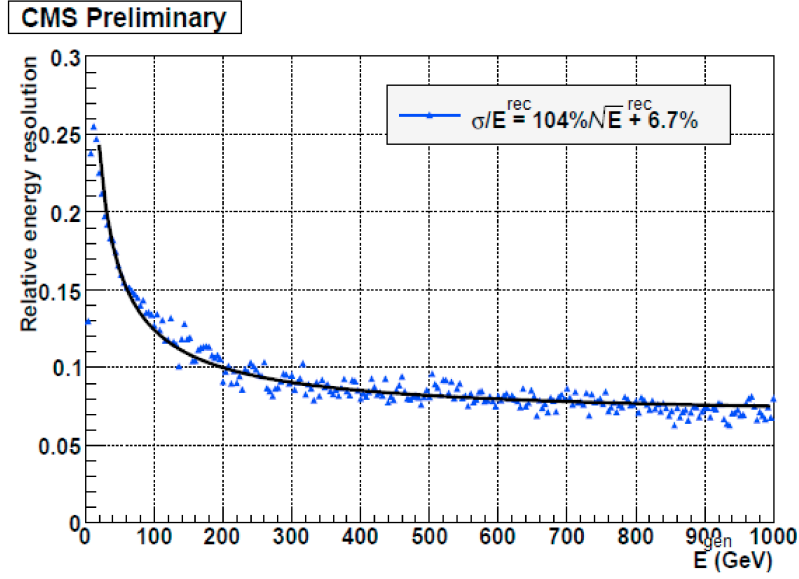


Figure 4.23: Energy resolution $\sigma(E^{\text{rec}} - E^{\text{gen}})/E^{\text{rec}}$ of a PF cluster as a function of the particle energy E^{gen} simulated in the Particle-Flow superclusters in the barrel **ECAL** [168].

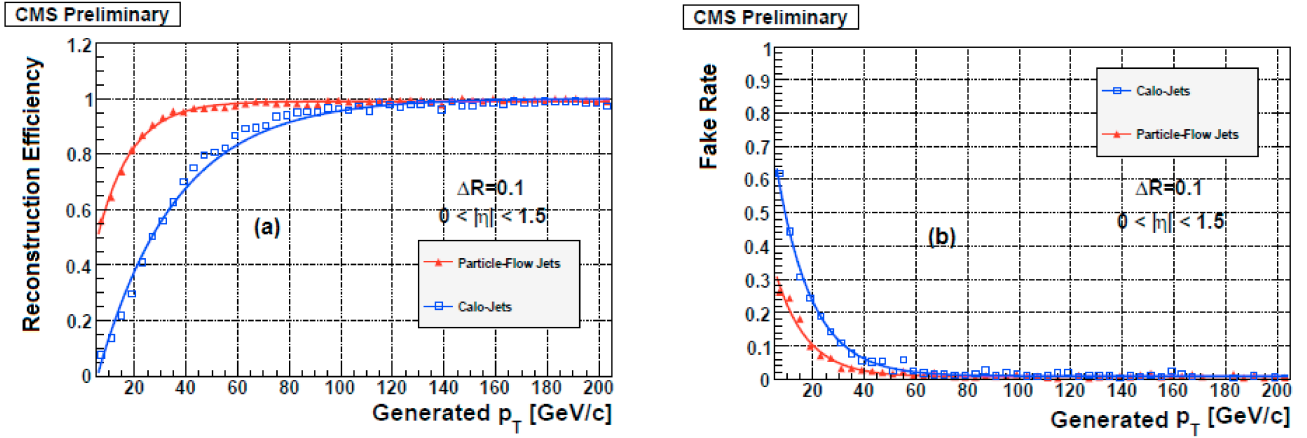


Figure 4.24: Jet reconstruction efficiency (a) and mismatching jet rate (b) for **PFJets** (red) and **Calo-Jets** (blue) as a function of the **GenJet** p_T . The barrel region of the **CMS** is considered [168].

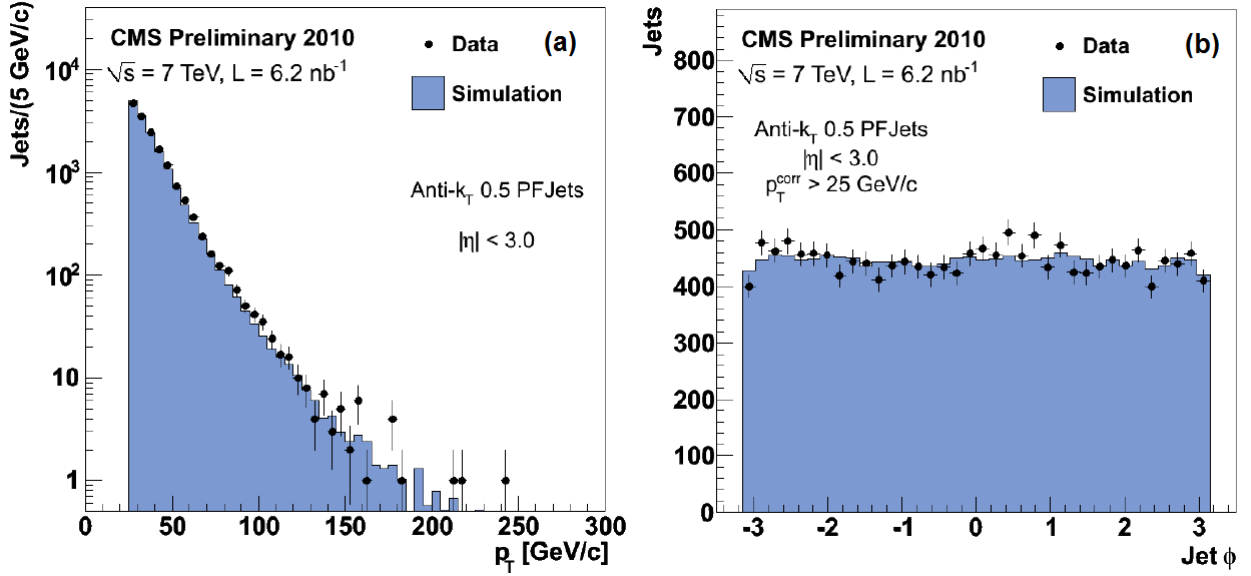


Figure 4.25: Basic **PF** jet properties in di-jet back-to-back events in the Monte Carlo simulations (blue) and data (black). The distributions of the **PF** jet transverse momentum (a) and azimuth (b) are depicted [169].

4.5.7.1 Jets in this analysis

The PF jets are reconstructed by means of the Anti- k_T algorithm with a cone radius parameter $R = 0.5$. To mitigate the effect of pile-up interactions, a track based algorithm, called “PFnoPU” [170] from the package PF2PAT [171] is used. The algorithm removes from PF jets about 80% of charged hadrons that do not originate from the primary vertex. For remaining 20% of pile-up charged hadrons the correction C_{offset} (4.13) rescales the energy of calorimeter deposits [163]. In addition, we apply the standard relative $C_{rel}(\eta)$ and absolute $C_{abs}(p_T^{raw})$ corrections (4.15) to the jet energy. Afterwards, jets are preselected by requiring $|\eta| < 2.2$ and $p_T \geq 20$ GeV.

4.5.8 Identification of b jets

Heavy flavor jets originates from c or b quarks. Their characteristics allow to discriminate between these jets and jets originating from light quarks and gluons. These characteristics are:

- the production of heavy long-lived hadrons, e.g. B-mesons with a lifetime $\tau \simeq 1.5$ ps and a flight distance of $c\tau \simeq 450 \mu\text{m}$. This results in displaced secondary vertices [172] and tracks⁶ not compatible with the primary vertex. These tracks have sizable impact parameters, **IP**, with respect to the primary vertex.
- About 19% of heavy-flavor jets contains a lepton from weak decays in the fragmentation. Since the b quark is relatively massive, its decay products, including the lepton, have a larger transverse momentum with respect to the jet axis.

The simplest b-tagging algorithms can use just the track **IP** as a single observable to discriminate b jets against non-b jets. More complex methods, like the Combined Secondary Vertex, **CSV**, algorithm [173], combine several of the b hadron characteristics to achieve a higher discrimination power. Each of these algorithms yields a single discriminator value for each jet. The jets are tagged, if their discriminator values are larger than the thresholds defined as the loose (**L**), medium (**M**) and tight (**T**) working points, **WP**. The loose, medium and tight working points are adjusted [174] to misidentification probabilities of 10%, 1% and 0.1%, respectively, for light-flavor jets with an average p_T of about 80 GeV.

The current analysis exploits two different b-taggers:

- the **TCHE (IP-based)** algorithm, based on the track transverse and longitudinal **IP**, given by equations (4.6) and (4.7), and used to perform b-jet identification at the Level-2.5 and Level-3 of the triggers, as discussed in Section 5.2
- the Combined Secondary Vertex, **CSV**, algorithm which is used to tag jets during the offline event reconstruction.

4.5.8.1 The IP-based algorithm

The IP-based algorithm calculates the distance between the primary interaction vertex and the track at the point of its closest approach

$$d = \sqrt{d_{xy}^2 + d_z^2}, \quad (4.17)$$

where d_{xy} and d_z are the transverse and longitudinal impact parameters defined in formulae (4.6) and (4.7) respectively. The d is positive (negative) if the angle between the perpendicular to the track at the point of closest approach to the **PV** and the direction of the jet is less (larger) than 90° . Figure 4.26 illustrates the definition of the impact parameter d .

A jet is identified as originated from the b quark, if there are at least N tracks with a significance of the impact parameter above a given threshold. The tracks are ordered in decreasing impact parameter significance, d/σ_d , where σ_d is the uncertainty of the impact parameter d (4.17). Using the significance of impact parameter of the second track as a discriminator of the algorithm, b jets are identified at the trigger with high efficiency. To select b jets of high purity, the third track is the better choice. Figure 4.27 shows the distribution of the impact parameter significance for all tracks in jets selected in data and MC simulations [174].

Good agreement for distributions of the impact parameter significance in data and Monte Carlo is observed with the exception of a small difference in the region around zero. As it is expected, the probability to have tracks with large positive values of the impact parameter significance is higher for b jets and lower for light-flavor jets.

⁶An example is the B-meson decay via a charmed hadron, $\overline{B}_s \rightarrow D_s^+ l^- \nu_l \rightarrow \pi^+ K^+ K^- l^- \nu_l$ leading to four tracks.

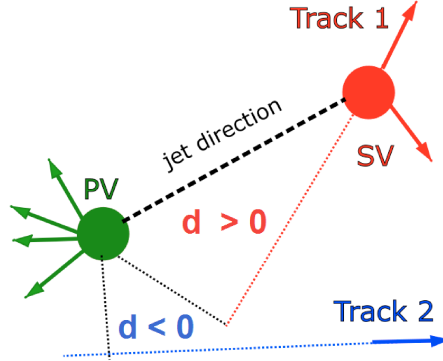


Figure 4.26: The impact parameters of tracks in jets. PV denotes the primary vertex, and SV represents the secondary interaction vertex.

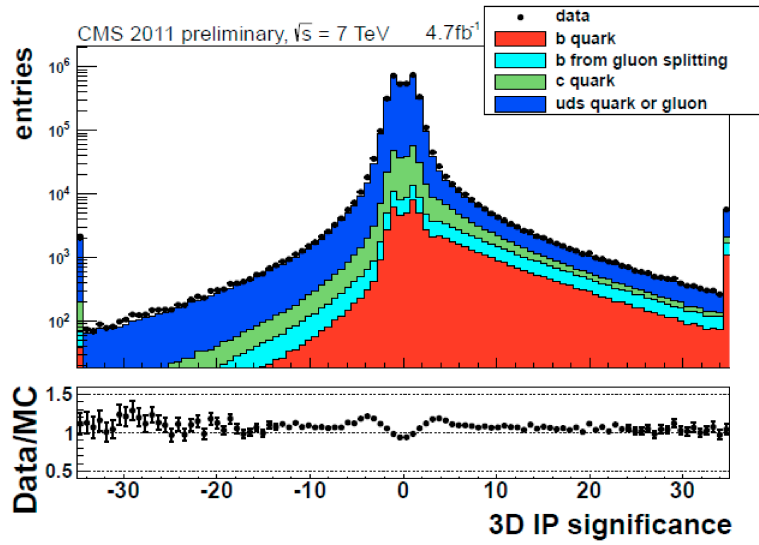


Figure 4.27: Distributions of the three-dimensional impact parameter significance of tracks, associated with b (red), c (green), light-flavor (blue) jets and jets (cyan) originated by b quarks from the gluon splitting, with $p_T > 1$ GeV, at least eight hits associated to the track and a good fit quality, $\chi^2/\text{ndof} < 5$ [174].

4.5.8.2 The b-tagging algorithms using secondary vertices

The PF jets reconstructed in the analysis are b-tagged also using information from secondary vertices. Due to the high resolution of the CMS tracking system, it is possible to directly reconstruct the **SV**, the space point where the b hadron decays, as depicted in Figure 4.26. The presence of a secondary decay vertex and the kinematic variables associated with it can be used to discriminate between b and non-b jets.

The CSV method involves properties of the secondary vertices, together with track-based lifetime information. The secondary vertices are reconstructed in an inclusive way inside the jets using the Adaptive Vertex Fitter, **AVF**, as discussed in subsection 4.5.2. The secondary vertex reconstruction in the CSV algorithm defines three categories of jets:

- 1) Jets, where at least one secondary vertex is reconstructed.
- 2) Jets, where no secondary vertex is reconstructed. The pseudo vertex is created from tracks having the transverse impact parameter significance greater than two and not compatible with the primary vertex.
- 3) Jets, where neither 1) or 2) are fulfilled.

A set of variables related to the secondary vertex as well as information from track impact parameters are combined into a single tagging variable, the CSV discriminator, to discriminate between b jets and non-b jets. The choice of variables entering into the combination depends on the jet category. The average track impact parameter significance is used in all categories. The invariant mass, multiplicity, energy and average rapidity of tracks associated to the secondary or pseudo vertices are utilized to discriminate jets of the 1) and 2) categories. The distance between the primary vertex and the secondary vertex in the transverse plane divided by its error is additionally used in the category 1). Since the distributions of most of the variables are significantly different for b, c and udsg (light-flavor) jets, these variables are combined into three likelihood functions, respectively. Two ratios of the likelihood function for b jets over the likelihood function for c jets and the likelihood function for b jets over the likelihood function for light-flavor jets are used to discriminate separately b jets against c and udsg jets, respectively [173]. The distribution of the CSV discriminator, defined as a sum of the two ratios, is presented in Figure 4.28 for jets originating from different quark flavors. Values of the discriminator are very close to one for b jets, while for c and light-flavor jets lower values of the CSV discriminator are preferred.

Of all the b-tagging algorithms, the CSV algorithm has the highest b-jet tagging efficiency, when the mistag rate from the light-flavor jets is less than 3%.

4.6 CMS analysis software and Physics simulation

A computing system [175] is needed to operate the CMS experiment, read out all subdetectors, convert raw data in physics objects like tracks and reconstruct scattering events to study the

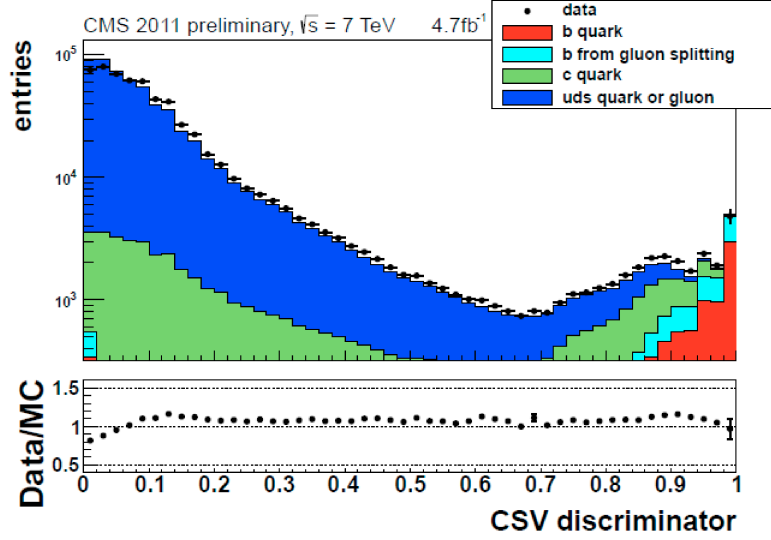


Figure 4.28: The distribution of the CSV discriminator for jets of b (red), c (green), light (blue) and b from gluon splitting (cyan) flavors [174].

underlying physics. Physics analyses require a dedicated software environment with tools to investigate large number of events. The special framework, called **CMSSW**, processes recorded data and reconstructs the physical objects on event basis. In addition, **CMSSW** executes Monte-Carlo simulations performing propagation of particles through the detector and reconstruction.

A significant amount of work on the computing system, including Monte-Carlo production and the development of **CMSSW** plug-in modules as analysis units, has been preceded the physics results of this thesis.

The **CMSSW** framework has been designed to be modular and been made of loosely coupled components with well-defined interfaces. Such stability of the system to process very large event samples is ensured. The software requires a reasonably computing architecture to efficiently reduce large-scale data and reconstruct events by means of fast-readout storage and network elements.

An event in the **CMS** is a single readout of the detector electronics which have been generated by particles. The trigger and **DAQ** systems select, out of the millions of events recorded in the detector, the most interesting 500 events per second. The system stores them for further analysis offline. **CMSSW** uses several event formats [176] with different levels of details and precision. The CMS event starts with **RAW** information recorded from the detector, plus the trigger decision and information on calibration of the detector. The **GEN-SIM-DIGI** extension of the **RAW** format is used to store the output of Monte Carlo simulations. **RECO** objects are obtained by applying specific detector reconstruction algorithms. They include the detector-specific filtering and correction of digitized data, primary and secondary vertex reconstruction, tracking and particle identification. Analysis Object Data, **AOD**, is a compact analysis format designed to allow **RECO** objects to be stored as a sufficiently compact collection in the CMS event. In

such way very large event samples can be processed in many centers. **AOD** data are usable directly in physics analyses. Also **AOD** events contain additional information needed to re-run the fitting of tracks, b-tagging or re-evaluate the energy and/or position of ECAL clusters using analysis-specific corrections.

The production of simulated events are done by Monte Carlo generators and stored as specific samples of events. In the search for the neutral MSSM Higgs bosons, the following Monte Carlo samples are relevant:

- Higgs signal samples generated with the `Pythia6` [177] program, where the Higgs boson masses assumed to be 90, 100, 120, 130, 140, 160, 180, 200, 250, 300 and 350 GeV;
- $t\bar{t}$ background events simulated by the `MadGraph` [178] program,
- QCD background events generated with the `Pythia6` and `Alpgen` [179] programs,

The signal samples are generated with a fixed set of MSSM parameters. In order to make the physics inference at any different point of the MSSM parameters, the proper cross section normalization is applied. `Pythia6` was configured such that only channels involving neutral MSSM Higgs bosons were considered. The cross sections and the corresponding uncertainties are provided by the LHC Higgs Cross Section Group [82, 180]. They are obtained from the `BBH@NNLO` [181] program for the $g b \rightarrow b \Phi$ channel. This Fortran code utilizes calculations of the cross section made in five-flavor scheme [182, 183]. The numerical results of `BBH@NNLO` are rescaled to take into account the corresponding MSSM Yukawa couplings. The `FeynHiggs` [184, 185, 186] code is used to derive the rescaling factors. Such renormalization of the cross section is reliable, since in the considered range of the MSSM parameters the Higgs boson width remains smaller than the Higgs mass resolution. The degeneracy in mass of two neutral MSSM Higgs bosons, A and H (h), is properly taken into account.

`MadGraph` and `Alpgen` generate the proton-proton collision only on the parton level, while `Pythia6` can perform fragmentation and hadronization. The `Alpgen` samples are produced requiring jets with $p_T > 20\text{GeV}$ in different flavor compositions: $2C + n_{\text{jets}}$, $2B + n_{\text{jets}}$, $4C$, $4B$, $4C + 1\text{jet}$, $4B + 1\text{jet}$, where $n_{\text{jets}} = 1, 2, 3$ are the number of light-flavor jets and XB , XC denote the presence at least X jets originated from b and c quarks, respectively, in events. The parton showering and hadronization in the `Alpgen` events are performed by the `Pythia6` program interfaced to `Alpgen`. All Monte Carlo events are simulated with pile-up interactions and the Level-1 and HLT responses.

Table 4.2 shows the list of the signal and background Monte Carlo datasets, including the numbers of available events and cross sections. The MSSM m_h^{max} benchmark scenario [95] with $\tan\beta = 20$ is used to evaluate cross sections of the Higgs boson produced in association with b quarks.

Table 4.2: The list of the generated events. The number of produced events and corresponding cross sections are given.

Name	Number of events	Cross section, pb
Higgs signal, $M_A = 90$ GeV	1.08M	316.8
Higgs signal, $M_A = 100$ GeV	1.08M	226.4
Higgs signal, $M_A = 120$ GeV	1.09M	118.8
Higgs signal, $M_A = 130$ GeV	1.61M	93.4
Higgs signal, $M_A = 140$ GeV	550K	62.9
Higgs signal, $M_A = 160$ GeV	550K	41.6
Higgs signal, $M_A = 180$ GeV	550K	26.7
Higgs signal, $M_A = 200$ GeV	549K	17.5
Higgs signal, $M_A = 250$ GeV	550K	6.71
Higgs signal, $M_A = 300$ GeV	545K	2.74
Higgs signal, $M_A = 350$ GeV	550K	1.12
$t\bar{t}$	3.70M	96.7
QCD $\hat{p} \in [30, 50]$	4.02M	$5.3 \cdot 10^7$
QCD $\hat{p} \in [50, 150]$	2.65M	$7.2 \cdot 10^6$
QCD $\hat{p} \in [150, \infty]$	514K	$4.8 \cdot 10^5$

5 Search for a neutral Higgs boson produced in association with b quarks

In the minimal SUSY extension of the Standard Model, introduced in Chapter 2, five physical Higgs bosons are expected after electroweak symmetry breaking. Three of them are neutral. Two of the neutral bosons h , H , are CP-even bosons and one boson A is CP-odd. At tree level, only two parameters, the mass of the pseudoscalar Higgs boson M_A and the ratio of the VEV of the two Higgs doublets, $\tan\beta = v_2/v_1$, define the Higgs sector. For considerably large values of $\tan\beta$, $\tan\beta \geq 30$, the Higgs couplings to u -type quarks are suppressed relative to the SM, while the couplings to d -type particles are enhanced as shown in equation (2.68). The predominant decay channel of the neutral Higgs bosons at $\tan\beta \geq 30$ [187] is into b-quarks with a branching fraction of about 98%. In addition, the CP-odd boson A degenerates in mass with either h or H within the experimental mass resolution. Therefore, the cross section of the neutral Higgs boson production in association with b quarks is effectively enhanced by the factor of $\sim 2 \cdot \tan^2\beta$.

Recent searches in the $\Phi \rightarrow b\bar{b}$ channel have been performed by CDF [188] and D0 experiments [189] at the Tevatron collider. Both experiments have reported an excess of events with about of 2σ significance with respect to the expectations from the SM background for Higgs boson masses in the range of 100 – 150 GeV.

In this Chapter I present the search for a resonance decaying into b quarks produced in association with at least one more b quark⁷. The analysis is performed using data corresponding to $2.7 - 4.8 \text{ fb}^{-1}$ integrated luminosity of pp collisions with a centre-of-mass energy of 7 TeV collected in 2011. The Chapter is organized as follows: Section 5.1 describes the analysis strategy. The online selection software used to preselect events prior a kinematic selection is discussed in Section 5.2. Sections 5.3 and 5.4 introduce the efficiency of the b-tagging algorithms and an overall b-tagging probability for the event. The offline event selection used in the search for the neutral MSSM Higgs bosons are described in Section 5.5. In Section 5.6 I discuss the background modeling. The MVA-based control sample, used to validate the method of background estimation, is explained in Section 5.7. The signal extraction and systematic uncertainties are presented in Sections 5.8 and 5.9, respectively. Finally, the observed cross sections and upper limits on the cross section times branching fraction are discussed in Sections 5.10, 5.11 and 5.12.

The analysis uses the relevant high-level physical objects built up during the event reconstruction, as discussed in Section 4.5. These objects are the primary and secondary vertices, the PF jets and an overall b-tagging probability.

⁷I use b to denote both b and \bar{b} quarks.

5.1 Analysis strategy

The signal is searched for in final states characterized purely by jets. The b jets reconstructed from Higgs boson decay products have the largest transverse momenta, called hereafter as leading jets, in the event. On average, the p_T spectrum of the b jets originating from the resonance decay typically has a peak at around half of the mass of the Higgs boson. This is illustrated in Figures 5.1 (a) and (b), where the transverse momentum distributions for leading and sub-leading jets are shown in signal and background events.

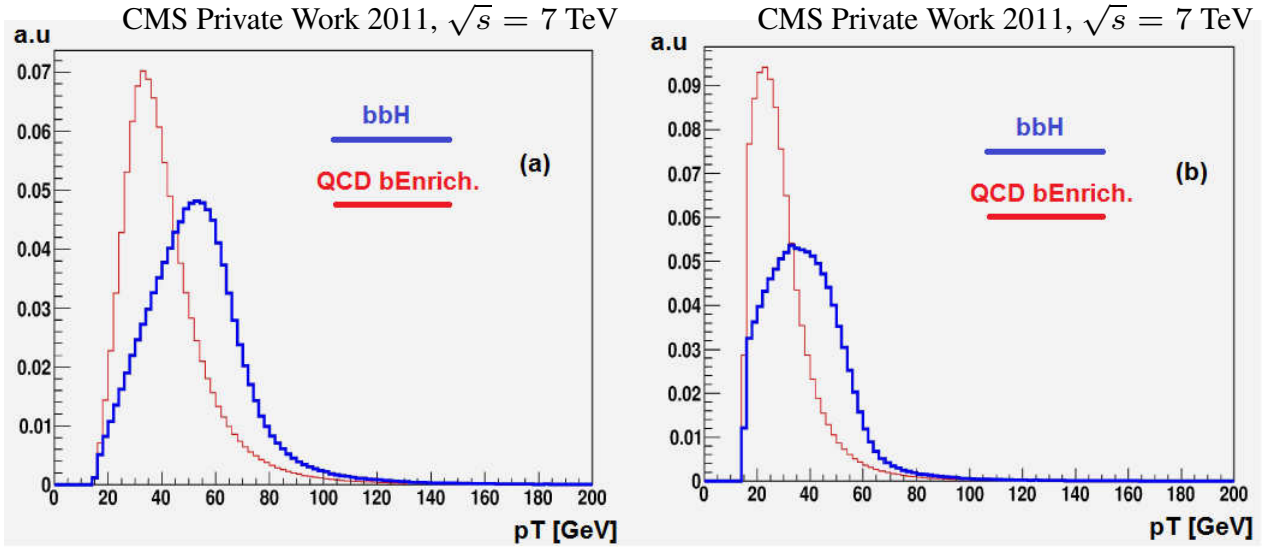


Figure 5.1: p_T distributions of the leading (a) and sub-leading (b) jets in simulated events. The blue histograms are obtained from the signal process, $bb + \Phi \rightarrow 4b + \text{jets}$, for $M_H = 120$ GeV, and the red histograms are the distributions in QCD events enriched by b quarks.

The accompanying b quarks are very soft with an average p_T of about 20 GeV.

The b jets of the Higgs boson decay are mostly produced within the inner tracker acceptance defined by the pseudorapidity range $|\eta| \leq 2.5$, as shown in Figure 5.2.

The peaks observed at $|\eta| \sim 2.5$ are because of the barrel-endcap boundary and material budget, which is maximal in this region.

The analysis selects events with at least three jets within the tracker acceptance imposing asymmetric requirements on their p_T . These three jets must be identified as jets originating from b quarks. The signal events are selected using a distribution in the two-dimensional space, defined by the invariant mass of the two leading b jets, M_{12} , and the variable X_{123} , which reflects the b-jet properties of three leading b-tagged jets in the event. A visible peak on top of the background continuum in the M_{12} projection would be taken as evidence of a Higgs signal.

Background to the searched signal topology pursued in this analysis is mostly stemming from heavy-flavor multijet QCD processes. In order to avoid the theoretical complications

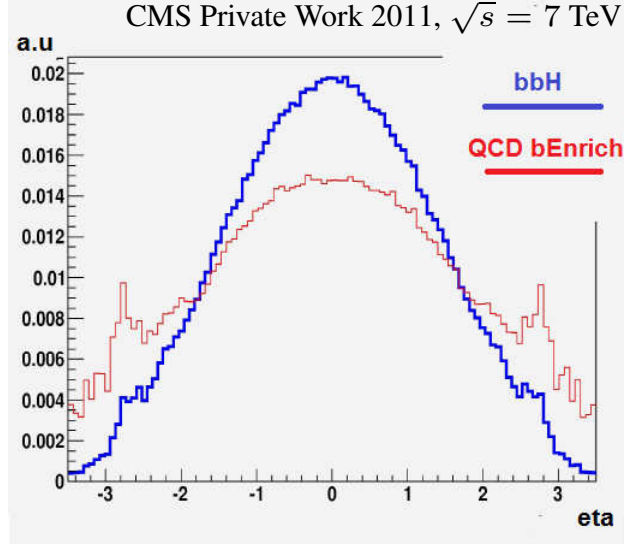


Figure 5.2: η distributions of the leading jet in the simulated events after reconstruction. The blue histogram is obtained from the signal process, $bb + \Phi \rightarrow 4b + \text{jets}$, for with $M_H = 120$ GeV, and the red histogram is the distribution in QCD events enriched by b quarks.

and technical limitations of predicting this background with good accuracy from Monte Carlo simulations, a method to estimate its contribution directly from data, composed of two b-tagged and one untagged jets, is applied. This data-driven approach relies on the fact that the vast majority of the background events in the triple b-tagged sample contain at least two real b jets. Two-dimensional (M_{12}, X_{123}) templates are derived from the selected double-b-tagged data by weighting events with b-tagging probabilities which correspond to the assumed flavors of the untagged jet. In such way the templates properly reflect the flavor composition in the accepted background events. Relative normalizations of the templates are estimated by fitting their linear combination to data.

There is a small contamination, less than 2%, of the double b-tagged sample from non-b jets. This contribution is evaluated using data and subtracted from each template.

To extract a possible Higgs signal yield, two-dimensional (2D) signal templates are derived from Monte Carlo simulations of the MSSM Higgs production, $pp \rightarrow bb + h/H/A \rightarrow 4b$. The data-driven background and MC signal templates are combined and fitted to data with the signal normalization being a free parameter of the fit.

Figure 5.3 illustrates the steps of the analysis, described above.

5.2 Trigger in the analysis

The large rate of hadronic interactions at LHC is a major challenge for this search. The background reduction of several orders of magnitude is needed with not too tight jet p_T thresholds

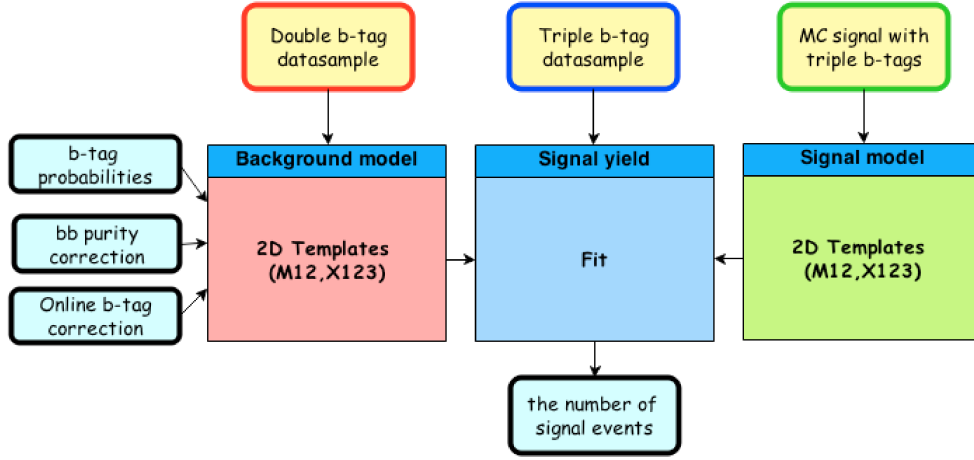


Figure 5.3: Sketch of all important procedures performed in the search for the neutral MSSM Higgs bosons.

to preserve low-mass resonances from being suppressed. This is achieved by introducing the b-jet identification in the trigger. The b-jet tagging is performed in two steps to reduce consuming CPU resources of the farm by the trigger.

First, events are accepted at the Level-1 of the trigger, if at least two jets with energy deposits in central towers of the electromagnetic and hadronic calorimeters are reconstructed, and their p_T values are above certain thresholds. Here these thresholds are chosen to be 36 GeV, denoted as `L1_DoubleJet36_Central`. The jet η must be in the range $|\eta| < 3$. To accommodate higher rates, when the luminosity becomes larger, the conditions have been changed. They require either three jets with p_T larger than 36 GeV for the first two leading jets and 12 GeV for the third leading jet or two jets with p_T larger than 44 GeV. In this case the Level-1 triggers are denoted as `L1_TripleJet36_36_12_Central` and `L1_DoubleJet44_Central`. The events accepted at the Level-1 are subject to the **HLT** path. The Level-1 jets seed initial clusters in the Anti- k_T algorithm with the cone radius parameter $R = 0.5$, to reconstruct either two or three jets at the Level-2. The p_T of these jets must be above determined thresholds in order to probe the jet for b-jet properties. The di-jet **HLT** path requires at least one jet with p_T larger than 46 GeV and at least one jet with p_T larger than 38 GeV. It is denoted as `HLT_CentralJet46_BTagIP3D_CentralJet38_BTagIP3D`. For the triple-jet **HLT** path, denoted as `HLT_CentralJet46_CentralJet38_CentralJet20_DiBTagIP3D`, there is one additional requirement of at least three jets with p_T larger than 20 GeV. At the larger luminosity the p_T criteria in the di-jet **HLT** are changed to 60 and 53 GeV for the leading and sub-leading jets, respectively. This **HLT** path is denoted as `HLT_CentralJet60_CentralJet53_DiBTagIP3D`. The jets, passed the p_T conditions, must be reconstructed in the central region $|\eta| < 2.4$. The jet energy corrections are applied both at the Level-1 and Level-2.

The Level-2.5 trigger invokes b-jet identification using only tracks reconstructed in the pixel tracker. After selecting tracks, passing quality criteria, the primary vertex is built as a common origin of the pixel tracks. If more than one primary vertex is found, mainly because of pile-up

interactions, one vertex, with the highest p_T^2 —sum of the associated tracks, is taken as the primary vertex. Up to four leading jets with $p_T \geq 20$ GeV are considered for b-tagging. The method of the b-jet identification, called the track counting high efficiency, TCHE, algorithm, and discussed in details in section 4.5.8 is applied. The tracks, assigned to each jet, are ordered in descending significance of three-dimensional (3D) impact parameter. The jet is b-tagged if the second ranked track in the considered list has the 3D impact parameter significance above 3 or 4⁸. If the number of b-tagged jets is at least two, the event is passed to the Level-3.

At the Level-3, tracks, within the selected Level-2 jets, are reconstructed using, in addition, information from the silicon tracker. At most four leading jets with $p_T \geq 20$ GeV are probed for the b-tagging. The Level-3 jet is identified as a b jet, if the 3D impact parameter significance of its second-ranked track is larger than 6. If at least two jets are b-tagged, the event is selected for the analysis.

The Table 5.1 summarizes the **HLT** paths and corresponding Level-1 seeds. In the notations HLT_CentralJet'x1'_BTagIP3D_CentralJet'x2'_BTagIP3D and L1_DoubleJet'x3'_Central the quantities x1, x2 and x3 are the p_T thresholds of the leading jets at the Level-2 and Level-1, respectively, and BTagIP3D denotes that at least two jets are b-tagged.

Table 5.1: The **HLT** paths and the appropriate Level-1 seeds used in the analysis.

HLT path	L1 seed
HLT_CentralJet46_BTagIP3D_CentralJet38_BTagIP3D	L1_DoubleJet36_Central
HLT_CentralJet46_CentralJet38_DiBTagIP3D	L1_DoubleJet36_Central
HLT_CentralJet46_CentralJet38_CentralJet20_DiBTag	L1_TripleJet36_36_12_Central
HLT_CentralJet60_CentralJet53_DiBTagIP3D	L1_DoubleJet44_Central

5.2.1 Data samples

The data are organized in samples of events triggered by the di-jet and triple-jet **HLT** paths. At the high luminosities of the 2011 data-taking the output rate of the di-jet trigger with the p_T thresholds of 46 and 38 GeV for the first leading jets reaches the value of about 100 Hz. The maximum output rate is restricted to 10 Hz. Therefore, the di-jet trigger is prescaled dynamically by a corresponding factor, the average value of which is 1.6. The prescale factor of N means that only one of N events is considered for processing at the **HLT** path. The data samples are split in the relevant LHC run ranges in which the average prescaling is the smallest.

The triggers, having lower p_T thresholds, allow to exploit relaxed jet p_T requirements in the offline analysis. This is important to search for the Higgs bosons with low masses. However,

⁸The minimal-allowed value of the TCHE discriminator is 4 for the run period 165970 until 168437, for the rest of the data taking the corresponding cut is required to be 3.

because of the prescaling imposed on such trigger, the total integrated luminosity of the triggered data is reduced.

The triple-jet trigger and di-jet triggers with higher p_T threshold do not have the prescaling. This leads to the higher integrated luminosity. The data triggered by these **HLT** paths allow to search for the Higgs boson with the medium-to-high masses

From the above reasons two analysis scenarios are defined:

- the low-mass scenario, where the MSSM Higgs boson, Φ with $M_\Phi < 180$ GeV is searched for;
- the medium-mass scenario, with $180 \text{ GeV} \leq M_\Phi \leq 350 \text{ GeV}$.

In the search for the Higgs bosons with $M_\Phi < 180$ GeV a set of triggers with low- p_T thresholds on jets is used, whereas a combination of low- and high- p_T threshold triggers are involved to study the hypotheses where the Higgs boson mass varies between 180 and 350 GeV.

The ranges of events selected by different triggers do not overlap in order to avoid double event counting. The effective luminosities of the triggered data are obtained using the CMS tool `lumicalc2.py` [190] and the certified JSON files⁹ [191, 192]. In the JSON format the LHC run is divided into sections of constant luminosity. The JSON files contain the sections and the corresponding integrated luminosities of the recorded data, when all sub-detectors of the CMS were working properly. Only luminosity section specified in the JSON files are used in the analysis.

5.2.1.1 Low-mass scenario

The low-mass scenario utilizes a data sample of a total luminosity of 2.67 fb^{-1} . Table 5.2 summarizes the datasets and LHC runs for each trigger used.

Table 5.2: The datasets, run ranges and corresponding integrated luminosities for the low di-jet mass triggers.

Dataset	Run range	Luminosity (pb^{-1})
HLT_CentralJet46_BTagIP3D_CentralJet38_BTagIP3D		
/MultiJet/Run2011A-PromptReco-v4/AOD	165970 - 166967	524.90
HLT_CentralJet46_CentralJet38_DiBTagIP3D		
/MultiJet/Run2011A-PromptReco-v4/AOD	167039 - 168437	265.75
/MultiJet/Run2011A-05Aug2011-v1/AOD	170826 - 172619	193.58

⁹JSON stands for Java Script Object Notation

/MultiJet/Run2011A-PromptReco-v6/AOD	172620 173198	-	251.12
/MultiJet/Run2011B-PromptReco-v1/AOD	178420 180252	-	453.33
HLT_CentralJet46_CentralJet38_CentralJet20_DiBTagIP3D			
/MultiJet/Run2011A-PromptReco-v6/AOD	173236 175770	-	246.53
/MultiJet/Run2011B-PromptReco-v1/AOD	175832 178380	-	732.73

5.2.1.2 Medium-mass scenario

The samples of the medium-mass analysis are of an integrated luminosity of 3.99 fb^{-1} . Table 5.3 summarizes the datasets and LHC runs for each trigger used.

Table 5.3: The datasets, run ranges and corresponding integrated luminosities for the triggers in the medium mass scenario.

Dataset	Run range	Luminosity (pb^{-1})
HLT_CentralJet60_CentralJet53_DiBTagIP3D		
/MultiJet/Run2011A-05Aug2011-v1/AOD	170826 - 172619	368.04
/MultiJet/Run2011A-PromptReco-v6/AOD	172620 - 175770	660.36
/MultiJet/Run2011B-PromptReco-v1/AOD	175832 - 180252	2180.78
HLT_CentralJet46_BTagIP3D_CentralJet38_BTagIP3D		
/MultiJet/Run2011A-PromptReco-v4/AOD	165970-166967	524.90
HLT_CentralJet46_CentralJet38_DiBTagIP3D		
/MultiJet/Run2011A-PromptReco-v4/AOD	167039 - 168437	265.75

5.2.2 L1/L2 efficiencies

In the Level-1 triggers and **HLT** paths at Level-2, which are reported in Table 5.1, the jets are reconstructed by the jet triggers as discussed in subsection 4.4.2. In addition, the jet triggers perform selection of jets imposing the thresholds on the jet p_T . The L1/L2 efficiencies of the di- and triple-jet triggers are determined as the multiplications of the selection efficiencies of the

jet triggers used at the Level-1 and Level-2. The efficiencies of the five Level-2 jet selections with the thresholds of 20, 38, 46, 53 and 60 GeV, obtained with respect to the jet p_T in zero-bias events [193], are used to factorize the efficiencies of the di- and triple-jet triggers. The zero-bias events are triggered only by the coincidence of signals in the two BPTX (Beam Position and Timing for LHC eXperiments) monitors [194]. The Level-2 jet triggers with the p_T thresholds of 20, 38, 46, 53 and 60 GeV are seeded by the Level-1 jet triggers with the selection cuts on the jet p_T equalued to 12, 36, 36, 44 and 44 GeV, respectively.

To estimate the efficiency for zero-bias events to pass through the Level-1 and Level-2 jet triggers as a function of p_T of the offline-reconstructed PF jet, the matching between the Level-2 and **PF** jets, $\Delta R(jet_{PF}, jet_{L2}) < 0.3$, is demanded. In addition, the PF jet is required to have $p_T > 10$ GeV and to be reconstructed in the central region of the detector, $|\eta| < 2.4$. Figure 5.4 shows the efficiencies of the Level-1 and Level-2 jet triggers as functions of the jet p_T .

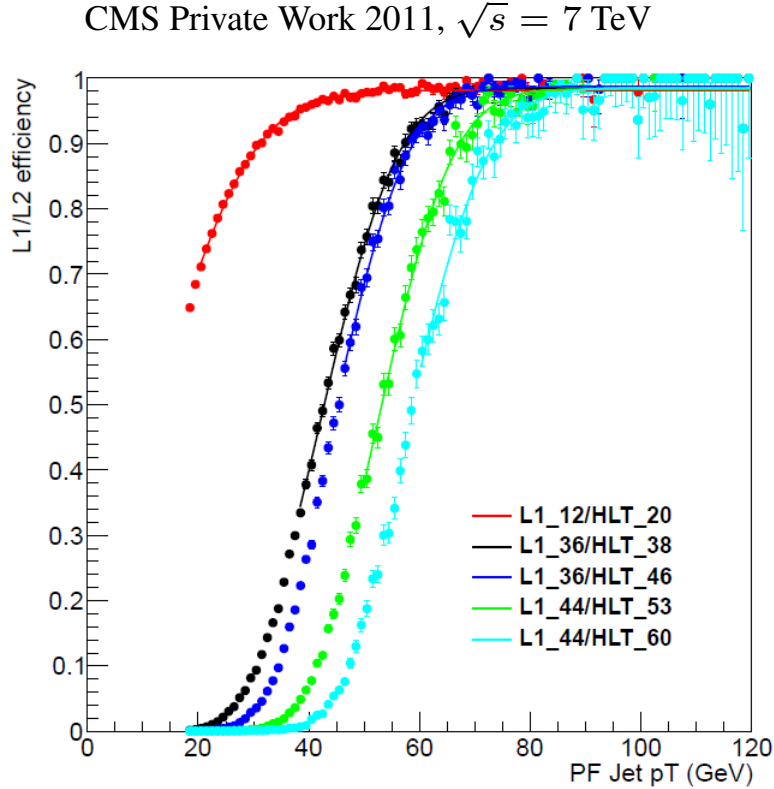


Figure 5.4: Efficiencies for the Level-2 selection with 20, 38, 46, 53 and 60 GeV thresholds on the jet p_T , seeded by the Level-1 jets selected using the cuts of 12, 36, 36, 44 and 44 GeV on the jet p_T .

The L1/L2 efficiency is fitted to the function

$$\varepsilon_{L1/L2}(p_T) = \frac{P}{2} \left(1 + \text{Erf} \left(\frac{p_T - \varepsilon_{50}}{s} \right) \right), \quad (5.1)$$

where the parameters P and s characterize the plateau and slope of the graphs at Figure 5.4. The parameter ϵ_{50} is the value of the jet p_T corresponding to the efficiency of 50%. $Erf(x)$ is the error function defined in Ref. [195],

$$Erf(x) = \frac{2}{\sqrt{\pi}} \int_0^x e^{-t^2} dt.$$

Table 5.4 summarizes the resulting parameters from the fit.

Table 5.4: Parameters of the L1/L2 efficiencies resulting from the fit.

L1/L2 trigger	plateau	slope	ϵ_{50}
HLT_Jet20	0.98150 ± 0.00096	19.58 ± 0.22	12.00 ± 0.11
HLT_Jet38	0.9844 ± 0.0020	15.16 ± 0.23	42.57 ± 0.08
HLT_Jet46	0.9871 ± 0.0019	14.91 ± 0.43	44.69 ± 0.21
HLT_Jet53	0.9831 ± 0.0028	14.75 ± 0.43	52.96 ± 0.15
HLT_Jet60	0.9852 ± 0.0032	15.75 ± 0.86	58.38 ± 0.43

The functions $\epsilon_{L1/L2}(p_T)$ are used to simulate the di- and triple-jet Level-1 and Level-2 triggers in the signal Monte Carlo samples. Each signal event is weighted by the multiplicative factor

$$w_{L1/L2} = \prod_{i=1}^{N_{jets}} \epsilon_{L1/L2}^i(p_{T,k}). \quad (5.2)$$

Here $\epsilon_{L1/L2}^i(p_{k,T})$ is the efficiency function, taken from Table 5.4, which corresponds to the Level-1 and Level-2 triggering of the jet with the rank k . k is 1 for the first leading jet, 2 for the second leading jet and 3 for the third leading jet. N_{jets} is the number of the reconstructed jets used to trigger events at the Level-1 and Level-2. For an example, to model the L1/L2 efficiency of the triple-jet trigger HLT_CentralJet46_CentralJet38_CentralJet20_DiBTagIP3D, the following weight is applied to signal events:

$$w_{L1/L2} = \epsilon_{L1/L2}^{HLT_46Jet}(p_{T,1}) \cdot \epsilon_{L1/L2}^{HLT_38Jet}(p_{T,2}) \cdot \epsilon_{L1/L2}^{HLT_20Jet}(p_{T,3}), \quad (5.3)$$

where $p_{T,1}$, $p_{T,2}$ and $p_{T,3}$ are the values of p_T for the first three leading jets, respectively.

5.3 Efficiency of b-jet identification

We use the mistag fraction and efficiency of the b-jet identification to model the background. Both the mistag fraction and efficiency of recognizing b jets determine the performance of the

b-tagging algorithms. The efficiency, ϵ_b , and the mistag fraction, $\bar{\epsilon}_b$, of a b-tagging algorithm are defined as

$$\epsilon_b = \frac{N_{b-jets}^{accepted}}{N_{b-jets}}, \quad \bar{\epsilon}_b = \frac{N_{non-b-jets}^{accepted}}{N_{non-b-jets}}, \quad (5.4)$$

where $N^{accepted}$ is the number of jets those values of the b-tagging discriminator exceeds the chosen working point. To illustrate the performance of the b-tagging algorithms in terms of the efficiency and mistag fraction multijet QCD events are generated with the `Pythia6` program. The jets are classified into b jets, c jets, and light-flavor jets. The gluon jets, which are splitted to $b\bar{b}$ and $c\bar{c}$ pairs, are considered as b and c jets, respectively. Figure 5.5 shows the efficiencies of the IP based b-tagging, TCHE, and the secondary vertex based, CSV, algorithms for non-b jets versus b jets with $p_T > 30$ GeV and $|\eta| < 2.5$.

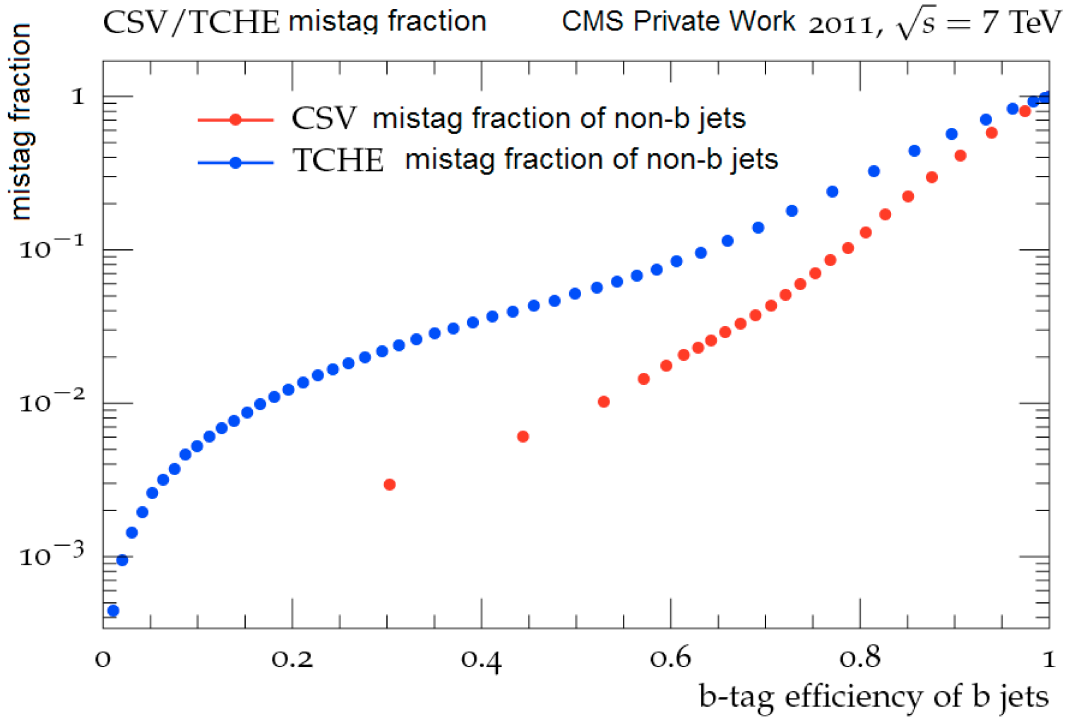


Figure 5.5: Using TCHE and CSV algorithms applied to jets in simulated QCD events, the mistag fraction of non-b jets is obtained as functions of the b-jet tagging efficiency.

At a misidentification probability for light-flavor plus c jets of 10%, a b-jet tagging efficiencies of $\sim 80\%$ and $\sim 85\%$ are achieved for the TCHE and CSV algorithms, respectively. At the tight working point with a mistag fraction of 0.1%, typical values of the b-jet tagging efficiencies for the IP-based and CSV algorithms are about 20% and 60%, respectively. The tight working point

of the CSV algorithm is used to tag PF jets in the search for the Higgs boson, and it is defined as

$$\text{CSV}T > 0.89. \quad (5.5)$$

To attribute a flavor to a reconstructed jet in Monte Carlo simulations, a matching needs to be done between the jet and the original parton, by inspecting the generated partons in a cone around the jet direction. A reconstructed jet is associated to a generated parton from the hard interaction or the parton shower, if the distance between them is $\Delta R < 0.3$.

The b-tagging efficiencies as functions of the jet p_T , η and flavor needed in a later stage of the analysis are obtained using jets with $p_T > 20$ GeV and $|\eta| < 2.5$ in the QCD samples generated by the `Pythia6` program. The tight working point (5.5) of the CSV algorithm, **CSV****T**, is chosen to get the parametrization of the efficiencies. Figure 5.6 shows the b-tagging efficiencies in the two-dimension space of the jet p_T and η for b, c and light-flavor jets.

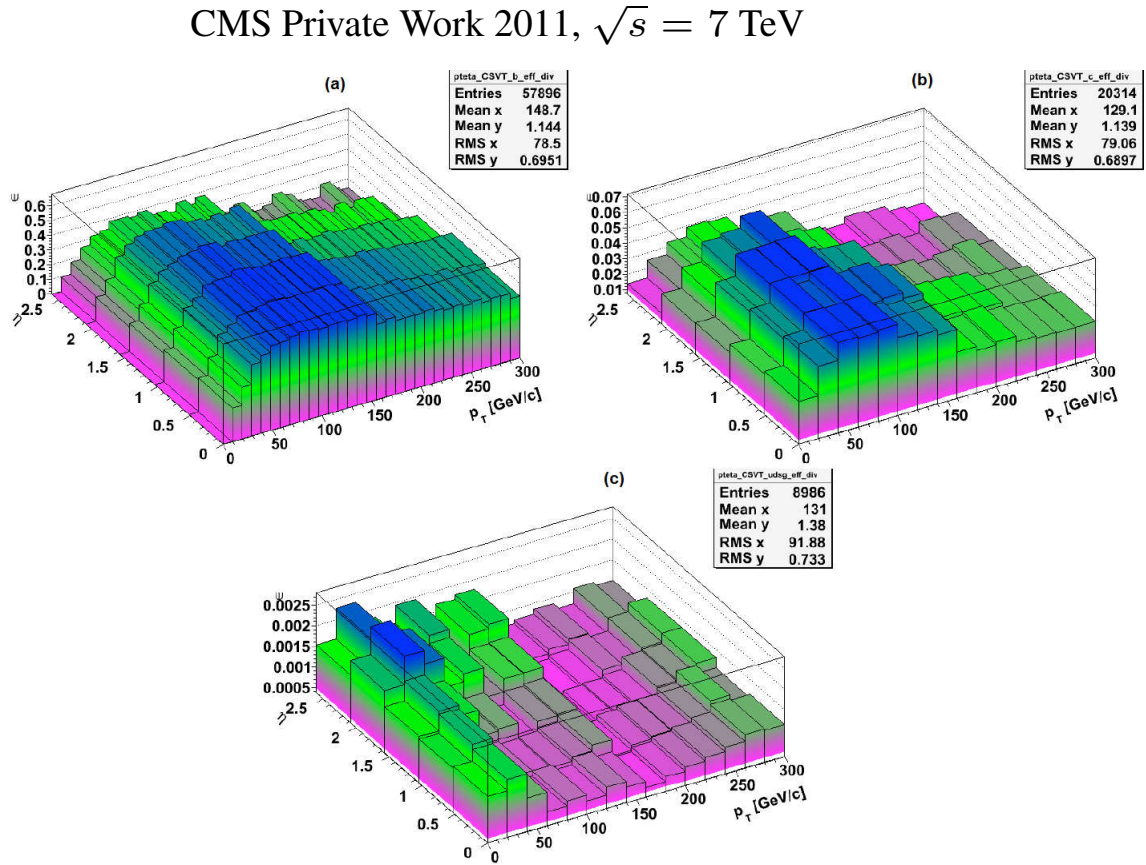


Figure 5.6: The offline b-tagging probabilities for b (a), c(b) and light-flavor (c) jets at the CSV working point.

The b-tagging efficiency at the CSVT working point shows an improvement with the increase of the jet p_T up to a maximum plateau of 60% at about $p_T = 50$ GeV. This can be clearly seen in the p_T projection of the efficiency for b jets shown in Figure 5.7. The efficiency slowly decreases from 60% to 40% for the jet p_T between 150 and 300 GeV.

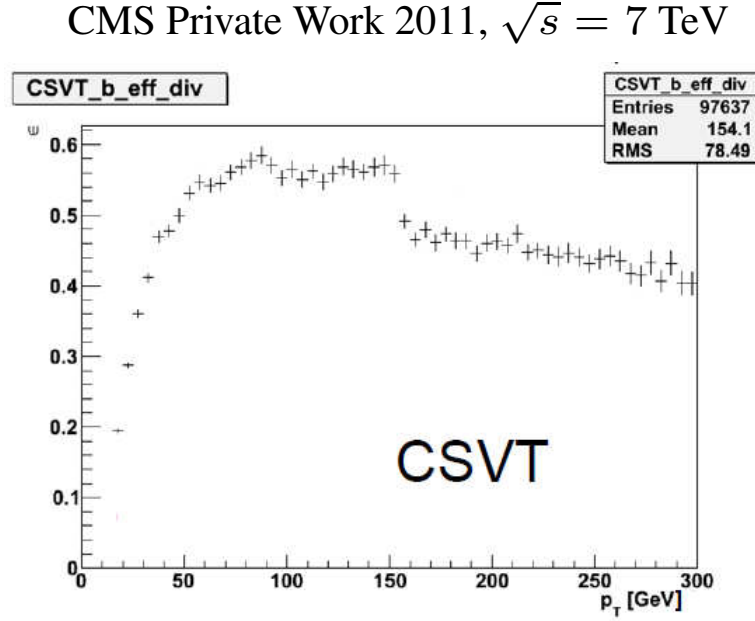


Figure 5.7: The CSV b-tagging efficiency for b jets as a function of p_T at the tight working point.

5.3.1 Relative trigger b-tagging efficiency

The relative trigger b-tagging efficiency characterizes the fraction of jets with the **CVST** tag, which have also b-tagged in the HLT. The relative trigger b-tagging probability is assessed in bins of the PF jet p_T and η , and defined as

$$\epsilon_b(trigger) = \frac{N([\text{btaggingTrigger}] \wedge [\text{referenceTrigger}] \wedge [\text{CSV}])}{N([\text{referenceTrigger}] \wedge [\text{CSV}])}. \quad (5.6)$$

Here the quantity $N([\text{BtaggingTrigger}] \wedge [\text{referenceTrigger}] \wedge [\text{CSV}])$ is the number of the PF jets in events when the triggers **[btaggingTrigger]** and **[referenceTrigger]** are fired. These jets are b-tagged by the **CSV** algorithm and matched to the Level-2 jets of the trigger **[btaggingTrigger]**. The quantity $N([\text{referenceTrigger}] \wedge [\text{CSV}])$ denotes the number of jets b-tagged by the **CVST** in events triggered by **[referenceTrigger]**. These quantities are evaluated in bins of the jet p_T and η .

The trigger [**btaggingTrigger**] implements the Level-3 trigger, performing the IP-based b-tagging algorithm. The trigger [**referenceTrigger**] reproduces the Level-1 and Level-2 kinematic preselection of jets. As the trigger [**referenceTrigger**] is placed both in the numerator and denominator of equation (5.6), effects of Level-1 and Level-2 selections are canceled out in the estimation of the efficiency. The relative trigger efficiency (5.6) is derived using Monte Carlo simulations of multijet QCD events enriched by b jets. The results on the relative trigger b-tagging efficiency are shown in Figure 5.8 for different jet flavors. Because of large statistical fluctuations in (p_T, η) bins, a bi-linear smoothing is applied. The relative trigger b-tagging efficiencies increase with the jet p_T up to a maximum plateaus of 60% at $p_T \simeq 100$ GeV, 40% at $p_T \simeq 100$ GeV, and 30% at $p_T \simeq 150$ GeV, for b, c and light-flavor jets, respectively.

CMS Private Work 2011, $\sqrt{s} = 7$ TeV

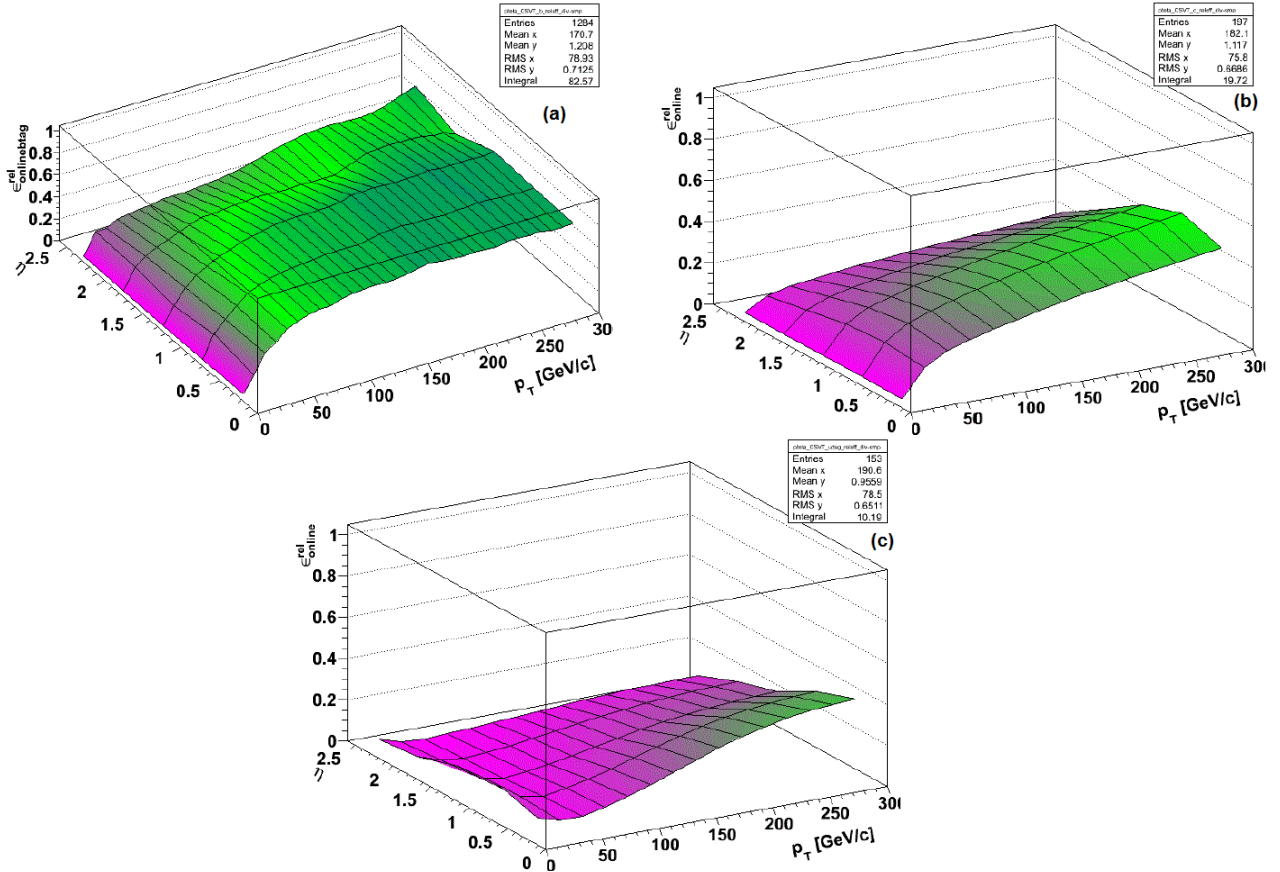


Figure 5.8: The relative trigger b-tagging efficiency for b (a), c(b) and light-flavor (c) jets at the CSVT working point.

5.3.2 Scale factors for the b-tagging efficiencies

For the CSV b-tagging algorithm used in the analysis, it is crucial to know the efficiency to identify b jets in data. There are a number of techniques [174] that can be applied to measure the efficiencies using data, and thus reduce the reliance on simulations. All the efficiency measurements that are done with data are also replicated in simulated samples using Monte Carlo generator information to identify jet flavors, and the scale factor,

$$SF_b = \frac{\epsilon_b^{data}}{\epsilon_b^{MC}}, \quad (5.7)$$

the ratio of efficiencies measured in data and simulated samples, is calculated.

The measurement of the mistag fraction $\bar{\epsilon}_b$ for light-flavor jets in data utilizes tracks with the negative impact parameter [174]. The IP-based algorithm, called the negative tagger (nTCHE), identifies the jet as negative-tagged, if there are at least two tracks with values of the impact parameter significance below a certain negative threshold. The negative tagging efficiency ϵ_- is given by the fraction of light-flavor jets tagged by the nTCHE. The mistag fraction $\bar{\epsilon}_b$, as estimated from Monte Carlo simulations, is found to be proportional to the negative tagging efficiency ϵ_- ,

$$\bar{\epsilon}_b^{MC} = R_{mistag} \epsilon_-^{MC}, \quad (5.8)$$

where R_{mistag} is the factor of proportionality. Then the mistag fraction in data is evaluated as

$$\bar{\epsilon}_b^{data} = R_{mistag} \epsilon_-^{data}. \quad (5.9)$$

To correct the mistag fraction predicted by simulations to that measured in data, a scale factor

$$SF_{udsg} = \frac{\bar{\epsilon}_b^{data}}{\bar{\epsilon}_b^{MC}} = \frac{\epsilon_-^{data}}{\epsilon_-^{MC}} \quad (5.10)$$

is introduced.

The analysis adopts the following parametrization of the scale factors SF_b (5.7) and SF_{udsg} (5.10):

$$\begin{aligned} SF_b(p_T) &= \frac{a \cdot (1 + b \cdot p_T)}{1 + c \cdot p_T}, \\ SF_{udsg}(p_T) &= d + m \cdot p_T + n \cdot p_T^2 + k \cdot p_T^3. \end{aligned} \quad (5.11)$$

where the parameters a, b, c, d, m, n and k are estimated from a fit [174]. Following the results presented in Ref. [174] equations (5.11) are expressed as

$$\begin{aligned} SF_b(p_T) &= \frac{0.902 \cdot (1 + 0.553 \cdot p_T)}{1 + 0.547 \cdot p_T}, \\ SF_{udsg}(p_T) &= 1.21 + 6.81 \times 10^{-4} \cdot p_T - 1.57 \times 10^{-6} \cdot p_T^2 + 2.83 \times 10^{-10} \cdot p_T^3. \end{aligned} \quad (5.12)$$

Figure 5.9 illustrates the parametrization (5.12) of the scale factors.

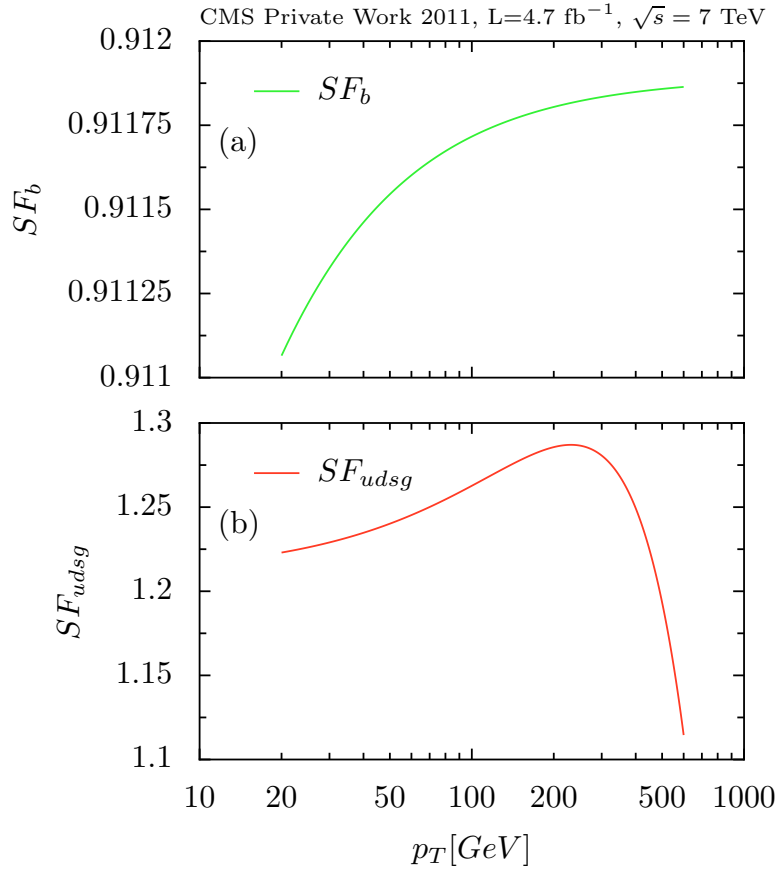


Figure 5.9: The scale factors SF_b (a) and SF_{udsg} (b) at the CSVT b-tagging point as functions of the jet p_T .

The ratio SF_b varies very little over the whole range of the jet p_T , $20 \text{ GeV} < p_T < 800 \text{ GeV}$, and equal to about of 0.9. The SF_{udsg} scale factor increases from 1.22 to 1.28 in the range of $20 \text{ GeV} < p_T < 350 \text{ GeV}$, and it decreases from 1.28 to 1.10 with the increase of the jet p_T from 350 to 800 GeV.

The offline b-tagging efficiencies of untagged and b-tagged jets in the double-btag background and triple-btag signal samples are multiplied by the scale factors SF_b and SF_{udsg} (5.11) to

correct for the difference between data and Monte Carlo efficiencies. The correction factor for background sample reads

$$w_{SF}^{Bkg} = SF_i(p_{T,m}), \quad (5.13)$$

while the correction factor for the signal is determined as

$$w_{SF}^S = SF_j(p_{T,1}) \cdot SF_k(p_{T,2}) \cdot SF_n(p_{T,3}). \quad (5.14)$$

Here the indices i , j , k and n are either b, c, or udsg, depending on the assumed flavor for the untagged jet m in the background events and the flavors of first, second and third leading jets in the case of the signal, respectively.

5.4 Event-wise b-tagging

The analysis uses the relevant high-level physical objects built up during the event reconstruction, as discussed in Section 4.5. These objects are the primary and secondary vertices, the **PF** jets and an overall b-tagging probability for the event, which is constructed on the secondary vertex mass.

The secondary vertex mass is the invariant mass, calculated from all tracks of the SV candidate. It provides an additional separation between b,c and udsg jets, even on top of the offline b-tagging criteria. Figure 5.10 shows the good flavor separation of the SV mass, M_{SV} , of b-tagged jets in a sample of simulated $t\bar{t}$ events. In the case, where no SV is reconstructed in a jet, the SV mass takes a fixed negative value, explaining the underflow bin in Figure 5.10.

To quantify the b-jet content of events, an event-wise b-tag X_{123} is introduced. It is built from masses of the SV candidates in jets. The SV mass range, shown in Figure 5.10, is divided into three bins, $B_j = 0, 1, 2$ for each jet j in the following manner:

- $B_j = 0$, if $M_{SV,j} \leq 1$ GeV;
- $B_j = 1$, if $1 < M_{SV,j} \leq 2$ GeV;
- $B_j = 2$, if $M_{SV,j} > 2$ GeV.

For an event with three leading jets we obtain three quantities B_1 , B_2 and B_3 , respectively, which determine the variable X_{123} as follows:

- $X_{123} = X_{12} + X_3$,

where

- $X_{12} = 0$, if $B_1 + B_2 < 2$;

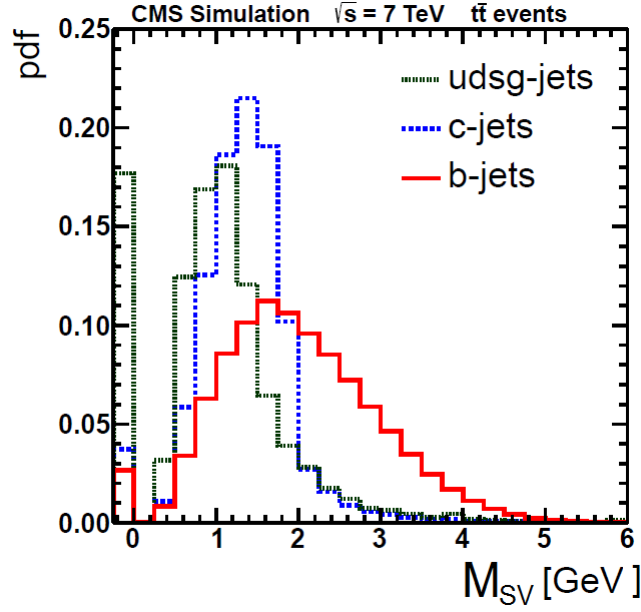


Figure 5.10: Normalized distribution of M_{SV} in jets for different flavors in simulated $t\bar{t}$ events.

- $X_{12} = 1$, if $2 \leq B_1 + B_2 < 3$;
- $X_{12} = 2$, if $B_1 + B_2 \geq 3$.

The larger the value of X_{12} is, the more likely two leading jets are b jets. The component X_3 depends on the third jet as

- $X_3 = 0$, if $B_3 < 2$;
- $X_3 = 3$, if $B_3 = 2$.

Again, X_3 is largest if the third jet is a b jet. By construction, X_{123} can have six discrete values ranging from 0 to 5. The intention of this mapping is to have each bin populated with sufficient statistics. Events with triple-b-tagged jets result typically to X_{123} values of 2 and 5.

5.5 Offline event selection

Events are required to have at least three PF reconstructed jets with $|\eta| < 2.2$, passing a certain quality requirement based on both primary vertex information and jet shape information [196]. At least one primary vertex must be reconstructed. If more than one primary vertex is found, the one with the highest p_T^2 -sum of the associated tracks is considered.

For the search in the low-mass scenario the offline selection demands that the three p_T -leading jets have to pass p_T cuts of

- $p_{T,1} > 46 \text{ GeV}$,
- $p_{T,2} > 38 \text{ GeV}$,
- $p_{T,3} > 20 \text{ GeV}$.

For the search in the medium-mass scenario the first three jets are required to pass the p_T cuts of

- $p_{T,1} > 60 \text{ GeV}$,
- $p_{T,2} > 53 \text{ GeV}$,
- $p_{T,3} > 20 \text{ GeV}$.

To suppress the contamination from gluon splittings into $b\bar{b}$ pairs, we impose the requirement of $\Delta R(\text{jet}_1, \text{jet}_2) > 1$ on the leading and sub-leading jets.

We define a “triple-b-tagged” sample, in which the signal is ultimately searched for, by requiring all three leading jets to pass a tight CSV b-tagging selection requirement (5.5). The total numbers of data events that pass the trigger and offline selection for the searches in the low- and medium-mass scenarios are 106626 and 89637, respectively. The efficiency of the trigger for signal events to pass the triple-b-tagging selection is 47-67% for a Higgs boson mass in the range of [90, 350] GeV.

For a “double-b-tagged” sample, which is instrumental in estimating the shape of the background, only two of the three leading jets have to pass the above-mentioned b-tagging requirement, while the third jet remains untagged.

5.6 Background modeling

The large irreducible background to the signal topology of at least three b jets stems largely from multijet QCD processes. The prediction of their production rates and kinematics involves complex calculations, which included contributions of high-order processes for flavor creations, excitations and gluon splitting. These calculations are characterized by large uncertainties. Therefore, a method to evaluate multijet QCD background from data, similar to the procedure employed by the CDF experiment [188], has been developed. Backgrounds from $t\bar{t}$ and Z+jets final states are estimated from Monte Carlo and found to be negligible.

This data-driven approach relies on the assumption that there are at least two real b jets in events with three b-tagged jets. From Monte Carlo results, which are shown in Table 5.5, this is the case in more than 98% of multijet QCD events which match the signal selection criteria. This fact is important because it reduces the possible flavor combinations in background events. The data-driven estimated background can be naturally subtracted from the data events selected for the signal search. Effect of the trigger selection of jets is automatically taken into account.

Table 5.5: Flavor content fractions of the background events, simulated by Alpgen and Pythia6 programs, which are accepted in the signal region.

Flavor content	Alpgen, [%]	Pythia6, [%]
bbb	62.4 +- 0.60	72.0 +- 4.10
bbc	6.56 +- 0.08	4.40 +- 0.41
bbq	4.53 +- 0.07	3.51 +- 0.16
bcb	18.0 +- 0.07	13.3 +- 0.52
bqb	6.82 +- 0.01	4.78 +- 0.06
non-bb	1.69 +- 0.01	2.01 +- 0.06

5.6.1 Double-b-tagged sample

The sample used to model the background is built from triggered events where two jets are b-tagged, and at least one additional jet is selected with the same offline requirements used for the signal region. In this way the biases due to the triggers are accounted for in the double-b-tagged region. No inference is made concerning the b-tagging of the third jet.

Events in the sample are categorized as bbX, bXb, Xbb topologies, depending on which jets are b-tagged, here represented by the lower-case letter b, and which jet is untagged, denoted by the upper-case letter X. The order of the jets is given with descending p_T . For example, bXb means an event where the leading and third jets are b-tagged and the sub-leading jet is untagged.

The di-jet mass M_{12} spectrum is used to search for the Higgs boson signal. Kinematics of $b\bar{b}$ pairs in the bbX and bXb event categories are different, resulting to different M_{12} shapes. However, in events, characterized by the same kinematics, it does not matter if the flavor X is either udsg or c. For example, the M_{12} spectrum would be the same in either bbq ¹⁰ or bbc events. It is worth mentioning that b-tagging is a major source of distinction between the different event categories. For example, considering the triple-b-jet background, the M_{12} spectra of three compositions, bbB, bBb and Bbb, are different due to different b-tagging probabilities for the untagged jet B.

5.6.2 Construction of the background templates

From the three double-b-tagged categories nine background templates, bbX, bXb, Xbb, with X=Q, C and B, are created. The capital letters represent the assumption on the flavor of the untagged jet to be either a light, Q, a charm, C, or a bottom, B, jet. The templates are 2D spectra (M_{12}, X_{123}) obtained by collecting events which are weighted by the b-tag probability for the untagged jet. The b-tag probabilities as functions of the jet p_T and η are obtained from Monte Carlo simulations and shown in Figures 5.6 and 5.8. Data/MC correction factors (5.12) are applied to correct b-tag efficiencies of b,c and udsg jets.

¹⁰Here and elsewhere a light (udsg) flavor is denoted as q.

The variable X_{123} in the double-b-tagged sample is similarly modeled using weights. Each of three possible values of the secondary vertex mass index, B_i ¹¹, for the untagged jet is taken in the construction of the templates with a weight according to the probability P_{B_i} that the untagged jet will be assigned to the given bin B_i . These probabilities have been determined for each flavor as functions of the jet p_T and η using simulated $t\bar{t}$ events. Figure 5.11 shows the probabilities P_{B_1} and P_{B_3} for b, c and udsg jets as functions of their p_T .

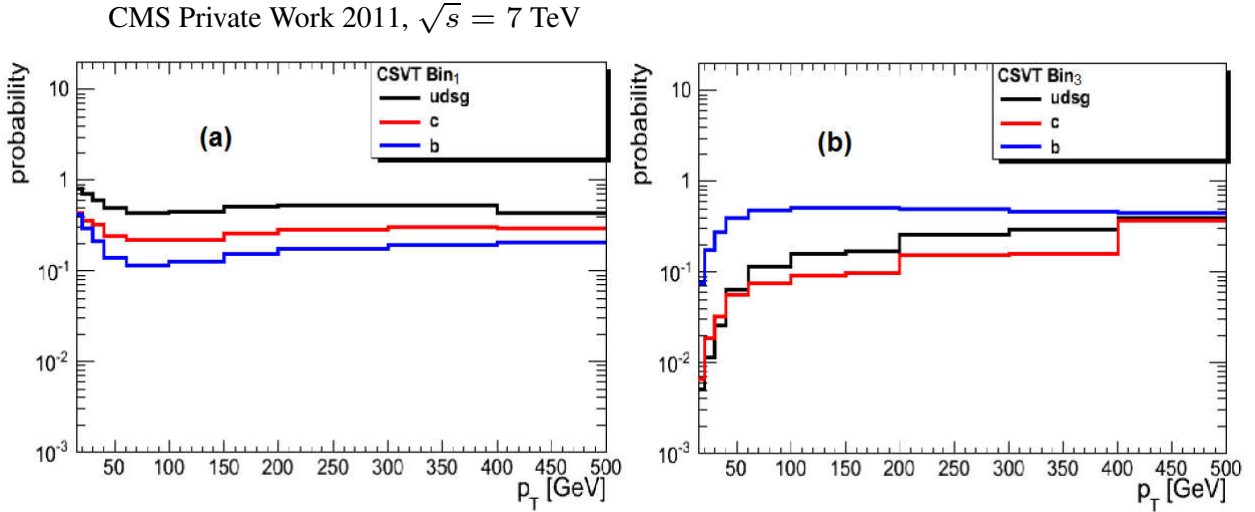


Figure 5.11: The probabilities P_{B_1} (a) and P_{B_3} (b) that the b, c or udsg jets will be assigned to the bins B_1 and B_3 of the SV mass distribution as a function of the jet p_T .

As expected, jets assigned to the bin B_1 of the SV mass distribution are more likely light-flavor jets, while b jet has the largest probability to be found in the bin B_3 . The probabilities, $P_{B_i}(flavor)$, of the jet of a certain flavor to be assigned to the bins B_i satisfy the condition

$$\sum_i P_{B_i}(flavor) \equiv 1.$$

Some of the nine templates are rather similar to each other in shape. Two templates are combined, if their ratios in all bins are close to 1. Following this procedure, the templates for the Xbb and bXb event categories, with X=Q, C, B, are merged:

- Bbb+bBb= (Bb) b,
- Cbb+bCb= (Cb) b,
- Qbb+bQb= (Qb) b.

Furthermore, when the third leading jet is an untagged jet of the flavors Q and C, then the bbQ and bbC templates are combined together:

¹¹Here i is either 1,2 or 3.

- $bbQ+bbC=bbX$.

After merging the total number of templates is reduced to five. As an example, these five M_{12} and X_{123} projections of templates are shown in Figure 5.12 for the low-mass scenario selection criteria.

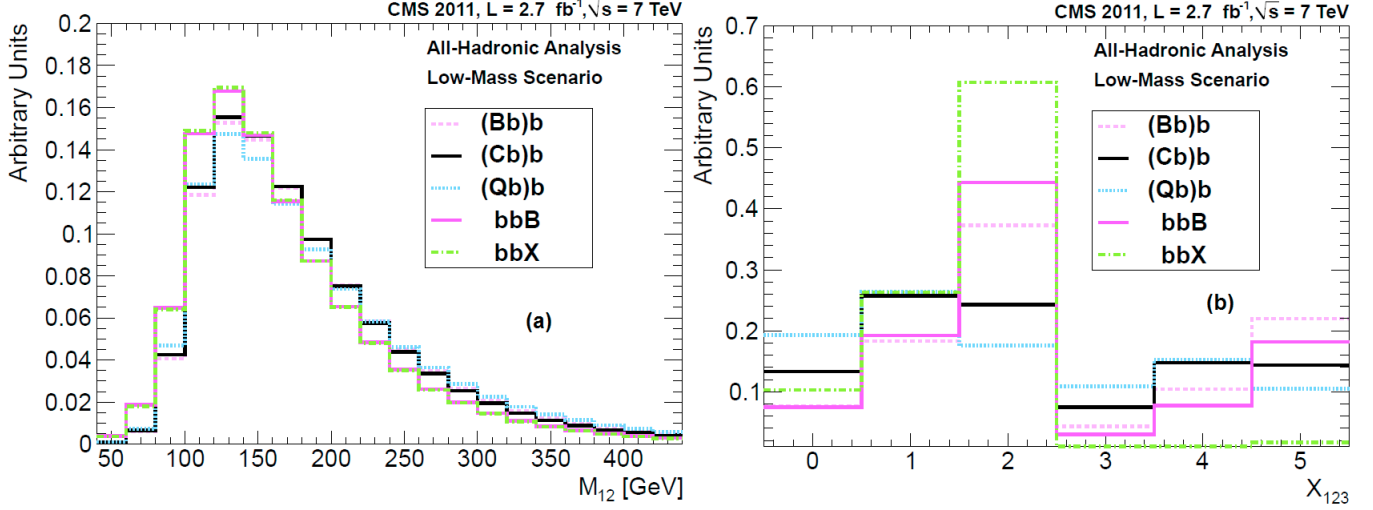


Figure 5.12: The M_{12} (a) and X_{123} (b) projections of the five templates $(Bb)b$, $(Cb)b$, $(Qb)b$, bbB , bbX for the CSVt b-tagging in the low-mass scenario.

The two-dimensional templates whose di-jet mass M_{12} spectra are very similar can be clearly distinguished with a help of X_{123} . For example, this is the case of the $(Bb)b$ and $(Cb)b$ templates, or bbB and bbX templates. This means that the obtained templates have different 2D shapes, what prevents from correlations of background fractions in the fit discussed later.

5.6.3 Trigger pattern corrections

The double-b-tagged and triple-b-tagged samples are different in the b-tag trigger patterns. Therefore, a correction must be applied to the templates derived from the double-b-tagged sample, if one wants to use them to describe triple-b-tagged distributions. The HLT requires that two Level-2 jets must be tagged. This determines the following b-tag trigger patterns in events:

- TTx ,
- TxT ,
- xTT ,

where the capital letter T represents the position of the b-tagged Level-3 jet. In the background templates all three trigger patterns may contribute to a certain flavor composition. For example, the bCb event category may include not only the pattern TxT , but also TTx and xTT . However,

studying the correlation of the b-tag trigger pattern with offline b-tagging in the data, we have found that in about 95% of the cases jets with trigger b-tagging are also identified offline as b jets. Figure 5.13 illustrates the fractions of events, corresponding to different b-tag trigger patterns, in the bbX, bXb and Xbb event categories. To construct the templates, we ignore events for which the b-tag trigger pattern does not match to the event category. However, events with the trigger pattern TTT are also accepted in the templates.

The background templates are then corrected for the 5% effect from this mismatch. Two correction factors are applied to the M_{12} and X_{123} projections of the templates. The M_{12} distribution in the event category i is weighted by the ratio

$$r_{M_{12},pattern}^{flav}(i) = \sum_{k \neq i} \frac{\varepsilon_b(trigger, i)^{flav}}{\varepsilon_b^B(trigger, k)}, \quad (5.15)$$

where $\varepsilon_b(trigger, i)^{flav}$ and $\varepsilon_b^B(trigger, k)$ are relative trigger b-tagging efficiencies (5.6) for the $flav$ and b jets in the event categories i and k , respectively. The quantity $flav$ is an assumed flavor of the untagged jet in the event category i . The index k denotes the non-matched trigger patterns, i.e $k \neq i$ is required. For example, to correct the template of the bXb category with $X=C$, the weight $r_{M_{12},pattern}^C(2)$ is applied on event-by-event basis,

$$r_{M_{12},pattern}^C(2) = \frac{\varepsilon_b^C(trigger, 2)}{\varepsilon_b^B(trigger, 1)} \oplus \frac{\varepsilon_b^C(trigger, 2)}{\varepsilon_b^B(trigger, 3)}. \quad (5.16)$$

The symbol \oplus in equation (5.16) means that two bCb sub-templates are weighted by different ratios of equation (5.16) and combined in the final step of the template production.

In order to factorize the effect from the non-matched b-tag trigger patterns in the X_{123} distribution, the MC-driven probability distribution functions $P_{B_i}^{flav, tPat}(j)$ are introduced. They describe the probability of the untagged jet with the assumed flavor $flav$ to be assigned to the bin B_i of the SV mass distribution in events of the category j with b-tag trigger pattern $tPat$. $P_{B_i}^{flav, tPat}(j)$ functions are obtained from the SV mass distribution applying the relative trigger b-tagging efficiencies and requiring the matching between the Level-2 and PF jets.

The probability distribution functions, **pdf**, of X_{123} , which are discussed in subsection 5.6.2 and shown in Figure 5.11, are built without such weighting and matching. We call such a **pdf** “offline”, $P_{B_i}^{flav, offline}(j)$.

The correction of the non-matched trigger patterns for the variable X_{123} reads

$$r_{X_{123},pattern}^{flav, tPat}(B_i, j) = P_{B_i}^{flav, tPat=j}(j) \cdot \frac{P_{B_i}^{flav, offline}(j)}{P_{B_i}^{flav, tPat \neq j}(j)}. \quad (5.17)$$

The final X_{123} projection of the template is obtained by summing sub-templates, corrected by the weights (5.17), over the three b-tag trigger patterns $tPat = xTT, T \times T, TTx$. The overall correction

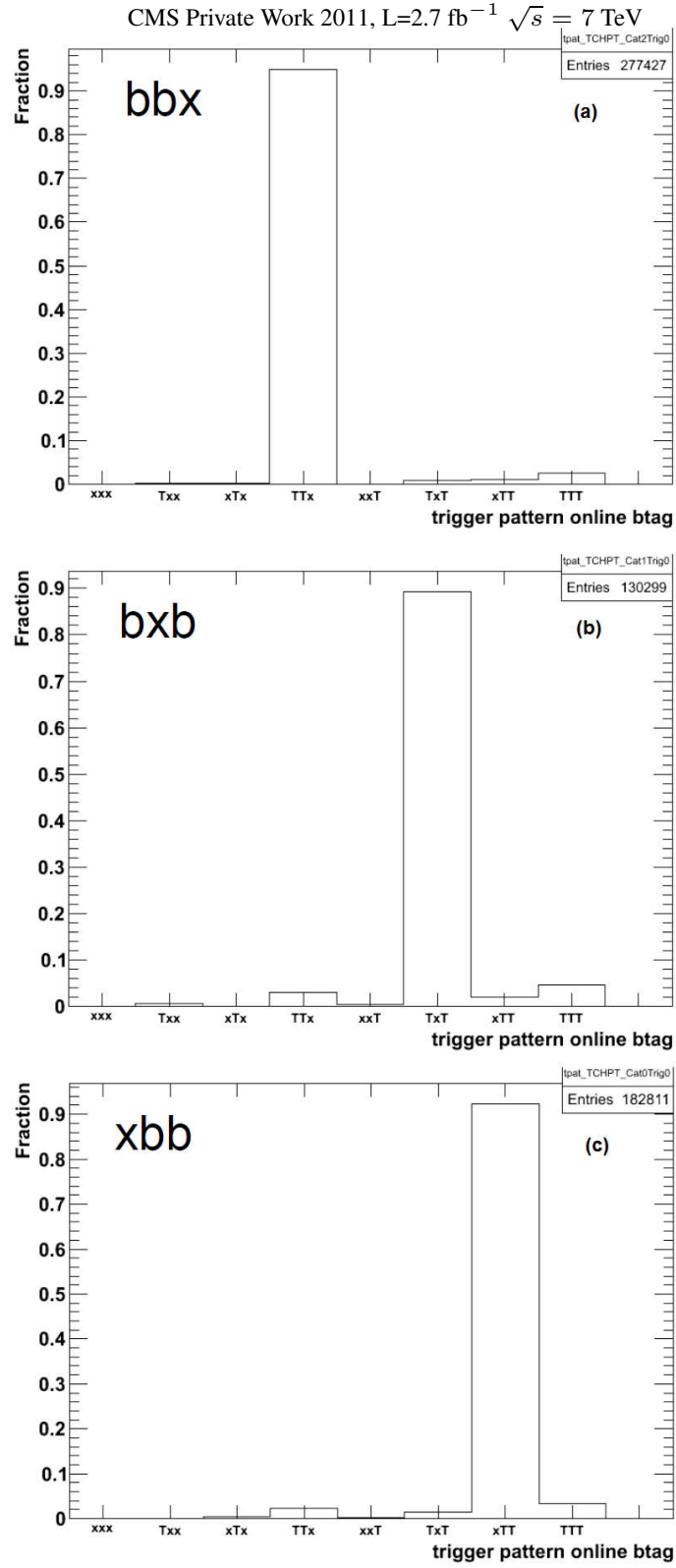


Figure 5.13: The b-tag trigger patterns for the bbb (a), bxb (b) and xbb templates from events selected in the low-mass scenario.

factor for the event category j , in each bin of the (M_{12}, B_i) space, is

$$r_{pattern}^{flav}(B_i, j) = r_{M_{12}, pattern}^{flav}(j) \cdot \sum_{tPat} r_{pattern}^{flav, tPat}(B_i, j). \quad (5.18)$$

This summation in equation (5.18) allows to avoid the introduction of new background templates. As examples, the effects of mismatched b-tag trigger patterns for the templates Xbb and bXb are illustrated in Figure 5.14.

CMS Private Work 2011, $\sqrt{s} = 7$ TeV

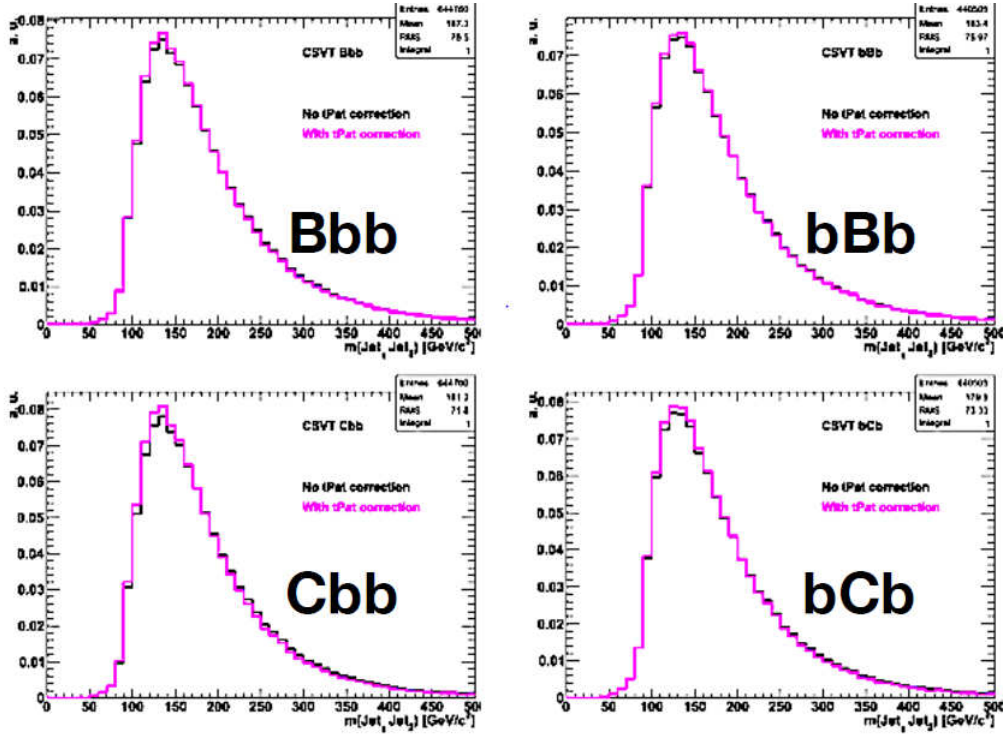


Figure 5.14: The M_{12} projections of the templates Xbb and bXb, where X=B, C, before (black) and after (pink) applying the trigger pattern correction (5.18).

5.6.4 Subtraction of non-bb contamination

The basic assumption, that the background in the double-b-tagged sample consists entirely of events with at least two b jets, is only approximately correct. Some impurity of bb pairs from non-b jets is expected, which may affect the spectrum of the templates. Although the contamination is expected to be very small, a distortion of the background templates by non-bb events could lead to a possible bias. This non-bb contribution is assessed from the measurement of the mistag fraction using the nTCHE tagger [174], as discussed in subsection 5.3.2. The double-b-tagged

event is treated as the non-bb background if at least one offline b-tagged jet is negative-tagged. The threshold, applied for the negative tagging, is determined from simulated multijet QCD events, requiring $R_{mistag} = 1$ in equation (5.8). It is defined as a function of the jet p_T for each event category and for each of the two b-tagged jets. We skip the negatively-tagged non-bb events during the templates creation. In Figure 5.15 absolute values of the nTCHE thresholds as functions of the jet p_T for the Xbb and bbX categories are shown.

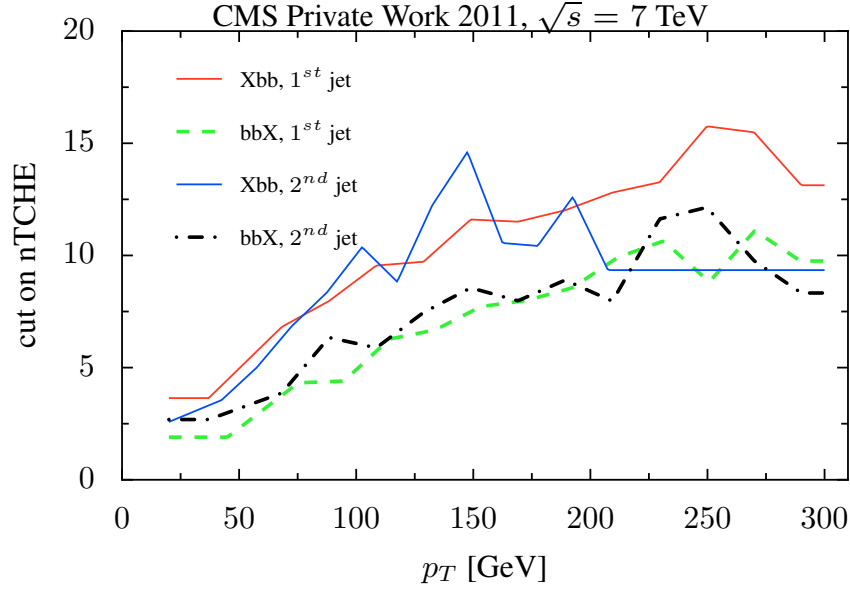


Figure 5.15: The absolute values of the nTCHE thresholds applied on the first (leading) and second (sub-leading) b-tagged jet in the Xbb and bbX samples at the CSV working point.

The absolute values of the nTCHE thresholds of the Xbb category are larger than the thresholds of the bbX category almost in the whole range of p_T , and the thresholds of both categories increase with growing jet p_T .

To validate the method of the non-bb subtraction, the fractions of non-bb events for each double-b-tagged category are estimated in bins of the di-jet invariant mass M_{12} in data events and Monte Carlo simulations. The fraction non-bb/bb is plotted in Figure 5.16. Monte Carlo predicts the fraction of non-bb events to be roughly 30% lower than what is obtained from data. The normalization of background is a free parameter in the fit of the templates to the data, therefore absolute values of such contamination are not important in the analysis. Only the effect of the non-bb impurity on shape of the templates is relevant. The M_{12} distributions with and without considering non-bb events in the double-b-tagged sample are shown in Figure 5.17.

The solid circles represent the normalized di-jet invariant mass distributions before the correction, the triangles indicate the estimated non-bb contribution, which amounts to $\sim 3-4\%$. The open squares are obtained after subtraction of the non-bb fraction and subsequent normalization. At most a marginal change in shape is found. Also the ratio of the corrected to the uncorrected

CMS Private Work 2011, $\sqrt{s} = 7$ TeV

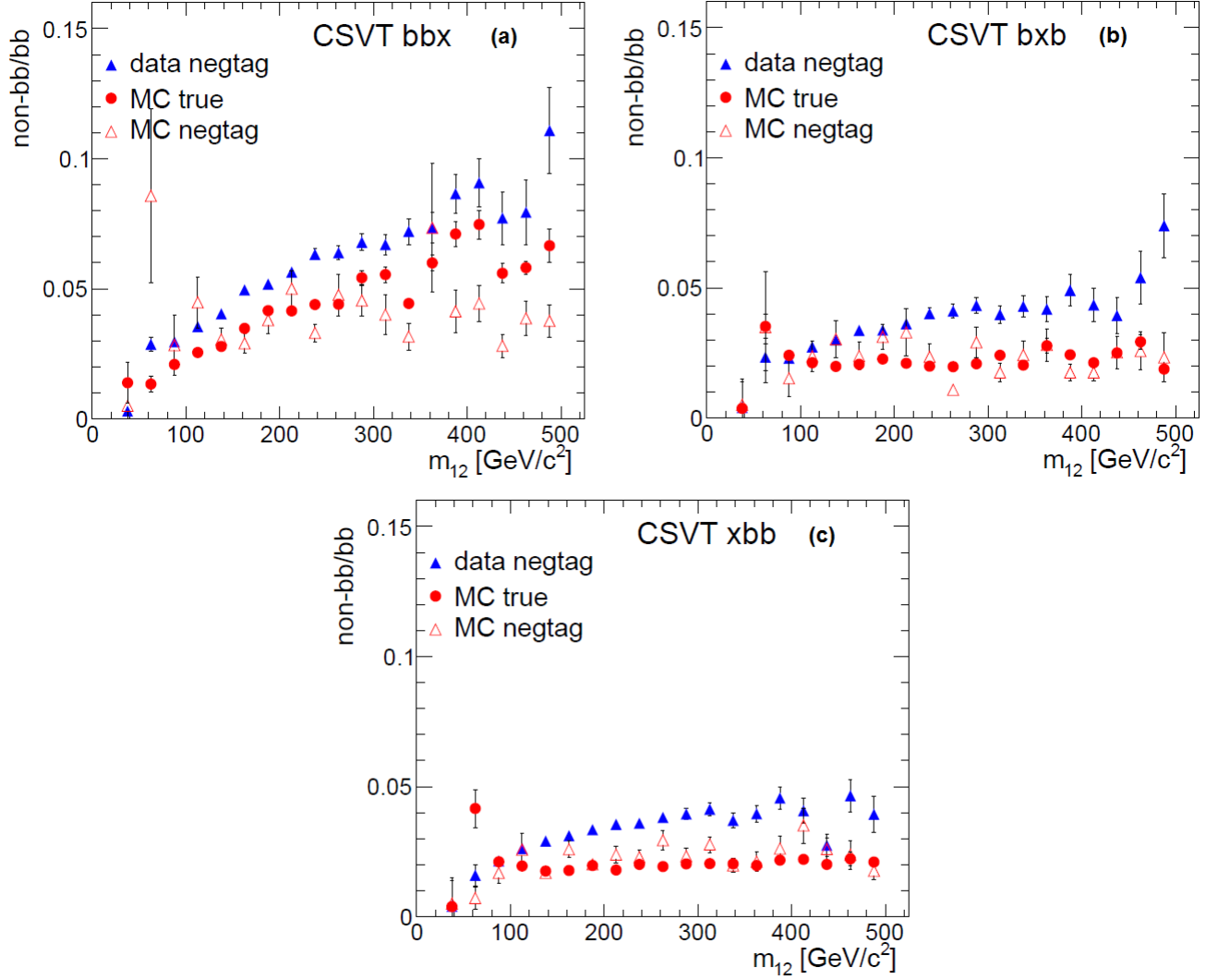


Figure 5.16: Fraction of non-bb events as a function of the di-jet mass M_{12} in the bbX (a), bXb (b) and Xbb (c) categories of the double-b-tagged sample, where b jets are tagged at the CSVt working point. The solid blue and open red triangles show the fractions of non-bb events obtained by the method of the negative fraction thresholds in data and Monte Carlo, respectively. The solid red circles represent the fractions obtained using the information from the Monte Carlo generator.

CMS Private Work 2011, $\sqrt{s} = 7$ TeV

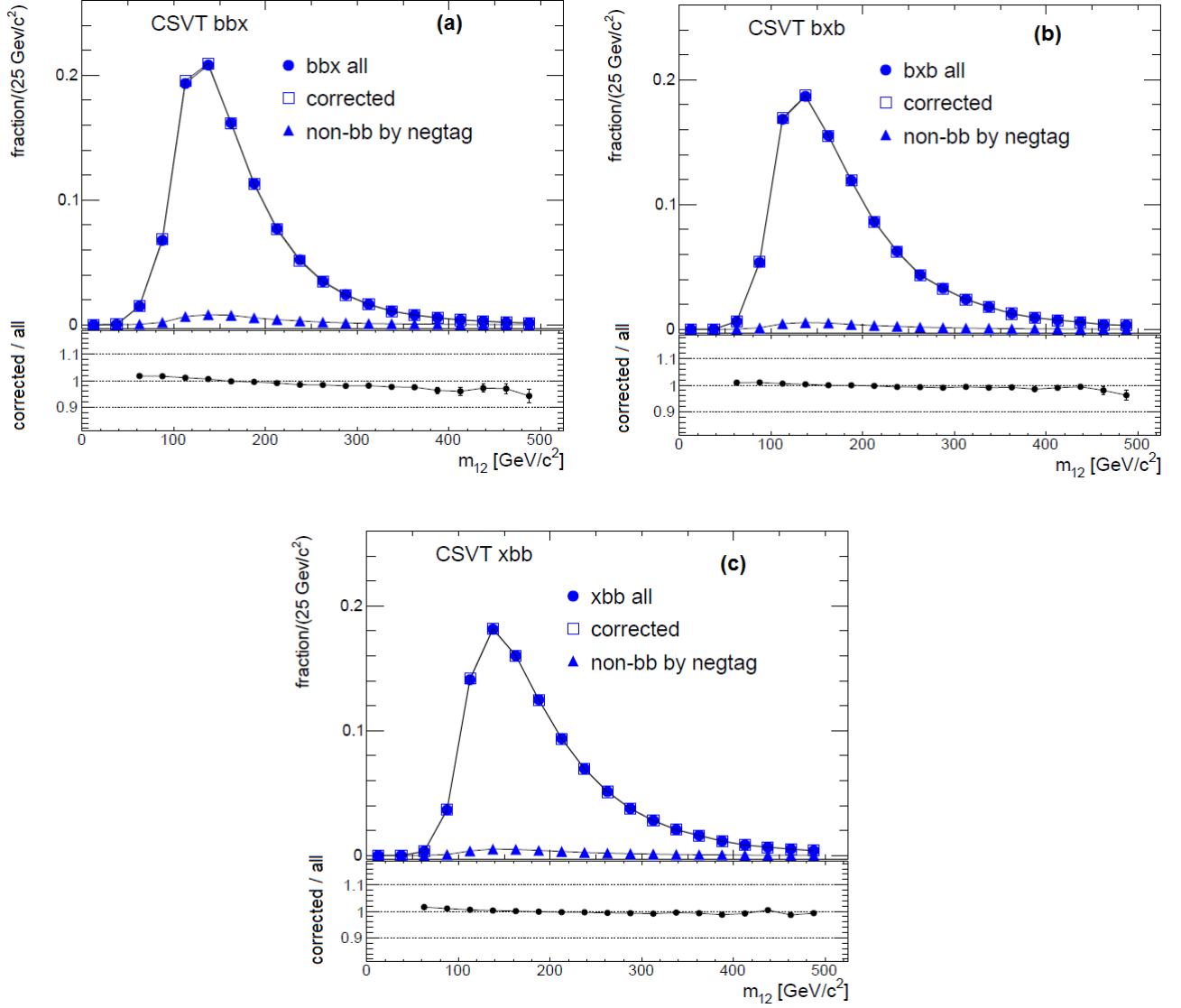


Figure 5.17: Normalized M_{12} spectra of the bbb (a), bxb (b) and xbb (c) categories before (circles) and after (squares) the correction, and the non-bb contribution (triangles) using events selected in the low-mass scenario. The ratios of the corrected over uncorrected di-jet invariant mass distributions are shown at the bottom of the plots.

shapes is shown in Figure 5.17. For the bbX sample a small negative slope for the ratio is observed. In other cases, the ratio is compatible with unity.

5.7 Test of background modeling in a signal-depleted data sample

In order to avoid possible bias in the selection procedure and background modeling, a blinding policy has been adopted. The di-jet mass distribution M_{12} has been never looked at in the triple-b-tagged sample until the analysis has been fixed and approved. During developing and commissioning the analysis, the M_{12} distributions has been only seen in the BDT control sample where the signal contribution was expected to be very small.

5.7.1 The BDT method

A control sample with three b-tagged jets is selected with criteria which suppress the signal. A Multivariate analysis (MVA) method called the gradient boosted-decision trees, **BDT**, is used. With the TMVA package [197], the **BDT** are trained using multijet QCD events, enriched by b quarks, for background and a mixture of signal events produced with Higgs boson masses of $M_H = 90, 120$ and 200 GeV. The signal events are simulated assuming the same production rate for these mass values.

The following variables are found to have discriminating power between the signal and background:

- $p_{T,3}/p_{T,1}$ - the ratio of the transverse momenta of the third and the leading jets;
- $p_{T,3}/p_{T,2}$ - the ratio of the transverse momenta of the third and the sub-leading jets;
- $|\eta_i|$ - the pseudorapidity of the three leading jets, $i = 1, 2, 3$;
- the event shape variables [198]:
 - aplanarity;
 - isotropy;
 - sphericity;
 - D ;
- $\Delta\eta_{13} = \eta_1 - \eta_3$ - the difference of the pseudorapidities of the leading and third jets;
- $\Delta\eta_{23} = \eta_2 - \eta_3$ - the difference of the pseudorapidities of the sub-leading and third jets;
- $\Delta p_{T,13} = p_{T,1} - p_{T,3}$ - the difference of the transverse momenta of the leading and third jets;

- $\Delta\phi_{i3} = \phi_i - \phi_3$, where $i = 1, 2$ - the difference of the azimuthal angles of the first and the third, and the second and third leading jets;
- $\Delta\phi_{23}^{boost12} = \phi_2^{boost12} - \phi_3^{boost12}$ - the difference of the azimuthal angles of the second and third leading jets in the reference frame of the first two leading jets;
- $\theta_i^{boost12}$, where $i = 1, 3$ - the polar angle of the first and third leading jets in the reference frame of the first two leading jets;
- $M_{ij}^{max} = \max(M_{ij}) / \sum_k p_{T,k}$, where $i, j = 1 \dots n, i \neq j$ - the ratio of the maximum value of the di-jet mass of all combinations of the n jets with $p_T > 5$ GeV and $|\eta| < 2.2$ to the sum of p_T of n jets in events passing the event selection, as discussed in the subsection 5.5;
- $M_{ij}^{min} = \min(M_{ij}) / \sum_k p_{T,k}$, where $i, j = 1 \dots n, i \neq j$ - the ratio of the minimum value of the di-jet mass of all combinations of the n jets with $p_T > 5$ GeV and $|\eta| < 2.2$ to the sum of p_T of n jets in events passing the event selection, as discussed in the subsection 5.5;

As examples, Figure 5.18 shows distributions of $p_{T,3}/p_{T,1}$, η_1 , sphericity and $\Delta\phi_{23}$. From Figure 5.18 one may conclude that these distributions are different in the background and signal events. Similar differences in shapes are found for the other quantities used in training the **BDT**.

CMS Private Work 2011, $\sqrt{s} = 7$ TeV

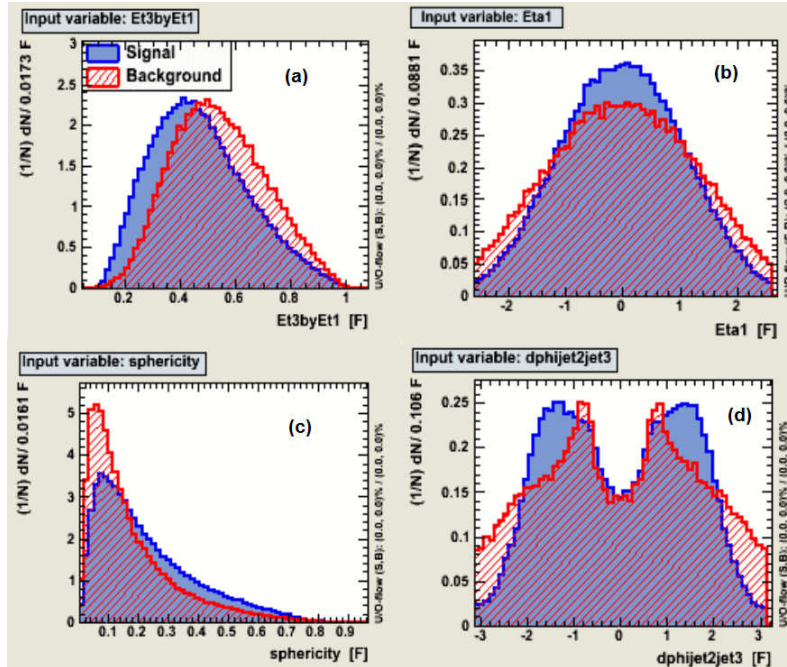


Figure 5.18: Normalized distributions of the input variables used in the MVA training: $p_{T,3}/p_{T,1}$ (a), η_1 (b), sphericity (c), $\Delta\phi_{23}$ (d).

The normalized BDT distributions for the signal and the background in a test sample independent of the sample used in the training are shown in the Figure 5.19. A good separation between the signal and the background is observed.

A control triple-b-tagged sample, corresponding to the highlighted region in Figure 5.19, is defined, where the signal will be depleted. The cut on the **BDT**, $\text{BDT} \leq -0.06$, is chosen what corresponds to an enhancement by a factor of 3 of the background to signal ratio.

CMS Private Work 2011, $\sqrt{s} = 7 \text{ TeV}$

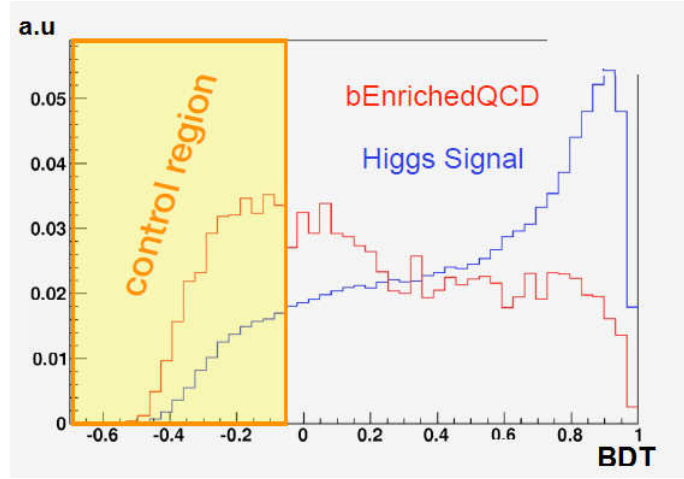


Figure 5.19: The distributions of the **BDT** for events in the signal (blue) and background (red) samples. The “control region” denotes the BDT discriminant range, where the signal is depleted.

In the control region, using the selection of the low-mass scenario, the expected signal fraction, S/B , for a Higgs boson with mass $M_H = 120 \text{ GeV}$ in the MSSM m_h^{max} scenario at $\tan \beta = 20$ is 0.0067. This is shown in Figure 5.20.

After selecting the control sample, the shape of the M_{12} distribution, obtained in simulated heavy-flavor multijet QCD events, is slightly changed at low values, as shown in Figure 5.21.

5.7.2 Closure test of background modeling

A priori estimates of the background normalizations is done for the bbX , bXb and Xbb double-b-tagged samples. Using QCD events simulated by the `Pythia6` program, the fractions of c and b flavors for the untagged jet are estimated. The light-flavor fraction is taken to be the complement of the heavy-flavor fractions. The fractions are parametrized as function of the jet p_T and varied from 4% to 8% and 4% to 6% in the case of b and c jets, respectively. Each of the nine double-b-tagged templates is weighted by the flavor fraction according to the assumed flavor of the untagged jet. The background predicted from double-b-tagged data sample is compared then with the triple-b-tagged data sample in the BDT control region. An agreement within a few

CMS Private Work 2011, $\sqrt{s} = 7$ TeV

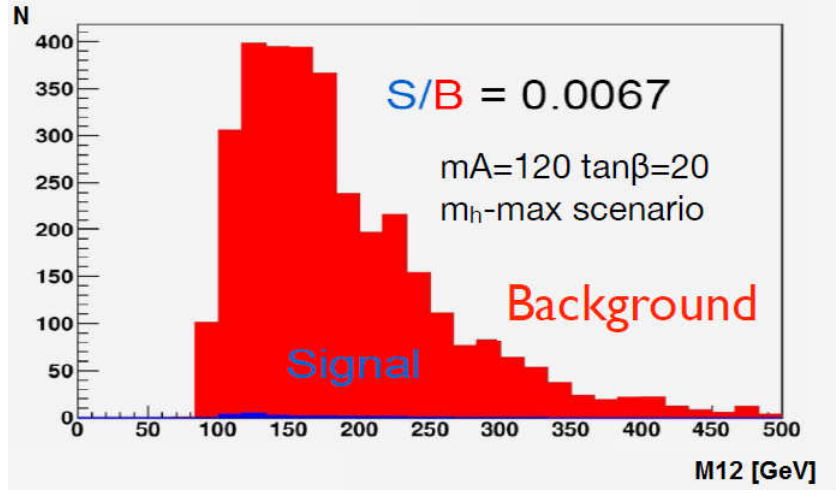


Figure 5.20: The di-jet mass M_{12} distribution for events selected in the low-mass scenario for the heavy-flavor multijet QCD enriched by b quarks (red) and Higgs boson signal with $M_H = 120$ GeV in the m_h^{max} scenario at $\tan = 20$ (blue) samples selected by the requirement $BDT \leq -0.06$.

CMS Private Work 2011, $\sqrt{s} = 7$ TeV

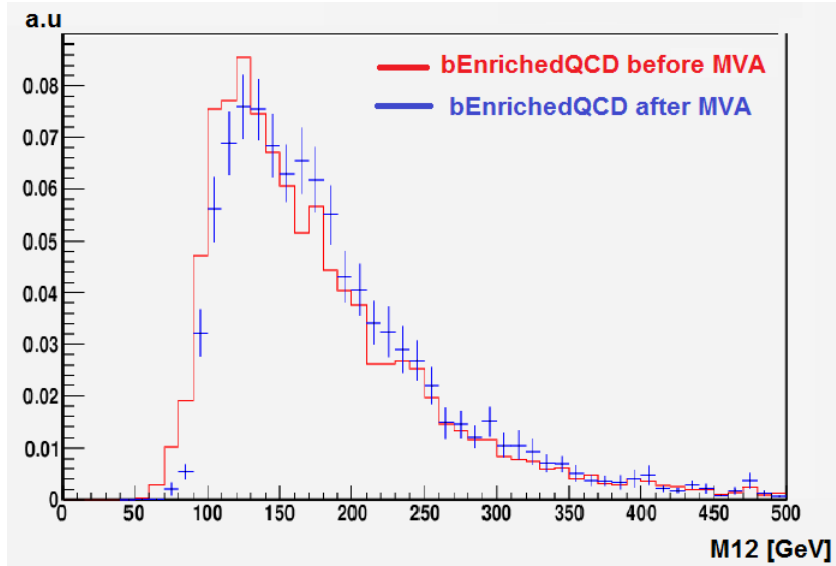


Figure 5.21: The distributions of di-jet invariant mass M_{12} in the low-mass scenario for the whole background sample (red) and for events in the control region (blue). Both distributions are normalized to unity.

per cent between the M_{12} distributions of events from the signal-depleted data sample and of the background prediction from extrapolation of the double-b-tagged data sample is shown in Figure 5.22 for the low-mass scenario. The ratio of the M_{12} distributions in the signal-depleted data sample and the extrapolation of the double-b-tagged data sample is close to 1, as shown in Figure 5.22.

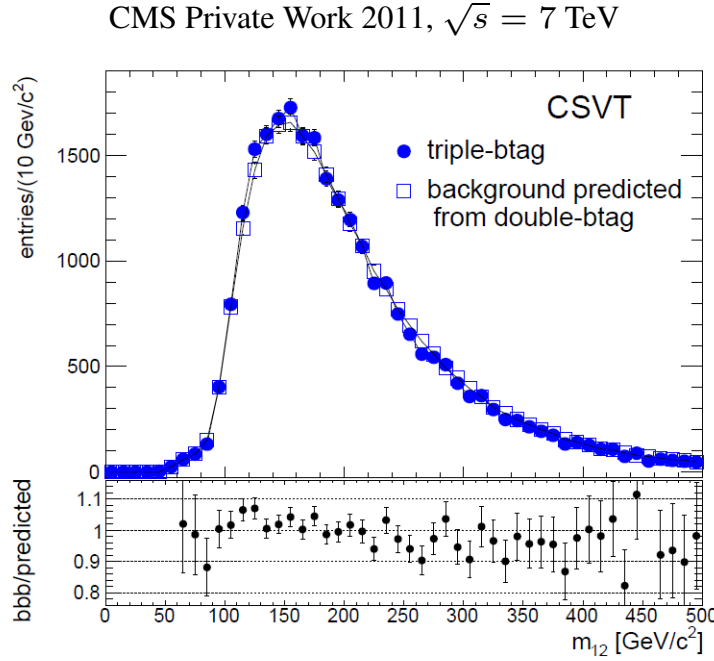


Figure 5.22: The M_{12} distributions of events in the BDT control sample (solid points) and of the background prediction from the extrapolation of the double-btag sample (open squares) and their ratio in the low-mass scenario.

The fit, discussed later in Section 5.8.4, of templates built in the BDT control samples is used to test the procedure of the background normalization. The fit results are plotted in Figure 5.23.

The fit shows $\chi^2/Ndf = 120/115$ with a corresponding probability of 0.33. According to the template fit, the dominant background contribution of about 70% is attributed to triple-b-jets events, in a good agreement with the Monte Carlo predictions summarized in Table 5.5.

5.8 Signal modeling

In order to measure the signal yield, the proper templates are derived for each Higgs mass hypothesis using the Monte Carlo samples generated for Higgs boson masses of 90, 100, 120, 130, 140, 160, 180, 200, 250, 300 and 350 GeV.

The modeling of the signal templates is based on the following chain:

CMS Private Work 2011, $\sqrt{s} = 7$ TeV

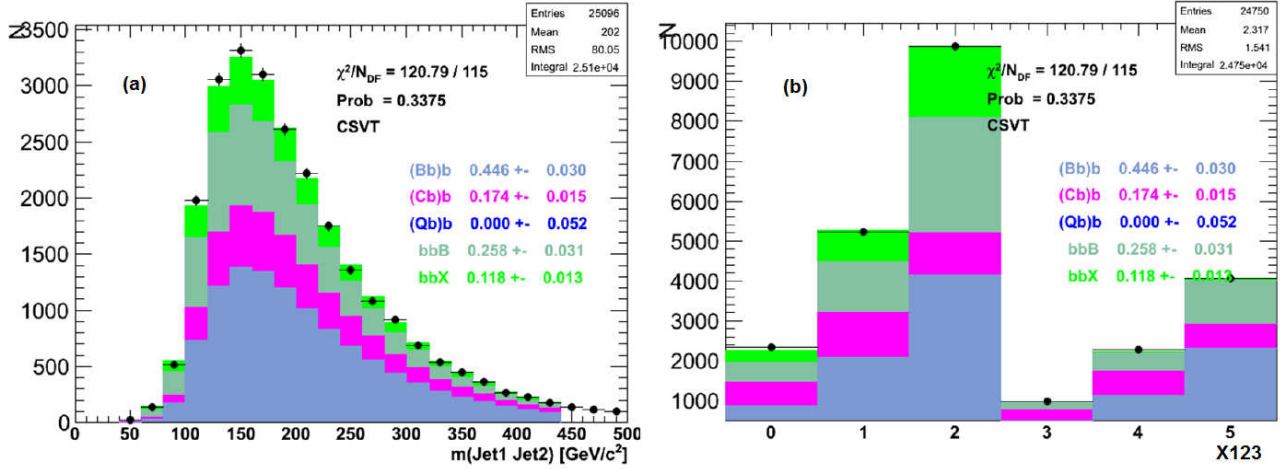


Figure 5.23: The M_{12} (a) and X_{123} projections after the fit of the (Bb) b, (Cb) b, (Qb) b, bbB bbX templates to the data using events from the BDT sample in the low-mass scenario. The dots are data and the stacked histograms are the combination of the templates normalized to data.

- selection of the events according to the criteria of the mass scenario, as discussed in subsection 5.5;
- splitting the signal sample into independent subsamples, applying the L1/L2 (5.1) and relative trigger b-tagging (5.6) efficiencies in the subsamples to simulate the trigger;
- application of the offline b-tagging efficiencies, shown in Figure 5.7, to model the CVS b-tagging at the tight working point;
- the pile-up reweighting, as described in subsection 5.8.1, to take into account pile-up interactions in data;
- combining the subsamples in proportions relative to the integrated luminosities of the triggers and calculation of selection efficiency of the merged signal samples.

For example, the signal events used in the low-mass scenario are splitted into two statistically equal subsamples to simulate the two triggers of the scenario. Each subsample is reweighted on an even-by-event basis by the same relative trigger and offline b-tagging efficiencies and the pile-up weights. The L1/L2 weights for the two triggers are different. In each subsample the signal template is built. Afterwards the signal templates are merged in fractions of 0.64 and 0.36 in accordance with the integrated luminosities for each trigger. The obtained two-dimensional histogram is normalized to unity. Figure 5.24 presents the distribution of M_{12} for the signal events with the Higgs boson mass of 120 GeV selected by the two triggers, “Trig0” and “Trig1”,

in the low-mass scenario. The distributions are summed and normalized to unity giving the signal template.

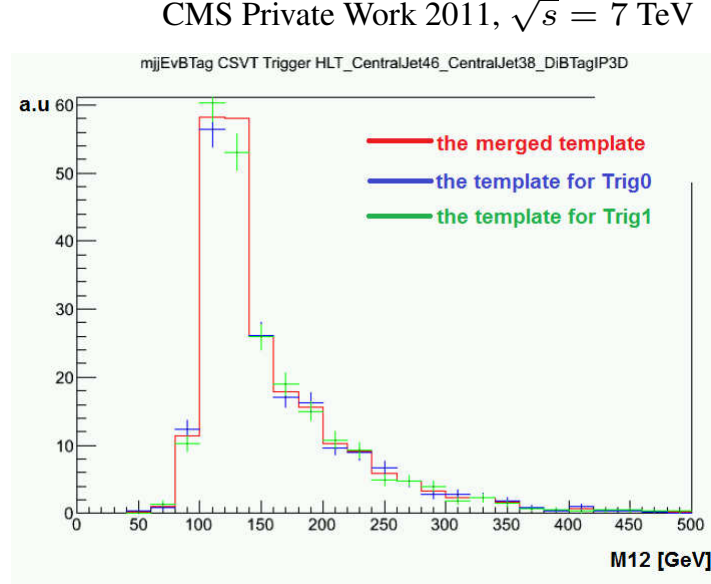


Figure 5.24: The M_{12} normalized to unity distributions of the signal events with the assumed Higgs boson mass of 120 GeV selected with “Trig0” (blue) and “Trig1” (green) triggers in the low-mass scenario. The red histogram, normalized to unity, represents M_{12} after merging the “Trig0” and “Trig1” distributions.

There are only marginal changes in shapes of the signal subtemplates caused by difference in the L1/L2 efficiencies of the two triggers.

The final signal templates, obtained by merging the histograms of the subsamples, are shown in Figure 5.25 for Higgs mass hypotheses of $M_H=120, 180$ and 250 GeV.

As expected, the X_{123} distributions are almost identical for the given masses, while the M_{12} projections are characterized by peaks around the assumed values of the Higgs boson mass.

5.8.1 Pile-up reweighting

The signal Monte Carlo samples are generated with pile-up interactions superimposed on the process of the Higgs boson production, $gg \rightarrow bb + \Phi(=h/H/A)$. These simulated additional interactions roughly cover the distribution of the number of pile-up interactions in the data. Therefore, the Monte Carlo samples must be reweighted such the distribution of the number of pile-up interactions matches the observed distribution in the data.

There are at least two relatively robust ways of obtaining the distribution of the observed number of pile-up interactions in the data. One of these is to simply count the number of reconstructed primary vertices in events of the data sample. The average number of additional vertices is proportional to the number of additional interactions with about 70% vertex reconstruction

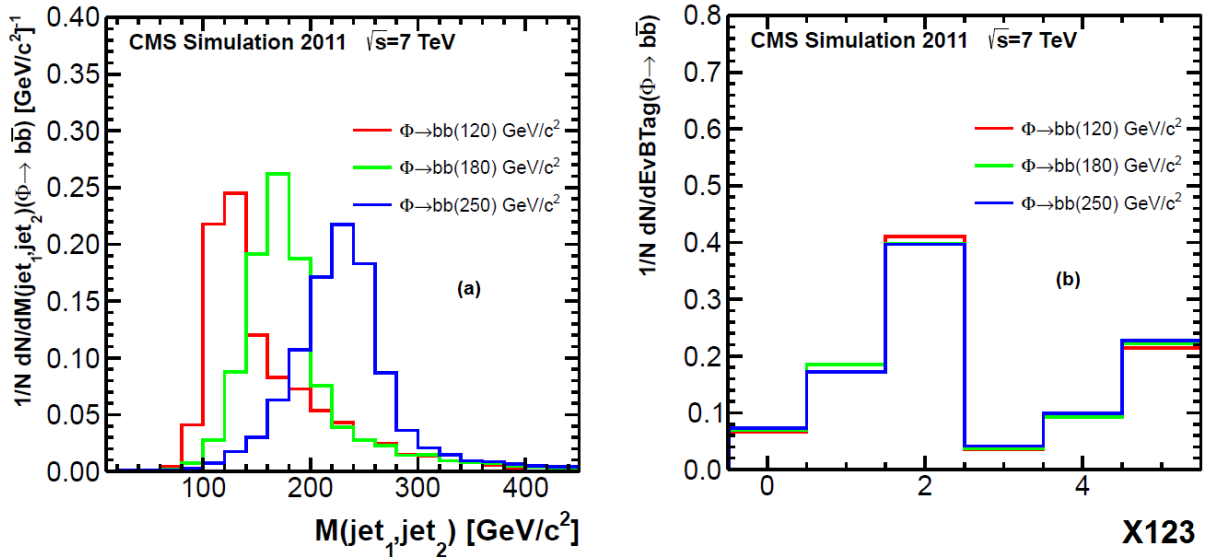


Figure 5.25: The M_{12} (a) and X_{123} (b) projections of the signal templates for three different masses of the Higgs boson, $M_A = 120, 180, 250$ GeV applying the low-mass scenario selection.

efficiency to be taken into account. So, the average number of reconstructed vertices divided by 0.7 is a good estimate of the number of additional interactions in the data.

However, the final distribution for the number of reconstructed primary vertices is sensitive to the settings of the primary vertex reconstruction and properties of underlying events, a priori different for data and MC. Additionally, the trigger may introduce a bias in the distribution for the number of reconstructed vertices.

Due to these reason, an approach, based on the measurement of the instantaneous luminosity, \mathcal{L}_{inst} is applied. Multiplying the instantaneous luminosity by the minimum bias cross section, $\sigma_{mb} \sim 71.3$, average number of pile-up interactions per bunch crossing, \mathbf{BX} , is

$$N_{BX}^{pile-up} = \frac{\mathcal{L}_{inst} \cdot \sigma_{mb}}{N_b}, \quad (5.19)$$

where N_b is the number of bunch crossings per second. The distribution of observed pile-up interaction in one luminosity section, \mathbf{LS} , corresponding to 23.3 seconds, is a Poisson distribution with the mean corresponding to $N_{BX}^{pile-up}$ (5.19). To obtain the distribution of the pile-up interactions for a full run, the Poisson distributions are summed up with fractions of the integrated luminosity in the \mathbf{LS} in the run.

The distributions of the number of pile-up interactions observed in the LHC 2011 runs and simulated in the Monte Carlo samples are shown in Figure 5.26. The distributions are normalized to unity.

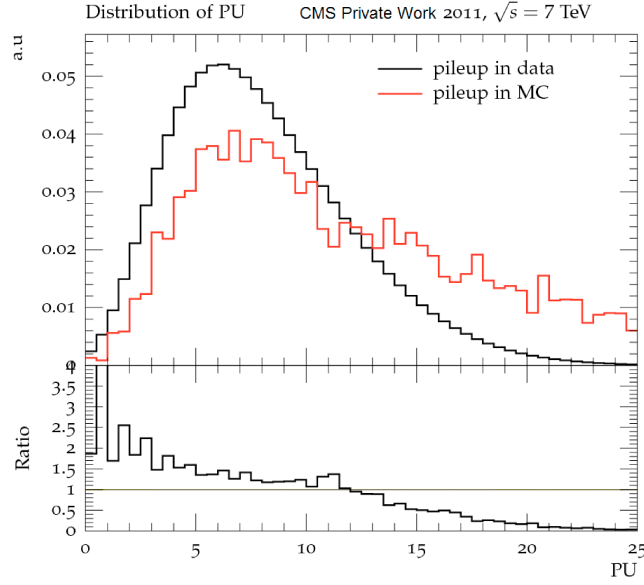


Figure 5.26: The distribution of the number of pile-up interactions per **BX** in data (black) and Monte Carlo (red).

The Data/MC ratio of the distribution of the number of pile-up interactions per **BX**, shown at the bottom of Figure 5.26, is used to reweight the signal Monte Carlo samples.

As a closure test, the signal events with the assumed Higgs boson mass of 120 GeV are reweighted by this ratio on the event-by-event basis. The distributions for the number of the **PV** selected, as discussed in Section 5.5, are obtained with and without applying the pile-up reweighting to the signal events. This is shown in Figure 5.27. Good agreement between the distributions of the number of the **PV** from data and Monte Carlo after the pile-up reweighting is found.

5.8.2 Di-jet mass resolution

The di-jet mass resolution is essential for mass measurements of the MSSM Higgs bosons produced in the channel $gg \rightarrow bb + \Phi (= h/H/A) \rightarrow 4b + \text{jets}$. To study the resolution in the measurements of the invariant mass of two leading jets, we calculate M_{12} in the signal samples. Using the information from the Monte Carlo generator, we distinguish between two categories of events:

- the two leading jets originate from b quarks of the Higgs boson decay;
- one or two leading jets are not stemming from the Higgs boson decay.

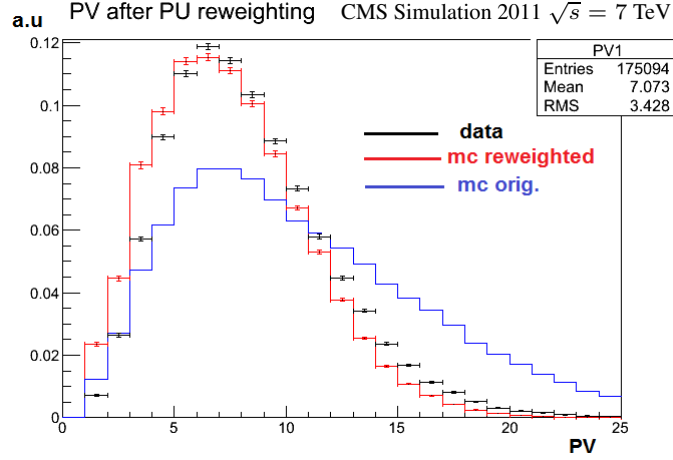


Figure 5.27: Distributions of the number of reconstructed primary vertices with (red) and without (blue) pile-up reweighting in simulated events, The black histogram is the distribution of the number of the **PV** observed in 2011 data.

From the di-jet mass distribution of events in the first category its peak position, M_{peak} , and its RMS are obtained. The mass resolution is defined as

$$\sigma_{M_{12}} = \frac{RMS}{M_{peak}}. \quad (5.20)$$

The distribution of the di-jet invariant mass of the jets from the Higgs boson is almost Gaussian. The M_{12} spectrum of events from the second category is used to estimate the combinatorial background. The purity of the Higgs boson signal is defined as

$$\text{purity} = \frac{N_{events}^{1^{st} \text{ categ.}}}{N_{events}^{1^{st} \text{ categ.}} + N_{events}^{2^{nd} \text{ categ.}}}, \quad (5.21)$$

where $N_{events}^{1^{st} \text{ categ.}}$ and $N_{events}^{2^{nd} \text{ categ.}}$ are numbers of the signal events in the first and second categories, respectively. The purity equals to unity, when all pairs of leading jets, contributing to M_{12} , stem from the Higgs boson. Zero purity corresponds to the case when there are no selected signal events with two leading jets originating from b quarks of the Higgs boson decay.

Figures 5.28 (a) and (b) shows M_{12} spectra of triple-b-tagged events in the two signal categories with the assumed Higgs boson masses of 120 and 200 GeV. The RMS of the green spectra, where the two leading jets stem from the Higgs boson decay, are 15 and 25 GeV, respectively. The positions of the corresponding peaks are at 117 GeV and 188 GeV, respectively. The combinatorial background has an asymmetric shape with a long tail to large mass values. The resolution of di-jet mass for jets stemming from the Higgs boson and the purity of the Higgs

signal as functions of the Higgs mass are shown in Figures 5.29 (a) and (b). The quantity $\sigma_{M_{12}}$ is slightly varying from 12% to 14% with increasing values of the Higgs boson mass.

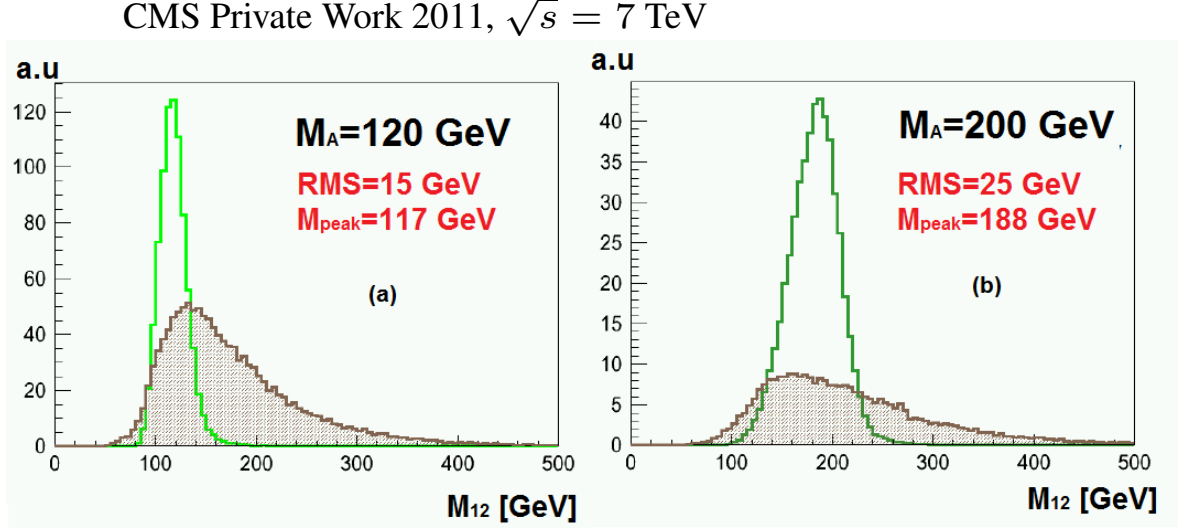


Figure 5.28: The M_{12} distributions in the triple-b-tagged signal samples generated with the Higgs boson masses of 120 GeV (a) and 200 GeV (b). The green distributions originate from events of the first category, while the brown distributions correspond to the second event category.

Two different modes of the purity estimation are considered. In the first case, the ratio (5.21) is calculated over all bins of the M_{12} distributions. This is illustrated as the black curve in Figure 5.29 (b). It is found that the signal with Higgs boson masses up to 100 GeV has large contamination of M_{12} from the combinatorial background which may reach up to 80%. In the case of medium masses of the Higgs boson, the combinatorial background is reduced to 40% and 30%, when the Higgs boson mass reach 180 and 350 GeV, respectively. In the second case, the purity calculation is restricted to the events in the mass window of \pm RMS around M_{peak} . In these events, the signal purity is increased by a factor varying between 2.5 for the M_H value of about 100 GeV and 1.2 for the Higgs mass of about 350 GeV, as demonstrated by the blue curve in Figure 5.29.

5.8.3 Signal efficiencies

The efficiencies of the signal trigger and offline selections, discussed in Sections 5.2 and 5.5, are estimated from simulated signal samples and summarized in Table 5.6. Figure 5.30 plots the efficiency of the signal selection in the low- and medium-mass scenarios as a function of the mass of the MSSM pseudoscalar Higgs boson.

CMS Private Work 2011, $\sqrt{s} = 7$ TeV

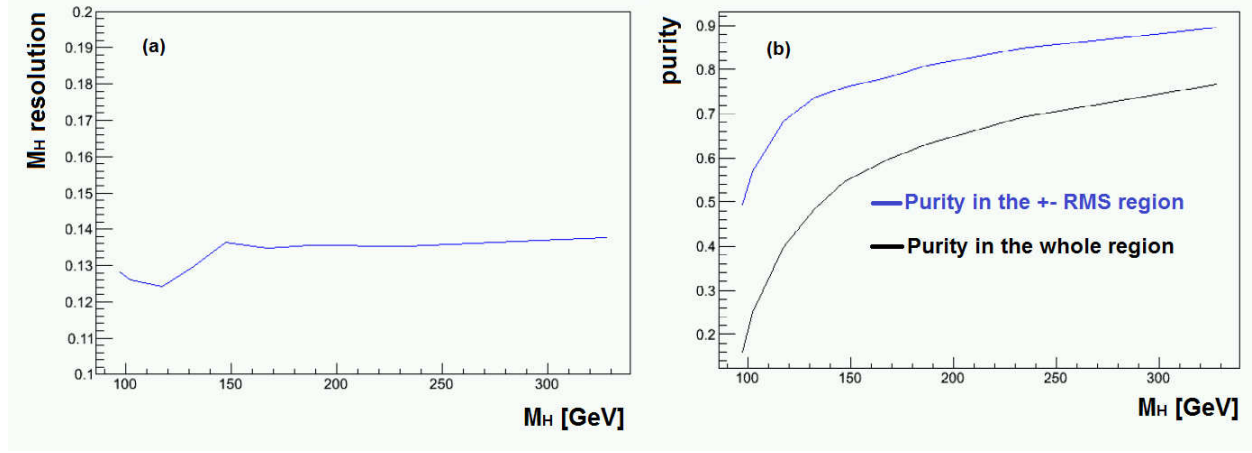


Figure 5.29: The di-jet mass resolution (a) and signal purities (b) as functions of the Higgs boson mass. The blue curve in (b) is the purity obtained for events within the \pm RMS window around M_{peak} , while the black graph is the purity estimated in the whole range of M_{12} values.

Table 5.6: Signal efficiencies ϵ_S for several masses of the MSSM pseudoscalar neutral Higgs boson in the low- and medium-mass scenarios.

M_A [GeV]	$\epsilon_S(\text{low-mass})$	$\epsilon_S(\text{medium-mass})$
90	0.129%	0.070%
100	0.179%	0.099%
120	0.342%	0.183%
130	0.430%	0.247%
140	0.522%	0.334%
160	0.707%	0.536%
180	0.876%	0.717%
200	1.001%	0.901%
250	1.256%	1.227%
350	1.416%	1.401%

The signal efficiencies in the medium-mass scenario are smaller than the efficiencies in the low-mass hypotheses. Depending on the Higgs boson mass, the efficiency varies from 0.13% to 1.40%, corresponding to the expected numbers of signal events from 351 to 6580 at an assumed Higgs boson production cross section of 100 pb.

The efficiency of the signal selection of the low-mass scenario is about two times larger than the efficiency of selection in the medium-mass scenario at low values of the Higgs boson mass. This is explained by the fact that the jet triggers of the low-mass scenario have lower p_T thresholds, making them more efficient, in comparison with the jet triggers of the medium-mass scenario. At medium Higgs boson masses, $250 \text{ GeV} < M_\Phi < 350 \text{ GeV}$, b jets, originating from the Higgs decay, have harder p_T spectra, suppress the discrepancy between the selection efficiencies of the low- and medium-mass scenarios.

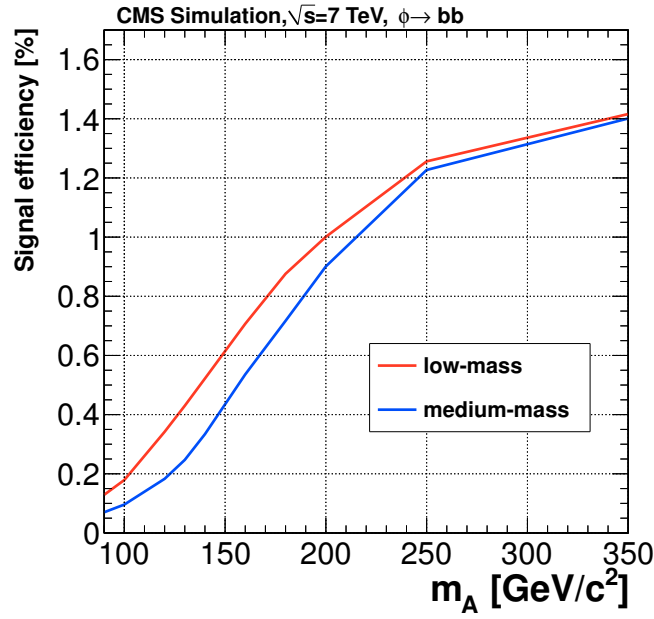


Figure 5.30: Signal efficiencies as function of M_A in the low-mass (red curve) and medium-mass (blue curve) scenarios.

5.8.4 Signal extraction from the data

A linear combination of the signal and background templates is fitted to data using a binned least-squares fit [199, 200] in the two dimensions, M_{12} and X_{123} . The χ^2 function minimized in the fit is defined as

$$\chi^2 = \sum_{ij} \frac{\left[N_{ij}^{obs} - \left(\sum_b f_b N_{ij}^b + f_s N_{ij}^s \right) \right]^2}{(\sigma_{ij}^{obs})^2 + (\sigma_{ij}^{templ})^2}, \quad (5.22)$$

where N_{ij}^{obs} is the number of observed events in the bin (i,j), N_{ij}^b and N_{ij}^s are the bin contents of the five background and one signal templates. The parameters f_b and f_s are free parameters to be

fitted. They represent the fractions of the background and signal, respectively. The parameters f_b are constrained to be non-negative. The templates content is scaled to the total number of observed events. The denominator in equation (5.22) is the sum of the quadratic errors of the number of observed events, σ_{ij}^{obs} , and the statistical uncertainty of the templates, σ_{ij}^{templ} , in the bin (i,j).

Due to statistical fluctuations, bins with no observed events may give numerically unstable solutions on the f_b and f_s parameters, which minimize the χ^2 function (5.22). The following two additional criteria are required in order to have a stable chi-square minimization:

- we restrict the fit to bins, where $N_{ij}^{obs} \geq 1$;
- the range and binning of (M_{12}, X_{123}) is adopted such that 80% of bins contain $N_{ij}^{obs} \geq 5$.

Therefore, the binning and range of X_{123} is fixed and defined as six bins of equal width in the range $(-0.5, 6)$. The binning and range of M_{12} is chosen to be flexible allowing us to avoid bins with low-event occupancy. The final configuration of the M_{12} projection covers the range of $[60, 440]$ GeV with bins of equal width.

5.8.5 Test of the fit with signal templates

The fitting procedure has been validated by artificial injection of the simulated signal events into the signal-depleted data sample. The fits are performed and the fractions of the injected signal events are compared with the fit results. We run 100 pseudo-experiments for Higgs boson masses of 90, 120, 180 and 250 GeV. In each pseudo-experiment the number of signal events added to the data histogram is

$$N^s = \varepsilon_s(M_H) \sigma_{NNLO}^{mhmax}(M_H, \tan \beta = 20) \mathcal{L}_{int}, \quad (5.23)$$

where $\varepsilon_s(M_H)$ is the signal efficiency reported in Table 5.6, $\sigma_{NNLO}^{mhmax}(M_H, \tan \beta = 20)$ is the cross section (2.75) of the Higgs boson production calculated with NNLO accuracy [181, 182, 183] in the MSSM m_h^{max} scenario at $\tan \beta = 20$ and \mathcal{L}_{int} is the integrated luminosity of either low- or medium-mass scenarios. \mathcal{L}_{int} amounts for 2.67 fb^{-1} and 3.99 fb^{-1} , respectively, for the selection in the low- and medium-mass scenarios. In each pseudo-experiment the injected signal is randomized accordingly to the Poisson distribution.

The results for each considered M_H value are summarized in Table 5.7. The statistical errors of the fitted parameter f_s , $\sigma(f_s)$, correspond to the variation of χ^2 around the minimum by $\Delta\chi^2 = 1$.

Table 5.7: The fit results on $f_s \cdot (N^s + N^{obs})$ and $\sigma(f_s) \cdot (N^s + N^{obs})$ for various masses of the MSSM pseudoscalar neutral Higgs in N^{obs} events of the triple-b-tagged BDT sample, when N^s signal events were injected.

M_A [GeV]	N^s	$f_s \cdot (N^s + N^{obs})$	$\sigma(f_s) \cdot (N^s + N^{obs})$
90	3733	4538	865
120	3804	3954	354
180	1969	2174	263
250	680	560	176

5.8.6 Background-only fit

A priori estimation of the background in both scenarios is needed to evaluate the expected upper limits on the Higgs boson cross sections, discussed later in Section 5.11. The fit (5.22) with unconstrained parameters f_b is performed in the triple-b-tagged sample without the inclusion of the signal template. The obtained results for the low- and medium-mass scenarios are given in Table 5.8 and Figures 5.31 and 5.32.

Table 5.8: The fractions of the various background templates in the data samples selected in the low- and medium-mass scenarios from the background-only fit.

Template	f_b (low-mass)	f_b (medium-mass)
(Bb) b	0.48 ± 0.02	0.46 ± 0.02
(Cb) b	0.13 ± 0.01	0.14 ± 0.01
(Qb) b	0.00 ± 0.01	0.00 ± 0.01
bbB	0.27 ± 0.01	0.29 ± 0.03
bbX	0.13 ± 0.01	0.11 ± 0.01

As can be seen from Figures 5.31 and 5.32, the background model fits the data well within the statistical uncertainty, given by the upper area of each bin of cyan color. According to the fit, events with three b jets constitute the largest contribution to the background, $(74.3 \pm 2.5)\%$, in the sample selected in the low-mass scenario. This is qualitatively expected and consistent with $(72.0 \pm 4.1)\%$ obtained from Monte Carlo samples generated by Pythia6, as listed in Table 5.5. The fit of background templates to the data converges with $\chi^2/Ndf = 121/112$ and $\chi^2/Ndf = 100/112$ for the triple-b-tagged sample selected in low- and medium-mass scenarios, respectively.

CMS 2011, $L=2.7 \text{ fb}^{-1}$, $\sqrt{s} = 7 \text{ TeV}$

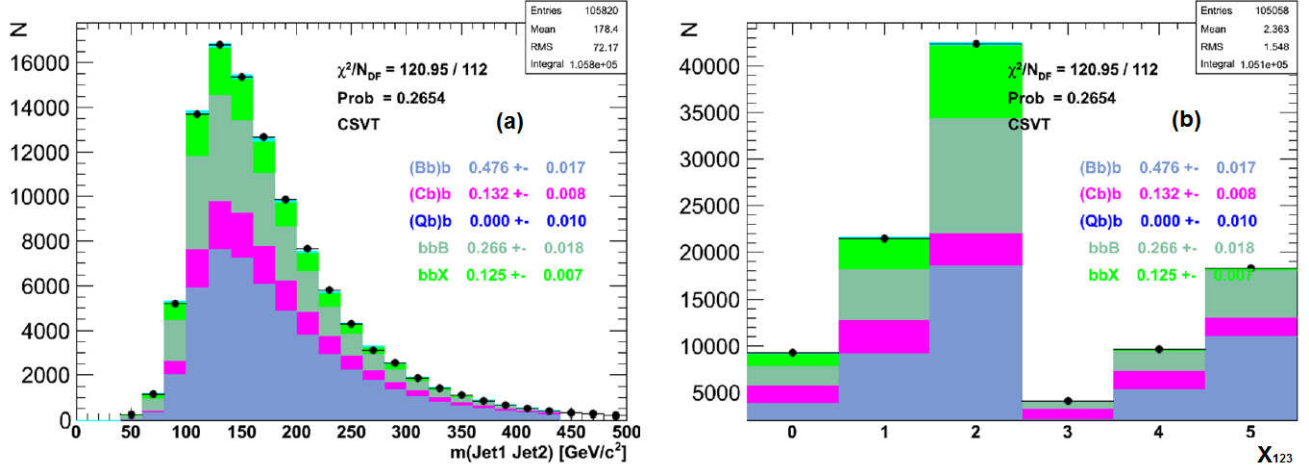


Figure 5.31: The results of the background-only fit in the triple-btag data sample selected in the low-mass scenario: the projection to di-jet invariant mass (a), the projection to the X_{123} axis (b). The cyan area corresponds to uncertainties originating from statistical errors of the templates.

CMS 2011, $L=4.0 \text{ fb}^{-1}$, $\sqrt{s} = 7 \text{ TeV}$

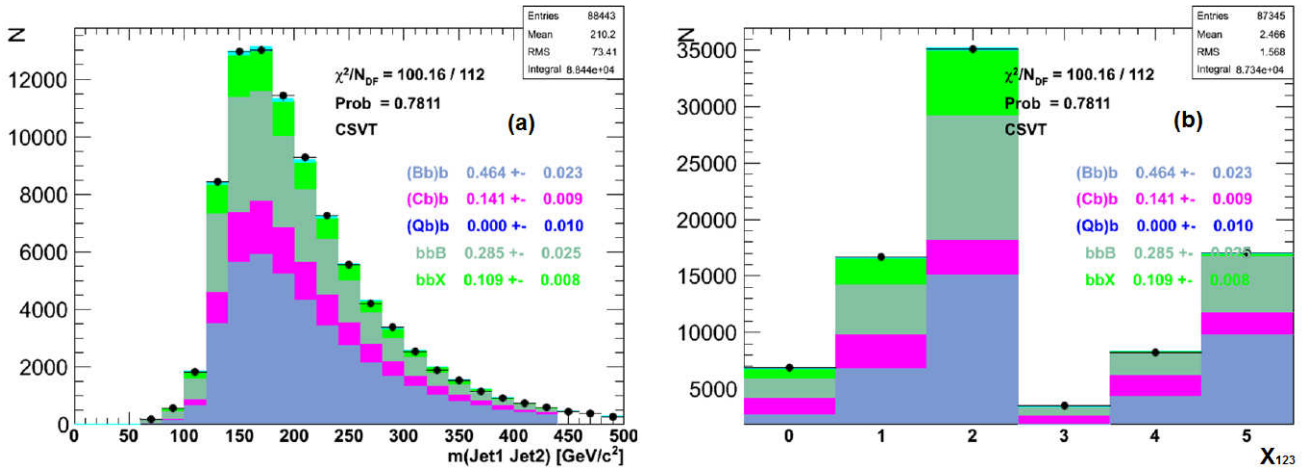


Figure 5.32: The results of the background-only fit in the triple-btag data sample selected in the medium-mass scenario: the projection to di-jet invariant mass (a), the projection to the X_{123} axis (b). The cyan area corresponds to uncertainties originating from statistical errors of the templates.

5.9 The systematic uncertainties

The systematic uncertainties are divided into two different types. The first type consists of uncertainties, that affect only the signal efficiency and thus the measured signal yields. They are called “signal yield” uncertainties. The uncertainties of the second type affect the signal efficiency, but also change the shapes of the signal and background templates. The shape change is quantified by its effect on the estimated signal fraction f_s . Such uncertainties are called “shape” uncertainties.

5.9.1 The uncertainties on the signal yield

There are several kinds of uncertainties altering the signal yield.

First, there is the luminosity uncertainty, measured to be 2.2%. The second source of uncertainty is the turn-on behavior of the the L1/L2 efficiency (5.1), given the rather low thresholds used in the event selection. Varying the parameters of equation (5.1) within the statistical errors given in Table 5.4, the relative change of at most 10% for the L1/L2 efficiency is observed. Next, there are a few sources of uncertainties affecting the measurement of the b-tagging efficiency and thus the scale factors $SF_{b,c,udsg}$. They are identified in Refs. [201, 174] and the uncertainties given there are taken. Effects of these uncertainties on the scale factors $SF_{b,c}$ and SF_{udsg} are shown in Figures 5.33 (a) and (b).

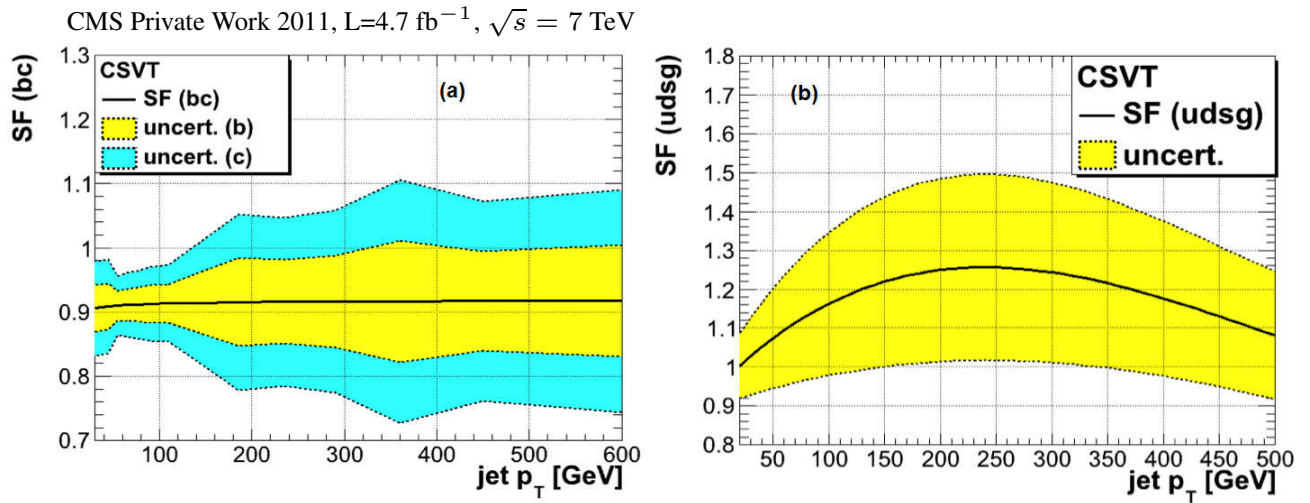


Figure 5.33: The combined statistical and systematic uncertainties on the scale factors $SF_{b,c}$ (a) as functions of the jet p_T , presented as bands of yellow, for b jets, and cyan, for c jets, colors. The systematic uncertainty on the scale factor SF_{udsg} as a function of the jet p_T (b).

The factor SF_c is conservatively taken as fully correlated with SF_b meaning that when the value of SF_b is varied by $\pm 2\sigma$ because of the uncertainty, the scale factor SF_c is also changed by $\pm 2\sigma$.

The scale factor $SF_{uds\bar{g}}$ is uncorrelated to SF_c and SF_b . From Figures 5.33 (a) and (b), the relative uncertainties on the scale factors are varied between 10% and 20% at low (high) and medium values of the jet p_T , respectively.

We have estimated from simulations of the triggers a relative uncertainty of 15% on the efficiency of the trigger b-tagging for each b-tagged jet at the **HLT** path. In addition, using simulated $t\bar{t}$ and multijet QCD events, we observe that the efficiency of the CSVT b-tagging depends on event topology, i.e. kinematic configuration of jets. This uncertainty is found to be about 5-8% for each b-tagged jet depending on the jet rank and p_T . The effect of this uncertainty on the template shapes is negligible.

Systematic uncertainties result also from the measurements of the jet energy correction \mathcal{E} , defined in equation (4.12). These effects are combined in the so-called uncertainty on the jet energy scale, **JES**. The relative JES uncertainty ranges between 1% and 4% depending on the jet p_T and η . As example, the JES uncertainties as functions of the jet p_T are shown in Figures 5.34 (a) and (b) for jets with $\eta = 1.0$ and $\eta = 2.0$, respectively.

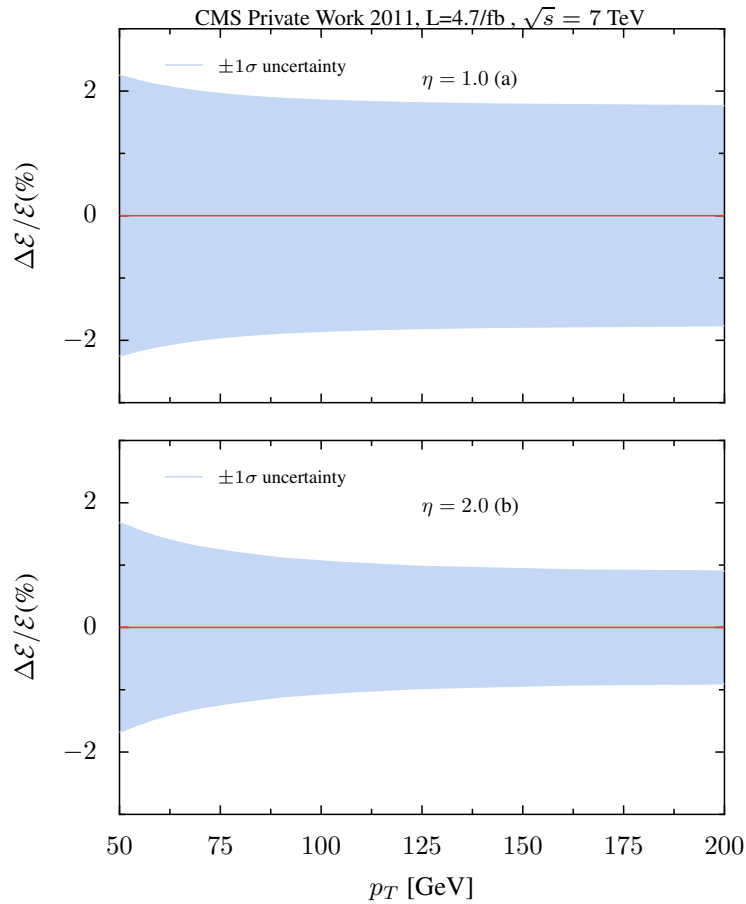


Figure 5.34: The relative uncertainties of the jet energy scale shown as a function of the jet p_T for the jet $\eta = 1.0$ (a) and $\eta = 2.0$ (b).

In the analysis we apply in the signal templates a correction on the jet energy resolution, **JER**, defined as

$$r^{JER}(p_{T,jet}, \eta_{jet}) = JER^{Data} / JER^{MC}.$$

This is done by modifying the 4-momenta of the reconstructed jets as follows

$$p_{i,jet_j}^{reco'} = \text{sign}(p_{i,jet_j}^{reco}) (|p_{i,jet_j}^{gen}| + r^{JER}(p_{T,jet}, \eta_{jet}^{reco}) \cdot (|p_{i,jet_j}^{reco}| - |p_{i,jet_j}^{gen}|)), \quad (5.24)$$

where $p_{i,jet_j}^{reco(gen)}$ is the i^{th} coordinate of the 4-momentum of the j^{th} jet at the reconstruction (generator) level. The resolution JER^{Data} is measured and results are summarized in Ref. [163]. The ratio r^{JER} and its uncertainty is show in Figure 5.35 for jets with $p_T = 100$ GeV as a function of the jet η . The relative uncertainty on the **JER** is between 6-9%. The impact of both the JES and JER uncertainties is evaluated along with the corresponding shape effects which are discussed below.

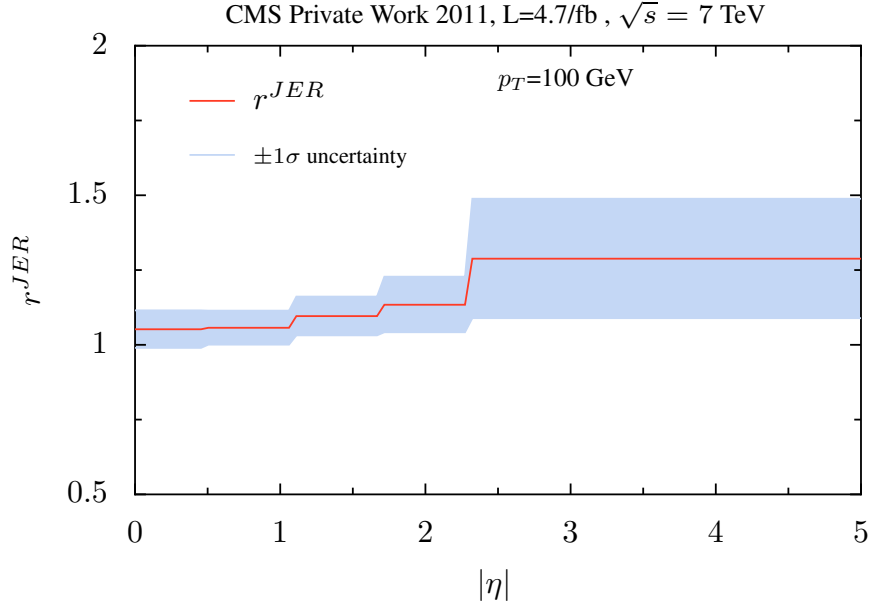


Figure 5.35: The ratio r^{JER} and its uncertainty as a function of the jet η for $p_T = 100$ GeV of the jet.

Figure 5.36 illustrates the relative effects of different uncertainties on the signal efficiency calculated for the Higgs boson masses of 100, 200 and 300 GeV. The green (red) bars of the plots indicate the relative effect on the signal efficiency ϵ_S from the $+2\sigma(-2\sigma)$ uncertainty variations,

$$\frac{\Delta\epsilon_S(\pm 2\sigma)}{\epsilon_S} = \frac{\epsilon_S(\pm 2\sigma) - \epsilon_S}{\epsilon_S},$$

where $\epsilon_S(\pm 2\sigma)$ is the estimated signal efficiency, when either $SF_{b,c}$, $SF_{uds g}$, JES or JER are shifted by $\pm 2\sigma$ of the corresponding uncertainty, and ϵ_S is the signal efficiency calculated at the

nominal values of these factors. The largest effect stems from the uncertainty on the scale factors $SF_{b,c}$ and ranges between 10-13%. The JER and JES uncertainties contribute to the uncertainty on the signal efficiency between 1 - 6%.

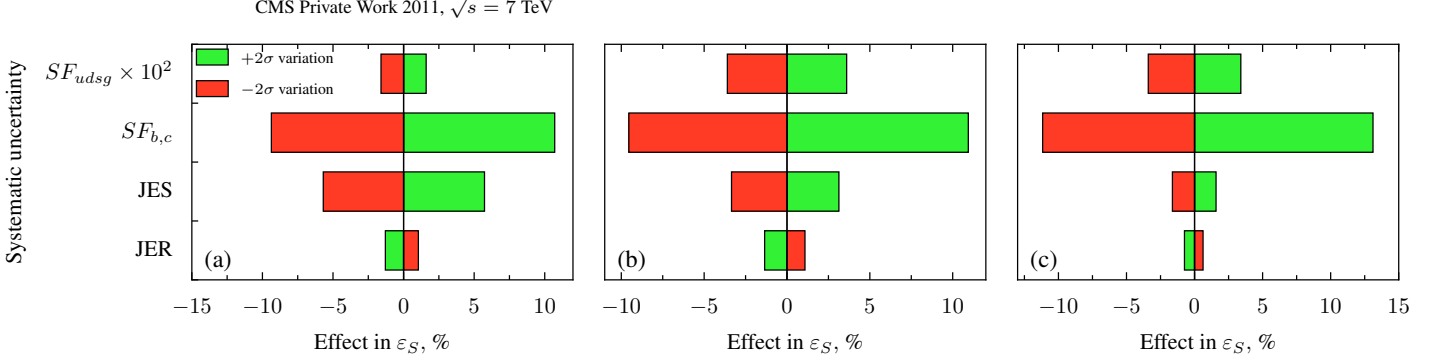


Figure 5.36: The effects of systematic uncertainties on the signal efficiency ϵ_S in the signal samples with the Higgs boson masses of 120 GeV (a), 200 GeV (b), 300 GeV (c). The green bars show the relative change of ϵ_S for a $+2\sigma$ variation of $SF_{b,c,uds g}$, JES and JER, while the red bars illustrates the relative effect for -2σ systematic shifts.

5.9.2 The shape uncertainties

The shape-altering effects from uncertainties on the jet energy scale, jet energy resolution, b-tagging efficiency and mistag fraction are accounted for in the fit by using nuisance parameters [202]. The parameters which describe signal and background and are not constrained in the analysis are called nuisance parameters. The systematic errors on the signal and background normalizations are parametrized in terms of these nuisance parameters.

Uncertainties on the b-tag efficiency and mistag fraction affect the shape of the background templates. We use the technique of continuous variation of the two-dimensional templates. The original χ^2 function (5.22) is modified to

$$\chi^{2,shape} = \chi^2 + \sum_{k=1}^{n_p} p_k^2, \quad (5.25)$$

where n_p is the number of nuisance parameters p_k which are mainly pulls. We consider the $\pm 2\sigma$ variations of the shapes, therefore the $\pm 1\sigma$ shape-altering effect in the fit is defined using piecewise-linear interpolation strategy

$$-2 \leq p_k \leq +2, \quad (5.26)$$

$$S_{\pm 1\sigma}(p_k) = S_0 + p_k \cdot \sum_{k=1}^{n_p} \left\{ \begin{array}{ll} \frac{S_{+2\sigma}^k - S_0}{2}, & p_k > 0 \\ \frac{S_0 - S_{-2\sigma}^k}{2}, & p_k < 0 \end{array} \right\}.$$

In equation (5.26) S_0 is unaltered shape, $S_{\pm 2\sigma}^k$ are the shapes after $\pm 2\sigma$ variations due to the uncertainty of the type k . An example of the shape altering for the Bbb and Cbb background templates due to variation of the scale factors $SF_{b,c}$ is demonstrated in Figures 5.37 (a) and (b). The $+2\sigma(-2\sigma)$ change of $SF_{b,c}$ leads to a shift of the M_{12} spectrum to higher (lower) values. This shift is within 10 GeV and its relative effect is significantly larger than the statistical error in the M_{12} region far above and below the peak. Such variation relatively affects the M_{12} shape at the maximum level of 5% and 10% for the Bbb and Cbb templates, respectively.

Another important shape-altering quantities are the JES and JER uncertainties. As an example, their relative effect are shown in Figure 5.38 for the signal template with a Higgs boson mass of 300 GeV. The JES and JER variations differently affect the signal M_{12} shape. The increase (decrease) of JES and JER factors shifts the spectrum to higher (lower) and lower (higher) values, respectively. Their relative effects in the shape changing are considerable and correspond at most to 30% and 20%, respectively.

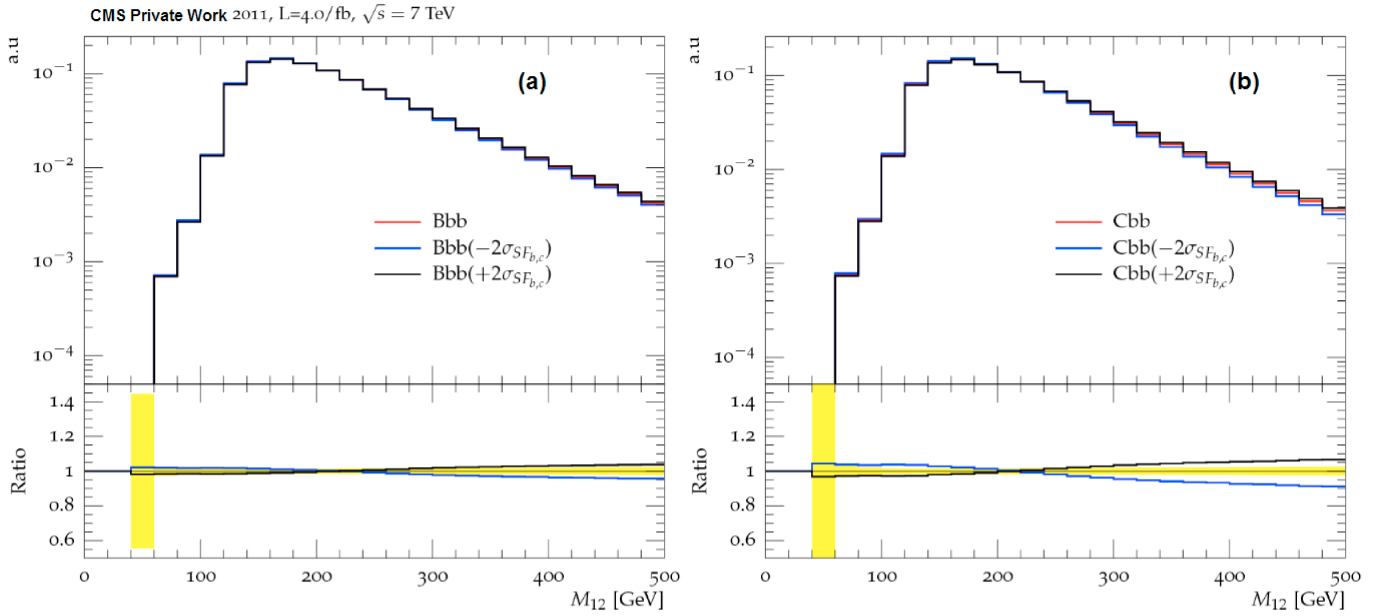


Figure 5.37: The change of the shape of the M_{12} projection under variations of the scale factors $SF_{b,c}$ within $\pm 2\sigma$ for the Bbb (a) and Cbb (b) background templates. The yellow band in the plot of the ratio indicates the statistical uncertainty in the bins of the background templates.

The effect of the shape uncertainty of the type k on the signal is defined by the difference between values of f_s given by fits with inclusion and without inclusion of the parameter p_k . For this purpose, we exclude p_k from the sum (5.25) and repeat the procedure for each of the $SF_{b,c}$, $SF_{uds g}$, JES, JER uncertainties and for each assumed value of the Higgs boson mass. The uncertainties arising from JES and $SF_{b,c,uds g}$ on the template shapes are found to increase f_s by a value in the range [0.001,0.004] depending on the Higgs boson mass. The shape-altering effect from JER uncertainty changes f_s by a value in the range [0.001,0.003].

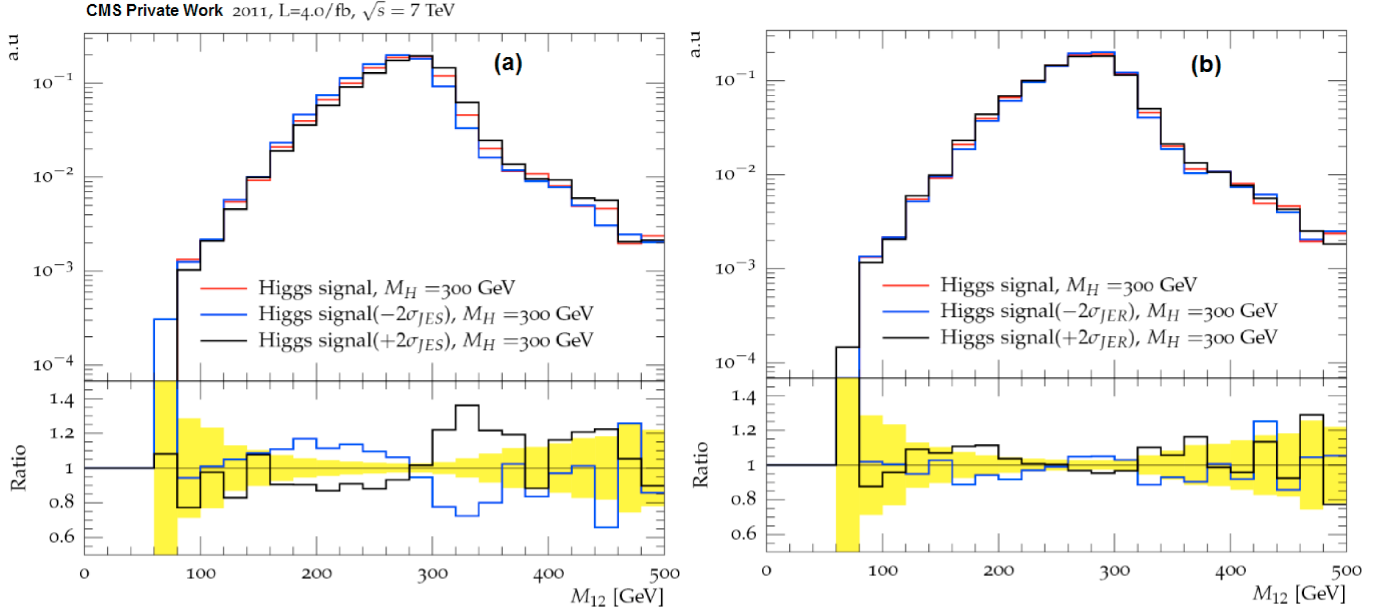


Figure 5.38: The change of the M_{12} shape under variations of JES (a) and JER (b) within $\pm 2\sigma$ for the signal template corresponding to the Higgs boson mass $M_H = 300$ GeV. The yellow band in the plot of the ratio indicates the statistical uncertainty in the bins of the signal template.

An additional systematic shape-altering uncertainty is coming from the impurity of the double-b-tagged sample and the trigger pattern correction. Using simulated QCD events, we estimate their relative effect on the fitted signal fraction f_s between 0.001 and 0.003, and between 0.001 and 0.004, depending on the Higgs boson mass, respectively for the bb-purity and trigger pattern corrections.

The statistical uncertainty of the offline b-tagging efficiency is propagated directly into the templates and accounted for. Its relative impact on f_s is found in the range [0.001,0.006] depending on the Higgs boson mass.

Table 5.9 summarizes the effects from the shape-altering systematic uncertainties on the signal fraction f_s .

Table 5.9: Summary of the shape-altering systematic uncertainties, expressed in their effects on the fitted signal fraction f_s .

Uncertainty	Δf_s
JES and b-tag	0.001 - 0.004
JER	0.001 - 0.003
bb purity correction	0.001 - 0.003
pattern correction	0.001 - 0.004

stat. error of offline b-tag	0.001 - 0.006
------------------------------	---------------

All systematic uncertainties are summarized in Table 5.10. The percentage in the “Value” column of Table 5.10 represent the size of these uncertainties. The table includes also the statistical uncertainties of the signal Monte Carlo samples which sizes are shown in Table 4.2.

Table 5.10: Summary of the systematic uncertainties.

Source	Value	Applied to	Type
luminosity	2.2%	signal	rate
signal MC statistics	1.1-2.6%	signal	rate
trigger L1/L2 efficiencies	10%	signal	rate
offline b-tag efficiency	3-10%	signal/background	rate/shape
mistag rate	10-20%	background	shape
b-tag efficiency on topology dependence	6%	signal	rate
relative online b-tag efficiency(per jet)	15%	signal	rate
bb purity correction	see text	background	shape
trigger pattern corrections	see text	background	shape
jet energy scale	1-2% ¹²	signal	rate/shape
jet energy resolution	6-9% ¹²	signal	rate/shape

5.10 Results

First, we test the background-only hypothesis by performing the fit (5.25) without including a signal template, but only a linear combination of the background templates, as described in subsection 5.8.6. Results are shown in Figures 5.32 and 5.33, and summarized in the Table 5.8. The background model fits data well within the uncertainty propagated from the templates, indicated by the area filled with cyan color.

Now, a signal template is included together with background templates in the fit, and the signal fraction f_s is allowed to vary freely. The fit is performed for the Higgs boson masses from 90 to 350 GeV. As an example, the fit result for the Higgs boson mass hypothesis of $M_H = 200$ GeV is illustrated in Figure 5.39. The shape-altering systematic variations, discussed in 5.9.2, are included in the fit.

The measured signal fractions are summarized in Table 5.11 for Higgs boson masses in the range of [90,350] GeV.

¹²This type of systematic uncertainty depends on the jet p_T and η . The size of the systematic effect varies between numbers shown in the appropriate cell.

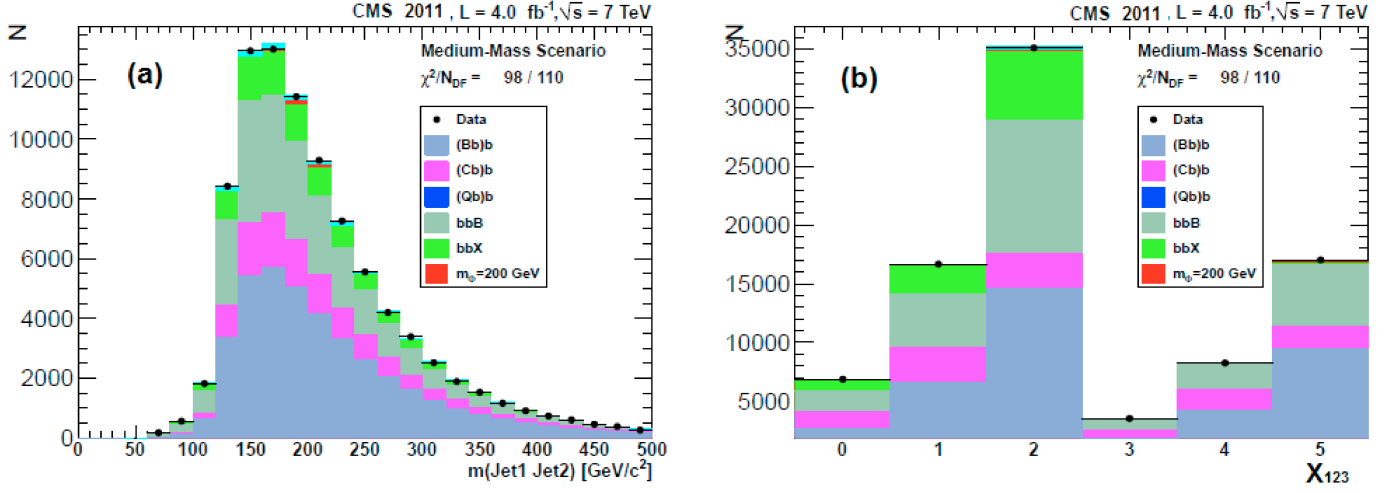


Figure 5.39: Results of the fit including a signal template for a Higgs boson with a mass of 200 GeV in the triple-b-tagged sample, of the medium-mass scenario: (a) the projection in the di-jet invariant mass, (b) the projection on the X_{123} axis.

Table 5.11: The signal fractions obtained by the fit and the number of observed signal events for different masses of the MSSM pseudoscalar Higgs boson. The uncertainties of the fractions include statistical and shape-altering systematics.

M_A [GeV]	fitted signal fraction f_s	number of observed events
90	-0.0205 ± 0.0138	-2194 ± 1677
100	-0.0383 ± 0.0164	-4094 ± 2308
120	-0.0082 ± 0.0104	-873 ± 1158
130	-0.0034 ± 0.0096	-365 ± 1031
140	-0.0044 ± 0.0097	-474 ± 1050
160	-0.0022 ± 0.0074	-235 ± 795
180	0.0021 ± 0.0077	189 ± 684
200	0.0109 ± 0.0069	968 ± 706
250	0.0041 ± 0.0043	360 ± 405
350	-0.0057 ± 0.0026	-508 ± 297

5.10.1 Cross sections

The cross section for the production of the neutral MSSM Higgs bosons as a function of M_A is measured in a model independent way. We convert the fitted values of the signal fraction f_s to the cross section times branching fraction using the formula

$$\sigma(M_A, pp \rightarrow b\bar{b} + \Phi) \times Br(\Phi \rightarrow b\bar{b}) = \frac{f_s(M_A)N^{data}}{\varepsilon_S(M_A)\mathcal{L}}, \quad (5.27)$$

where $f_s(M_A)$ and $\varepsilon_S(M_A)$ are the observed signal fractions given in Table 5.11 and the signal efficiencies, as defined in subsection 5.8.3, respectively. N^{data} and \mathcal{L} are the total number of data events in triple-b-tagged samples and the integrated luminosities, respectively. The event samples selected in the low- and medium-mass scenarios are treated separately. The systematic uncertainties affecting the signal efficiency are taken into account to calculate the error on the cross section. The errors from statistical, normalization and shape uncertainties are combined in quadrature. The measured cross section $\sigma(pp \rightarrow b\bar{b} + \Phi)$ times branching fraction $Br(\Phi \rightarrow b\bar{b})$ as a function of M_A is shown in Table 5.12 and Figure 5.40.

Table 5.12: The measured cross sections times branching fraction, $\sigma(pp \rightarrow b\bar{b} + \Phi) \times Br(\Phi \rightarrow b\bar{b})$ for different masses of the neutral pseudoscalar Higgs boson. The uncertainties includes normalization, statistical and shape-altering systematic effects.

M_A [GeV]	observed $\sigma(M_A) \times Br(\Phi)$ [pb]
90	-630 ± 481
100	-845 ± 477
120	-94 ± 125
130	-31 ± 89
140	-34 ± 75
160	-12 ± 42
180	7 ± 24
200	27 ± 20
250	7 ± 8
350	-9 ± 5

No significant evidence of the signal is observed in data.

5.11 Limit setting procedures in the Higgs boson search

In this analysis a theoretical model is given by the MSSM Lagrangian (2.34), and the LHC data are used to determine fundamental parameters of the Lagrangian, like coupling strengths or masses, by fitting the quantitative predictions of the model to experimental data. The CL_s method [203] provides a mean of setting upper limits on cross sections derived from data and constrains the possible range of fundamental parameters.

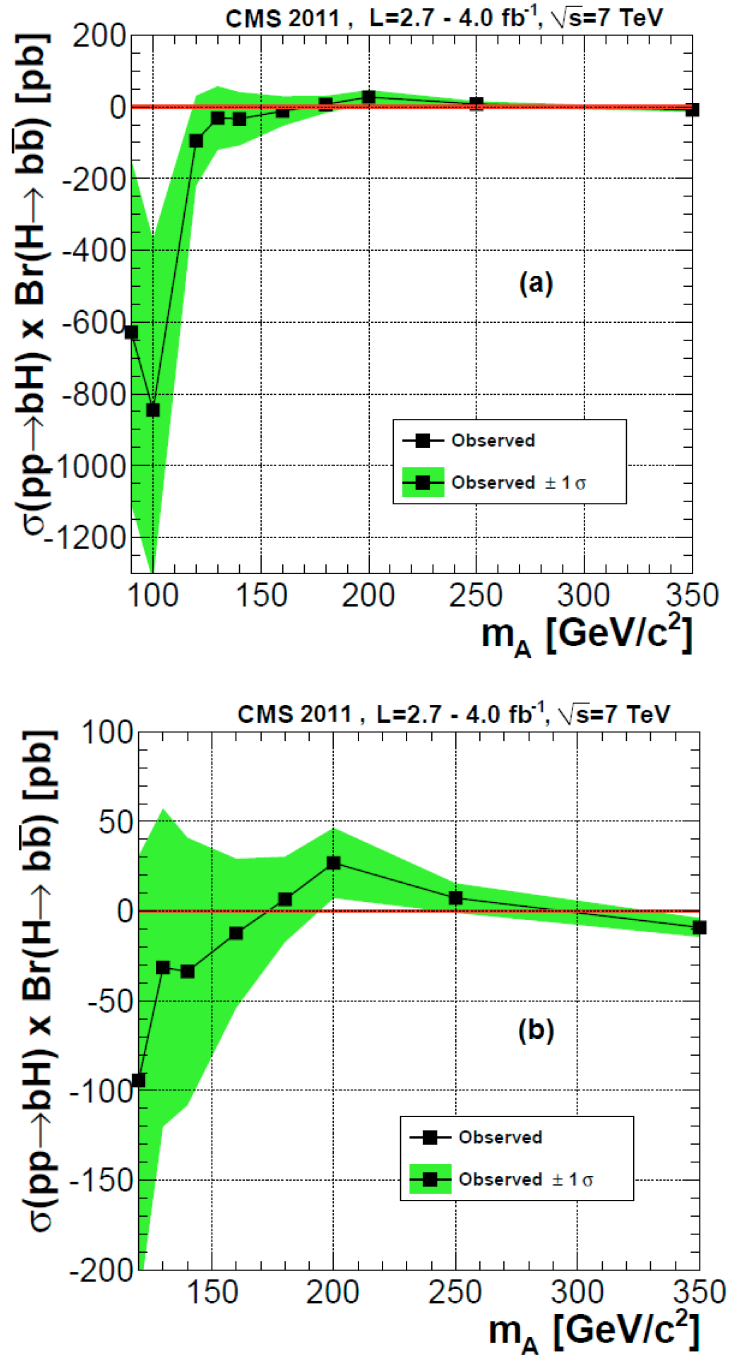


Figure 5.40: Measured cross sections times branching fractions as a function of the mass of the Higgs boson A . In (a) the full mass range and in (b) $M_A \geq 130 \text{ GeV}$ are shown.

To test the model, a factor μ is introduced to scale the cross section for the production of the Higgs bosons. This parameter is referred to as signal-strength modifier or parameter of interest. In the case when no evidence of signal is found, an upper limit on cross section times branching ratio is established. For these purposes a threshold on the signal-strength modifier, $\mu^{95\%}$, is calculated, and the hypothesis with the signal strength μ for a certain Higgs boson mass is excluded at the 95% confidence level ($CL_{95\%}$), if μ is larger than $\mu^{95\%}$.

We use the `Roostats` [204, 205] package to numerically evaluate the $\mu^{95\%}$ thresholds for the signal from the pseudoscalar Higgs boson A with $M_A = 90, 120, 130, 140, 160, 180, 200, 250$ and 350 GeV. `Roostats` is built on top of the `ROOT` [206] framework and on the classes of the `Roofit` toolkit [207], which provides a convenient description of the probability density functions needed to qualify the model to describe the data.

5.11.1 Profile likelihood ratios

The CL_S method considers a likelihood function $L(X|\mu, \{v_k\})$ as the probability density function, pdf, for the observation X to be predicted by the model with the certain parameter of interest μ and the set of nuisance parameters $\{v_k\}$. The set $\{v_k\}$ consists of the signal-yield uncertainties, $\{v_k^s\}$, and shape-altering nuisance parameters $\{p_k\}$,

$$\{v_k\} = \{v_k^s\} + \{p_k\}.$$

We refer $L(X|\mu, \{v_k\})$ to as the data model. The observation X is the two-dimensional distribution

$$X = (M_{12}, X_{123}).$$

Its values are used to construct a one-dimensional histogram $\{n_i\}$,

$$X \equiv \{n_i\} = (n_1, n_2, \dots, n_N),$$

with N bins and the number of entries n_i in the i^{th} bin.

The expectation $E[n_j]$ of the number of entries n_j to be observed in the bin j is written as

$$E[n_j](\mu, v_{yield}^s, \{p_k\}) = \mu \cdot s_j(v_{yield}^s, \{p_k\}) + b_j(\{p_k\}), \quad (5.28)$$

where the mean number of entries in the j^{th} bin from signal and background are

$$\begin{aligned} s_j(v_{yield}^s, \{p_k\}) &= v_{yield}^s \cdot s_{tot} \cdot \int_{bin_j} f^S(X, \{p_k\}) dX, \\ b_j(\{p_k\}) &= b_{tot} \cdot \int_{bin_j} f^B(X, \{p_k\}) dX. \end{aligned} \quad (5.29)$$

Here the $f^S(X, \{p_k\})$ and $f^B(X, \{p_k\})$ are the pdfs for the signal and background expectations. They are functions of the shape-altering nuisance parameters, $\{p_k\}$, and expressed as the

normalized 2D shapes $S_{\pm 1\sigma}(p_k)$ given in equation (5.26). The parameter v_{yield}^s , introduces the overall uncertainty on the signal yield as a multiplication of the factors v_k^s ,

$$v_{yield}^s = \prod_k v_k^s,$$

where the index k determines the type of the signal yield uncertainty, $k = \text{Lumi}, SF_{b,c}, SF_{udsg}, \text{JER or JES}$.

The total number of background events, b_{tot} , is estimated from the background-only fit, while the signal expectation s_{tot} is calculated as

$$s_{tot} = 1[pb^1] \cdot \epsilon_s(M_A) \cdot \mathcal{L}(M_A)_{int}[pb^{-1}], \quad (5.30)$$

where $\mathcal{L}(M_A)_{int}$ is the total luminosity of the data used in the mass scenario and expressed in pb^{-1} , $\epsilon_s(M_A)$ is the signal efficiency evaluated as a function of M_A , as discussed in subsection 5.8.3.

In the frequentist way of thinking, the nuisance parameters $\{v_k^s\}$ and $\{p_k\}$ are usually constrained by independent experiments or by theoretical assumptions. These constraints are modeled as outcomes of an auxiliary measurement by defining the pdf $\pi(v_k|\tilde{v}_k)$, being the probability of the experimental outcome v_k for the nuisance parameter of the type k to be observed assuming that its true value is \tilde{v}_k . This means that upon repeating the auxiliary experiment many times the observed nuisance parameters would randomly fluctuate around unknown a priori \tilde{v}_k^s and \tilde{p}_k . To determine the likelihoods $\pi(v_{yield}^s|\tilde{v}_{yield}^s)$ and $\pi(p_k|\tilde{p}_k)$, corresponding to the signal-yield and shape-altering nuisances, respectively, we choose the appropriate functions which are parametrized by \tilde{v}_k^s and \tilde{p}_k . The “log-normal” function is used for the likelihood of the signal-yield systematic uncertainties v_k^s

$$\pi(v_k^s|\tilde{v}_k^s) = \frac{1}{\sqrt{2\pi} \ln \delta_{v_k^s}} \frac{1}{v_k^s} \exp \left(-\frac{(\ln v_k^s - \ln \tilde{v}_k^s)^2}{2(\ln \delta_{v_k^s})^2} \right), \quad (5.31)$$

where $\delta_{v_k^s}$ is the relative effect on the signal efficiency ϵ_s due to the $\pm 1\sigma$ systematic variation of the k^{th} signal-yield uncertainty, $k = \text{Lumi}, SF_{b,c}, SF_{udsg}, \text{JER or JES}$,

$$\delta_{v_k^s} = 1 + \left| \frac{\epsilon_s(+1\sigma_k) - \epsilon_s(-1\sigma_k)}{\epsilon_s} \right|. \quad (5.32)$$

The mean \tilde{v}_k^s , usually called nominal value, of the log-normal pdf is constant and equal to unity for all types of the signal-yield uncertainty.

The standard normal distribution is used to constraint the shape-altering nuisance parameters p_k

$$\pi(p_k|\tilde{p}_k) = \frac{1}{\sqrt{2\pi}\sigma_{p_k}} \exp \left(-\frac{(p_k - \tilde{p}_k)^2}{2\sigma_{p_k}^2} \right), \quad (5.33)$$

where \tilde{p}_k is fixed to zero and σ_{p_k} is unity. The pdf $\pi(p_k|\tilde{p}_k)$ for the different shape-altering nuisances p_k are equal.

In general, the likelihood function $L(X|\mu, \{v_k\})$ for a specific set of measurements $X = \{n_i\}$ in a single experiment is the product of Poisson probabilities for all bins times the likelihood to observe the values of nuisance parameters $\{v_k\}$ from independent experiments

$$L(X|\mu, \{v_k^s, p_k\}) = \prod_{j=1}^N \frac{E[n_j](\mu, v_{yield}^s, \{p_k\})^{n_j}}{n_j!} e^{-E[n_j](\mu, v_{yield}^s, \{p_k\})} \cdot \prod_k \pi_k(v_k^s|\tilde{v}_k^s) \cdot \prod_k \pi_k(p_k|\tilde{p}_k). \quad (5.34)$$

To assess the agreement of the measurements $X = \{n_i\}$ with one prediction $(E[n_o](\mu, v_{yield}^s, \{p_k\}))$, we consider the profile likelihood ratio

$$\lambda(\mu) = \frac{L(X|\mu, \{\hat{v}_k\})}{L(X|\hat{\mu}, \{\hat{v}_k\})}. \quad (5.35)$$

Here $\{\hat{v}_k\}$ in the numerator denotes the values of $\{v_k\}$ that maximize $L(X|\mu, \{v_k\})$ for a certain value of μ , being the conditional maximum-likelihood estimator of $\{v_k\}$. It is a function of μ . The denominator of $\lambda(\mu)$ (5.35) is the maximized likelihood function, i.e. $\hat{\mu}$ and $\{\hat{v}_k\}$ are unconditional maximum-likelihood estimators of μ and $\{v_k\}$. The nominator and denominator of equation (5.35) depend on the Higgs boson mass probed. Figure 5.41 illustrates the negative logarithm of the profile likelihood ratio (5.35) as a function of μ for the signal model corresponding to the pseudoscalar mass $M_A = 200$ GeV.

The presence of the nuisance parameters in the definition (5.35) broadens the profile likelihood ratio relative to what one would have if the nuisances were fixed. This reflects the loss of information about μ due to the systematic uncertainties.

The profile likelihood ratio can be used to derive the lower, $\mu_{low}^{95\%}$, and upper, $\mu_{up}^{95\%}$, limits on the parameter of interest μ . If one assumes that Wilks' theorem [208] to be valid for the data model, then $-2\ln(\lambda(\mu))$ is asymptotically distributed as a χ^2 with one degree of freedom. In this case, the p-values [209] of χ^2 are used to impose the limits and determine the 95% confidence interval $CI_{95\%}$:

$$\mu_{low}^{95\%} \leq \mu \leq \mu_{up}^{95\%}. \quad (5.36)$$

The p-value for $CI_{95\%}$ is 0.05. This means that predictions of the signal hypothesis with μ values outside $CI_{95\%}$ (5.36) can be experimentally observed only in less than 5% of all cases. Thus such μ values are not considered and said to be excluded at the 95% confidence level. The p-value of 0.05 is reached at $\chi^2 = 3.84$ for one degree of freedom [210]. This corresponds to $-\ln(\lambda(\mu)) = 1.92$, which is show in Figure 5.41 as a vertical horizontal line. Therefore $-\ln(\lambda(\mu)) = 1.92$ determines $CI_{95\%}$ which is shown as the vertical green lines in Figure 5.41.

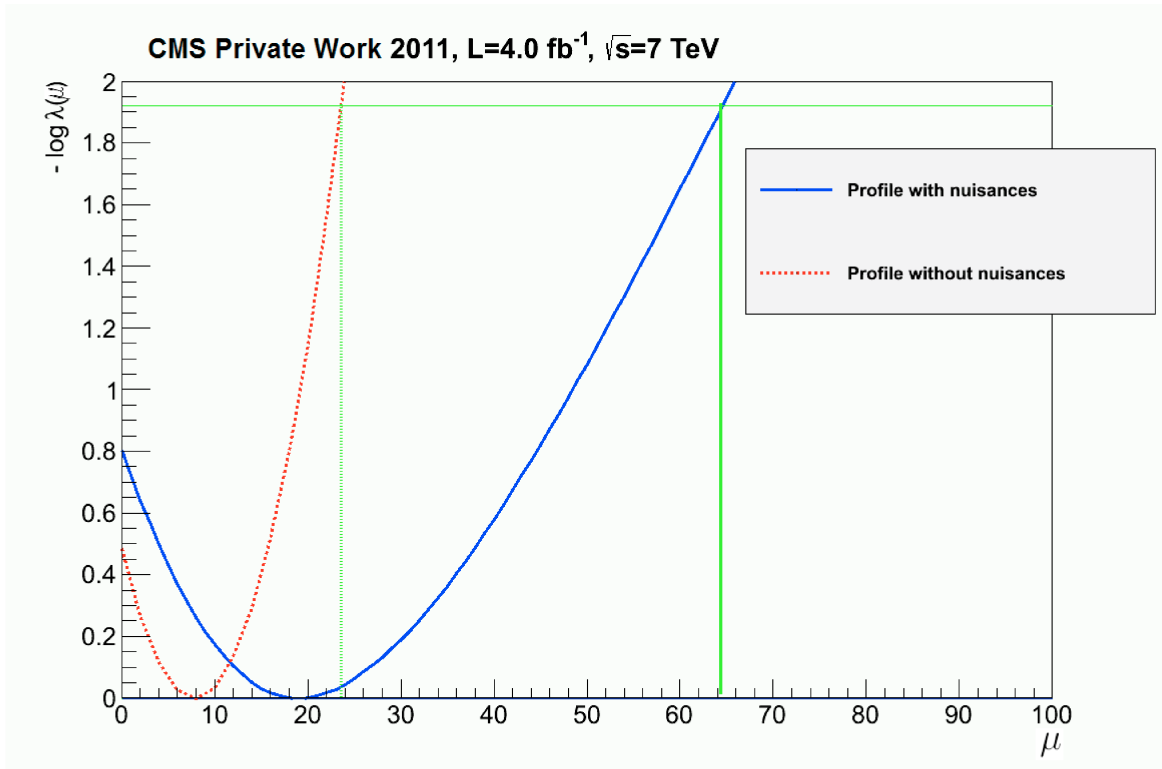


Figure 5.41: Measured $-\ln(\lambda(\mu))$ as a function of the signal strength μ for the signal with the pseudoscalar Higgs boson mass $M_A = 200$ GeV: The blue graph shows the behavior of $-\ln(\lambda(\mu))$ calculated with the conditional and unconditional maximum-likelihood estimators $\{\hat{\hat{v}}_k\}$ and $\{\hat{v}_k\}$. The red one is the case when the nuisance parameters $\{v_k\}$ are fixed to their true values.

The maximum-likelihood estimator $\hat{\mu}$ can be used to make a statement on the observed cross section times branching fraction, σ_{obs} . The unconditional maximum-likelihood estimator $\hat{\mu}$ is determined by the minimum of $-\ln(\lambda(\mu))$, as shown in Figure 5.41. This provides the following observed cross section and the upper 95% CL limit for the signal model with $M_A = 200$ GeV:

- $\sigma_{obs} = 20$ pb;
- $\sigma_{up}^{95\%} = 64$ pb.

These numbers are in a good agreement with the results of the χ^2 fit shown in Table 5.12.

5.11.2 Test statistic

To derive the 95% CL upper limits on the cross sections, we use the CL_S method [203] which employs test statistic. Here, we follow the prescription outlined in Ref. [211]. From the definition (5.35) of $\lambda(\mu)$, one notes that $0 \leq \lambda \leq 1$, with λ near 1 implying good agreement between the data and the hypothesized value of μ . Eventually, it is more convenient to use the quantity

$$t_\mu = -2\ln(\lambda(\mu)), \quad (5.37)$$

as the basis of a statistical test. Higher values of t_μ indicates on increasing incompatibility between the data and the hypothesized μ .

To quantify the level of disagreement we compute the p-value [209]

$$p_\mu = \int_{t_{\mu,obs}}^{\infty} f(t_\mu|\mu) dt_\mu, \quad (5.38)$$

where $t_{\mu,obs}$ is the value of t_μ observed in data and $f(t_\mu|\mu)$ denotes the pdf of t_μ as a function of the signal strength μ . The p-values less than the threshold $\alpha = 0.05$ indicate large incompatibility of μ with the data. When using the test statistic t_μ , the data set $\{n_i\}$ may give such low p-value in two distinct cases: the maximum-likelihood estimated signal strength $\hat{\mu}$ may be found greater or less than the hypothesized value μ .

Analytic evaluation of $f(t_\mu|\mu)$ is in general impossible. One way to approximate the pdf of t_μ is to evaluate t_μ for a large number of simulated toy measurements [211]. First, a toy measurement $X = \{n_i\}$ is obtained by Monte Carlo simulations generating Poisson random numbers $\{n_i\}$ for every considered bin i with an expected number of events $E[n_i](\mu, \{v_k^s\}, \{p_k\})$. Also we consider the statistical fluctuations in the auxiliary measurements described by $\prod_k \pi_k(v_k^s|\tilde{v}_k^s)$ and $\prod_k \pi_k(p_k|\tilde{p}_k)$. Therefore we also generate random numbers $\{v_k\}$ distributed according to $\pi_k(v_k|\tilde{v}_k)$ simultaneously with $X = \{n_i\}$. Next, we find the values of the nuisance parameters $\{\hat{v}_k\}$ performing the maximum-likelihood fit, using equation (5.34), to the simulated toy measurement $X = \{n_i\}$ for a given value of μ . Then the unconditional likelihood fit of $L(X|\mu, \{v_k\})$ is performed to obtain $\hat{\mu}$ and \hat{v}_k . Finally, the test statistic t_μ is calculated using equations (5.35)

and (5.37). By repeating this procedure a certain number of different toy experiments, we obtain the distribution $f(t_\mu|\mu)$. In principle, it is possible to determine the distribution with arbitrary precision. However, computational costs increase with the number of toy experiments. To calculate the median (expected) upper limits, we additionally, compute $f(t_\mu|\mu = 0)$ using the background only predictions

$$E_{bkg}[n_j](\{p_k\}) = b_j(\{p_k\}).$$

There is another, computationally less expensive, alternative to obtain the pdf $f(t_\mu|\mu)$. The method is based on approximate analytical expressions as described in Ref. [212]. This approach, referred to as the asymptotic method, is stating that for large values of $\{n_i\}$ in the measurement X , the test statistic t_μ can be approximated by

$$t_\mu \equiv -2\ln(\lambda(\mu)) = \frac{(\mu - \hat{\mu})^2}{\sigma^2} + \mathcal{O}\left(\frac{1}{\sqrt{N}}\right). \quad (5.39)$$

Here the unconditional maximum-likelihood estimator $\hat{\mu}$ follows a Gaussian distribution with a mean μ' and standard deviation σ , and $N = \sum_i n_i$ represents the data sample size. The standard deviation σ of $\hat{\mu}$ is obtained from the covariant matrix V_{ij} of the estimators for all parameters, μ and $\{v_k\}$

$$V_{ij}^{-1} = -E \left[\frac{\partial^2 \ln(L(X|\mu, \{v_k\}))}{\partial \theta_i \partial \theta_j} \right], \quad (5.40)$$

where $\theta_i = \{\mu, \{v_k\}\}$ and the expectation value $E[\dots]$ assumes the strength parameter μ' . V_{ij}^{-1} is a function of μ' and therefore, $\sigma = V_{00}^{-1/2}$ is dependent on μ' as well. The mean value μ' is unknown a priori. We can only guess on μ' . The statistical procedure of the analysis considers only two possible choices of μ' :

- $\mu' = \mu$, to test if the hypothesized μ describes the dataset X well;
- $\mu' = 0$, to find what p-value to expect if the data correspond to the background-only hypothesis. In this case the smaller p-value we expect for the background-only model, the more sensitive to discovery our analysis is.

If $\hat{\mu}$ is Gaussian distributed and N is large enough to neglect the $\mathcal{O}(1/\sqrt{N})$ term in equation (5.39), then the test statistic t_μ follows a non-central χ^2 -distribution for one degree of freedom [212]

$$f(t_\mu|\Lambda) = \frac{1}{2\sqrt{2\pi}} \frac{1}{\sqrt{t_\mu}} \left[\exp\left(-\frac{1}{2}(\sqrt{t_\mu} + \sqrt{\Lambda})^2\right) + \exp\left(-\frac{1}{2}(\sqrt{t_\mu} - \sqrt{\Lambda})^2\right) \right], \quad (5.41)$$

where the non-centrality parameter Λ is

$$\Lambda = \frac{(\mu - \mu')^2}{\sigma^2}. \quad (5.42)$$

In the case of $\mu' = \mu$ the pdf in (5.41) becomes the central χ^2 -distribution. If $\mu' = 0$, the non-centrality parameter $\Lambda = \frac{\mu^2}{\sigma^2}$ is non-zero, and we need to estimate it. A special, artificial data set, that is called the Asimov data set, X^A [212], is introduced to determine Λ . The Asimov data $X^A = \{n_i^A\}$ are equal to their expectation values when all statistical fluctuations are suppressed:

$$n_i^A = E[n_i](\mu', \{v_k'^s\}, \{p_k'\}) = \mu' \cdot s_i(\{v_k'^s\}, \{p_k'\}) + b_i(\{p_k'\}). \quad (5.43)$$

Here $\{v_k'^s\}$ and $\{p_k'\}$ are sets of the nuisance parameters which are found by profiling the likelihood function $L(X|\mu', \{v_k\})$:

$$\mu' = \hat{\mu}, \quad v_k'^s = \hat{v}_k^s, \quad p_k' = \hat{p}_k.$$

Finally, Λ is expressed in terms of the test statistic t_μ^A , evaluated on the Asimov data X^A , as

$$\Lambda = \frac{(\mu - \mu')^2}{\sigma^2} = -2 \ln(\lambda^A(\mu)) \equiv t_\mu^A, \text{ where} \quad (5.44)$$

$$\lambda^A(\mu) = \frac{L(X^A|\mu, \{\hat{v}_k\})}{L(X^A|\hat{\mu}, \{\hat{v}_k\})} \equiv \frac{L(X^A|\mu, \{\hat{v}_k\})}{L(X^A|\mu', \{v_k'\})}.$$

In practice, to get the non-centrality parameter Λ for the case of $\mu' = 0$, we calculate the test statistic t_μ^A using results of the background-only fit, shown in Table 5.8, as Asimov dataset X^A .

The significance, Z_μ , of the hypothesis with the parameter of interest μ to observe the test statistic $t_{\mu,obs}$ in the measurement X is related to the p-value as

$$Z_\mu = \Phi^{-1}(1 - p_\mu) = \Phi^{-1}(F(t_{\mu,obs}|0)) = \Phi^{-1}(2\Phi(\sqrt{t_{\mu,obs}}) - 1), \quad (5.45)$$

where $\Phi^{-1}(1 - p_\mu)$ and $\Phi(x)$ are the quantile and cumulative functions of the standard normal distribution [213]. The function $F(t_\mu|\Lambda)$ in (5.45) is the cumulative distribution of t_μ (5.41) which is defined [212] as

$$F(t_\mu|\Lambda) = \Phi(\sqrt{t_\mu} + \sqrt{\Lambda}) + \Phi(\sqrt{t_\mu} - \sqrt{\Lambda}) - 1. \quad (5.46)$$

Because the significance Z_μ is a monotonic function of $\sqrt{t_\mu}$, we can set up the 95% CL upper limit on t_μ by finding the root $t_\mu^{95\%}$ of the equation

$$Z_\mu^{95\%} = \Phi^{-1}(2\Phi(\sqrt{t_\mu^{95\%}}) - 1) = 1.64.$$

The 95% confidence interval $CI_{95\%}$ for the signal strength μ is determined as

$$\mu_{low}^{95\%} \leq \mu \leq \mu_{up}^{95\%}, \text{ where} \quad (5.47)$$

$$\mu_{up/low}^{95\%} = \hat{\mu} \pm \sigma \sqrt{t_\mu^{95\%}}.$$

The unknown, so far, standard deviation σ is estimated from the Asimov data set X_A , as

$$\sigma_A^2 = \frac{\mu^2}{t_\mu^A}. \quad (5.48)$$

where t_μ^A is the test statistic obtained on the Asimov data set X^A .

5.11.3 Sensitivity of the analysis

To characterize the sensitivity of the search for the Higgs boson, we are interested not in the observed significance Z_μ obtained from a single data set, but rather in the expected, more precisely, median significance $\text{med}[Z_\mu]$, which characterizes the probability to discover the signal¹³ with the strength μ assuming that there is no signal in the data. The quantity $\text{med}[Z_\mu]$ is defined as

$$\text{med}[Z_\mu] = \Phi^{-1}(2\Phi(\sqrt{t_\mu^A}) - 1). \quad (5.49)$$

The numerical value of $\text{med}[Z_\mu]$ is anticorrelated to the probability for an upward background fluctuation. Hence, the larger $\text{med}[Z_\mu]$ is, the higher the sensitivity of the analysis is expected. The median significance $\text{med}[Z_\mu]$ is related to the probability β of a type II error [214], which occurs when the signal hypothesis is a priori false, but erroneously fails to be rejected. The probability β of the type II error for $CI_{95\%}$ is estimated as

$$\beta = \int_0^{t_\mu^{95\%}} f(t_\mu|0) dt_\mu. \quad (5.50)$$

From the relations

$$\begin{aligned} 1 - \beta &= \int_{t_\mu^{95\%}}^\infty f(t_\mu|0) dt_\mu = \int_{t_\mu^{95\%}}^{t_\mu^A} f(t_\mu|0) dt_\mu + \frac{1}{2}, \Rightarrow \\ \beta &= \frac{1}{2} - \int_{t_\mu^{95\%}}^{t_\mu^A} f(t_\mu|0) dt_\mu, \end{aligned} \quad (5.51)$$

and

$$\text{med}[Z_\mu] \sim \sqrt{t_\mu^A}, \quad (5.52)$$

¹³Hereafter under the signal we mean the data model containing the signal s_j and the background b_j expectations.

we conclude that

$$\lim_{\text{med}[Z_\mu] \sim \sqrt{t_\mu^A} \rightarrow \infty} \beta \rightarrow 0. \quad (5.53)$$

This means that the probability β is monotonically decreasing with the increase of $\text{med}[Z_\mu]$. The probability β is proportional to the overlapping between the pdf $f(t_\mu|\mu' = \mu)$ and $f(t_\mu|\mu' = 0)$. A significantly large distance between $t_{\mu, \text{obs}}$ and t_μ^A , and, therefore, between Z_μ and $\text{med}[Z_\mu]$, will qualitatively indicate the presence of the non-background contribution in the particular measurement X .

Figure 5.42 illustrates the pdfs $f(t_\mu|\mu' = \mu)$ (red) and $f(t_\mu|\mu' = 0)$ (blue), obtained from toy experiments, which characterize the expectation from signal of the strength μ and background only to be compatible with the measurement X shown as the black vertical line. The Higgs model corresponding to $M_A = 200$ GeV in the two cases of $\mu = 27.5$ and $\mu = 45$ is shown at (a) and (b), respectively.

CMS Private Work 2011, $\sqrt{s} = 7$ TeV

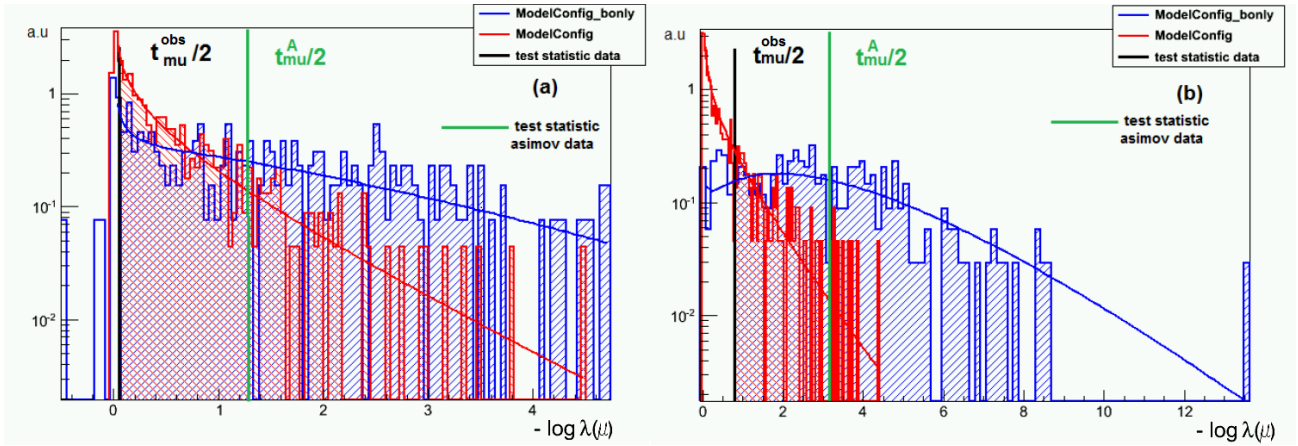


Figure 5.42: The pdf of the test statistic for the signal with $M_A = 200$ GeV (red) and background-only (blue) models for the hypothesized values $\mu = 27.5$ (a) and $\mu = 45$ (b). The measured t_μ and expected t_μ^A are shown as black and green vertical lines, respectively. The solid curves in colors correspond to asymptotic predictions of formula (5.41). All nuisance parameters $\{v_k\}$ are maximum-likelihood fitted.

The plots contain the histograms representing the distributions of the test statistic from 500 toy experiments. The solid curves show the asymptotic predictions given by equation (5.41). We see the good agreement between two approaches for calculating the probability distribution functions $f(t_\mu|\mu' = \mu)$ and $f(t_\mu|\mu' = 0)$. The black and green vertical lines in the plots indicate the values of $t_\mu^{\text{obs}}/2$ and $t_\mu^A/2$.

The smaller the overlapping between $f(t_\mu|\mu' = \mu)$ (red) and $f(t_\mu|\mu' = 0)$ (blue) is, the higher the sensitivity of the analysis is expected. This is directly related to the effects coming from

systematic uncertainties in our analysis. Any change of nuisances $\{v_k\}$ modifies shapes of the pdfs $f(t_\mu|\mu' = \mu)$ and $f(t_\mu|\mu' = 0)$, and that reflects in the probability β . Figure 5.43 shows what happens with both $f(t_\mu|\mu' = \mu)$ and $f(t_\mu|\mu' = 0)$, if one fixes the nuisance parameters at their nominal values.

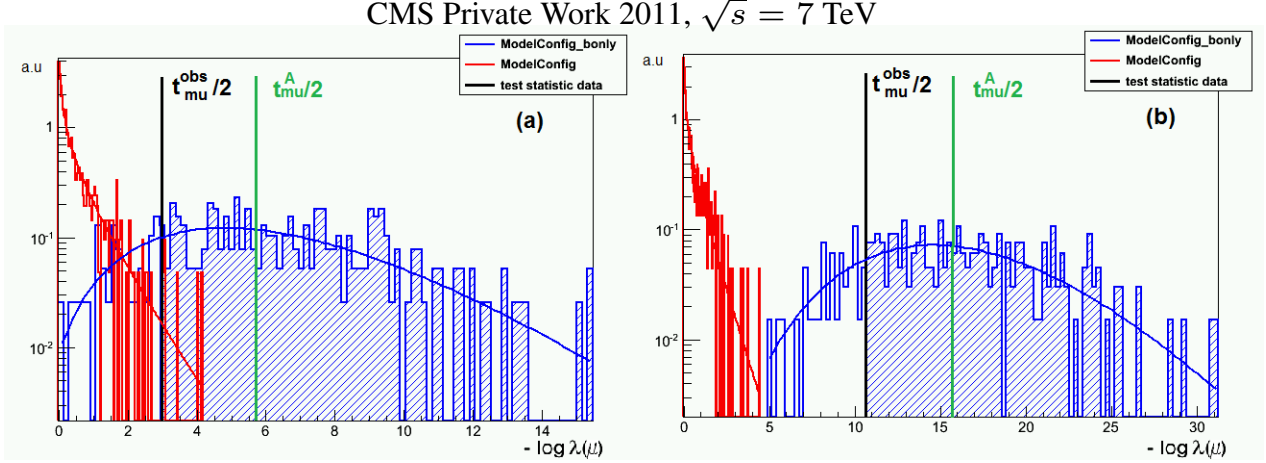


Figure 5.43: The pdf of the test statistic in the signal with $M_A = 200$ GeV (red) and background-only (blue) models for the hypotheses with $\mu = 27.5$ (a) and $\mu = 45$ (b). Measured t_μ and expected t_μ^A are shown as black and green vertical lines, respectively. The solid curves in colors correspond to asymptotic predictions of the formula (5.41). All nuisance parameters $\{v_k\}$ are fixed at their nominal values.

Comparing Figures 5.42 and 5.43, we note that the overlapping between red and blue pdfs is significantly reduced when the nuisance parameters are fixed. The probability β is getting smaller, and it even approaches zero for the case of $\mu = 45$. No upward fluctuations in the data models appear now. Both hypotheses of $\mu = 27.5$ and $\mu = 45$ are excluded at the 95% confidence level.

Hence, to increase the analysis sensitivity, what is identical to the β probability decreasing, in the future, significant reduction of systematic uncertainties will be required for preventing the loss of information on the signal strength μ .

5.11.4 The asymptotic CL_S technique and exclusion limits

Given a measurement $X = \{n_i\}$ and the corresponding observed test statistics $t_{\mu,obs}$ as well as the corresponding distributions $f(t_\mu|\mu' = \mu)$ and $f(t_\mu|\mu' = 0)$, the statistical significance of the observation whether it arose by chance, needs to be determined. Previously, we have introduced the p-value (5.39) as a measure of the disagreement between the measurement X and prediction from the model with hypothesized signal strength μ . In the CL_S method, this p-value is denoted

as “ CL_{S+B} ”,

$$CL_{S+B} = \int_{t_{\mu,obs}}^{\infty} f(t_{\mu}|\mu) dt_{\mu}. \quad (5.54)$$

CL_{S+B} is the cumulative probability of observing a measurement X' with $t'_{\mu,obs} \geq t_{\mu,obs}$ assuming that the signal model is true and resulted to the measurement outcome. Therefore, large values of CL_{S+B} suggest a high chance that the observation $X = \{n_i\}$ is compatible with the expectation

$$E[n_i](\mu, \mathbf{v}_{yield}^s, \{p_k\}) = \mu \cdot s_i(\{\mathbf{v}_{yield}^s\}, \{p_k\}) + b_i(\{p_k\}).$$

The probability to observe a measurement that has a larger $t_{\mu=0,obs}$ than the observed one, when background is only expected, is given by the p-value, called “ $1 - CL_B$ ”,

$$1 - CL_B = \int_{t_{\mu=0,obs}}^{\infty} f(t_{\mu=0}|0) dt_{\mu}. \quad (5.55)$$

The quantity CL_B is a measure for the disagreement of X with the background-only expectation: the larger CL_B is, the more incompatible the observations $X = \{n_i\}$ with the expectations $b_i(\{p_k\})$ are. We should distinguish between the test statistics $t_{\mu=0,obs}$ and t_{μ}^A : their definitions, given by (5.35) with $\mu = 0$ and (5.44), where $\mu \neq 0$, are different. For the Higgs boson searches $1 - CL_B$ estimates how frequently a signal would be observed from background fluctuations.

We define the ratio

$$CL_S(\mu) = \frac{CL_{S+B}(\mu)}{1 - CL_B}, \quad (5.56)$$

which is a measure of how well the set $\{\mu, \hat{\nu}_k\}$ of our hypothesis can be statistically distinguished from the set $\{\hat{\mu}, \hat{\nu}\}$ preferred by nature. In the literature, this is referred to as CL_S ¹⁴ confidence level [203]. Small values of $CL_S(\mu)$ suggest that X strongly disfavors the set $\{\mu, \hat{\nu}_k\}$. Normalizing to $1 - CL_B$ ensures the confidence of statements, even in the cases when the best-fitted estimations $\{\hat{\mu}, \hat{\nu}_k\}$, are more likely from the background fluctuations in data.

We want to find the maximum $\mu^{\alpha\%}$ of the signal strength μ that a prediction $\{\mu, \hat{\nu}_k\}$ is statistically not distinguished from the nature favored set $\{\hat{\mu}, \hat{\nu}_k\}$. The $\alpha\%$ indicates on the confidence level of CL_S ,

$$CL_S(\mu) \geq (1 - \alpha), \quad \mu \leq \mu^{\alpha\%}. \quad (5.57)$$

A prediction corresponding to $\mu > \mu^{\alpha\%}$ is statistically distinguished and excluded at the $\alpha\%$ confidence level. The quantity $\mu^{\alpha\%}$ is referred to as exclusion limit for the parameter of interest μ . We use $\alpha = 0.95$ to set the exclusion limit on μ .

¹⁴Further on, we omit CL_S in the name of the confidence level.

An issue still open to question is the way to find the value of $\mu^{\alpha\%}$. One can invert the relation (5.57)

$$\mu^{\alpha\%} = CL_S^{-1}(1 - \alpha), \quad (5.58)$$

and obtain the needed value. In general, analytical solving of the equation (5.58) is not possible. In the current analysis the inversion (5.58) is done numerically by scanning the hypothesis test results, $CL_{S+B}(\mu)$, CL_B and $CL_S(\mu)$, for various values of the parameter μ . The exclusion limit $\mu^{\alpha\%}$ is derived when $CL_S(\mu)$ intersects the desired level of $1 - \alpha$. The RooStats framework [204, 205] provides a class, `HypoTestInverter`, which implements the scan over a range of μ values. We use 100 points in the range $1 \leq \mu \leq 1001$ to obtain $\mu^{95\%}$ for the signal hypotheses with the Higgs boson masses between 90 and 350 GeV. To perform fast calculations of the p-values (5.54) and (5.55), the asymptotic formulae of the probability density $f(t_\mu|\mu')$ (5.41) and the corresponding cumulative $F(t_\mu|\mu')$ (5.46) functions are used. Such approach to evaluate CL_{S+B} , CL_B and CL_S are known in the literature as “asymptotic” CL_S method [212].

Running the `HypoTestInverter` code on the Asimov data set X^A provides the CL_S numbers expected from background-only events. For the nice presentation of results, the error bands for the expected $CL_S(\mu)$, $\text{med}[CL_S(\mu)]$, which are corresponding to $\pm N\sigma$ variations of $\hat{\mu}$, are usually depicted in plots. N^{15} is either 1 or 2. To find the bands, we map the $\pm N\sigma$ variation of t_μ^A ,

$$\begin{aligned} \sqrt{t_{\mu,+N\sigma}^A} &= \frac{\hat{\mu}}{\sigma} + N, \\ \sqrt{t_{\mu,-N\sigma}^A} &= \max[\frac{\hat{\mu}}{\sigma} - N, 0], \end{aligned} \quad (5.59)$$

into $\text{med}[CL_S(\mu)]$ plane, iteratively performing for each hypothesized μ .

For a vivid example of the scanning procedure and deriving $\text{med}[CL_S(\mu)]$, we run the CL_S test of the Higgs model for $M_A = 200$ GeV over 5 equally distributed points in the range of $10 \leq \mu \leq 80$. Figure 5.44 shows the obtained results for CL_{S+B} , $1 - CL_B$, CL_S , $\text{med}[CL_S]$ and $\pm 1(2)\sigma$ bands.

As expected, the observed CL_{S+B} is lowering, while $1 - CL_B$ increasing with μ . The upper limit $\mu_{up}^{95\%}$ is determined from the intersection of the $CL_S(\mu)$ curve with the red horizontal line indicating the p-value=0.05. The following values of the observed and expected upper limits are obtained from the scan:

- $\mu_{up}^{95\%} = 57.47$,
- $\text{med}[\mu_{up}^{95\%}] = 37.09$,

¹⁵Sometimes 1σ band is called “68%” band, while 2σ one is “95%” band.

CMS Private Work 2011, $\sqrt{s} = 7$ TeV

Asymptotic CL Scan for the parameter of interest

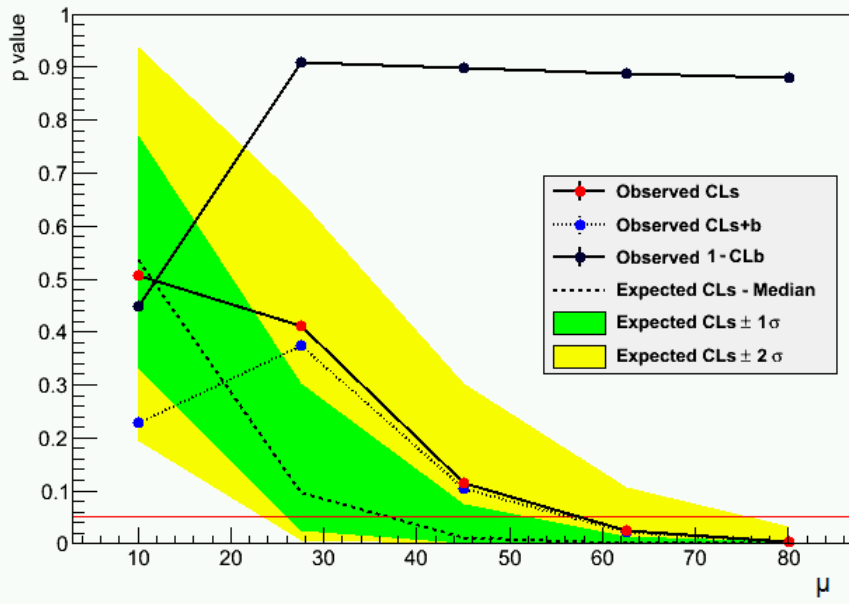


Figure 5.44: The scan of the asymptotic CL_{S+B} (blue), $1 - CL_B$ (black), CL_S (red) using data. The signal model with $M_A = 200$ GeV is used in the calculations. The dashed line indicates $\text{med}[CL_S]$ obtained from Asimov data set. The green (yellow) area corresponds to the $\pm 1(2)\sigma$ error band for $\text{med}[CL_S]$. The red horizontal line is placed at 0.05 corresponding to the 95% confidence level $CL_{95\%}$.

- $\text{med}[\mu_{up}^{95\%}] + 1\sigma = 52.04,$
- $\text{med}[\mu_{up}^{95\%}] - 1\sigma = 26.05,$
- $\text{med}[\mu_{up}^{95\%}] + 2\sigma = 76.06,$
- $\text{med}[\mu_{up}^{95\%}] - 2\sigma = 23.36.$

Comparing $\mu_{up}^{95\%}$ and $\text{med}[\mu_{up}^{95\%}]$, we find that there is an upward fluctuation in the data, and this corresponds to 1.2σ effect visible in the 95% CL upper limits on the observed cross section $\sigma_{obs}(M_A = 200 \text{ GeV})$ times branching fraction.

It is worth to mention that the computing time of the asymptotic five-points scan is about 4 seconds, which is much less than 7 minutes needed on average for the CL_S technique which generates 500 toy experiments to calculate the pdfs in five scan points.

5.12 95% CL upper limits on cross sections

Using the asymptotic CL_S method, we repeatedly perform the scan of the signal strength μ in the data for the Higgs boson mass range from 90 to 350 GeV using data. The normalizations of the background templates are free parameters. To realize the maximum likelihood fit with unconstrained background, we introduce five nuisance parameters $\{v_{back}^m\}$, one for each background template: $m = (\text{Bb}) \text{ b}, (\text{Cb}) \text{ b}, (\text{Qb}) \text{ b}, \text{bbB}$ and bbX . These nuisance parameters are distributed as the log-normal random variables with the large variance. The background expectations $b_i(\{p_k\})$ (5.28) are modified by the factors $\{v_{back}^m\}$ as

$$b_j(\{p_k\}) \rightarrow \sum_{m=1}^5 v_{back}^m \cdot b_{j,m}(\{p_k\}), \quad (5.60)$$

The 95% CL observed and the median expected limits on the cross section times branching fraction as a function of the pseudoscalar mass M_A are shown in Table 5.13 and Figure 5.45.

Table 5.13: Observed and median expected limits at the 95% CL on $\sigma(pp \rightarrow bb + \Phi) \times BR(\Phi \rightarrow b\bar{b})$.

M_A [GeV]	observed $\mu_{up}^{95\%}$ [pb]	med[$\mu_{up}^{95\%}$] [pb]
90	537	897
100	451	708
120	174	251
130	149	175
140	116	138

160	74.7	84.1
180	45.7	49.8
200	55.5	36.2
250	28.1	19.4
350	7.55	10.8

All observed limits are well within the expected $\pm 2\sigma$ band. There is no indication of a statistically significant excess.

5.12.1 95% CL lower limits on the MSSM $\tan\beta$ parameter

As the final step of the analysis, we perform the interpretation of obtained 95% CL upper limits on $\sigma(pp \rightarrow bb + \Phi) \times BR(\Phi \rightarrow b\bar{b})$ within the MSSM m_h^{max} [95, 92] scenario. This benchmark scenario is an improved version of the maximal mixing benchmark scenario [215, 56] which is defined in equation (2.64). The m_h^{max} conditions, for a given $\tan\beta$ and fixed SUSY scale M_S , maximize not only the theoretical upper bounds on the mass of the lightest CP-even Higgs boson h , M_h^{max} , as given in equation (2.62), but predict also the chargino and neutralino masses to be beyond the reach of LEP-2 [215, 56]. This is achieved by requiring relatively small values of the Higgsino mass parameter $|\mu|$. The values of the Higgsino mass parameter are either +200 or -200 GeV. Using this benchmark scenario, the most conservative bounds on $\tan\beta$ is obtained.

In the effective coupling approximation [80] the MSSM cross section $\sigma(pp \rightarrow b\Phi)$ reads

$$\sigma(gg \rightarrow bb + h/H/A)^{MSSM} = \frac{g_{(h/H/A,b\bar{b})}^{2,MSSM}(\tan\beta)}{g_{(H,b\bar{b})}^{2,SM}} \sigma^{NNLO,SM}(gb \rightarrow b + H), \quad (5.61)$$

where the ratios of the couplings, $g_{(h/H/A,b\bar{b})}^{2,MSSM}(\tan\beta)/g_{(H,b\bar{b})}^{2,SM}$, are non-trivial functions of $\tan\beta$ and the factor Δ_b given in equation (2.76) [91, 92, 93, 94], including the SUSY NNLO correction. $\sigma^{NNLO,SM}(gb \rightarrow bH)$ is the cross section of the Standard Model Higgs boson produced in association with b quarks. The cross section $\sigma^{NNLO,SM}(gg \rightarrow bb + H)$ is estimated with the NNLO accuracy and dependent on the Higgs boson mass M_H . In general, formula (5.61) is not written in terms of analytical functions, but rather Monte Carlo generators are used to numerically estimate it. We have used several Monte Carlo codes to numerically parametrize $\sigma(gg \rightarrow bb + \Phi(= h/H/A))^{MSSM}$ as a function of M_A and $\tan\beta$:

- FeynHiggs [80], [216], [184] to evaluate the ratios of couplings $\frac{g_{(h/H/A,b\bar{b})}^{2,MSSM}(\tan\beta)}{g_{(H,b\bar{b})}^{2,SM}}$, the Higgs boson masses $M_{h/H/A}$ and branching fractions $Br(h/H/A \rightarrow b\bar{b})$ at NLO;
- BBH@NNLO [181], [182], [183] to calculate the NNLO SM cross section $\sigma^{NNLO,SM}(gb \rightarrow bH)$ in the 5-flavor scheme as discussed in Section 2.9.

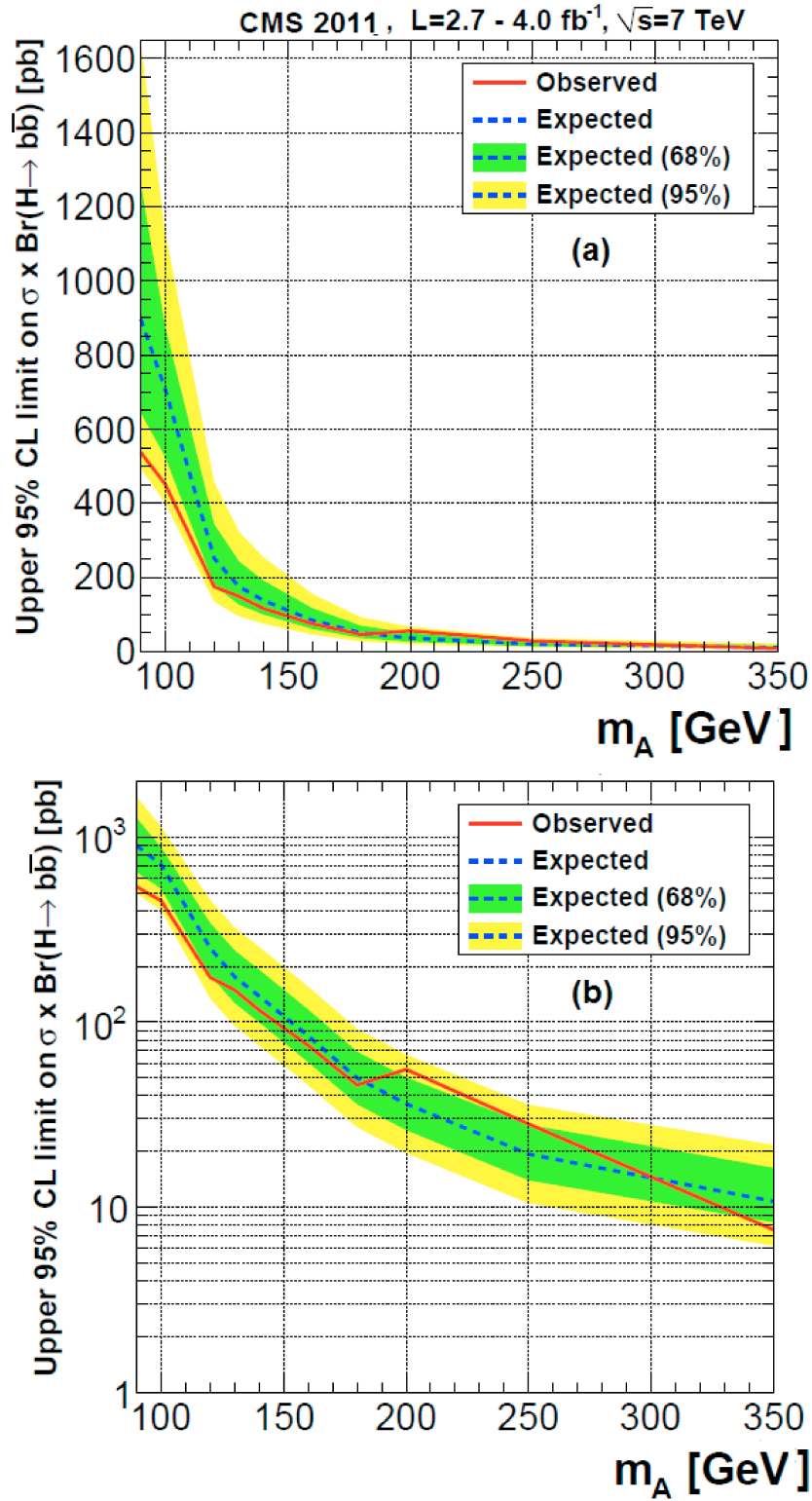


Figure 5.45: The observed 95% CL upper limits on the cross section times the branching fraction, (a) linear scale and (b) logarithmic scale for the ordinate.

To parametrize the response of the Monte Carlo generators in each bin of the $(M_A, \tan\beta)$ plane, two scans of $\sigma(gg \rightarrow bb + h/H/A)^{MSSM}$ constrained by requirements of the m_h^{max} scenario at 7 TeV energy are performed for $\mu = +200$ and $\mu = -200$ GeV [217]. Steps of 1 GeV for M_A between 90 and 1000 GeV and of 1 for $\tan\beta$ between 1 and 60 are used. Two-dimensional histograms are filled with the values of $\sigma(gg \rightarrow bb + h/H/A)^{MSSM}$. Figure 5.46 shows, as an example, the two-dimensional scan for $\mu = +200$ GeV.

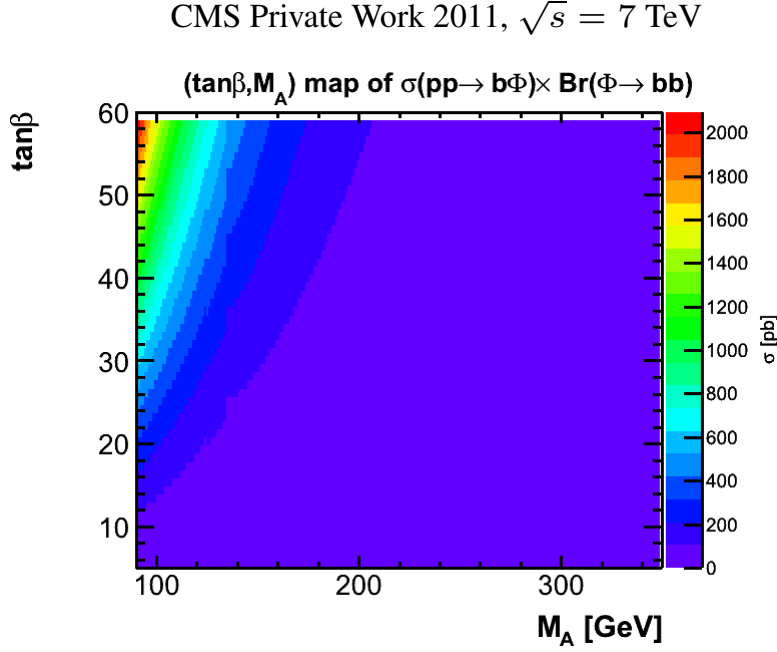


Figure 5.46: The scan of the cross section $\sigma(pp \rightarrow bb + \Phi)^{MSSM} \times Br(\Phi \rightarrow b\bar{b})$ as a function of $\tan\beta$ and M_A . The m_h^{max} benchmark scenario with $\mu = +200$ GeV is used.

The derivation of limits on $\tan\beta$ from the limits on the cross section is based on the knowledge of the functional form

$$\tan\beta(\sigma[gg \rightarrow bb + \Phi]^{MSSM} \times Br(\Phi \rightarrow b\bar{b})),$$

the inverse function of equation (5.61). The linear interpolation of the cross section values stored in bins of the scan histograms is used to parametrize $\tan\beta$ as a function of $\sigma(gg \rightarrow bb + \Phi)^{MSSM} \times Br(\Phi \rightarrow b\bar{b})$ when M_A is varied between 90 and 350 GeV. The $\tan\beta(\sigma[gg \rightarrow bb + \Phi]^{MSSM} \times Br(\Phi \rightarrow b\bar{b}))$ dependence for the Higgs signal of $M_A = 200$ GeV is depicted in Figure 5.47. As expected, the $\tan\beta$ function reads

$$\tan\beta(\sigma[gg \rightarrow bb + \Phi]^{MSSM} \times Br(\Phi \rightarrow b\bar{b})) \sim \sqrt{\sigma(gg \rightarrow bb + \Phi)^{MSSM} \times Br(\Phi \rightarrow b\bar{b})}.$$

The 95% CL observed, median limits and error bands on the $\tan\beta$ parameter are obtained using

the following prescription:

$$\begin{aligned}
\tan\beta^{95\%} &= \tan\beta(\mu_{up}^{95\%}), \\
\text{med}[\tan\beta^{95\%}] &= \tan\beta(\text{med}[\mu_{up}^{95\%}]), \\
\text{med}[\tan\beta^{95\%}] \pm N\sigma &= \tan\beta(\text{med}[\mu_{up}^{95\%}] \pm N\sigma),
\end{aligned} \tag{5.62}$$

where $N=1$ or 2 .

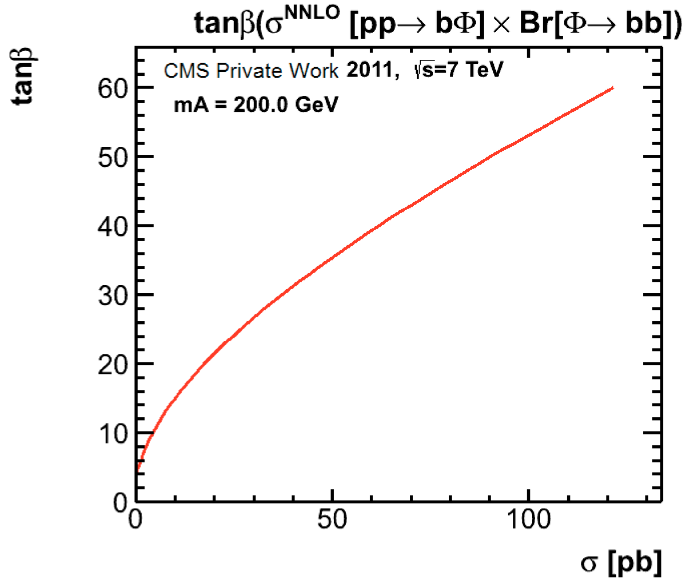


Figure 5.47: The function $\tan\beta(\sigma[gg \rightarrow bb + \Phi]^{MSSM} \times Br(\Phi \rightarrow b\bar{b}))$ obtained for the fixed $M_A = 200$ GeV in the m_h^{max} benchmark scenario with the Higgsino mass parameter $\mu = +200$ GeV.

The uncertainties of the renormalization and factorization scales, μ_r and μ_f , parton distribution functions and the strong coupling α_s have large impacts on cross-section predictions at the LHC [218]. They are considered as follows:

- **The $\mu_{r,f}$ scale uncertainties.** The scale uncertainties are the consequence of missing higher order corrections in the evaluated cross section. For the Higgs boson production processes, $\mu_f = \mu_r = M_H/2$ is chosen as a most likely value for the renormalization and factorization scales [96, 219]. An estimation of the uncertainty on the cross section is done by variations of $\mu_{r,f}$ in the interval $[M_H/4, M_H]$. Figure 5.48 (a) illustrates the effect from the variations of the scales $\mu_{r,f}$ to $\sigma(pp \rightarrow bb + \Phi)^{MSSM} \times Br(\Phi \rightarrow b\bar{b})$ at $M_A = 200$ GeV.
- **Parton distribution function uncertainties.** Calculation of physics observables at the level of quarks are done using quark and gluon momentum distributions, hereafter denoted as parton distribution functions, inside the proton. These distributions cannot be computed

in the framework of perturbative quantum field theory and need to be measured. Both parton distribution functions and α_s uncertainties, mostly arising from experimental uncertainties, are quadratically combined to the $pdf + \alpha_s$ uncertainty. The LHC Higgs Cross Section Working Group (LHC Higgs XSWG) [82, 218] gave recommendations on how to estimate an impact from the $pdf + \alpha_s$ uncertainty on cross sections. Using these recommendations, the effect of the $pdf + \alpha_s$ uncertainty on the $\sigma(pp \rightarrow bb + \Phi)^{MSSM} \times Br(\Phi \rightarrow b\bar{b})$ at $M_A = 200$ GeV is shown in the Figure 5.48 (b).

We include these uncertainties in our analysis following the prescription from LHC Higgs XSWG [218]. The signal expectation s_j (5.29) in the j^{th} bin of the observable X is modified by two multiplicative nuisances parameters v_{yield}^{QCD} and $v_{\text{yield}}^{pdf+\alpha_s}$,

$$s_j(v_{\text{yield}}^{QCD}, v_{\text{yield}}^{pdf+\alpha_s}, \{v_{\text{yield}}^s\}, \{p_k\}) = v_{\text{yield}}^{QCD} \cdot v_{\text{yield}}^{pdf+\alpha_s} \cdot \{v_{\text{yield}}^s\} \cdot s_{\text{tot}} \cdot \int_{\text{bin}_j} f^S(X, \{p_k\}) dX \quad (5.63)$$

We model the uncertainties v_{yield}^{QCD} and $v_{\text{yield}}^{pdf+\alpha_s}$ by the log-normal distribution

$$\pi(v_{\text{yield}}^{QCD, pdf+\alpha_s} | \tilde{v}_{\text{yield}}^{QCD, pdf+\alpha_s}) = \frac{1}{\sqrt{2\pi} \ln \delta_{\text{yield}}^{QCD, pdf+\alpha_s}} \frac{1}{v_{\text{yield}}^{QCD, pdf+\alpha_s}} \times \exp\left(-\frac{(\ln v_{\text{yield}}^{QCD, pdf+\alpha_s} - \ln \tilde{v}_{\text{yield}}^{QCD, pdf+\alpha_s})^2}{2(\ln \delta_{\text{yield}}^{QCD, pdf+\alpha_s})^2}\right), \quad (5.64)$$

where $\delta_{\text{yield}}^{QCD, pdf+\alpha_s}$ [220] is the relative variation of $\sigma(pp \rightarrow bb + \Phi)^{MSSM} \times Br(\Phi \rightarrow b\bar{b})$. The modification (5.63) of the signal expectation and the nuisance likelihoods (5.64) change the profile likelihoods ratio $\lambda(\mu)$ (5.35), the basis for the test statistic in the CL_s method. Figure 5.49 shows the effect from v_{yield}^{QCD} and $v_{\text{yield}}^{pdf+\alpha_s}$ on the quantity $-\ln(\lambda(\mu))$. The presence of the nuisance parameters v_{yield}^{QCD} , $v_{\text{yield}}^{pdf+\alpha_s}$ broadens the profile likelihood function shifting the upper limit $\mu^{95\%}$ from 65 to 67 pb.

Figure 5.50 and Table 5.14 present the 95% CL observed and expected median lower limits on $\tan\beta$ as a function of M_A . The MSSM m_h^{max} benchmark scenario with $\mu = +200$ GeV is used to translate model-independent upper limits on the cross section, $\mu^{95\%}$, to $\tan\beta^{95\%}$. The green and yellow bands correspond to $\pm 1\sigma$ and $\pm 2\sigma$ of the median expected limit $\text{med}[\tan\beta^{95\%}]$.

Next, we derive the 95% CL exclusion limit as the function $\tan\beta$ and M_A in the m_h^{max} scenario with $\mu = -200$ GeV. Figure 5.51 shows the obtained result together with previous limits set by Tevatron [221] and by LEP [222] experiments. All points of the observed $\tan\beta^{95\%}$ in this analysis are well within the expected $\pm 2\sigma$ bands, $\text{med}[\tan\beta^{95\%}] \pm 2\sigma$. The improvement of the sensitivity at relatively low values of $\tan\beta$ for the search in the $pp \rightarrow bb + \Phi \rightarrow 4b$ channel is nicely seen. The current analysis does not confirm the excess over the expected SM background for high values of $\tan\beta$, in the range $100 \leq M_A \leq 150$ GeV, as it was previously reported by CDF and D0 experiments [221].

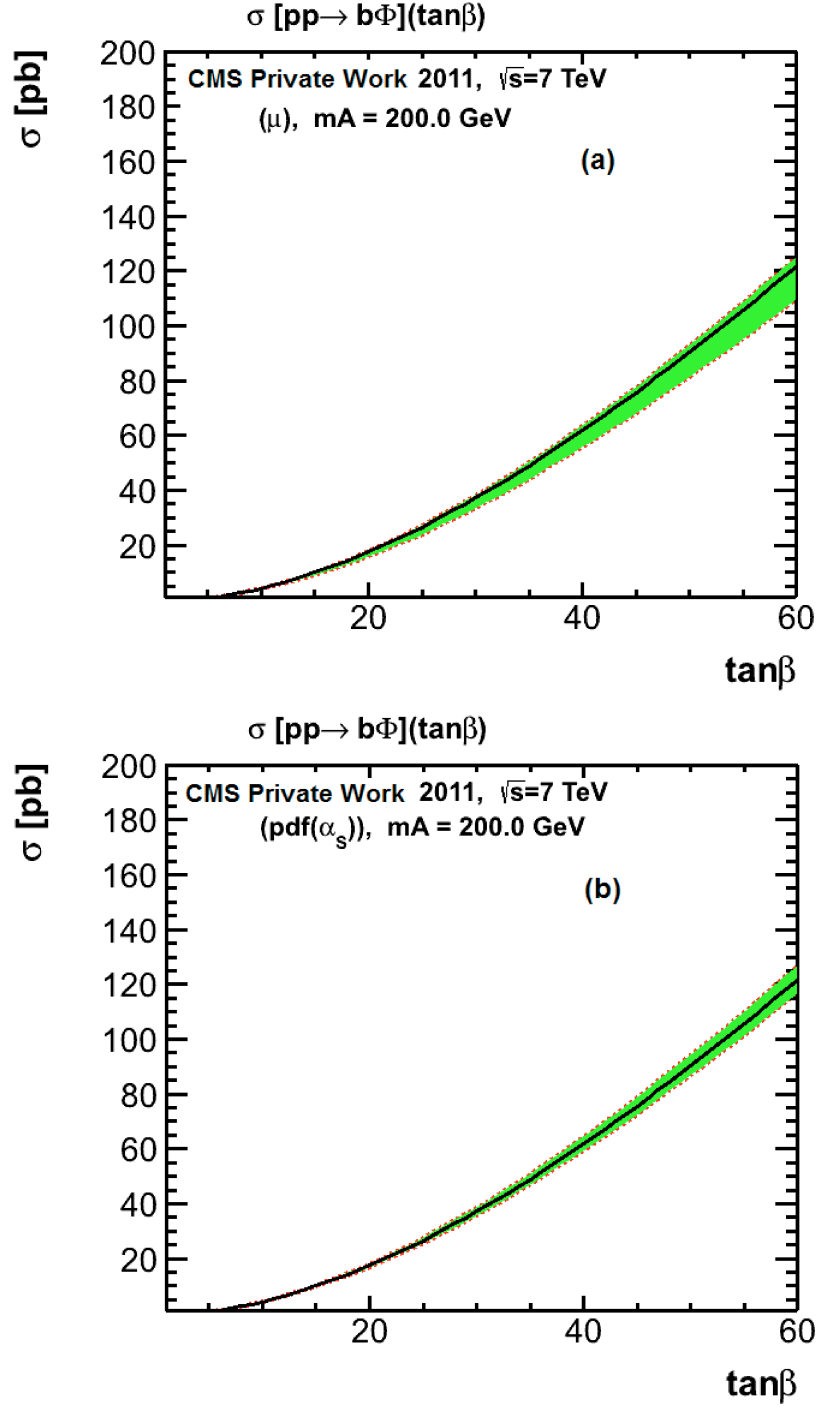


Figure 5.48: The effect of the scale $\mu_{r,f}$ (a) and $pdf + \alpha_s$ (b) uncertainties on the cross section as a function of $\tan\beta$ at $M_A = 200$ GeV in the m_h^{max} benchmark scenario with the Higgsino mass parameter $\mu = +200$ GeV. The green band (and red dashed curves) indicates the interval of the cross section variations due to the uncertainties.

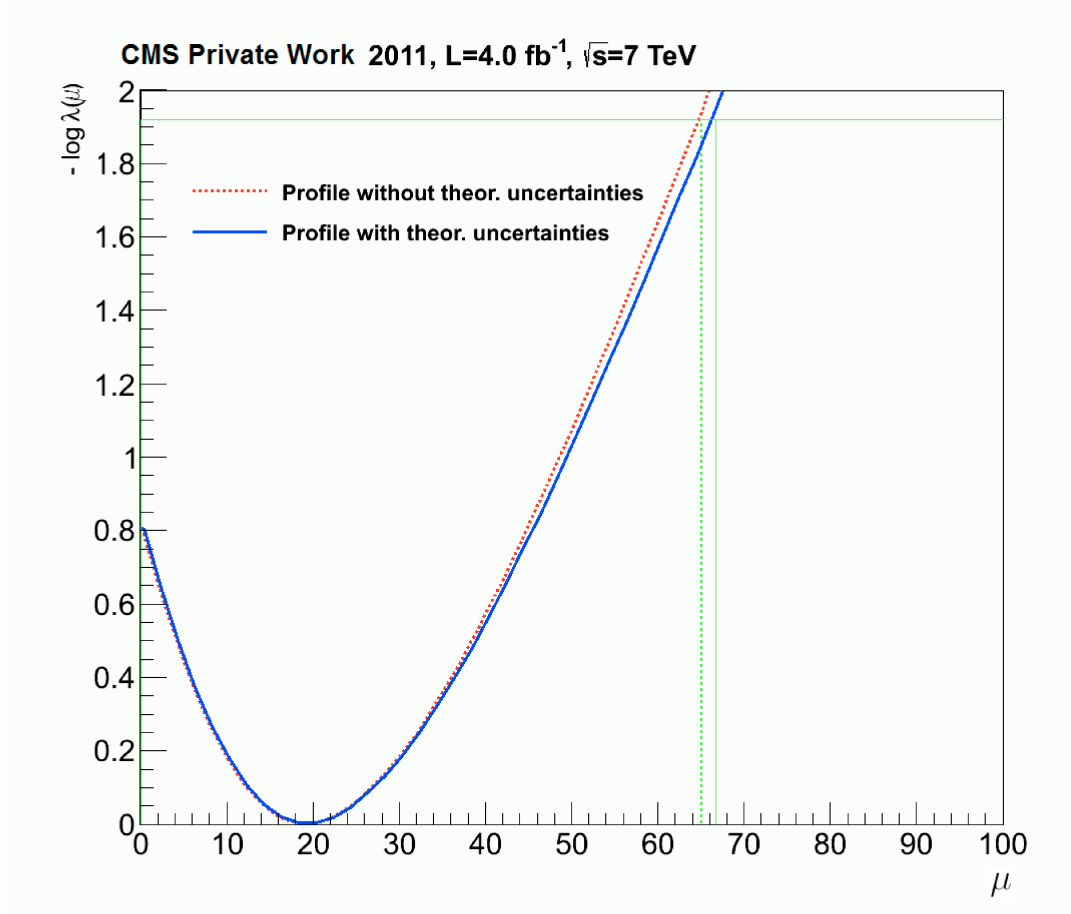


Figure 5.49: Measured $-\ln(\lambda(\mu))$ as a function of the signal strength μ . The expectation values s_j in the data model $L(X|\mu, \{v\})$ correspond to the signal hypothesis of the Higgs mass $M_A = 200$ GeV. The blue graph shows the behavior of $-\ln(\lambda(\mu))$ including the scale and parton distribution uncertainties. The red dashed curve corresponds to the case when the $\mu_{r,f}$ and $pdf + \alpha_S$ uncertainties are not considered.

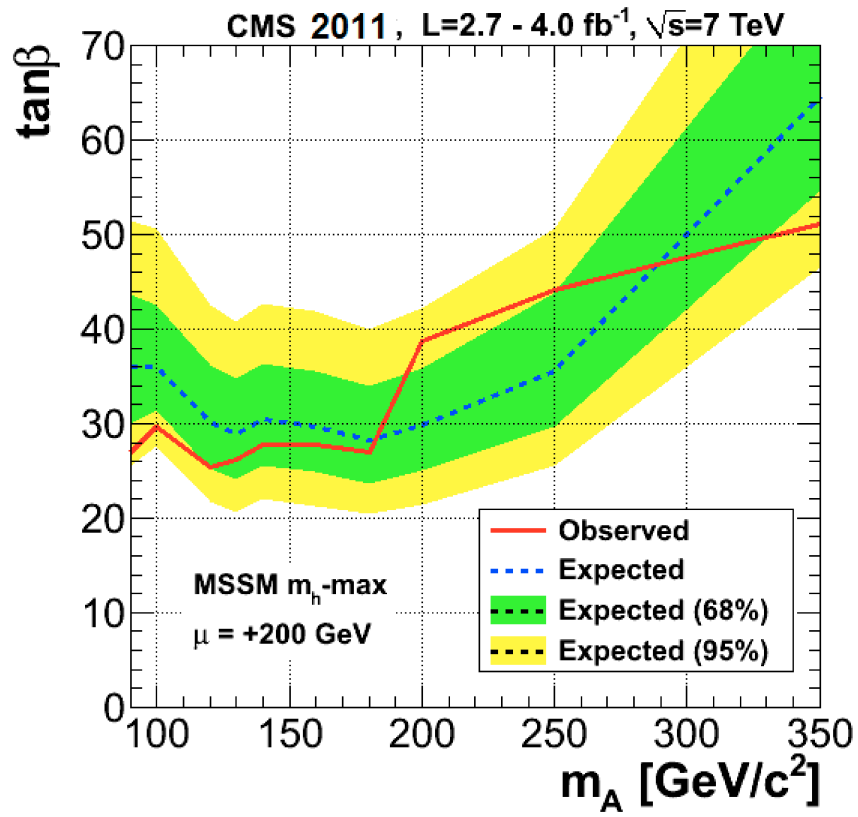


Figure 5.50: Observed and median expected 95% CL upper limits on $\tan\beta$ as a function of M_A in the m_{max}^h scenario for $\mu = +200$ GeV. The expected 1σ (green) and 2σ (yellow) bands are also shown.

Table 5.14: Observed and median expected lower limits at 95% CL on $\tan\beta$ in the m_h^{max} benchmark scenario for the Higgsino mass parameter $\mu = +200$ GeV.

M_A [GeV]	observed $\tan\beta^{95\%}$	med[$\tan\beta^{95\%}$]
90	27.0	36.0
100	29.7	36.0
120	25.4	30.2
130	26.2	28.8
140	27.7	30.4
160	27.8	29.7
180	27.0	28.3
200	38.8	29.9
250	44.1	35.6
350	51.1	64.7

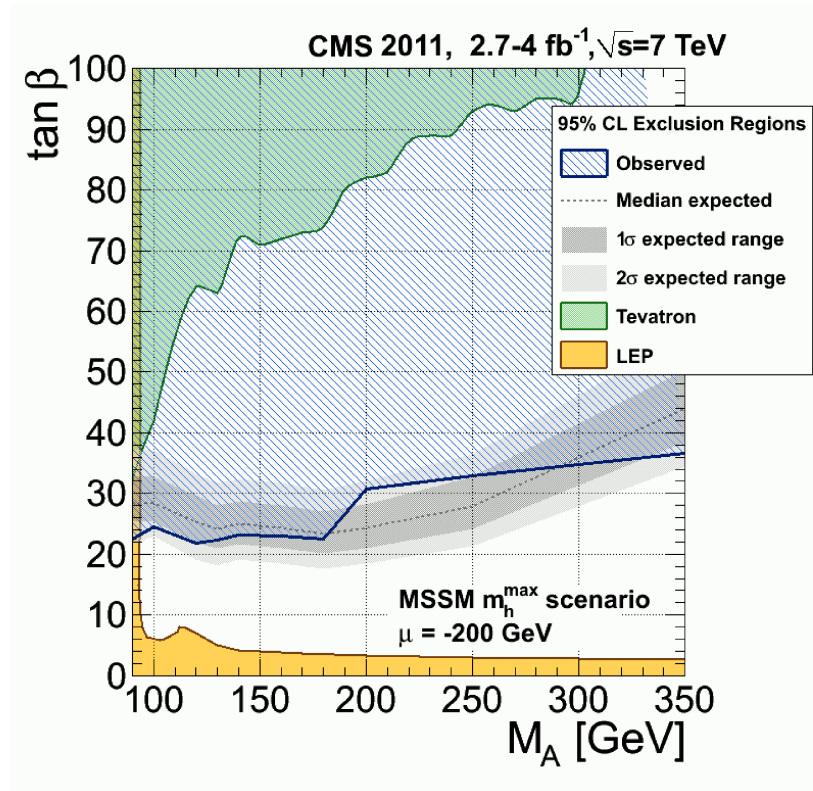


Figure 5.51: Observed and median expected 95% CL upper limits on $\tan\beta$ versus M_A in the m_h^{max} scenario for $\mu = -200$ GeV. One- and two-standard deviation ranges for the expected upper limit are represented by the gray bands. Previous exclusion regions from LEP [222] and Tevatron in the multi-b jet channel [221] are overlaid.

6 Conclusions

In this thesis, a search for neutral Higgs bosons in the channel $pp \rightarrow bb + \Phi \rightarrow 4b$ with $\Phi = h, H$ and A has been performed using data of the CMS experiment at the LHC. In the analysis events with at least three jets within the tracker acceptance were selected imposing asymmetric requirements on their p_T . These three jets must be identified as b jets. Two analysis scenarios were adopted to perform a search for additional neutral Higgs bosons of low and medium masses, respectively.

To model the background, two-dimensional templates, based on the invariant mass of the two leading b jets and the variable, reflecting b-jet content of the three leading jets, were derived from selected double-b-tagged data. Signal was modeled by templates obtained from Monte Carlo samples applying simulation of the High Level Trigger and correction for multiple interactions in a single bunch crossing. The resolution of the invariant mass of two leading jets, used to search for a signal, was estimated to be about 13%.

A Multivariate analysis method, called the gradient boosted-decision trees, was used to select a control sample with three b-tagged jets where the ratio of background to signal was enhanced by a factor of 3. During development and commissioning of the analysis, we tested the background modeling using distributions obtained in this MVA-based control sample.

The systematic uncertainties affecting the signal efficiency and changing shapes of the signal and background templates were identified. They were quantified by their effects on the number of the observed signal events.

Using a binned least-squares fit of the signal and background templates to data of a total luminosity of 2.67 and 3.99 fb⁻¹. in the low-mass and medium-mass scenarios, respectively, the signal and background yields were obtained. No significant evidence of a signal was observed in the data. The upper limit at the 95% confidence level on the signal cross section times branching fraction as a function of the pseudoscalar mass M_A was estimated exploiting the asymptotic CL_S method. The observed limit is decreasing from 537 to 7.55 pb with an increase of M_A from 90 to 350 GeV, respectively. This is well within the expected $\pm 2\sigma$ band.

We performed the interpretation of the obtained 95% CL upper limits on $\sigma(pp \rightarrow bb + \Phi) \times BR(\Phi \rightarrow b\bar{b})$ within the MSSM m_h^{max} scenario. The 95% CL observed and expected median lower limits on the MSSM parameter $\tan\beta$ were obtained as functions of M_A for the two choices of the Higgsino mass parameter, $\mu = \pm 200$ GeV. The 95% confidence level bounds on $\tan\beta$ varies from about 27 to 51 and from about 22 to 37 for the considered range of M_A in the m_h^{max} scenario for $\mu = +200$ GeV and $\mu = -200$ GeV, respectively. This analysis has excluded a region of the parameter space previously unexplored for this final state and did not confirm the excess over the expected SM background in the 100-150 GeV mass range for large values of $\tan\beta$, reported by the CDF and D0 experiments.

The result of this analysis extends the sensitivity for MSSM searches in the $\Phi \rightarrow b\bar{b}$ channel down to values of $\tan\beta$, never reached before for the masses M_A between 90 and 350 GeV.

Bibliography

- [1] Steven Weinberg. The Quantum theory of fields. Vol. 1: Foundations. 1995.
- [2] Michael E. Peskin and Daniel V. Schroeder. An Introduction to quantum field theory. 1995, ISBN-9780201503975.
- [3] F. Halzen and Alan D. Martin. QUARKS AND LEPTONS: AN INTRODUCTORY COURSE IN MODERN PARTICLE PHYSICS. 1984, ISBN-9780471887416.
- [4] Gordon L. Kane. MODERN ELEMENTARY PARTICLE PHYSICS. 1987, ISBN-9780201624601.
- [5] S.L. Glashow. Partial Symmetries of Weak Interactions. *Nucl.Phys.*, 22:579–588, 1961.
- [6] Steven Weinberg. A Model of Leptons. *Phys.Rev.Lett.*, 19:1264–1266, 1967.
- [7] Abdus Salam. Weak and Electromagnetic Interactions. *Conf.Proc.*, C680519:367–377, 1968.
- [8] Howard Georgi. *Lie algebras in particle physics*. Number 54 in Frontiers in physics ; 54 ; The advanced book program ; Frontiers in physics. Perseus Books ; Westview Press, Reading, Mass. ; Boulder, Colo. [u.a.], 2. ed. edition, 1999.
- [9] G. Abbiendi et al. A Simultaneous measurement of the QCD color factors and the strong coupling. *Eur.Phys.J.*, C20:601–615, 2001, hep-ex/0101044.
- [10] Stephen Thornton and Jerry Marion. *Classical Dynamics of Particles and Systems*. 5th edition edition, 2004.
- [11] S. Schael et al. Precision electroweak measurements on the Z resonance. *Phys.Rept.*, 427:257–454, 2006, hep-ex/0509008.
- [12] T. Affolder et al. Search for a fourth-generation quark more massive than the Z0 boson in $p\bar{p}$ collisions at $\sqrt{s} = 1.8$ TeV. *Phys.Rev.Lett.*, 84:835–840, 2000, hep-ex/9909027.
- [13] Nicola Cabibbo. Unitary Symmetry and Leptonic Decays. *Phys.Rev.Lett.*, 10:531–533, 1963.
- [14] Makoto Kobayashi and Toshihide Maskawa. CP Violation in the Renormalizable Theory of Weak Interaction. *Prog.Theor.Phys.*, 49:652–657, 1973, KUNS-242.

- [15] Ling-Lie Chau and Wai-Yee Keung. Comments on the Parametrization of the Kobayashi-Maskawa Matrix. *Phys.Rev.Lett.*, 53:1802, 1984, BNL-34643.
- [16] Michael Dine. TASI lectures on the strong CP problem. pages 349–369, 2000, hep-ph/0011376.
- [17] Jihn E. Kim and Gianpaolo Carosi. Axions and the Strong CP Problem. *Rev.Mod.Phys.*, 82:557–602, 2010, 0807.3125.
- [18] Y. Ashie et al. Evidence for an oscillatory signature in atmospheric neutrino oscillation. *Phys.Rev.Lett.*, 93:101801, 2004, hep-ex/0404034.
- [19] Q.R. Ahmad et al. Direct evidence for neutrino flavor transformation from neutral current interactions in the Sudbury Neutrino Observatory. *Phys.Rev.Lett.*, 89:011301, 2002, nucl-ex/0204008.
- [20] Hans Peter Nilles. Supersymmetry, Supergravity and Particle Physics. *Phys.Rept.*, 110:1–162, 1984.
- [21] Gerard 't Hooft. Dimensional regularization and the renormalization group. *Nucl.Phys.*, B61:455–468, 1973.
- [22] William A. Bardeen, A.J. Buras, D.W. Duke, and T. Muta. Deep Inelastic Scattering Beyond the Leading Order in Asymptotically Free Gauge Theories. *Phys.Rev.*, D18:3998, 1978.
- [23] D.I. Kazakov. Beyond the standard model: In search of supersymmetry. pages 125–199, 2000, hep-ph/0012288.
- [24] J. Wess and B. Zumino. Supergauge Invariant Extension of Quantum Electrodynamics. *Nucl.Phys.*, B78:1, 1974.
- [25] Abdus Salam and J.A. Strathdee. Supergauge Transformations. *Nucl.Phys.*, B76:477–482, 1974.
- [26] Abdus Salam and J.A. Strathdee. On Superfields and Fermi-Bose Symmetry. *Phys.Rev.*, D11:1521–1535, 1975.
- [27] J. Wess and B. Zumino. Supergauge Transformations in Four-Dimensions. *Nucl.Phys.*, B70:39, 1974.
- [28] Howard E. Haber. Introductory low-energy supersymmetry. 1993, hep-ph/9306207.
- [29] W. de Boer. Grand unified theories and supersymmetry in particle physics and cosmology. *Prog.Part.Nucl.Phys.*, 33:201–302, 1994, hep-ph/9402266.

- [30] D.I. Kazakov. Supersymmetry in particle physics: the renormalization group viewpoint. *Phys.Rept.*, 344:309–353, 2001, hep-ph/0001257.
- [31] L. O’Raifeartaigh. Spontaneous Symmetry Breaking for Chiral Scalar Superfields. *Nucl.Phys.*, B96:331, 1975.
- [32] Lawrence J. Hall, Joseph D. Lykken, and Steven Weinberg. Supergravity as the Messenger of Supersymmetry Breaking. *Phys.Rev.*, D27:2359–2378, 1983.
- [33] Sanjeev K. Soni and H. Arthur Weldon. Analysis of the Supersymmetry Breaking Induced by N=1 Supergravity Theories. *Phys.Lett.*, B126:215, 1983.
- [34] Hans Peter Nilles. Dynamically Broken Supergravity and the Hierarchy Problem. *Phys.Lett.*, B115:193, 1982.
- [35] Riccardo Barbieri, S. Ferrara, and Carlos A. Savoy. Gauge Models with Spontaneously Broken Local Supersymmetry. *Phys.Lett.*, B119:343, 1982.
- [36] Hans Peter Nilles, M. Srednicki, and D. Wyler. Weak Interaction Breakdown Induced by Supergravity. *Phys.Lett.*, B120:346, 1983.
- [37] J. Goldstone. Field Theories with Superconductor Solutions. *Nuovo Cim.*, 19:154–164, 1961.
- [38] Jeffrey Goldstone, Abdus Salam, and Steven Weinberg. Broken Symmetries. *Phys.Rev.*, 127:965–970, 1962.
- [39] M.A. Lopez-Osorio, E. Martinez-Pascual, and J.J. Toscano. Some comments on unitarity gauge. *Rev.Mex.Fis.*, 50:107–119, 2004.
- [40] Steven Weinberg. General Theory of Broken Local Symmetries. *Phys.Rev.*, D7:1068–1082, 1973.
- [41] V. Elias, D.G.C. McKeon, and T.N. Sherry. Summation of higher order effects using the renormalization group equation. *Int.J.Mod.Phys.*, A20:1065–1088, 2005, hep-th/0408152.
- [42] B.C. Allanach. SOFTSUSY: a program for calculating supersymmetric spectra. *Comput.Phys.Commun.*, 143:305–331, 2002, hep-ph/0104145.
- [43] Vernon D. Barger, M.S. Berger, and P. Ohmann. The Supersymmetric particle spectrum. *Phys.Rev.*, D49:4908–4930, 1994, hep-ph/9311269.
- [44] Stephen P. Martin. Two loop effective potential for a general renormalizable theory and softly broken supersymmetry. *Phys.Rev.*, D65:116003, 2002, hep-ph/0111209.
- [45] Youichi Yamada. Two loop renormalization of tan beta and its gauge dependence. *Phys.Lett.*, B530:174–178, 2002, hep-ph/0112251.

- [46] B.C. Allanach, M. Battaglia, G.A. Blair, Marcela S. Carena, A. De Roeck, et al. The Snowmass points and slopes: Benchmarks for SUSY searches. *Eur.Phys.J.*, C25:113–123, 2002, hep-ph/0202233.
- [47] Georg Weiglein. The LHC / LC study group and the snowmass points and slopes. pages 911–918, 2003, hep-ph/0301111.
- [48] Nabil Ghodbane and Hans-Ulrich Martyn. Compilation of SUSY particle spectra from Snowmass 2001 benchmark models. 2002, hep-ph/0201233.
- [49] LEP Higgs Working Group. Papers and notes. http://lephiggs.web.cern.ch/LEPHIGGS/papers/July2005_MSSM/index.html, January 2005.
- [50] R. Barate et al. Observation of an excess in the search for the standard model Higgs boson at ALEPH. *Phys.Lett.*, B495:1–17, 2000, hep-ex/0011045.
- [51] B.C. Allanach, A. Djouadi, J.L. Kneur, W. Porod, and P. Slavich. Precise determination of the neutral Higgs boson masses in the MSSM. *JHEP*, 0409:044, 2004, hep-ph/0406166.
- [52] Y. Okada, Masahiro Yamaguchi, and T. Yanagida. Renormalization group analysis on the Higgs mass in the softly broken supersymmetric standard model. *Phys.Lett.*, B262:54–58, 1991.
- [53] John R. Ellis, Giovanni Ridolfi, and Fabio Zwirner. On radiative corrections to supersymmetric Higgs boson masses and their implications for LEP searches. *Phys.Lett.*, B262:477–484, 1991.
- [54] Abdelhak Djouadi. The Anatomy of electro-weak symmetry breaking. II. The Higgs bosons in the minimal supersymmetric model. *Phys.Rept.*, 459:1–241, 2008, hep-ph/0503173.
- [55] A. Arbey, M. Battaglia, A. Djouadi, F. Mahmoudi, and J. Quevillon. Implications of a 125 GeV Higgs for supersymmetric models. *Phys.Lett.*, B708:162–169, 2012, 1112.3028.
- [56] Marcela S. Carena, S. Heinemeyer, C.E.M. Wagner, and G. Weiglein. Suggestions for benchmark scenarios for MSSM Higgs boson searches at hadron colliders. *Eur.Phys.J.*, C26:601–607, 2003, hep-ph/0202167.
- [57] Georges Aad et al. Observation of a new particle in the search for the Standard Model Higgs boson with the ATLAS detector at the LHC. *Phys.Lett.*, B716:1–29, 2012, 1207.7214.
- [58] Serguei Chatrchyan et al. Observation of a new boson at a mass of 125 GeV with the CMS experiment at the LHC. *Phys.Lett.*, B716:30–61, 2012, 1207.7235.
- [59] S. Heinemeyer, O. Stal, and G. Weiglein. Interpreting the LHC Higgs Search Results in the MSSM. *Phys.Lett.*, B710:201–206, 2012, 1112.3026.

- [60] Lawrence J. Hall, David Pinner, and Joshua T. Ruderman. A Natural SUSY Higgs Near 126 GeV. *JHEP*, 1204:131, 2012, 1112.2703.
- [61] Marcela Carena, Stefania Gori, Nausheen R. Shah, and Carlos E.M. Wagner. A 125 GeV SM-like Higgs in the MSSM and the $\gamma\gamma$ rate. *JHEP*, 1203:014, 2012, 1112.3336.
- [62] R. Benbrik, M. Gomez Bock, S. Heinemeyer, O. Stal, G. Weiglein, et al. Confronting the MSSM and the NMSSM with the Discovery of a Signal in the two Photon Channel at the LHC. *Eur.Phys.J.*, C72:2171, 2012, 1207.1096.
- [63] Manuel Drees. A Supersymmetric Explanation of the Excess of Higgs–Like Events at the LHC and at LEP. *Phys.Rev.*, D86:115018, 2012, 1210.6507.
- [64] Marcela S. Carena and Howard E. Haber. Higgs boson theory and phenomenology. *Prog.Part.Nucl.Phys.*, 50:63–152, 2003, hep-ph/0208209.
- [65] Howard E. Haber, Ralf Hempfling, and Andre H. Hoang. Approximating the radiatively corrected Higgs mass in the minimal supersymmetric model. *Z.Phys.*, C75:539–554, 1997, hep-ph/9609331.
- [66] John R. Ellis, Giovanni Ridolfi, and Fabio Zwirner. Radiative corrections to the masses of supersymmetric Higgs bosons. *Phys.Lett.*, B257:83–91, 1991.
- [67] Howard E. Haber and Ralf Hempfling. Can the mass of the lightest Higgs boson of the minimal supersymmetric model be larger than $m(Z)$? *Phys.Rev.Lett.*, 66:1815–1818, 1991.
- [68] S.L. Glashow, Dimitri V. Nanopoulos, and A. Yildiz. Associated Production of Higgs Bosons and Z Particles. *Phys.Rev.*, D18:1724–1727, 1978.
- [69] J. Finjord, G. Girardi, and P. Sorba. The Needle in the Large p_T Haystack: Higgs Versus Quark or Gluon Jets Together With 0 in Hadronic Reactions. *Phys.Lett.*, B89:99, 1979.
- [70] E. Eichten, I. Hinchliffe, Kenneth D. Lane, and C. Quigg. Super Collider Physics. *Rev.Mod.Phys.*, 56:579–707, 1984.
- [71] D.R.T. Jones and S.T. Petcov. Heavy Higgs Bosons at LEP. *Phys.Lett.*, B84:440, 1979.
- [72] R.N. Cahn and Sally Dawson. Production of Very Massive Higgs Bosons. *Phys.Lett.*, B136:196, 1984.
- [73] Duane A. Dicus and Scott S.D. Willenbrock. Higgs Bosons From Vector Boson Fusion in e^+e^- , ep and pp Collisions. *Phys.Rev.*, D32:1642, 1985.
- [74] H.M. Georgi, S.L. Glashow, M.E. Machacek, and Dimitri V. Nanopoulos. Higgs Bosons from Two Gluon Annihilation in Proton Proton Collisions. *Phys.Rev.Lett.*, 40:692, 1978.

- [75] Risto Raitio and Walter W. Wada. Higgs Boson Production at Large Transverse Momentum in QCD. *Phys.Rev.*, D19:941, 1979.
- [76] A.S. Bagdasaryan, R. Sh. Egorian, S.G. Grigorian, and Sergei G. Matinyan. Some Peculiarities of Conjoined Hadroproduction of Standard Higgs Boson and Heavy Quark Pair. *Sov.J.Nucl.Phys.*, 46:315, 1987.
- [77] John N. Ng and Pierre Zakarauskas. A QCD Parton Calculation of Conjoined Production of Higgs Bosons and Heavy Flavors in $p\bar{p}$ Collision. *Phys.Rev.*, D29:876, 1984.
- [78] R. Michael Barnett, Howard E. Haber, and Davison E. Soper. Ultraheavy Particle Production from Heavy Partons at Hadron Colliders. *Nucl.Phys.*, B306:697, 1988.
- [79] Duane A. Dicus and Scott Willenbrock. Higgs Boson Production from Heavy Quark Fusion. *Phys.Rev.*, D39:751, 1989.
- [80] T. Hahn, S. Heinemeyer, F. Maltoni, G. Weiglein, and S. Willenbrock. SM and MSSM Higgs boson production cross-sections at the Tevatron and the LHC. 2006, hep-ph/0607308.
- [81] HXSWG. Lhc higgs cross section working group. <https://twiki.cern.ch/twiki/bin/view/LHCPhysics/CrossSections>, 2013.
- [82] S. Dittmaier et al. Handbook of LHC Higgs Cross Sections: 1. Inclusive Observables. 2011, 1101.0593.
- [83] M. Spira, A. Djouadi, D. Graudenz, and P.M. Zerwas. Higgs boson production at the LHC. *Nucl.Phys.*, B453:17–82, 1995, hep-ph/9504378.
- [84] Robert V. Harlander and William B. Kilgore. Higgs boson production in bottom quark fusion at next-to-next-to leading order. *Phys.Rev.*, D68:013001, 2003, hep-ph/0304035.
- [85] Robert V. Harlander and William B. Kilgore. Next-to-next-to-leading order Higgs production at hadron colliders. *Phys.Rev.Lett.*, 88:201801, 2002, hep-ph/0201206.
- [86] Robert V. Harlander and William B. Kilgore. Production of a pseudoscalar Higgs boson at hadron colliders at next-to-next-to leading order. *JHEP*, 0210:017, 2002, hep-ph/0208096.
- [87] Michael Spira. HIGLU: A program for the calculation of the total Higgs production cross-section at hadron colliders via gluon fusion including QCD corrections. 1995, hep-ph/9510347.
- [88] Abdelhak Djouadi. The Anatomy of electro-weak symmetry breaking. I: The Higgs boson in the standard model. *Phys.Rept.*, 457:1–216, 2008, hep-ph/0503172.

- [89] Alan D. Martin, R.G. Roberts, W.J. Stirling, and R.S. Thorne. MRST2001: Partons and α_s from precise deep inelastic scattering and Tevatron jet data. *Eur.Phys.J.*, C23:73–87, 2002, hep-ph/0110215.
- [90] A.D. Martin, R.G. Roberts, W.J. Stirling, and R.S. Thorne. NNLO global parton analysis. *Phys.Lett.*, B531:216–224, 2002, hep-ph/0201127.
- [91] Marcela S. Carena, David Garcia, Ulrich Nierste, and Carlos E.M. Wagner. Effective Lagrangian for the $\bar{t}bH^+$ interaction in the MSSM and charged Higgs phenomenology. *Nucl.Phys.*, B577:88–120, 2000, hep-ph/9912516.
- [92] Marcela S. Carena, S. Heinemeyer, C.E.M. Wagner, and G. Weiglein. MSSM Higgs boson searches at the Tevatron and the LHC: Impact of different benchmark scenarios. *Eur.Phys.J.*, C45:797–814, 2006, hep-ph/0511023.
- [93] S. Dawson, C.B. Jackson, L. Reina, and D. Wackeroth. Hadronic Higgs production with heavy quarks at the Tevatron and the LHC. 2006, hep-ph/0603112.
- [94] Jaume Guasch, Petra Hafliger, and Michael Spira. MSSM Higgs decays to bottom quark pairs revisited. *Phys.Rev.*, D68:115001, 2003, hep-ph/0305101.
- [95] Msusy = 1 tev, xt = 2 tev, m2 = 0.2 tev || = 0.2 tev, and mg = 0.8 tev.
- [96] A.D. Martin, W.J. Stirling, R.S. Thorne, and G. Watt. Parton distributions for the LHC. *Eur.Phys.J.*, C63:189–285, 2009, 0901.0002.
- [97] Stefan Dittmaier, 1 Kramer, Michael, and Michael Spira. Higgs radiation off bottom quarks at the Tevatron and the CERN LHC. *Phys.Rev.*, D70:074010, 2004, hep-ph/0309204.
- [98] S. Dawson, C.B. Jackson, L. Reina, and D. Wackeroth. Exclusive Higgs boson production with bottom quarks at hadron colliders. *Phys.Rev.*, D69:074027, 2004, hep-ph/0311067.
- [99] Robert Harlander, Michael Kramer, and Markus Schumacher. Bottom-quark associated Higgs-boson production: reconciling the four- and five-flavour scheme approach. 2011, 1112.3478.
- [100] John M. Campbell, R. Keith Ellis, F. Maltoni, and S. Willenbrock. Higgs-Boson production in association with a single bottom quark. *Phys.Rev.*, D67:095002, 2003, hep-ph/0204093.
- [101] Z. Sullivan and Pavel M. Nadolsky. Heavy quark parton distribution functions and their uncertainties. *eConf*, C010630:P511, 2001, hep-ph/0111358.
- [102] Marcela S. Carena, J.R. Espinosa, M. Quiros, and C.E.M. Wagner. Analytical expressions for radiatively corrected Higgs masses and couplings in the MSSM. *Phys.Lett.*, B355:209–221, 1995, hep-ph/9504316.

- [103] Marcela S. Carena, M. Quiros, and C.E.M. Wagner. Effective potential methods and the Higgs mass spectrum in the MSSM. *Nucl.Phys.*, B461:407–436, 1996, hep-ph/9508343.
- [104] J.F. Gunion, A. Stange, and S. Willenbrock. Weakly coupled Higgs bosons. 1995, hep-ph/9602238.
- [105] *Technical proposal*. LHC Tech. Proposal. CERN, Geneva, 1994. Cover title : CMS, the Compact Muon Solenoid : technical proposal.
- [106] *ATLAS: technical proposal for a general-purpose pp experiment at the Large Hadron Collider at CERN*. LHC Tech. Proposal. CERN, Geneva, 1994.
- [107] ALICE Collaboration. Technical design reports. <http://aliweb.cern.ch/Documents/TDR/index.html>, September 2006.
- [108] LHCb Collaboration. Technical design reports. <http://lhcb.web.cern.ch/lhcb/TDR/TDR.htm>, August 2003.
- [109] Oliver Sim Bruening, Paul Collier, P Lebrun, Stephen Myers, Ranko Ostojic, John Poole, and Paul Proudlock. *LHC Design Report*. CERN, Geneva, 2004.
- [110] Karlheinz Schindl. The injector chain for the LHC. Technical Report CERN-OPEN-99-052, Jan 1999.
- [111] Thomas Sven Pettersson and P Lefe. The Large Hadron Collider: conceptual design. Technical Report CERN-AC-95-05 LHC, CERN, Geneva, Oct 1995.
- [112] Bayatian et al. *CMS Physics: Technical Design Report Volume 1: Detector Performance and Software*. Technical Design Report CMS. CERN, Geneva, 2006. There is an error on cover due to a technical problem for some items.
- [113] LHC Programme Coordination web pages. Overview - lhc commissioning strategy with beam 2009. <http://lhc-commissioning.web.cern.ch/lhc-commissioning/phases/2009/LHC-beamcom-2009-strategy.htm>, August 2009.
- [114] LHC Programme Coordination web pages. Lhc luminosity plots for the 2011/2012. <http://lpc.web.cern.ch/lpc/lumiplots.htm>, August 2011.
- [115] John M. Campbell, J.W. Huston, and W.J. Stirling. Hard Interactions of Quarks and Gluons: A Primer for LHC Physics. *Rept.Prog.Phys.*, 70:89, 2007, hep-ph/0611148.
- [116] W. Kittel and E.A. De Wolf. *"Soft Multihadron Dynamics"*. World Scientific Publishing Company, Incorporated, 2005.
- [117] J.R. Cudell et al. Benchmarks for the forward observables at RHIC, the Tevatron Run II and the LHC. *Phys.Rev.Lett.*, 89:201801, 2002, hep-ph/0206172.

- [118] Vardan Khachatryan et al. Transverse momentum and pseudorapidity distributions of charged hadrons in pp collisions at $\sqrt{s} = 0.9$ and 2.36 TeV. *JHEP*, 1002:041, 2010, 1002.0621.
- [119] Bayatian et al. Cms physics: Technical design report volume 2: Physics performance. *J. Phys. G*, 34(CERN-LHCC-2006-021. CMS-TDR-8-2):995–1579. 669 p, 2007. revised version submitted on 2006-09-22 17:44:47.
- [120] Search for a standard model like Higgs boson in the decay channel $H \rightarrow ZZ \rightarrow l+l- q \bar{q}$ at CMS. Technical Report CMS-PAS-HIG-12-024, CERN, Geneva, 2013.
- [121] Forward-backward asymmetry of Drell-Yan pairs. Technical Report CMS-PAS-EWK-11-004, CERN, Geneva, 2012.
- [122] Combination of ATLAS and CMS results on the mass of the top-quark using up to 4.9 fb^{-1} of $\sqrt{s} = 7$ TeV LHC data. Technical Report ATLAS-CONF-2013-102, CERN, Geneva, Sep 2013.
- [123] Johannes Albrecht. Search for New Physics in rare decays at LHCb. *Nucl.Phys.Proc.Suppl.*, 241-242:49–54, 2013, 1209.1208.
- [124] V.A. Polychronakos and V. Tcherniatine. The Effect of Inclined Tracks and the Lorentz Angle on the Spatial Resolution of the Interpolating Cathode Strip Chambers. Technical Report SSC-GEM-TN-92-137, 1992.
- [125] D Giordano and G Sguazzoni. Cms reconstruction improvements for the tracking in large pile-up events. *Journal of Physics: Conference Series*, 396(2):022044, 2012.
- [126] CMS Collaboration. CMS: The electromagnetic calorimeter. Technical design report. Technical Report CERN-LHCC-97-33, CMS-TDR-4, 1997.
- [127] CMS Collaboration. CMS: The hadron calorimeter technical design report. Technical Report CERN-LHCC-97-31, 1997.
- [128] Particle Data Group. Atomic and nuclear properties of materials. http://pdg.lbl.gov/2012/AtomicNuclearProperties/HTML_PAGES/301.html, December 2012.
- [129] Eidelman et al. Review of Particle Physics. *Physics Letters B*, 592:1+, 2004.
- [130] P. Lecoq, I. Dafinei, E. Auffray, M. Schneegans, M.V. Korzhik, O.V. Missevitch, V.B. Pavlenko, A.A. Fedorov, A.N. Annenkov, V.L. Kostylev, and V.D. Ligun. Lead tungstate (pbw04) scintillators for {LHC} {EM} calorimetry. *Nuclear Instruments and Methods in Physics Research Section A: Accelerators, Spectrometers, Detectors and Associated Equipment*, 365(2-3):291 – 298, 1995.

- [131] A.A Annenkov, M.V Korzhik, and P Lecoq. Lead tungstate scintillation material. *Nuclear Instruments and Methods in Physics Research Section A: Accelerators, Spectrometers, Detectors and Associated Equipment*, 490(1-2):30 – 50, 2002.
- [132] CMS Electromagnetic Calorimeter Group, P. Adzic, N. Almeida, D. Andelin, I. Anicin, Z. Antunovic, R. Arcidiacono, M. W. Arenton, E. Auffray, S. Argiro, and et al. Radiation hardness qualification of PbWO₄ scintillation crystals for the CMS Electromagnetic Calorimeter. *Journal of Instrumentation*, 5:3010, March 2010, 0910.3423.
- [133] P. Adzic, R. Alemany-Fernandez, C.B. Almeida, N.M. Almeida, G. Anagnostou, et al. Energy resolution of the barrel of the CMS electromagnetic calorimeter. *JINST*, 2:P04004, 2007.
- [134] Serguei Chatrchyan et al. Energy calibration and resolution of the CMS electromagnetic calorimeter in pp collisions at $\sqrt{s} = 7$ TeV. Technical Report CMS-EGM-11-001, CERN-PH-EP-2013-097, 2013, 1306.2016.
- [135] Arie Bodek. Performance of a prototype CMS hadron barrel calorimeter in a test beam. *IEEE Trans.Nucl.Sci.*, 46:407–409, 1999, hep-ex/9810033.
- [136] Victor Daniel Elvira. Measurement of the pion energy response and resolution in the cms hcal test beam 2002 experiment. Technical Report CMS-NOTE-2004-020, CERN, Geneva, Sep 2004.
- [137] G.L. Bayatyan et al. Cms tridas project: Technical design report, volume 1: The trigger systems. Technical Report CERN-LHCC-2000-038 ; CMS-TDR-6-1, 2002.
- [138] W. Adam et al. The CMS high level trigger. *Eur.Phys.J.*, C46:605–667, 2006, hep-ex/0512077.
- [139] G.L. Bayatyan et al. Cms tridas project: Technical design report, volume 2: The data acquisition and high-level trigger. Technical Report CERN-LHCC-2000-026 ; CMS-TDR-6-2, 2002.
- [140] Wikipedia. The Kalman Filter . http://en.wikipedia.org/wiki/Kalman_filter.
- [141] Matteo Cacciari, Gavin P. Salam, and Gregory Soyez. The Anti-k(t) jet clustering algorithm. *JHEP*, 0804:063, 2008, 0802.1189.
- [142] Wolfgang Adam, Boris Mangano, Thomas Speer, and Teddy Todorov. Track reconstruction in the cms tracker. Technical Report CMS-NOTE-2006-041, CERN, Geneva, Dec 2006.
- [143] R. Fruehwirth, P. Kubinec, W. Mitaroff, and M. Regler. Vertex reconstruction and track bundling at the {LEP} collider using robust algorithms. *Computer Physics Communications*, 96(2-3):189 – 208, 1996.

- [144] Susanna Cucciarelli, Marcin Konecki, Danek Kotlinski, and Teddy Todorov. Track reconstruction, primary vertex finding and seed generation with the pixel detector. Technical Report CMS-NOTE-2006-026, CERN, Geneva, Jan 2006.
- [145] Wolfram Erdmann and PSI. Offline Primary Vertex Reconstruction with Deterministic Annealing Clustering. Technical Report CMS IN-2011/014, Jun 2011.
- [146] Thomas Speer, Kirill Prokofiev, R Frhwirth, Wolfgang Waltenberger, and Pascal Vanlaer. Vertex fitting in the cms tracker. Technical Report CMS-NOTE-2006-032, CERN, Geneva, Feb 2006.
- [147] Wolfgang Waltenberger. Adaptive Vertex Reconstruction. Technical Report CMS-NOTE-2008-033, CERN, Geneva, Jul 2008.
- [148] S. Baffioni, C. Charlot, F. Ferri, D. Futyan, P. Meridiani, et al. Electron reconstruction in CMS. *Eur.Phys.J.*, C49:1099–1116, 2007.
- [149] Emilio Meschi, T Monteiro, Christopher Seez, and Pratibha Vikas. Electron reconstruction in the cms electromagnetic calorimeter. Technical Report CMS-NOTE-2001-034, CERN, Geneva, Jun 2001.
- [150] M. Anfreville, D. Bailleux, J.P. Bard, A. Bornheim, C. Bouchand, et al. Laser monitoring system for the CMS lead tungstate crystal calorimeter. *Nucl.Instrum.Meth.*, A594:292–320, 2008.
- [151] Li-Yuan Zhang, D. Bailleux, A. Bornheim, Ke-Jun Zhu, and Ren-Yuan Zhu. Performance of the monitoring light source for the CMS lead tungstate crystal calorimeter. *IEEE Trans.Nucl.Sci.*, 52:1123–1130, 2005.
- [152] Y Yang. Inter-calibration of the cms barrel electromagnetic calorimeter using $\pi^0 \rightarrow \gamma\gamma$ decays. Technical Report CMS-CR-2007-069, CERN, Geneva, Oct 2007.
- [153] W. Adam, R. Fruhwirth, A. Strandlie, and T. Todorov. Reconstruction of electrons with the Gaussian sum filter in the CMS tracker at LHC. *eConf*, C0303241:TULT009, 2003, physics/0306087.
- [154] CMS Collaboration. Photon reconstruction and identification at $\sqrt{s} = 7$ tev. Technical Report CMS-PAS-EGM-10-005, CERN, 2010. Geneva, 2010.
- [155] Vardan Khachatryan et al. Prompt and non-prompt J/ψ production in pp collisions at $\sqrt{s} = 7$ TeV. *Eur.Phys.J.*, C71:1575, 2011, 1011.4193.
- [156] Michael H. Seymour. Jets in hadron collisions, 2000, hep-ph/0007051.
- [157] Gavin P. Salam. Towards Jetography. *Eur.Phys.J.*, C67:637–686, 2010, 0906.1833.

- [158] Gavin P. Salam and Gregory Soyez. A Practical Seedless Infrared-Safe Cone jet algorithm. *JHEP*, 0705:086, 2007, 0704.0292.
- [159] CMS Workbook. Twiki workbookjetanalysis. <https://twiki.cern.ch/twiki/bin/view/CMSPublic/WorkBookJetAnalysis>, July 2012.
- [160] CMS Collaboration. Performance of jet reconstruction with charged tracks only. Technical Report CMS-PAS-JME-08-001, CERN, 2009. Geneva, Aug 2009.
- [161] CMS Collaboration. Determination of the jet energy resolutions and jet reconstruction efficiency at cms. Technical Report CMS-PAS-JME-09-007, CERN, 2009. Geneva, Jul 2009.
- [162] CMS Collaboration. Commissioning of TrackJets in pp Collisions at 7 TeV. Technical Report CMS-PAS-JME-10-006, CERN, 2009. Geneva, Jul 2010.
- [163] Serguei Chatrchyan et al. Determination of Jet Energy Calibration and Transverse Momentum Resolution in CMS. *JINST*, 6:P11002, 2011, 1107.4277.
- [164] Matteo Cacciari and Gavin P. Salam. Pileup subtraction using jet areas. *Phys.Lett.*, B659:119–126, 2008, 0707.1378.
- [165] Arno Heister, Olga Kodolova, Viktor Konoplyanikov, Sergey Petrushanko, James Rohlf, Christopher Tully, and A Ulyanov. Measurement of jets with the cms detector at the lhc. Technical Report CMS-NOTE-2006-036, CERN, Geneva, Feb 2006.
- [166] CMS Collaboration. Jet energy resolution in cms at sqrt(s)=7 tev. Technical Report CMS-PAS-JME-10-014, CERN, Geneva, 2011.
- [167] CMS Collaboration. Cms strategies for tau reconstruction and identification using particle-flow techniques. Technical Report CMS-PAS-PFT-08-001, CERN, Geneva.
- [168] CMS Collaboration. Particle-flow event reconstruction in cms and performance for jets, taus, and met. Technical Report CMS-PAS-PFT-09-001, CERN, 2009. Geneva, Apr 2009.
- [169] CMS Collaboration. Commissioning of the particle-flow reconstruction in minimum-bias and jet events from pp collisions at 7 tev. Technical Report CMS-PAS-PFT-10-002, CERN, Geneva, 2010.
- [170] CMS Collaboration. Jet Energy Corrections: Official Software Tools for applying JEC Corrections and Uncertainties. <https://twiki.cern.ch/twiki/bin/view/CMSPublic/WorkBookJetEnergyCorrections#JetEnCorPFnoPU2012>, July 2013.
- [171] CMS Collaboration. Particle Flow in PAT (PF2PAT). <https://twiki.cern.ch/twiki/bin/view/CMSPublic/SWGuidePF2PAT>, February 2011.

- [172] K Nakamura and Particle Data Group. Review of particle physics. *Journal of Physics G: Nuclear and Particle Physics*, 37(7A):075021, 2010.
- [173] C. Weiser. A combined secondary vertex based B-tagging algorithm in CMS. Technical Report CERN-CMS-NOTE-2006-014, 2006.
- [174] CMS Collaboration. b-Jet Identification in the CMS Experiment. Technical Report CMS-PAS-BTV-11-004, 2012.
- [175] CMS Collaboration. CMS: The computing project. Technical design report. Technical Report CERN-LHCC-2005-023, 2005.
- [176] The CMS collaboration. Data Formats and Data Tiers in CMS. <https://twiki.cern.ch/twiki/bin/view/CMSPublic/WorkBookDataFormats>, February 2008.
- [177] Torbjorn Sjostrand, Stephen Mrenna, and Peter Z. Skands. PYTHIA 6.4 Physics and Manual. *JHEP*, 0605:026, 2006, hep-ph/0603175.
- [178] Johan Alwall, Pavel Demin, Simon de Visscher, Rikkert Frederix, Michel Herquet, et al. MadGraph/MadEvent v4: The New Web Generation. *JHEP*, 0709:028, 2007, 0706.2334.
- [179] Michelangelo L. Mangano, Mauro Moretti, Fulvio Piccinini, Roberto Pittau, and Antonio D. Polosa. ALPGEN, a generator for hard multiparton processes in hadronic collisions. *JHEP*, 0307:001, 2003, hep-ph/0206293.
- [180] Trevor Vickey Michael Spira, Monica Vazquez Acosta. MSSM Neutral Higgs. <https://twiki.cern.ch/twiki/bin/view/LHCPhysics/MSSMNeutral>, December 2013.
- [181] Robert V. Harlander and William B. Kilgore. Higgs boson production in bottom quark fusion at next-to-next-to-leading order. *Phys. Rev. D*, 68:013001, Jul 2003.
- [182] Stefan Dittmaier, Michael Krämer, and Michael Spira. Higgs radiation off bottom quarks at the fermilab tevatron and the cern lh. *Phys. Rev. D*, 70:074010, Oct 2004.
- [183] S. Dawson, C. B. Jackson, L. Reina, and D. Wackeroth. Exclusive higgs boson production with bottom quarks at hadron colliders. *Phys. Rev. D*, 69:074027, Apr 2004.
- [184] M. Frank, T. Hahn, S. Heinemeyer, W. Hollik, H. Rzehak, et al. The Higgs Boson Masses and Mixings of the Complex MSSM in the Feynman-Diagrammatic Approach. *JHEP*, 0702:047, 2007, hep-ph/0611326.
- [185] S. Heinemeyer, W. Hollik, and G. Weiglein. FeynHiggs: A Program for the calculation of the masses of the neutral CP even Higgs bosons in the MSSM. *Comput.Phys.Commun.*, 124:76–89, 2000, hep-ph/9812320.

- [186] S. Heinemeyer, W. Hollik, and G. Weiglein. The Masses of the neutral CP - even Higgs bosons in the MSSM: Accurate analysis at the two loop level. *Eur.Phys.J.*, C9:343–366, 1999, hep-ph/9812472.
- [187] A. Djouadi and R. M. Godbole. Electroweak symmetry breaking at the LHC. pages 47–74, 2009, 0901.2030.
- [188] T. Aaltonen et al. Search for Higgs Bosons Produced in Association with b -quarks. *Phys.Rev.*, D85:032005, 2012, 1106.4782.
- [189] Victor Mukhamedovich Abazov et al. Search for neutral Higgs bosons in the multi- b -jet topology in 5.2fb^{-1} of $p\bar{p}$ collisions at $\sqrt{s} = 1.96$ TeV. *Phys.Lett.*, B698:97–104, 2011, 1011.1931.
- [190] Luminosity POG of the CMS experiment. The official CMS Luminosity Calculation Tools. <https://twiki.cern.ch/twiki/bin/viewauth/CMS/LumiCalc>, September 2013.
- [191] CMS collaboration. Datasets for pp-collisions in 2011. <https://twiki.cern.ch/twiki/bin/viewauth/CMS/Collisions2011Analysis>, 2012.
- [192] Luminosity POG of the CMS experiment. [Cert_160404-180252_7TeV_PromptReco_Collisions11_JSON.txt](#), [Cert_170249-172619_7TeV_ReReco5Aug_Collisions11_JSON_v3.txt](#).
- [193] Zero bias and HF-based minimum bias triggering for pp collisions at 14 TeV in CMS. Technical Report CMS-PAS-QCD-07-002, 2007.
- [194] CMS Collaboration. BSC Triggers . <https://twiki.cern.ch/twiki/bin/viewauth/CMS/BSCTrigger>, 2012.
- [195] Inc. Wolfram Research. Erf function. <http://mathworld.wolfram.com/Erf.html>, 2012.
- [196] Pileup Jet Identification. Technical Report CMS-PAS-JME-13-005, CERN, Geneva, 2013.
- [197] Andreas Hoecker, Peter Speckmayer, Joerg Stelzer, Jan Therhaag, Eckhard von Toerne, and Helge Voss. TMVA: Toolkit for Multivariate Data Analysis. *PoS, ACAT*:040, 2007, physics/0703039.
- [198] Stephen Mrenna. Event Shapes. http://cepa.fnal.gov/psm/simulation/mcgen/lund/pythia_manual/pythia6.3/pythia6301/node213.html, October 2013.
- [199] K. Pearson. On the criterion that a given system of deviations from the probable in the case of a correlated system of variables is such that it can be reasonably supposed to have arisen from random sampling. *The London, Edinburgh, and Dublin Philosophical Magazine and Journal of Science*, 50:157–175, 1900.
- [200] W. G. Cochran. The χ^2 test of goodness of fit. *AMS*, 23:315, 1952.

- [201] CMS Collaboration. b Tag Vertexing Physics Object Group . <https://twiki.cern.ch/twiki/bin/viewauth/CMS/BtagPOG>, October 2013.
- [202] Inc. Wikimedia Foundation. Nuisance parameter. http://en.wikipedia.org/wiki/Nuisance_parameter, January 2014.
- [203] A.L. Read. Presentation of search results: the cls technique. *J. Phys. G: Nucl. Part. Phys.*, 28:010001, Jul 2002.
- [204] Lorenzo Moneta. The RooStats Wiki. <https://twiki.cern.ch/twiki/bin/view/RooStats>, October 2013.
- [205] G. Schott and for the RooStats Team. RooStats for Searches. *ArXiv e-prints*, March 2012, 1203.1547.
- [206] I. Antcheva et al. ROOT - A C++ framework for petabyte data storage, statistical analysis and visualization. *Computer Physics Communications*, 180(12):2499 – 2512, 2009.
- [207] W. Verkerke and D. Kirkby. The RooFit toolkit for data modeling. *ArXiv Physics e-prints*, June 2003, physics/0306116.
- [208] S.S. Wilks. The Large-Sample Distribution of the Likelihood Ratio for Testing Composite Hypotheses. *Annals Math.Statist.*, 9(1):60–62, 1938.
- [209] Inc. Wikimedia Foundation. p-value. <http://en.wikipedia.org/wiki/P-value>, December 2013.
- [210] Inc. Wikimedia Foundation. Table of χ^2 value vs p-value. http://en.wikipedia.org/wiki/Chi-squared_distribution#Table_of_.CF.872_value_vs_p-value, February 2014.
- [211] Combination of SM Higgs Searches. Technical Report CMS-PAS-HIG-11-032, CERN, Geneva, 2011.
- [212] Glen Cowan, Kyle Cranmer, Eilam Gross, and Ofer Vitells. Asymptotic formulae for likelihood-based tests of new physics. *Eur.Phys.J.*, C71:1554, 2011, 1007.1727.
- [213] Inc. Wikimedia Foundation. Normal distribution. http://en.wikipedia.org/wiki/Normal_distribution, December 2013.
- [214] Inc. Wikimedia Foundation. Type II error. http://en.wikipedia.org/wiki/Type_I_and_type_II_errors#Type_II_error, February 2014.
- [215] Marcela S. Carena, S. Heinemeyer, C.E.M. Wagner, and G. Weiglein. Suggestions for improved benchmark scenarios for Higgs boson searches at LEP-2. 1999, hep-ph/9912223.
- [216] S. Heinemeyer, W. Hollik, and G. Weiglein. The masses of the neutral cp-even higgs bosons in the mssm: Accurate analysis at the two-loop level. *The European Physical Journal C - Particles and Fields*, 9(2):343–366, 1999.

- [217] Michael Spira, Monica Vazquez Acosta, and Trevor Vique. Available Xsection scans . https://twiki.cern.ch/twiki/bin/view/LHCPhysics/MSSMNeutral#Available_Xsection_scans, December 2013.
- [218] LHC Higgs Cross Section Working Group. Higgs Cross Section Calculation at 7, 8 and 14 TeV . <https://twiki.cern.ch/twiki/bin/view/LHCPhysics/CrossSectionsCalc>, December 2013.
- [219] Charalampos Anastasiou, Stephan Buehler, Franz Herzog, and Achilleas Lazopoulos. Inclusive Higgs boson cross-section for the LHC at 8 TeV. *JHEP*, 1204:004, 2012, 1202.3638.
- [220] LHC Higgs Cross Section Working Group. An update in CERN Report 3. <https://twiki.cern.ch/twiki/bin/view/LHCPhysics/CERNYellowReportPageAt7TeV>, September 2013.
- [221] T. Aaltonen et al. Search for Neutral Higgs Bosons in Events with Multiple Bottom Quarks at the Tevatron. *Phys.Rev.*, D86:091101, 2012, 1207.2757.
- [222] S. Schael et al. Search for neutral MSSM Higgs bosons at LEP. *Eur.Phys.J.*, C47:547–587, 2006, hep-ex/0602042.